Characterization of the Timing Properties of the SuperNEMO Demonstrator. Extraction of the SuperNEMO Sensitivity to the Axial-Vector Coupling Constant

Malak Hoballah

université
PARIS-SACLAY

Characterization of the Timing Properties of the SuperNEMO Demonstrator. Extraction of the SuperNEMO Sensitivity to the Axial-Vector Coupling Constant

Caractérisation temporelle du calorimètre du démonstrateur SuperNEMO. Etude de la sensibilité de SuperNEMO à la constante de couplage axial-vecteur

Thèse de doctorat de l'université Paris-Saclay

École doctorale n°576 Particules, Hadrons, Energie et Noyau : Instrumentation, Imagerie, Cosmos et Simulation (PHENIICS)
Spécialité de doctorat : physique des particules
Graduate School : Physique
Référent : Faculté des sciences d'Orsay

Thèse préparée dans l'unité de recherche **IJCLab** (Université Paris-Saclay, CNRS), sous la direction de **Laurent SIMARD**, Maître de conférences

Thèse soutenue à Paris-Saclay, le 15 Septembre 2022, par

Malak HOBALLAH

Composition du jury

Marie-Hélène SCHUNE Directrice de recherche, Laboratoire de physique des 2 infinis - Irène Joliot-Curie	Présidente
Corinne AUGIER Professeure, Université Claude Bernard Lyon 1	Rapporteure & Examinatrice
Antoine KOUCHNER Professeur, Université de Paris	Rapporteur & Examinateur
Fedor ŠIMKOVIC Professeur, Comenius University Bratislava	Examinateur
Emmanuel CHAUVEAU Chargé de recherche, Laboratoire de Physique des 2 infinis - Bordeaux	Examinateur
Laurent SIMARD Maître de conférences, Université Paris-Saclay	Directeur de thèse

THESE DE DOCTORAT
NNT : 2022UPASP086

université PARIS-SACLAY

ÉCOLE DOCTORALE
Particules, hadrons, énergie et noyau : instrumentation, imagerie, cosmos et simulation (PHENIICS)

Titre : Caractérisation temporelle du calorimètre du démonstrateur SuperNEMO. Etude de la sensibilité de SuperNEMO à la constante de couplage axial-vecteur

Mots clés : Double beta désintégration, neutrinos de Majorana, violation du nombre leptonique, résolution temporelle, calibration temporelle, quenching de la constante de couplage axial-vecteur

Résumé : La désintégration double bêta sans neutrinos ($0\nu\beta\beta$) est une désintégration radioactive hypothétique au-delà du Modèle Standard, caractérisée par la violation du nombre leptonique et l'émission de deux électrons et aucun antineutrino électronique. L'expérience SuperNEMO est conçue pour rechercher cette désintégration. Sa sensibilité d'exclusion est de 10^{26} ans sur la demi-vie $0\nu\beta\beta$, correspondant à une masse de Majorana effective de $<m_{\beta\beta}> <$ 40-100 meV . Pour le bon fonctionnement du détecteur, une caractérisation des propriétés temporelles du calorimètre a été réalisée. Le calorimètre a été étaloneé en temps et la résolution temporelle a été extraite pour chaque module optique à l'aide de prise de données dédiées avec une source ^{60}Co placée derrière le calorimètre. La source ^{60}Co est émet deux gammas (quasi) simultanément et la détection s'effectue avec des coïncidences entre les différents modules optiques. L'étalonnage du temps a atteint une précision de $<\sim$ 0,2 ns, suffisante pour effectuer le rejet du bruit de fond à l'aide des calculs de temps de vol. La résolution temporelle moyenne pour les photomultiplicateurs 8" des murs est de 0,619 $\pm$ 0,002 (stat) + 0,049 (sys) - 0,004 (sys) pour les gammas à 1 MeV.

Le taux de décroissance $0\nu\beta\beta$ dépend fortement de la constante de couplage du vecteur-axial g_A, et la contrainte de cette constante est cruciale pour estimer précisément ce taux. Des calculs théoriques plus précis de la double désintégration bêta permise par le modèle standard ont conduit à de nouvelles dépendances du taux en foction de facteurs d'espace de phase avec différentes cinématiques. Par conséquent, une mesure précise de l'énergie de chaque électron peut contraindre la constante de couplage du vecteur axial. La sensibilité de SuperNEMO au quenching de la constante de couplage du vecteur axial a été étudiée à l'aide de données simulées dans l'environnement SuperNEMO.

Après avoir introduit la physique des neutrinos et des désintégrations double-bêta, et en détail l'expérience SuperNEMO, je présente le travail détaillé effectué pour extraire la résolution temporelle et calibrer en temps le calorimètre SuperNEMO, et l'analyse pour estimer la sensibilité de SuperNEMO au quenching de la constante de couplage du vecteur axial g_A.

université PARIS-SACLAY

ÉCOLE DOCTORALE
Particules, hadrons, énergie et noyau : instrumentation, imagerie, cosmos et simulation (PHENIICS)

Title : Characterization of the Timing Properties of the SuperNEMO Demonstrator. Extraction of the SuperNEMO Sensitivity to the Axial-Vector Coupling Constant

Keywords : Double beta decay, Majorana neutrinos, Violation of the leptonic number, Time resolution, Time calibration, Quenching of the axial-vector coupling Constant

Abstract : Neutrinoless double-beta decay ($0\nu\beta\beta$) is a hypothetical radioactive decay beyond the Standard Model, characterized by the violation of the leptonic number through the emission of two electrons and no electron anti-neutrinos. The SuperNEMO experiment is designed to search for this decay. Its exclusion sensitivity is 10^{26} years on the $0\nu\beta\beta$ half-life, corresponding to an effective Majorana mass at $<m_{\beta\beta}> <$ 40-100 meV. For the correct performance of the detector, a timing study of the calorimeter has been performed. The calorimeter has been calibrated in time and the time resolution has been extracted for each optical module using dedicated data taking runs with a ^{60}Co source placed behind the calorimeter. The ^{60}Co source emits two gammas (almost) simultaneously and the detection is performed by finding coincidences between the different optical modules. The time calibration reached a precision of $<\sim$ 0.2 ns, sufficient to perform background rejection using time of flight calculations. The mean time resolution for 8" photomultipliers of the main walls is found to be 0.619 $\pm$ 0.002 (stat) + 0.049 (sys) - 0.004 (sys) for gammas at 1 MeV.

The $0\nu\beta\beta$ decay rate depends strongly on the axial-vector coupling constant g_A, and constraining of this constant is crucial to estimate accurately this rate. More accurate theoretical calculations of the double beta decay allowed by the standard model have led to new dependencies of the rate on phase space factors with different kinematics. Therefore, an accurate measurement of the energy of each electron can constrain the axial-vector coupling constant. The sensitivity of SuperNEMO to the quenching of the axial-vector coupling constant has been studied using simulated data in the SuperNEMO environment.

After introducing the physics of neutrinos and double-beta decays, and in details the SuperNEMO experiment, I present the detailed work performed to extract the time resolution and calibrate in time the SuperNEMO calorimeter, and the analysis to find the sensitivity of SuperNEMO to the quenching of the axial-vector coupling constant g_A.

Table des matières

Introduction

Neutrinos are neutral particles of the Standard Model (SM) that were formalized as massless. In the decades that had passed, experiments have discovered neutrinos oscillations where neutrino of a given flavr can be converted into a neutrinos of another flavor. This proved that the formalism of massless neutrinos in the Standard Model was not correct, highlighting the need for beyond the SM description. As mentioned, neutrinos are neutral, then the particle could be identical to its anti-particle and hence a Majorana particles. Or otherwise, a Dirac particle. The Majorana nature of the neutrino is introduced as extension of Standard Model, and could explain both the smallness of the neutrinos masses via the see-saw mechanism and the matter-antimatter asymmetry currently observed in the universe. The neutrino mass term in the Lagrangian can therefore either be a Dirac one, like for charged fermions, a Majorana mass term, or a combination of both.

The method to determine the nature of neutrinos is by searching for the neutrinoless double beta decay. It is the counter part of the double beta decay but without the emission of two neutrinos, i.e the electrons will carry the full energy of the decay. This decay not allowed by the SM as it violates the leptonic number by two. If this hypothetical decay is observed, it would prove the Majorana nature regardless of the decay mechanism.

The search for neutrinoless double beta decay is pursued by many experiments following different experimental approaches. Among them, SuperNEMO is using a tracker-calorimeter method. Its demonstrator is at the end of commissioning phase and is planned to start taking data in 2023. With its detection technique, it is able to study several double beta isotopes, but the current isotope used is 6.23 kg of ^{82}Se installed in the form of thin foils. The foils are surrounded by a wire drift chamber with cells operating in Geiger mode, allowing a 3D reconstruction of the charged particle tracks. Then, this setup is surrounded by a calorimeter made of plastic scintillators coupled to radio-pure photomultipliers that register individual particle energies and time of detection. Eventually, everything will be enclosed by a magnetic coil to identify charged particles, anti-radon tent, a gamma and a neutron shielding. This detector technique allows an efficient particle identification and background rejection to achieve ultra-low background.

The first chapter of this thesis provides an introduction to neutrino physics, double beta decay and neutrinoless double beta decay. Provided also is a modest introduction of the current models of nuclear matrix element calculations and the importance of determining the value of the axial-vector coupling constant. At the end there is an overview of the current state of art of the different experiments.

The second chapter is a detailed description of the SuperNEMO detection technique, in particular for the demonstrator.

Chapter three is where the first part of my thesis work is presented. Here, I

show the method followed using a ^{60}Co gamma emitting source to perform time calibration to the full calorimeter. Where I synchronize the different optical modules to a single reference optical module of choice. I also describe how I extract the time resolution for gammas for every optical module, using the same data.

Chapter four is the second part of my thesis. I introduced the claims that the axial-vector coupling constant is quenched and how we can study them by studying the SM allowed double beta decay energy spectra. The determination of the quenching factor is very important for a good calculation of the decay rate of double beta decay, and in a less straightforward manner the neutrinoless double beta decay. I present the results of the analysis performed using simulated data samples inside the SuperNEMO environment (geometry and background). I extract the best method (amongst those tried) and show that SuperNEMO can set constraint on the quenching value of the axial-vector coupling constant. Also, I show that SuperNEMO with its detection technique is able to have higher sensitivity to constrain the axial-vector coupling constant value, using the ability to measure the full kinematics of the final state.

1 - Neutrinos

1.1 . The Standard Model

The Standard Model of particle physics (SM) is a gauge theory describing particle interactions, meaning its dynamics and basic structure is set by the gauge interaction and must follow the local symmetry group SU(3)×SU(2)$_L$×U(1). The model describes the interaction of elementary particles, called fermions, of the three fundamental forces of nature : the weak, strong and electromagnetic, though this model doesn't describe the fourth force, that is gravity. These interactions occur via the exchange of spin-1 gauge fields known as bosons. SU(3) describes the color charge of the strong force, SU(2)$_L$ the left handed chirality and U(1) the hypercharge, SU(2)$_L$×U(1) describes the electroweak interaction. The latter is what interests us in studying neutrinos.

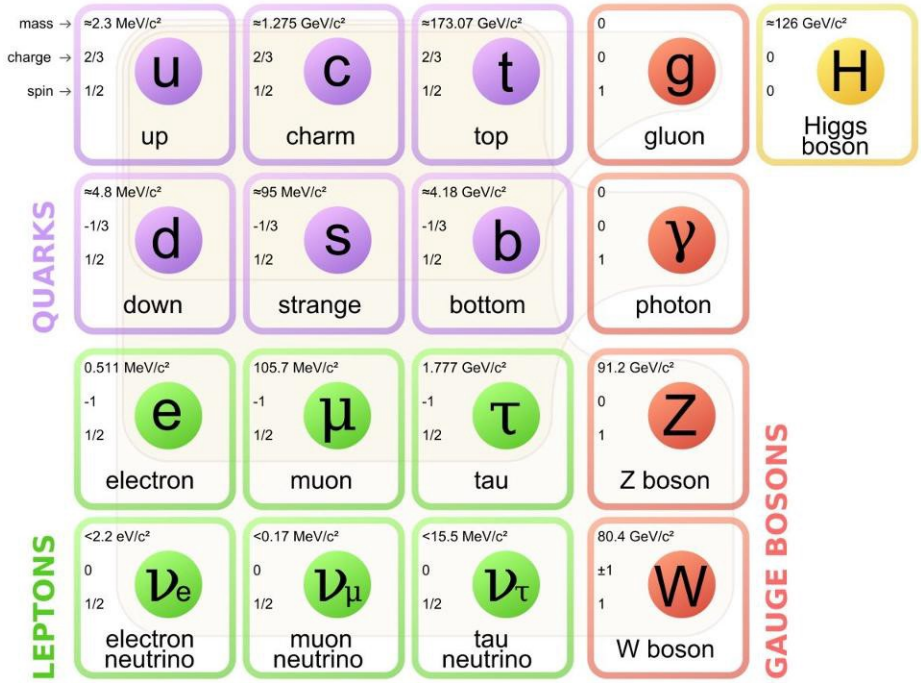

Figure 1.1 – The elementary particles of nature according to the Standard Model of particle physics.

1.1.1 . Fermions

In the Standard Model, elementary particles are called fermions when having a half odd integer spin and obeying the Pauli exclusion principle. They are the building blocks of matter and can be classified into three generations that have similar

interaction properties and are identical in their properties (gauge interactions) but differ only by their mass and flavor quantum number (see figure 1.1).

Quarks : The up, down, charm, strange, top and bottom quarks (and their 6 anti-quarks) carry spin, mass, color and electric charges that allow them to experience all the four fundamental forces of nature. They are held together by the strong force to form hadrons of which the most stable are the protons and neutrons that make up the atomic nuclei and hence most of the visible matter around us.

Leptons : The electron, muon, tau and corresponding neutrinos (see figure 1.1) are different from the quarks in the sense that they are colorless and do not interact via the strong force. Neutrinos are neutral particles and do not interact via the electromagnetic force.

1.1.2 . Bosons

Bosons are spin-1 particles, they are 8 massless gluons and 1 massless photon, for the strong and electromagnetic interactions, respectively, and 3 massive bosons ($W^{\pm}$ and Z) for the weak interaction.

1.1.3 . The Problem of Gauge Boson Masses : Spontaneous Symmetry Breaking

The gauge symmetry (mentioned in the beginning) is broken by the vacuum, which triggers the Spontaneous Symmetry Breaking (SSB) of the electroweak group to the electromagnetic subgroup. The SSB mechanism generates the masses of the weak gauge bosons ($W^{\pm}$ and Z^0), and gives rise to the appearance of a physical scalar particle in the model, the so-called 'Higgs' boson. The fermion masses and mixings are also generated through the SSB [1].

The Standard Model derives the charged and neutral currents that describe the weak force, and the gauge symmetry insures the renormalizability of the Lagrangian. However, the gauge bosons in the model are massless particles and this poses a problem for the W and Z bosons as they need to be massive particles to describe reality. So, the difficulty now is to break the gauge symmetry while also conserving the renormalizability of the Lagragian, so we need a new scalar field.

We consider a Lagrangian that is invariant under a group of transformations of local SU(2)×U(1) and has a degenerate set of states with minimal energy. By selecting arbitrarily one of these states as the ground state of the system, it is said that the symmetry is spontaneously broken to the subgroup $U(1)_{QED}$ (see figure 1.2). By following these steps, we find that $W^{\pm}$ and Z bosons have acquired masses, but not the photon because $U(1)_{QED}$ is an unbroken (or true) symmetry. This method introduces a new scalar particle into the model called the Higgs boson which particles interact with and acquire their masses [1].

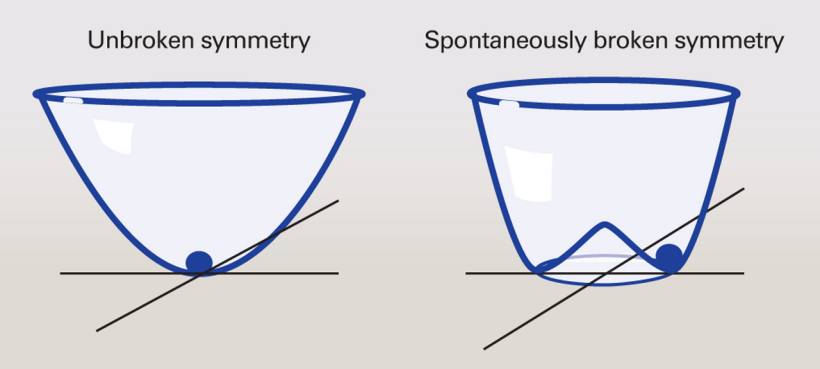

Figure 1.2 – To the right : A vanishing quantum field at its lowest energy state, in this case the symmetry is said to be unbroken. To the right : The field interacts with its self it creates an energy "hump" and has to minimize its energy state and break the symmetry.

1.1.4 . Beyond the Standard Model

Although the Standard Model provides good description for most of the particle interactions, it still has many limitations and cannot explain :

- Matter and Anti-Matter Asymmetry : There is no process in the Standard Model that allows a violation of the leptonic or baryonic number, and hence there should not be an excess of matter over anti-matter. The existence of the universe with matter dominating still remains to be explained. The Sakharov conditions (CP violation, baryonic number violation, interactions out of thermal equilibrium) give a way that enables this asymmetry, but the conditions require physics beyond the SM.

- Neutrino Masses : When the SM was formalized, neutrinos were considered massless, but the detection of neutrino oscillations proved that neutrinos indeed possess mass. The constrains from single beta decay and cosmological studies show that they are very light compared to the other fermions. As their masses are much smaller compared to the ones of charged leptons and quarks, the origin of their masses can be different : either they can be Dirac like the other fermions where the particles are different from their anti-particle. Or they can be Majorana particles such that the particles are identical to their own anti-particles.

- Dark Matter and Dark Energy : The SM currently describes only 5% of the universe, that is matter as we know it. There exists 27% of the universe labeled as dark matter and the rest as dark energy. No candidate is provided by the SM for dark matter, and dark energy cannot be explained.

1.2 . Neutrino Formalism

In the SM Lagrangian, we can separate the charged and neutral current interactions in order to study the weak force. The Lagrangian concerning the relevant

interactions of neutrinos then becomes as in equation (1.1) :

$$\mathcal{L}_{SM} = -\frac{g}{\sqrt{2}} \sum_{\alpha=e,\mu,\tau} \overline{\nu}_{\alpha L} \gamma^{\mu} l_{\alpha L} W_{\mu} - \frac{g}{2cos\theta_W} \sum_{\alpha=e,\mu,\tau} \overline{\nu}_{\alpha L} \gamma^{\mu} \nu_{\alpha L} Z_{\mu} + h.c \quad (1.1)$$

One notices that the first part of the equation contains the W boson and hence reflects the charged current concerned with neutrino absorption and emission by, or with the same flavour charged lepton, while the other part contains the Z neutral boson that couples to a neutrino and its own anti-neutrino.

The number of active neutrinos that experience the interactions above is determined by the width of the Z boson which is measured precisely at the Large Electron-Positron collider (LEP) (see figure 1.3), the number is found to be 3 hence the three neutrino flavors : electron (ν_e) , muon (ν_μ) and tau (ν_τ) neutrinos. This is true if the masses of neutrinos is less than 45.5 GeV/c^2. Hence, this does not exclude the possibility of having other neutrinos that cannot feel the weak interaction, they are called sterile neutrinos and are beyond the SM physics [2].

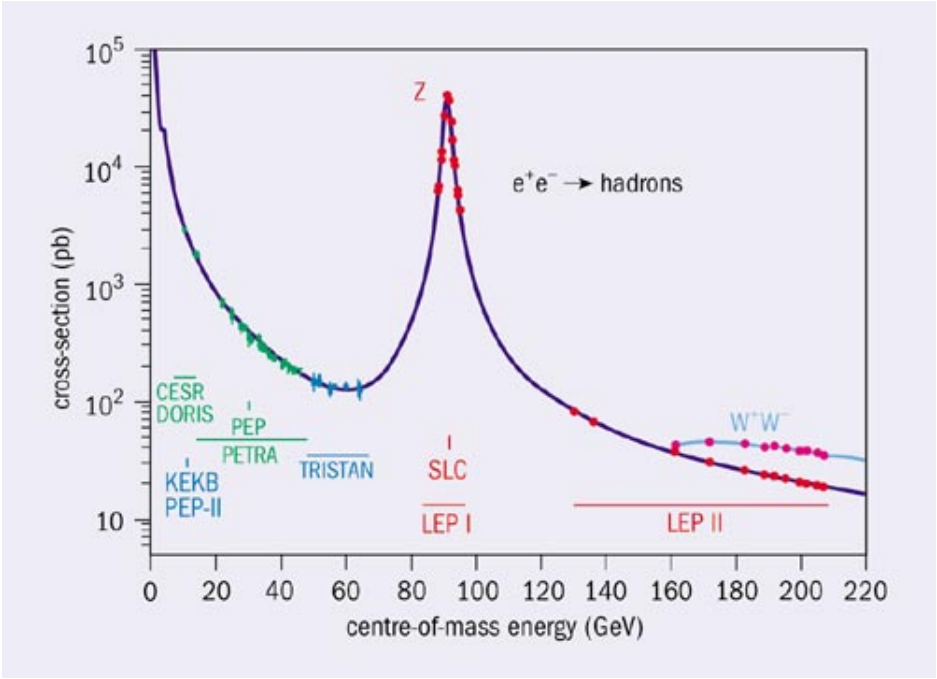

Figure 1.3 – The e^+e^- annihilation cross-section to hadrons, from initial low energies in early colliders to the maximum energy at LEP. The fit of the Z peak gave back a mass of 91.1875 $\pm$ 0.0021 GeV [3].

Since neutrinos are neutral particles and only interact through weak force and gravity (due to their mass, discussed in chapter 1.2.1), so they were not detected

by seeing its interaction in the detector. When the first studies of the beta decays started (equation 1.2), neutrinos were not hypothesized yet and it was a surprise that these decays exhibit a continuous spectrum, and scientists started to worry about the validity of energy conservation law. To solve this problem, Pauli suggested the existence of a new particle later named neutrino, that is emitted along with the electron and is not directly detected as it interacts very weakly with ordinary matter due to its very small cross-section and generally escapes the detector. One can have its energy attributed to the "missing" energy of the decay at the detector end [4].

$$ {}^{Z}_{A}X \rightarrow {}^{Z+1}_{A}Y + e^{-} + \overline{\nu_e} \tag{1.2} $$

To insure a conservation of the leptonic number (which is an accidental symmetry of the SM), the neutrino in equation (1.2) should be an anti-neutrino particle.

It has been long thought that neutrinos are massless until the observation of neutrino oscillations and later the experimental discovery confirming that neutrinos are massive, by the Super-Kamiokande and the Sudbury Neutrino observatories, which were recognized with the 2015 Nobel Prize for Physics [5]. The oscillation of neutrinos from one flavor to another was only possible if they had mass contrary to what was hypothesized in the SM.

1.2.1 . Neutrino Oscillations

The first observation of the oscillations happened in the 1960s when a deficit was observed in number of detected electron neutrinos coming from the sun, at the Davis experiment in the Homestake mine [6]. It was thought that either the Solar Standard Model is wrong, or the neutrinos are changing into other particles which are not detected. In 1957, the idea of neutrino oscillations from one flavor to another as a purely quantum mechanical phenomenon was introduced.

Neutrino Mixing

To talk about oscillations, we first introduce the idea of neutrino mixing. It is the idea that we describe neutrino with different basis that do not coincide : on one side the flavor basis (so the tau, electron and muon flavors) and on the other the mass states which have definite masses. Neutrinos interact as flavor states but propagate as mass states, but the two states are not aligned which is common in quantum mechanics, and the connection between these two is a unitary matrix called the Pontecorvo-Maki-Nakagawa-Sakata (PMNS) matrix (see equation 1.3)

$$ |\nu_\alpha> = \sum_i U^*_{\alpha i} |\nu_i> \qquad \alpha = e, \mu, \tau \;\; ; \;\; i = 1, 2, 3 \tag{1.3} $$

The unitary matrix then enters into the charged current (CC) Lagrangian (equation 1.1) where the flavor states of the neutrinos are expressed in terms of the mass states as in equation (1.4).

$$\mathcal{L}_{CC} = -\frac{g}{\sqrt{2}} \sum_{k\alpha} U^*_{\alpha i} \overline{\nu}_{kL} \gamma^\rho l_{\alpha L} W_\rho + h.c \tag{1.4}$$

So, if a neutrino is produced, it is described by a superposition of massive states in which the weight is given by the entries of the PMNS matrix. For the mixing of the 3 neutrino flavors the PMNS matrix is described as follows :

$$U_{\alpha i} = U_{PMNS} = \begin{pmatrix} 1 & 0 & 0 \\ 0 & c_{23} & s_{23} \\ 0 & -s_{23} & c_{23} \end{pmatrix} \begin{pmatrix} c_{13} & 0 & s_{13}e^{i\delta} \\ 0 & 1 & 0 \\ -s_{13}e^{-i\delta} & 0 & c_{13} \end{pmatrix} \begin{pmatrix} c_{12} & s_{12} & 0 \\ -s_{12} & c_{12} & 0 \\ 0 & 0 & 1 \end{pmatrix}$$

$$\begin{pmatrix} 1 & 0 & 0 \\ 0 & e^{i\alpha_{21}/2} & 0 \\ 0 & 0 & e^{i\alpha_{31}/2} \end{pmatrix}$$

where there are three mixing angles denoted as : $c_{ij} = cos(\theta_{ij})$ and $s_{ij} = sin(\theta_{ij})$ with $i, j = 1, 2, 3$. The Dirac phases δ that are physical and the Majorana phases α that depend on the nature of neutrinos : if they are Dirac particles, then only the Dirac phases contribute, while if they are Majorana particles then two extra phases are added (the Majorana phases). These two phases are associated to the CP violation.

Scientists have been studying oscillations through solar (θ_{12}, Δm^2_{12}), atmospheric (θ_{23}, Δm^2_{23}), reactor (θ_{13}, Δm^2_{13}) and accelerator (θ_{23}, δ_{CP}) experiments and have been able to constrain the mixing angle parameters of the PMNS matrix and two mass-squared differences between two neutrino flavors.

For neutrino oscillations happening most of the time in vacuum, the Hamiltonian eigenvalues (that are the energies) depend on the masses, and the difference between the production of the neutrino in a certain flavor and its detection in a different one, adding its propagation (which describes that there is a mass state), these two points ensures that neutrino have masses.

Oscillation Probability

A neutrino of a certain flavor α is produced by a certain decay, it is a superposition of the different mass eigenstates. Evolving this state in space and time by the solution of the Schrodinger equation with free Hamiltonian and projecting over the detection flavor state β, the probability of oscillation is retrieved as :

$$P(\nu_\alpha \to \nu_\beta) = |\sum_i U^*_{\alpha i} U_{\beta i} e^{-i\frac{\Delta m^2}{2E}L}|^2 \tag{1.5}$$

Where Δm^2 is the difference of mass phases of the massive neutrinos that are acquired while propagating or oscillating, and L is the distance traveled from source to the detector. Equation (1.5) implies two things, that neutrinos should be

massive particles and there indeed is neutrino mixing otherwise the neutrino states do not evolve.

1.2.2 . Dirac Mass

In the SM, neutrinos do not acquire masses and they do not mix. Neutrinos, contrary to other fermions, are not sensitive to right handed current and hence they do not have Dirac masses. To solve the latter problem, we first introduce right handed neutrinos and then a Lagrangian of a Yukawa interaction (y_ν) between the leptonic doublet (L), the Higgs field (H) and the right handed neutrino (ν_R) emerges as in equation (1.6).

$$\mathcal{L} = -y_\nu \overline{L}.\tilde{H}\nu_R + h.c \tag{1.6}$$

Where

$$L = \begin{pmatrix} \nu_L \\ e_L \end{pmatrix} \quad and \quad \tilde{H} = \begin{pmatrix} H^{0,*} \\ -H^- \end{pmatrix} \tag{1.7}$$

Equation (1.6) is SU(2) invariant and respects all the symmetries and when the Higgs comes in, it will give mass to the neutrinos as in equation (1.8).

$$m_\nu \sim y_\nu v_H \tag{1.8}$$

The neutrino mass then has a dependence on the Yukawa and Higgs couplings, the Higgs field expectation value is known to be around 246 GeV, but we know that neutrinos have an sub-eV scale mass, so the Yukawa coupling needs to be 10^{-12}, or even less, which is extremely small compared to the couplings to the other fermions and this is not understood.

1.2.3 . Majorana Neutrinos

Why Look for Majorana Neutrinos

The unexplainability of the smallness of the Yukawa coupling mentioned above led to the consideration of another theory to describe the masses. In 1937, Ettore Majorana hypothesized the existence of neutrinos that are their own anti-particles, this scenario is possible only if the particle is neutral and that the total lepton number is not conserved in order to generate their masses [7].

The Majorana mass term is another way to describe the neutrino masses, it is Lorentz invariant, meaning it is allowed in the Lagrangian but it however breaks the SU(2) (gauge) symmetry. In order to have an SU(2) invariant term, it is necessary to introduce a dimension 5 operator (divided by a scale M), which is usually introduced when you extend the Standard Model, as in equation (1.9).

$$-\mathcal{L}^L_{mass} = \lambda \frac{L.HL.H}{M} = \frac{\lambda v_H^2}{M} \nu_L^T C^\dagger \nu_L \tag{1.9}$$

Where C is the charge conjugate matrix and $\lambda = \frac{g_{eff}}{2}$ is a dimensionless coefficient corresponding to the effective coupling of the interaction. Notice that we have to divide by a mass term to keep an equality to the Lagrangian in terms of dimensionality. The final form of equation (1.9) becomes :

$$\mathcal{L}^L_{mass} = -\frac{\lambda v_H^2}{M}(\overline{\nu}_L \nu_L^c + \overline{\nu_L^c}\nu_L) \tag{1.10}$$

Equation (1.10) describes the mass term for left handed neutrinos under the Majorana hypothesis, it actually is not renormalizable in the SM since it is not invariant under SU(2) x U(1), but it is allowed if you introduce new physics at high energies to cut off the infinities created. The mass "M" term can be looked at as a very heavy particle that can not be seen at low energies but it mediates the interaction which gives rise to these neutrino masses. This heavy particle will be called a Majorana particle and a Majorana mass term will be associated as :

$$m_R = \frac{g_{eff} v_H^2}{M} \tag{1.11}$$

Since the particle is the same as its anti-particle, one can see from equation (1.9) that there is a violation of the leptonic number by 2, which is not allowed in the SM as leptonic number conservation is a true symmetry.

See-Saw Mechanism

Combining both the Dirac mass term and the Majorana mass term will give rise to what we call the see-saw mechanism and the Lagrangian becomes as in equation (1.12) :

$$L_{mass} = \frac{1}{2}\left(\overline{\nu_L}\ \overline{\nu_R}^c\right)\begin{pmatrix} m_L & m_D \\ m_D & m_R \end{pmatrix}\begin{pmatrix} \nu_L^c \\ \nu_R \end{pmatrix} + h.c \tag{1.12}$$

Where m_L and m_R represent the Majorana masses of the left and right handed neutrinos, respectively. m_D represents the Dirac mass of neutrinos.

Looking at equation (1.12), multiplying the matrices will describe how the neutrinos and anti-neutrinos couple together. We look for the eigenvalues of the matrix in order to know the masses of the neutrinos.

As mentioned before, the left handed Majorana term is not renormalizable in the SM, as it doesn't obey the right symmetries, we set it to zero :

$$m_L = 0 \tag{1.13}$$

Then, the mass eigenvalues are :

$$\lambda = \frac{m_R}{2} \pm \frac{m_R}{2}\sqrt{1 + \frac{4m_D^2}{m_R^2}} \tag{1.14}$$

If we have a right handed Majorana mass term that is a lot bigger than the Dirac mass term, i.e $m_R >> m_D$, then we can simplify equation (1.14) to become :

$$\lambda_1 = m_R \quad and \quad \lambda_2 = \frac{2m_D^2}{m_R} \tag{1.15}$$

So, what the see-saw mechanism does is that it takes the Dirac mass of the neutrinos mentioned in subsection (1.2.2), and splits them into 2 heavy right handed Majorana neutrinos and 2 light Majorana neutrinos as in equations (1.15), respectively.

Type 1 See-Saw Type 1 see-saw mechanism is the simplest and most popular mechanism to describe the neutrino masses. It says that if the right handed neutrinos Majorana mass is very large at the Grand Unification Theory scale, meaning about 10^{15} GeV and the Dirac masses are of the electroweak scale, meaning about 100 GeV then the mass eigenvalues in equation (1.15) become :

$$M_\nu \sim \frac{m_D^2}{m_R} \sim 0.01eV \quad and \quad m_R \sim 10^{15}GeV \tag{1.16}$$

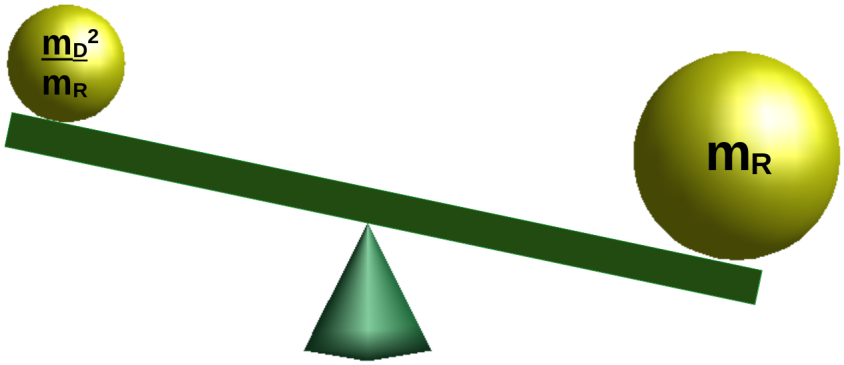

Figure 1.4 – A schematic representation of the Seesaw Mechanism. "m_D" represents the Dirac mass of the order of 100 GeV and "m_R" is the right handed Majorana mass term of the GUT scale $\sim 10^{15}$ GeV

The key experiment to test whether neutrinos are Majorana particles or not, is by hunting for a hypothetical decay called the neutrinoless double-beta decay, this process violates the leptonic number by two units and it is forbidden by the standard model.

1.2.4 . Mass Hierarchy

Since we are only able to determine the difference of masses between neutrino mass eigenstates, moreover for the two mass differences, only one has a determined

sign(Δm_{12}) from the solar neutrino oscillations. There is still two possibilities for mass ordering : normal or inverted, illustrated in figure (1.5). For normal hierarchy, two neutrinos will have very small weight and the third will be heavier, while it is the opposite for inverted hierarchy, chances are better for detection in the latter case.

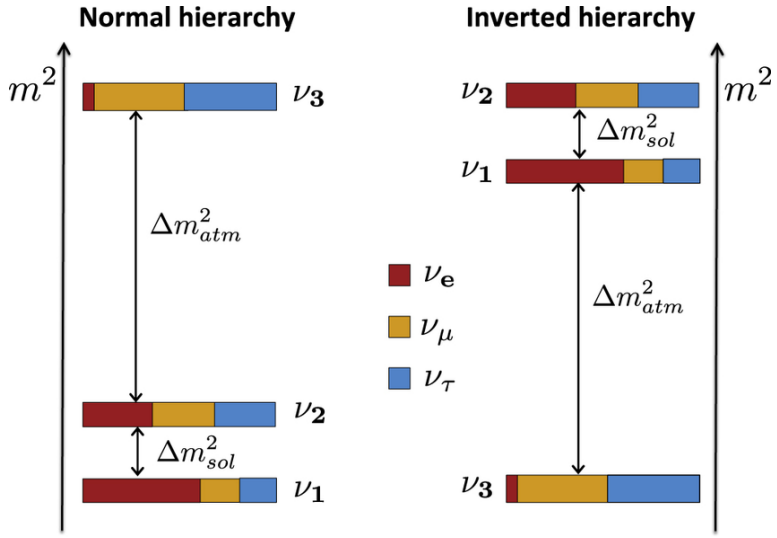

Figure 1.5 – The normal and inverted hierarchy of neutrino masses according to the mass difference retrieved from atmospheric and solar studies of neutrino oscillations. The colors represent couplings between a given mass state and the flavor states.

1.2.5 . Limits on Neutrino Masses

Beta Decay Kinematics

Beta decay kinematics is one of the way to measure the neutrino mass, it is done by observing a large number of beta decays to have enough statistics near the end-point, where you are sensitive to the neutrino mass. The KATRIN experiment is expected to observe $\sim 10^{11}$ [8] beta decays per second and the aim is to find a deviation at the tail, or edge, of the spectrum, see figure (1.6).

The broad spectrum of beta decays shown in figure (1.6) occurs because the neutrino can carry off different amounts of kinetic energy. The cutoff of the spectrum tail is shifted to lower energies for an increasing neutrino mass, so the experiments aim to measure the end point of the spectrum. There is no model dependence, but rather a direct measurement of the neutrino mass. The current best limit on neutrino mass from beta decay experiments is from the KATRIN experiment where $m_\beta = \sum |U_{ei}|^2 m_i^2 < 0.8$ eV at 90% CL [8].

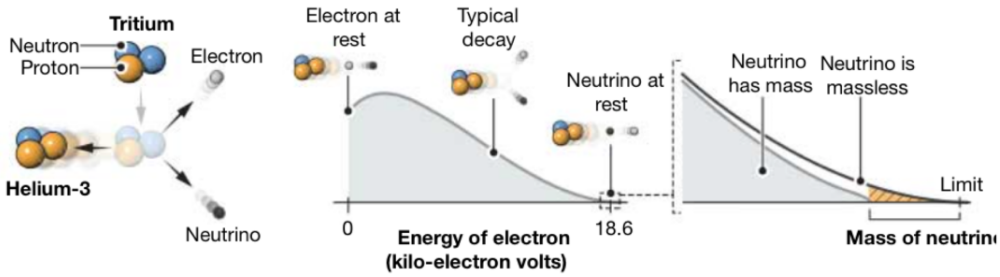

Figure 1.6 – Energy spectrum of beta decay of Helium-3 atom in case of massless and massive neutrinos.

Cosmological Constraints

Cosmological limits on the neutrino mass depend on the neutrinos that have a characteristic scale in the early universe describing how far they can travel before they scatter. The latter depends on their mass and it is called the "free streaming scale". Before reaching this scale, i.e when they are moving around, this is when they change, or inhibit, the structure formation of the universe, so depending on how this structure formation turns out, it can point out limits on the neutrino mass, see figure 1.7. This constraint can be extracted from Planck-CMB, BAO, type Ia supernovae, galaxy surveys and weak lensing measurements. These limits are set on the sum of neutrino masses to be $\sum m_i < 120$ meV [11].

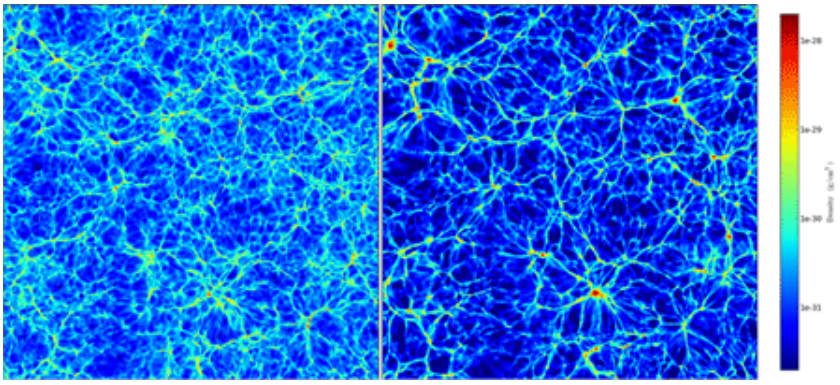

Figure 1.7 – Density distribution in the universe : To the left : With massive neutrinos ($m_\nu = 1.9$ eV) and to the right : With massless neutrinos ($m_\nu = 0$ eV). The maps are produced through numerical simulations, the colors represent the density of ordinary (baryonic) matter [12].

Technique	Sensitivity	Current limit
Cosmological Modeling of Astrophysical Observations	$\sum m_i$	$\sum m_i < 120$ meV (95% CL)
Beta Decay Kinematics	$\sum \lvert U_{ei}\rvert^2 m_i^2$	$\sum U_{ei}^2 m_i^2 < 800$ meV (90% CL)

Table 1.1 – Limits set on sum of neutrino from different calculation techniques [11] [13] [8].

1.2.6 . Double-Beta Decay

The two neutrino double beta ($2\nu\beta\beta$) decay (equation (1.17), figure (1.8)) is a second-order weak process of the Standard Model. This decay mode, consisting of two simultaneous disintegrations, in the same nucleus, of two neutrons into two protons with the emission of two electrons and two electron anti-neutrinos, was first considered in 1935 [10] :

$$ {}^{A}_{Z}X \rightarrow {}^{A}_{Z+2}Y + 2e^{-} + 2\overline{\nu_e} \tag{1.17} $$

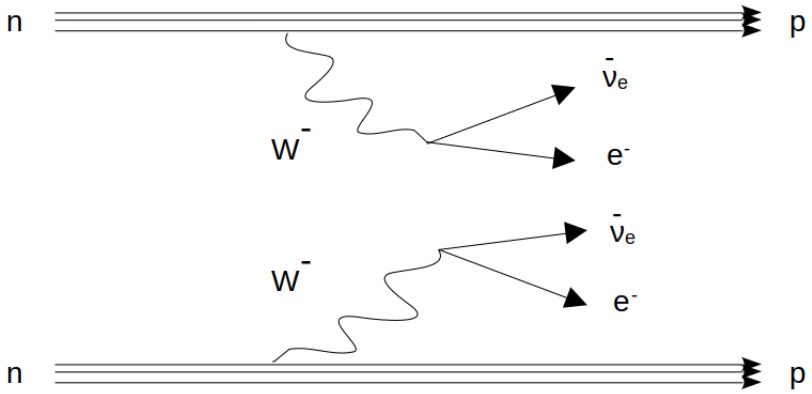

Figure 1.8 – Feynman diagram of the $2\nu\beta\beta$ decay that is allowed by the SM.

The first direct observation of the $2\nu\beta\beta$ disintegration of ^{82}Se was performed with a time projection chamber as a detector in 1987 [14]. Since then, it has been repeatedly observed in 12 even-even nuclei with typical lifetime of the order of $10^{18} - 10^{21}$ years [9].

With such long half-lives, for $2\nu\beta\beta$ to be a competitive decay mode, the single β decay must be either energetically forbidden (the mass of the resulting daughter nucleus being higher than its parent, as seen in figure 1.9) or highly suppressed (by selection rules e.g in ^{48}Ca isotope where there is high difference in the angular momentum between parent and daughter nuclei).

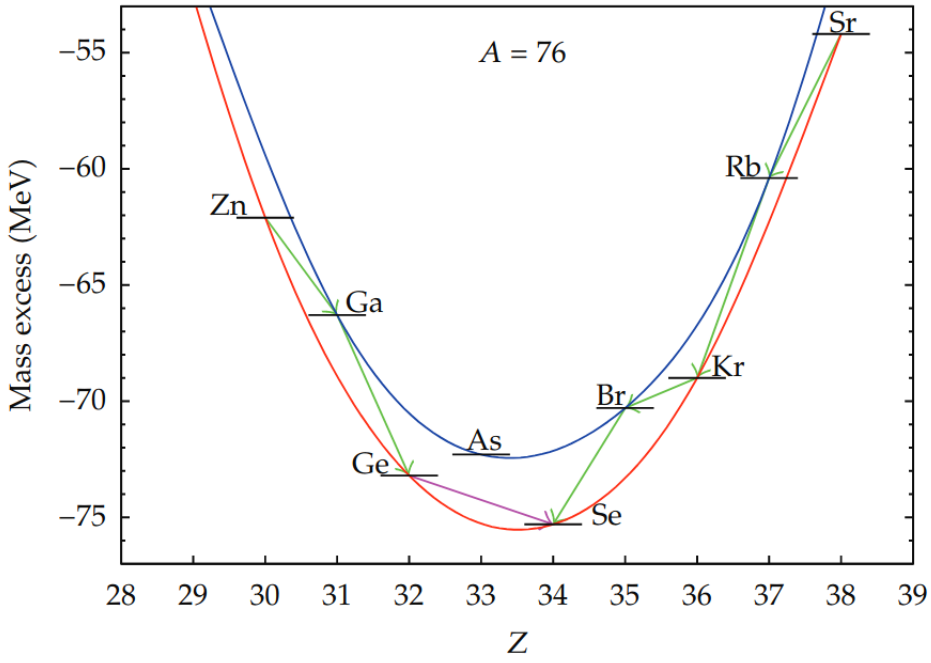

Figure 1.9 – The single-beta decay between ^{76}Ge and ^{76}As is energetically forbidden, hence leaving the double beta decay, represented by the pink arrow, the only decay channel. The two mass parabolas exist because of the pairing interaction that lowers the energy of even-even nuclei with respect to odd-odd ones [17].

1.2.7 . Neutrinoless Double-Beta Decay

The $0\nu\beta\beta$ decay (equation 1.18) is a hypothetical radioactive process in which two neutrons inside a nucleus transform simultaneously into two protons emitting two electrons (figure 1.10).

$$ {}^{A}_{Z}X \rightarrow {}^{A}_{Z+2}Y + 2e^{-} \tag{1.18} $$

The reaction described in 1.18 is forbidden by the Standard Model as it violates the Leptonic number conservation which is a fundamental symmetry in the SM. It is also a key process to study the nature of neutrinos and would prove that they are Majorana particles. And according to the Schechter-Valle Theorem, if neutrinoless double beta decay is observed it would mean that neutrinos are of Majorana nature. This implication is model independent as it is true regardless of the decaying mechanism [16].

The $2\nu\beta\beta$ process final state is quite different from that of $0\nu\beta\beta$, in the sense that in the first decay the two neutrinos are emitted contrary to the latter. One would think as a first glimpse that differentiating between the two processes would be easy by excluding events that contain neutrinos, but as neutrinos have such

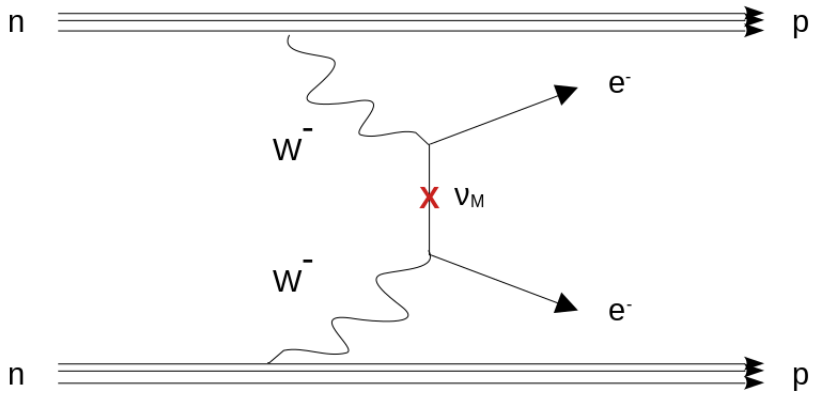

Figure 1.10 – Neutrinoless double-beta decay process in the case of exchange of a Majorana neutrino, where the right handed anti-neutrino is absorbed as a left handed neutrino.

a small cross-section for interaction, it would need an extremely out of normal size (even impossible) material detector in order to tag it. So, we are restricted to measuring the charged decay products of its interaction, i.e. electrons and possibly daughter nucleus.

Ideally, we get to measure the energy of the emitted electrons from the two double beta decay processes. As for $2\nu\beta\beta$, the energy of the process is shared by two electrons and two undetectable neutrinos, while for $0\nu\beta\beta$ the whole energy is shared only with the two electrons. And since the amount of extracted energy from a process is fixed (by the difference in mass between daughter and parent nuclei), the $0\nu\beta\beta$ should exhibit a signal of a mono-energetic peak and the energy of the process, while the $2\nu\beta\beta$ will have a smeared, continuous energy spectrum (since the energies of the two neutrinos undetectable), see figure 1.11.

As mentioned above, the energy of the process is shared by the observed final state particles, but the amount of shared energy is not fixed; i.e. at some point, the two electrons can carry no energy (they are created at rest) or they can carry (approximately) the full energy (neutrinos (almost) at rest), see figure (1.6). The consequence of this continuous energy spectrum is that the tail of the $2\nu\beta\beta$ electron energies spectrum runs up to the signal of the hypothetical $0\nu\beta\beta$ process, i.e to the full energy carried by only the two emitted electrons, see also figure 1.11.

Since the hypothetical $0\nu\beta\beta$ is a very rare process, and to avoid this confusion between the tail of the energy spectrum and the searched signal, detectors need to have a very good energy resolution along with ultra-low background [15] to avoid the natural radio-activity that contributes in the MeV energy region.

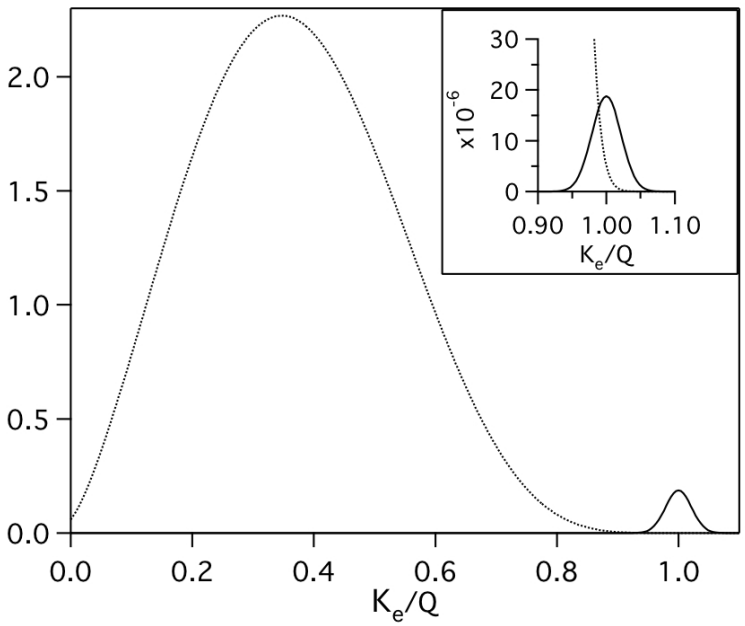

Figure 1.11 – The continuous spectrum of the $2\nu\beta\beta$ decay is shown and at the tail the signal of the $0\nu\beta\beta$, this signal is expected as a peak smeared by the energy resolution.

Common Leptonic Number Violating Mechanisms of $0\nu\beta\beta$

At least four lepton number violating mechanisms can induce a $0\nu\beta\beta$ decay [25] :

- Light Majorana neutrino exchange Is the most commonly discussed mechanism of $0\nu\beta\beta$ decay, see figure 1.10.

- Admixture of right-handed currents in electroweak interactions Exhibits a presence of right-handed currents (RHC) in the electroweak Lagrangian and hence can be used as an alternative mechanism for $0\nu\beta\beta$. The lepton number violation mechanism is characterized by the coupling between right-handed currents of quarks and leptons, or right-handed quark and left-handed lepton currents. This mechanism predicts distinguishable angular and single energy distributions of the final state electrons than those of the other mechanisms, requiring an experiment capable of reconstructing the full topology of the decaying particles.

- $0\nu\beta\beta$ decay accompanied by a Majoron emission It is a light or massless boson that weakly couples to the neutrino, and has a continuous spectrum of the energy sum of the two decay electrons, E_{total}. The phase space of the process

determines the shape of the distribution and depends on the spectral index n, as $G^{0\nu} \propto (Q_{\beta\beta} - E_{total})^n$. Decays with higher n are harder to separate from $2\nu\beta\beta$ (n=5) and other backgrounds as they have broader E_{total} distributions peaking at lower energy values.

- R-parity violating SUSY models Can trigger $0\nu\beta\beta$ decay via short range exchange of heavy superpartners, such as gluino or neutralino, or long range exchange of squarks and neutrinos. The kinematics of the electrons emitted in the decay are the same as in the light neutrino exchange mechanism and therefore the same half-life limit can be used to set limits on SUSY parameters.

Rate of $0\nu\beta\beta$

Many hypothesis have been set to describe the decay process, but the simplest and most widely spread mechanism is the exchange of a light Majorana neutrino.

Looking at the Feynman diagram in figure (1.10), one can write the decay rate as in equation 1.19.

$$(T^{0\nu}_{1/2})^{-1} = g_A^4 G^{0\nu} |M^{0\nu}|^2 (\frac{< m_{\beta\beta} >}{m_e})^2 \tag{1.19}$$

Where :

- g_A is the axial-vector coupling constant with unquenched value at 1.269.

- $m_{\beta\beta}$ is the effective Majorana mass, it describes how the Majorana neutrinos are coupled to the two vertices connecting to the electrons, and this coupling is included in the PMNS matrix. It is defined as :

$$< m_{\beta\beta} >= \sum_{i=1}^{3} U_{ei}^2 m_i \tag{1.20}$$

To get the value of $<m_{\beta\beta}>$ one would have to know the values of the mixing angles, Makorana phases, neutrinos masses and the completely unknown Majorana phases. It is also called the effective light Majorana mass.

- m_e is the electron mass.

- $G^{0\nu}$ is the phase space factor, it is related to the conservation of energy and momentum, it describes the difference in initial and final energy and momentum of the system : the higher the $Q_{\beta\beta}$-value is, the higher the rate of the process is going to be.

- $M^{0\nu}$ is the nuclear matrix element (NME) associated with the light Majorana-neutrino exchange, it describes how the nuclear decay occurs and summarizes the nuclear effects (initial and final state of nucleons, shape of the nucleus, energy exchange, ... etc). The calculation of this parameter is extremely difficult since it describes a system with many nucleons interacting. Many approximations are used in the calculations, and many models exist with different approximations and

techniques for the calculation, hence there is a large spread between them and not all nuclei can be calculated by the same models, as in figure (1.12).

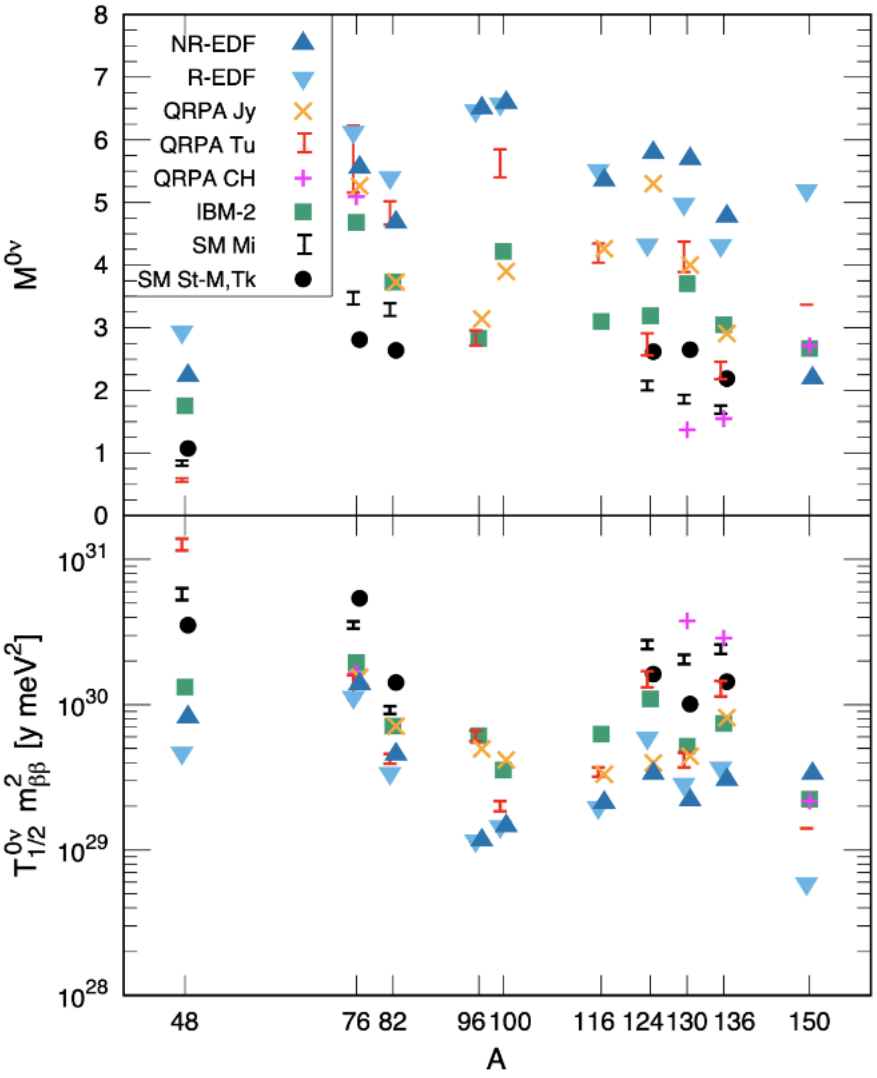

Figure 1.12 – Figure showing the different nuclear matrix elements calculations for different isotopes using different methods for the $0\nu\beta\beta$ (top) and the corresponding expected half-life multiplied by the effective mass per method (bottom), from [15].

Interpreting existing results as a measurement of $\langle m_{\beta\beta} \rangle$ and preparing for new experiments depend imperatively on the knowledge of the corresponding NMEs that govern the decay rate [18]. As the models use many approximations, various physics effects were not included and hence the values of NMEs are larger (or

smaller) than what is expected. The current route in the field is to reduce effect of NMEs values by theoretical models [19].

The theoretical neutrinoless double beta decay NME is expressed as :

$$M^{0\nu} = M^{0\nu}(GT) + M^{0\nu}(T) + M^{0\nu}(F) \tag{1.21}$$

Where $M^{0\nu}$(GT), $M^{0\nu}$(T) and $M^{0\nu}$(F) are the axial vector Gamow-Teller (GT) NME, tensor (T) and the vector Fermi (F) NMEs, respectively.

Nuclear Matrix Elements Models

There are many approaches for calculating the NME, some are summarized here :

- The Nuclear (Interacting) Shell Model (ISM) : This model uses only nucleon states in the valence space near the Fermi surface. The small number of active nucleons and oscillator shells considered implies that the low-lying states can be well described and reproduced, but the effects of pairing correlations may not be fully taken into account and may lead to an underestimation of the NME. This method is better suited for smaller nuclei [20], since the larger the number of nucleons becomes the more shells have to be taken into account and the number of nuclear states soon becomes so colossal that the shell model will be intractable [21]).

- The Quasi-Particle Random-Phase Approximation (QRPA) : This model contains few correlations but a large number of simple interactions of single-particle orbits. These parameters are constrained to values that reproduce the measured $2\nu\beta\beta$ half-lives. Such inputs help reduce uncertainties on the model. In principle, this approach can be applied to all nuclei except for a few very light ones [22].

- The Interacting Boson Model (IBM) : This model is cut from the full shell-model space where nucleon pairs are represented as bosons with specific quantum numbers. This description relies more on adjusting the model parameters to match the observables. It is suitable for describing intermediate and heavy atomic nuclei, and altering few parameters, it reproduces the most of the low-lying states of the corresponding nuclei [21].

- The Energy-Density Functional (EDF) and the Generator Coordinate Methods (GCM) : These models mix many mean fields with different properties, whereas the other methods use simple mean fields that the states and

orbitals feel. A large number of single-particle states are included, but only a number of selected correlations is used, and sometimes resulting in an overestimation of the NME. The **Projected Hartree–Fock–Bogoliubov Method (PHFB)** is a related approach [20].

A reliable calculation of NMEs will help in choosing the best nuclides to study for $0\nu\beta\beta$ decay searches as the NME uncertainty can reduce the experimental sensitivity on $<m_{\beta\beta}>$ by up to a factor of 5 [24].

Higher-State Dominance and Single-State Dominance

Taking as an example the $2\nu\beta\beta$ decay of ^{82}Se to ^{82}Kr, which is modeled as a β transition between the ground state of ^{82}Se and the 1^+ state of the intermediate nucleus ^{82}Br, and then another transition between the latter and the ground state of ^{82}Kr. If one single intermediate 1^+ state contributes dominantly to the transition, then it is said that the process is single-state dominant (SSD), and if many intermediate states are involved, then it is higher state dominant (HSD).

In the two scenarios, the shape of the sum of electron energy distribution is very similar. But the differentiation between the single electron energy distribution is possible, especially at low energies since the SSD model has an increased probability to emit low energy electrons. See figure 1.13 where this difference is presented for ^{100}Mo. The latter point reduces the efficiency of detection, if the SSD model is chosen. Therefore a large statistics with precise energy measurements is the key to differentiate between the two models.

Quenching of the Axial-Vector Coupling Constant (g_A)

At the nuclear level, β decay can be considered as a mutual interaction of the hadronic and leptonic currents mediated by massive vector bosons $W^{\pm}$ that can be expressed as mixtures of vector and axial-vector couplings, g_V and g_A respectively. These couplings contributions enter the theory when the hadronic current is renormalized at the nucleon level [23]. The conserved vector-current hypothesis and partially conserved axial-vector-current hypothesis yield the free-nucleon values $g_V = 1.00$ and $g_A = 1.27$ [23]. But the value of g_A is affected, inside nuclear matter, by many-nucleon correlations.

It is well known that the theoretically calculated strengths of Gamow-Teller beta decay transitions to individual final states are significantly larger than the experimental ones. The effect is known as the axial-vector current matrix elements quenching [18]. The Gamow-Teller NME is expressed as :

$$M^{0\nu}(GT) = (\frac{g_A^{eff}}{g_A})^2 M_M^{0\nu}(GT) \tag{1.22}$$

Where :

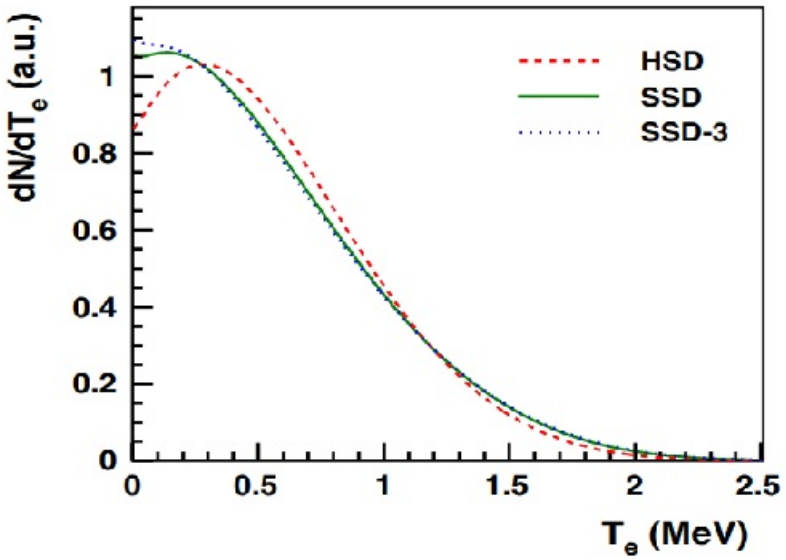

Figure 1.13 – Theoretical distributions of the individual electron kinetic energy for ^{100}Mo $2\nu\beta\beta$ decay in the case of the three models HSD, SSD and SSD-3.

- g_A^{eff} is the effective axial-vector coupling.
- g_A is the axial-vector coupling.
- $M_M^{0\nu}(GT)$ is the GT model NME without the renormalization or quenching effect.

Because $2\nu\beta\beta$ and $0\nu\beta\beta$ decays share the same initial and final nuclear states and similar transition operators, a detailed study of $2\nu\beta\beta$ decay is the key to well grounded $0\nu\beta\beta$ NME predictions. By studying the decay rate of $2\nu\beta\beta$ we can get the corresponding NME, but there is no experimental way to get the NME of the $0\nu\beta\beta$ unless we know the rate and effective neutrino mass. If this quenching also exists for $0\nu\beta\beta$, it can significantly reduce the half-life of the decay by as much as a factor of 2-3 [18].

With more studies on the $2\nu\beta\beta$ decay isotopes by different collaborations, there is an imperative need to have more accurate description of the decay rate [24], one was introduced by F. Simkovic et al. in their paper [26] :

$$(T_{1/2}^{2\nu})^{-1} \simeq (g_A^{eff})^4 |M_{GT-3}^{2\nu}|^2 \frac{1}{|\xi_{31}^{2\nu}|^2} (G_0^{2\nu} + \xi_{31}^{2\nu} G_2^{2\nu}) \tag{1.23}$$

Where :

- $G_2^{2\nu}$ and $G_0^{2\nu}$ are phase-space factors that have different dependencies on lepton energies and this dependency can be distinguished from the energy spectrum of the decaying isotope.

- $M^{2\nu}_{GT-3}$ is a nuclear matrix element included in the ratio $\xi^{2\nu}_{31} = M^{2\nu}_{GT-3}/M^{2\nu}_{GT}$. $M^{2\nu}_{GT-3}$ is sensitive only to contributions from low-energy intermediate states due to rapid suppression in the energy denominator, while $M^{2\nu}_{GT}$ is also sensitive to contributions from the high-lying states in the intermediate odd-odd nucleus [24].

$\xi^{2\nu}_{31}$ probes complementary physics to the $2\nu\beta\beta$ half-life. This parameter can be determined experimentally by fitting the $2\nu\beta\beta$ electron energy spectrum to extract the leading and second order contributions in equation 1.23 (i.e $G^{2\nu}_0$ and $G^{2\nu}_2$).

The dependency of $G^{2\nu}_0$ and $G^{2\nu}_2$ on different leptonic energies generates distinguishable energy spectra according to their corresponding dominance, which is determined by the value of $\xi^{2\nu}_{31}$, as in figure 1.14.

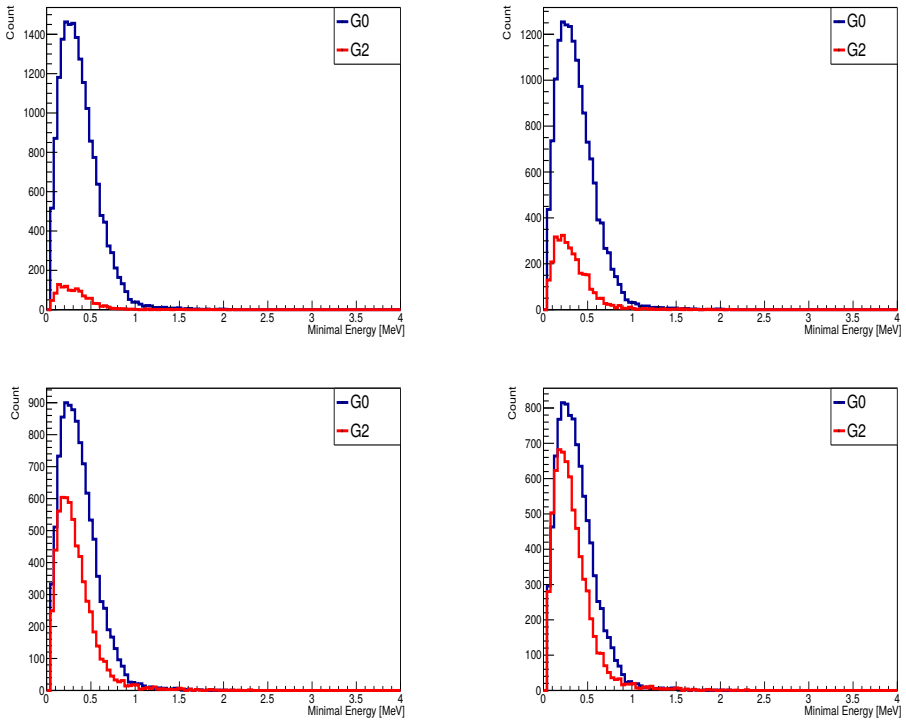

Figure 1.14 – Contributions of $G^{2\nu}_0$ and $G^{2\nu}_2$ processes on the $2\nu\beta\beta$ minimum energy spectra for different values of ξ_{31}. From left to right starting top row the value of $\xi^{2\nu}_{31}$ is : 0.1, 0.3, 0.8 and 1.0, respectively.

1.3 . State of Art

Experiments have been searching over the years for a direct detection of the $0\nu\beta\beta$. As mentioned before, this extremely rare process will be hard to detect as it is going to be smeared by the tail of the $2\nu\beta\beta$ energy spectrum and, inevitably,

by the background. The half-life of the SM allowed double beta decay is going to be determined experimentally by the following equation :

$$T_{1/2} = \frac{ln(2) \times N_A}{M} \times \frac{\epsilon \times m \times t}{N_{signal}} \tag{1.24}$$

Where :

- N_{signal} is the number of observed double beta events.
- m is the mass of the double beta source.
- M is the source isotope molar mass.
- N_A is Avogadro's' number.
- t is the exposure time in [years].
- ϵ is the detector efficiency which is evaluated from simulations, and it is represented as (Number of events correctly selected)/(Total number of generated events)

Equation 1.24 would be applied under the condition of observing a significant signal, other wise, if nothing is observed (like in the current hunt for $0\nu\beta\beta$ signal), a lower limit is set on the half-life of the process :

$$T^{0\nu}_{1/2} > \frac{ln(2)N_A}{M} \frac{\epsilon_{0\nu} mt}{N^{0\nu}_{excluded}} \tag{1.25}$$

Where $N^{0\nu}_{excluded}$ is the number of excluded events at a given confidence level (typically 90%) above which the signal wouldn't have been observed.

If a large number of background events is expected, i.e the background is said to have a Gaussian statistical behavior where the number of excluded events scale with $\sqrt{Nbkg}$, a good approximation of the equation then becomes :

$$T^{0\nu,limit}_{1/2} \propto \epsilon \sqrt{\frac{mt}{b\Delta E}} \tag{1.26}$$

Where :

- b is the background rate, expressed in [counts/keV/kg/yr].
- ΔE is the energy resolution of the detector.

Hence an experiment should aim to have high detection efficiency, large isotope mass, very low background rate, long data taking periods and a very good energy resolution to reduce the smearing of the $2\nu\beta\beta$ tail.

1.3.1 . Choice of the $\beta\beta$ Isotope

The selection of the isotope undergoes several conditions :

- Reasonably naturally abundant source to be deployed in large quantities.
- Feasible enrichment to achieve maximum purity.
- High $Q_{\beta\beta}$ value, as the β/γ environmental background decreases at higher energies.

- Long $2\nu\beta\beta$ half-life to reduce the $2\nu\beta\beta$ background with respect to the $0\nu\beta\beta$ signal in the region of interest (ROI) that is located around the end-point of the $2\nu\beta\beta$ tail at $Q_{\beta\beta}$.

An approximation of the effect of $2\nu\beta\beta$ on the signal of $0\nu\beta\beta$ is the following : the $2\nu\beta\beta$ counts within one peak width (δE) centered on $Q_{\beta\beta}$ will contribute to the $0\nu\beta\beta$ peak region and be a background. We approximate the $2\nu\beta\beta$ fraction in this region by :

$$factor \propto \frac{\delta^6 Q_{\beta\beta}}{m_e} \tag{1.27}$$

Where :

- $\delta = \Delta E/Q_{\beta\beta}$ is the relative Full Width at Half Maximum (FWHM) at the $Q_{\beta\beta}$-value.

- m_e is the electron mass.

From here we can approximate the fraction of the signal (S) of $0\nu\beta\beta$ to the background (B), $2\nu\beta\beta$, as :

$$\frac{S}{B} \propto (\frac{Q_{\beta\beta}}{\Delta E})^6 \frac{T_{1/2}^{2\nu\beta\beta}}{T_{1/2}^{0\nu\beta\beta}} \tag{1.28}$$

This highlights the need to have detectors with very good energy resolution, and an isotope with high $Q_{\beta\beta}$-value.

Isotopes like ^{48}Ca, ^{96}Zr and ^{150}Nd are considered as golden candidates, because their $Q_{\beta\beta}$ lies well above 3 MeV and so they are less affected by natural radioactive background. Unfortunately, these isotopes also have a very low natural isotopic abundance and their enrichment is more difficult with the usual separation technique (e.g centrifugation).

Emitters like ^{82}Se, ^{100}Mo and ^{116}Cd feature a $Q_{\beta\beta}$ value between 2.8 and 3.1 MeV, so they are barely affected by the β/γ natural radioactivity and though their isotopic abundance is low, their enrichment is feasible.

1.3.2 . Background Suppression

All the detectors searching for $0\nu\beta\beta$ are located in deep underground laboratories, where the cosmic rays flux is strongly suppressed. They are usually equipped with passive or active shields to further decrease the background produced by external sources and environmental radioactivity present in all materials (lab and experiment equipment, rocks,...) that produce problematic isotopes mainly : ^{214}Bi with Q_β = 3.27 MeV and ^{208}Tl with Q_β = 4.99 MeV from the natural ^{238}U and ^{232}Th decay chains, respectively. These isotopes can contribute to the background because of their high Q_β values that is close to the typical $Q_{\beta\beta}$ values between 2 and 4 MeV. These contaminations can be found either in the $\beta\beta$ sources or outside, but the background generated inside the $\beta\beta$ sources is the most problematic.

All the materials of the detectors must be carefully selected for their naturally high radiopurity and stored to avoid later contamination. Additional background suppression can be performed through several techniques to accept or reject signals by exploiting pulse-shape discrimination, active veto or full topological reconstruction.

1.3.3 . Signal Identification and Background Rejection

A key goal to any experiment is to design a detector that can discriminate between signal and background events effectively while having a high signal detection efficiency, the way to achieve the desired background rejection is via the energy resolution.

As mentioned before, the signal of the $0\nu\beta\beta$ is the emission of two e^- having an energy sum equal to the $Q_{\beta\beta}$ of the isotope. The discrimination between such 2 e^- signal and the background is by observing the spatial topology and timing of the event. Events may be divided into single-site and multiple-site events following their scattering and energy deposition, by utilizing the pulse shape discrimination and topology reconstruction. Some detectors use the former mentioned features to discriminate using multiple detection channels, mainly scintillation and ionization.

Timing is an important distinction technique, especially for α backgrounds. Take as an example the ^{222}Rn decay with a half-life of 3.8 days. This isotope is problematic as it emanates from the laboratory rocks and diffuses into the detector contaminating it. The β decay of ^{214}Bi is one of ^{222}Rn descendants, will be shortly followed by the alpha decay of ^{214}Po which has a half-life of 164 μs, so this coincidence in time can be used to identify the ^{222}Rn contamination levels and reject them, This is the so-called BiPo method.

Spatial discrimination depends on the distribution of the events in the detector. Signal events should be uniformly distributed throughout the detector from the source material, as well as other uniformly distributed contamination. While background events coming from the detector materials (or source material) may be localized to "hot spots", in non-homogeneous (or discrete) detectors, these spots can be identified by other detector components and vetoed out, while in homogeneous detectors they can be rejected by choosing a fiducial volume cut.

The usage of these two discrimination techniques (and other non-mentioned ones like the identification of the decay daughter on an event-by-event basis), allows the measurement of these backgrounds and constraint the $0\nu\beta\beta$ analysis.

1.3.4 . Experimental Status

As mentioned above, there are two types of experiments : homogeneous and non-homogeneous (or discrete).

Homogeneous Detectors

This detection technique, also called the calorimetric technique (figure 1.15), has already been employed by several experiments. One can summarize the pros and cons of using such technique as follows :

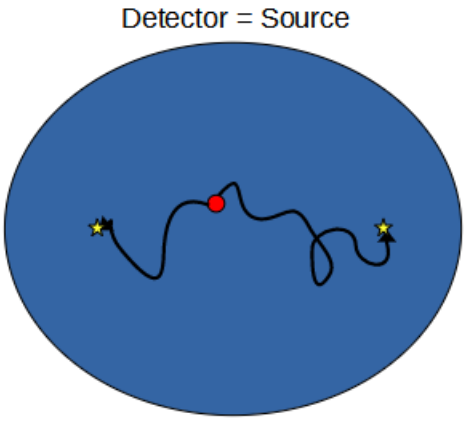

Figure 1.15 – Schematic representation of a homogeneous detector.

(+) As this method reaches high efficiency of detection, a large mass of source material is achievable.

(+) A very high energy resolution is guaranteed using a proper detector ($\sim$ 0.1 $\%$ FWHM with Ge diodes and bolometers).

(-) As the source material must be embedded inside the detector structure, constraints on the detector materials arise, but this is not a problem for some detectors like bolometers and loaded liquid scintillators.

(-) Topological reconstruction of the decaying events might be difficult in some cases (excluding gaseous time projection chambers (TPC)), but this comes in facing with the price of having high energy resolution.

Non-Homogeneous Detectors

Also called discrete detectors, their source is separated from the detector itself, as seen in figure 1.16. One can summarize the pros and cons of using such technique as follows :

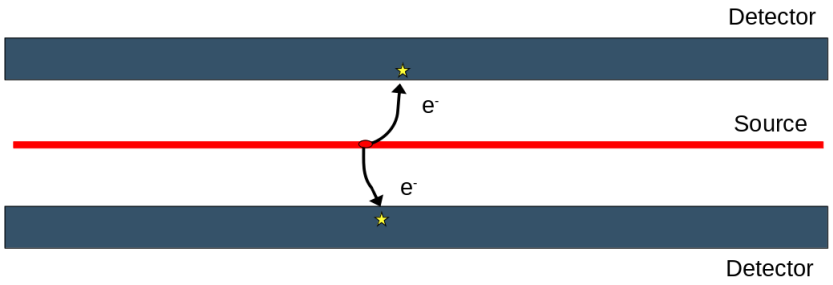

Figure 1.16 – Schematic representation of a non-homogeneous detector.

(+) Topological reconstruction of the decaying particles of the event is possible, allowing a very high background rejection. But this comes again at the price of having lower energy resolution than several of the homogeneous detectors, which decreases the efficiency.

(-) The energy resolution is limited (order of $\sim$ 10 $\%$ FWHM), and also a limitation is due to the fact that the source is relatively far from the detector and emitted electrons suffer energy loss.

(-) Achieving large masses of isotopes is hard due to the need of large scale detectors, creating more inactive materials, and the electron self-absorption inside the source. Only masses of tens of kilograms are used until now, though reaching 100 kgs sources seems doable.

This type of detectors can study the event topology which is very important to reject efficiently radioactive backgrounds and achieve an understanding of the decaying mechanisms leading to the $0\nu\beta\beta$. NEMO-3 and SuperNEMO belong to these types of detectors.

Current Status of Experiments

Semi-conductors or Ge-Diodes : Mainly the high-purity Ge-detectors (HPGe). Despite the low $Q_{\beta\beta}$ value, and consequently the reduced phase space factor of ^{76}Ge, such detector can achieve high purity of the source at large volumes, as the impurities are removed during the crystallizing process. Also they achieve a very good energy resolution value at the order of $\sim$ 0.1 $\%$ FWHM. Experiments that follow this technique are GERDA, MAJORANA and LEGEND [20] [27].

- GERDA : The Germanium Detector Array (GERDA) experiment is located at Gran Sasso. It holds 86$\%$-enriched ^{76}Ge HPGe detectors, they are immersed in a cryostat of liquid-Ar to keep down the number of nearby mechanical components, see figure 1.17. The experiment went through two phases : First phase used 17.8 kg of enriched coaxial detectors, and during data taking, they were augmented by 3.63 kg in five broad energy Ge p-type point-contact detectors. The results of this phase

disproved previous claims of a $0\nu\beta\beta$ signal [29]. The second phase, GERDA-II, featured very high background rejection on the order of 0.5 10^{-3} counts/keV/kg/yr and an increase in enrichment of the source to 35.8 kgs. The results of this phase set lower limits to $T^{0\nu}_{1/2} > 1.8 \times 10^{26}$ years at 90% CL, converting to a limit on the effective Majorana mass of $m_{\beta\beta} <$ 79-180 meV at 90% CL [28].

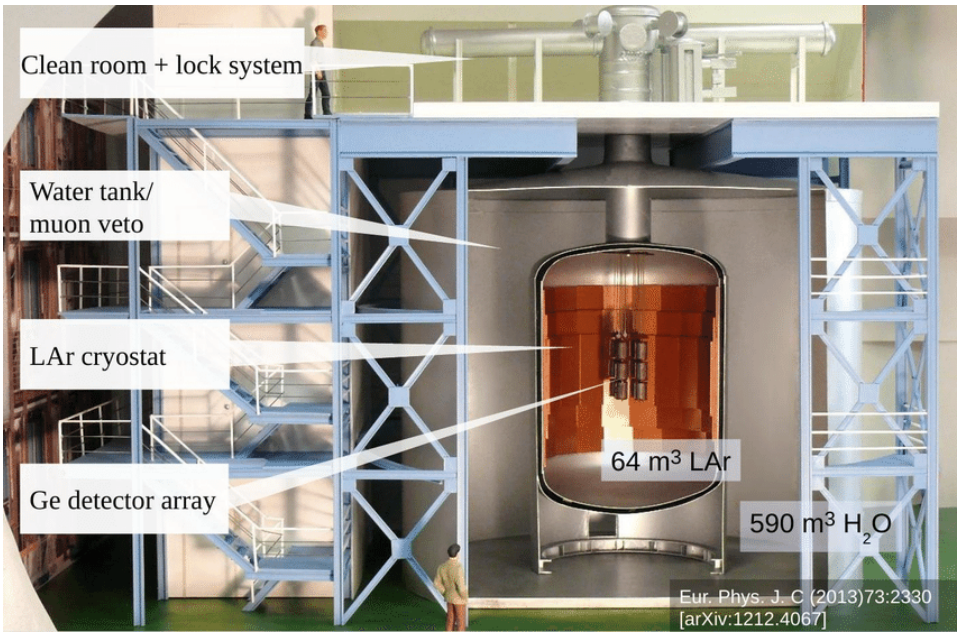

Figure 1.17 – Schematic figure showing the GERDA setup. Enriched ^{76}Ge diodes are immersed in liquid Argon, which acts as an active shielding.

- MAJORANA : the Demonstrator features 29.7 kgs of 88% enriched Ge detectors, which are cooled using a cryostat. They feature an excellent pulse shape discrimination to reach the low background levels. They aim to prove the feasibility of a ton scale detector. Results showed a lower limit at 2.7×10^{25} years at 90% confidence level with $m_{\beta\beta} <$ 200-430 meV [30].

- LEGEND : The Large Enriched Germanium Experiment for Neutrinoless Double-Beta Decay (LEGEND) results from a common effort of both GERDA and MAJORANA collaborators. It aims to pursue a ton scale Ge-based experiment with ultra-low background and excellent energy resolution. The first phase, LEGEND-200 will feature 200 kg of enriched isotope and expecting to set limits at $\sim 10^{28}$ years and $m_{\beta\beta} <$ 15-50 meV with a background of 0.6 count.(FWHM.ton.year)$^{-1}$. The next phase will be LEGEND-1000 with 1000 kg of source material and a background of $\lesssim$ 0.1 count.(FWHM.ton.year)$^{-1}$ [31].

Bolometers : They are cryogenic calorimeters operating at very low temperatures of ∼10 mK, to reduce the heat capacity and therefore enhance the sensitivity

to the increase of temperature. An absorber is connected to a thermal bath of very low temperature via weak thermal link, the temperature is registered by a sensitive thermometer. They possess a very good energy resolution (close to Ge-diodes) and are intrinsically low in radioactivity due to the crystal growth process.

The usual rise of temperature is on the order of $\sim$ 0.1 mK per MeV of deposited energy. The most widely used readout in the $0\nu\beta\beta$ search is neutron-transmutation-doped Ge or Si highly sensitive thermometers.

The existence of such detectors in large scales faces great difficulties as it is challenging operate detectors at such ultra-low temperatures. The most significant case for $0\nu\beta\beta$ is using ^{130}Te with TeO_2 bolometers.

- CUORE : The Cryogenic Underground Observatory for Rare Events (CUORE) consists of 750 kg of TeO_2 absorber crystal distributed in 19 towers and cooled to 7 mK by a powerful dilution refrigerator, see figure 1.18. Taking advantage of the large natural abundance of ^{130}Te, the experiment uses un-enriched Te source. The detector is surrounded by layers of γ-ray and neutron shielding, inside the cryogenic volume is embedded a shielding from low background Roman Pb shields. Additional shielding was deployed outside the cryostat. First results on the $0\nu\beta\beta$ was extracted from a total exposure of 372.5 kg.year of ^{130}Te and a lower limit on the half-life was set to 3.2×10^{25} years (90% CL) with $m_{\beta\beta}$ < 75-350 meV [32].

Figure 1.18 – The CUORE detector with the crystal towers. To avoid any contamination of the crystals, the construction of the detector has to be performed in clean rooms.

- CUPID : CUORE Upgraded with Particle Identification (CUPID), an upgrade from CUORE, low background discrimination is given by the measurement of the

light, in addition to the heat. CUPID is looking to improve signal sensitivity mainly through the identification of dominant α backgrounds in CUORE. An approach is to study the Cherenkov light from the β signal in TeO_2. Another approach is to use scintillating bolometers to spot the α particles, like the $Zn^{82}Se$ crystals in CUPID-0 or the $Zn^{100}MoO_4$and $Li_2{}^{100}MoO_4$ crystals in the CUPID-Mo experiment. Future plans exist on developing a ton scale CUPID experiment that has a background of $\sim$ 0.1 count.(ROI.ton.year)$^{-1}$ and $T^{0\nu}_{1/2} > 10^{27}$ years [33].

- AMORE : Advanced Molybdenum Based Rare Process Experiment (AMoRE) is ^{100}Mo based and uses $CaMoO_4$ scintillating crystals that are enriched to $\sim 96\%$ in ^{100}Mo. The signal readout is made by metallic magnetic calorimeter sensors. The light absorption from an event generates phonons that are collected by an Au film coupled to the sensors on the crystals and then measured by this sensor by a superconducting quantum interference device. AMORE-Pilot is the piloting phase of the experiment, results have been published and lower limits have been set to 9.5 $\times 10^{22}$ years on ^{100}Mo. The last phase of the experiment aims to reach a limit of 10^{26} years with $m_{\beta\beta}$ < 1.2-2.1 eV[34].

Time Projection Chambers (TPC) : This technique provides lower energy resolution than the preceding techniques, but the mass scalability makes it an attractive detector technology. Two energy channels are produced in the detection medium of a TPC : ionization and scintillation. TPCs can be operated in both liquid (more compact) and gas (better topological reconstruction) phase, in which ^{136}Xe is the widely used isotope for the double beta search.

The choice of a liquid-phase detectors Xe TPCs for $0\nu\beta\beta$ decay searches follows the desire for a compact detector with low-radioactive-background. The resulting energy resolution from such choice is lower than that of gas-phase detectors. The discrimination of multi-site background and spatial distribution works well with a few millimeter precision, despite the fact that scattering decreases the resolution of the two electron tracks.

- EXO-200 : It is a prototype of the Enriched Xenon Observatory (EXO), it is a cylindrical shape single phase liquid TPC of 110 kg of Xe enriched to 80.6% in ^{136}Xe. For ionization collection, the experiment used a central cathode with detector planes at both ends consisting of crossed-wire grids, as for scintillation collection a large-area avalanche photodiodes was used, see figure 1.19. Different shieldings were installed to act as vetos and lower background, adding the low radioactive materials used in the construction. The data taking of the experiment went over two phases : the first was in 2011 and reported the first observation of $2\nu\beta\beta$ in ^{136}Xe in which they produced precise measurements of the half-life of the decay. Then the experiment was upgraded with low noise electronics and Rn suppression system, producing lower limits on the $0\nu\beta\beta$ of 3.5×10^{25} years (90%CL) with $m_{\beta\beta}$ < 93-286 meV [35].

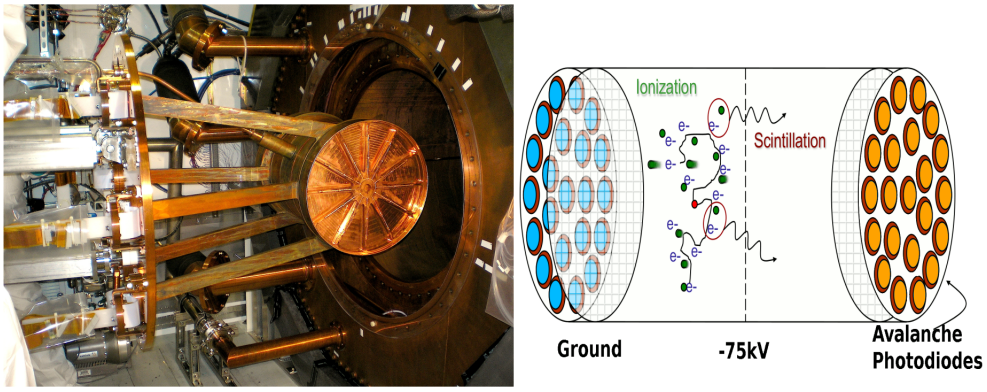

Figure 1.19 – To the left : The EXO-200 detector is assembled with the cryostat (right). Electrical control and signal line feedthroughs can be seen right. To the right : working principle of the detector.

- nEXO : is a planned TPC, after the success of EXO-200, with 5000 kg single phase liquid Xe enriched to 90% in ^{136}Xe. The expected energy resolution is 2.4% FWHM at $Q_{\beta\beta}$ using low noise silicon photomultipliers. nEXO experiment is said to reach a half-life sensitivity of 1.35×10^{28} years at 90% CL with $m_{\beta\beta}$ < 5-20 meV in 10 years of data taking, covering the parameter space associated with the inverted neutrino mass ordering, along with a significant portion of the parameter space for the normal ordering scenario, for almost all nuclear matrix elements. The performance of this experiment comes from the large source volume, good energy resolution and the background rejection advantage of a TPC [36].

- NEXT : The Neutrino Experiment with a Xenon TPC (NEXT) is a planned experiment technology based on the use of TPCs operating at a typical pressure of 15 bar and using electroluminescence to amplify the signal. The experiment features an excellent energy resolution at 0.3% FWHM at $Q_{\beta\beta}$, adding the tracking capabilities that allows a full topological reconstruction for signal discrimination. The fully active detector region will allow a scaling up the detector to large masses. [37]

- PandaX-III : The Particle and Astrophysical Xenon Experiment III (PandaX-III) uses high pressure TPC liquid Xe chambers. Charges are read out by microbulk micromegas modules. It features a good energy resolution and low background. It is expected that the ton scale experiment will set a lower limit on the half-life at 10^{27} years after 3 years of data taking.

Liquid Scintillators : Such detectors are loaded with very large masses of $\beta\beta$ source hence very low background is achievable because it is more easy to purify a liquid, but on the other hand they suffer from poor energy resolution adding the absence of event topological reconstruction. These detectors typically have two components : solvants that form the bulk, and fluors as dopants having

emission spectrum that is a better match for the photodetectors. This type of detectors suffer from an irreducible background of solar neutrinos scattering off atomic electrons, and the way to work around this is since the elastic scattering direction are correlated to the sun's direction one would observe the directional Cherenkov light emitted and separate it from the isotropic scintillation light that has a higher intensity.

- KamLand-Zen : Kamioka Liquid Scintillator Antineutrino Detector - Zero Neutrino Double Beta Decay Search (KamLand-Zen) uses ^{136}Xe enriched to 90% that is dissolved in liquid scintillator mixed with fluor. This combination is contained inside a nylon mini-balloon suspended in liquid scintillator inside another main balloon. Then, everything is covered by a stainless steel spherical vessel filled with a buffer oil, this vessel mounts photomultipliers (PMTs) to detect the signal, see figure 1.20. The second phase of the experiment which featured reduced background from the previous phase by a factor of 10 through purification of the scintillator and Xenon gas, set the best lower limits on the $0\nu\beta\beta$ half-life at 2.3×10^{26} years at 90% CL with $m_{\beta\beta} <$ 36-156 meV [38].

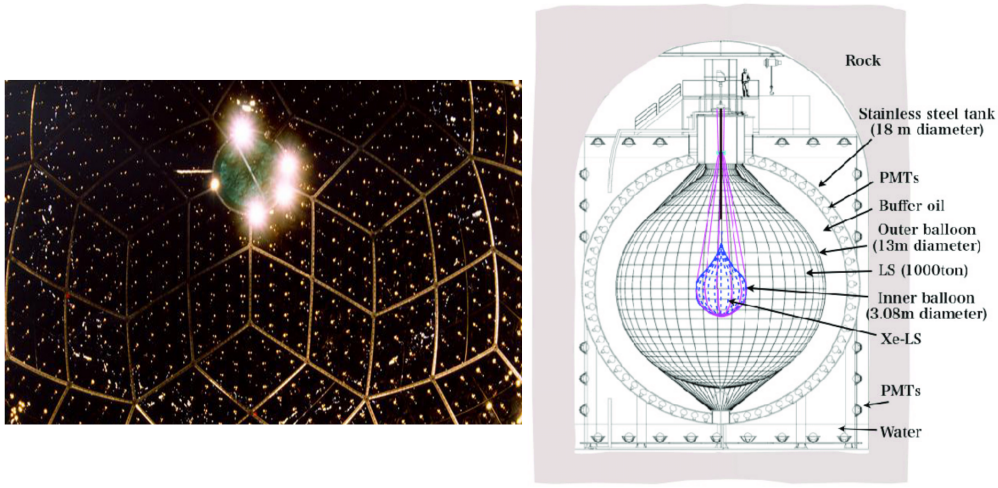

Figure 1.20 – To the left : The inside of KamLand-Zen, the middle is the mini-balloon filled with liquid scintillator, and the wall is filled PMTs. To the right : The general scheme of the detector with the different components.

- ZICOS : The Zirconium Complex in Liquid Scintillator (ZICOS) experiment, it is an attempt to study the dissolving high concentration of tetrakis zirconium in liquid scintillator. The studies go around the ability to reject the background with this technique. The expected sensitivity to be reached is $T_{1/2}^{0\nu\beta\beta} > 2 \times 10^{26}$ years and $\sim 10^{27}$ years with improved discrimination [39].

- CANDLES : CAlcium fluoride for the study of Neutrinos and Dark matters by Low Energy Spectrometer (CANDLES) uses ^{48}Ca isotope to search for the $0\nu\beta\beta$

signal. It uses scintillator crystals suspended inside a liquid scintillator vessel. The scintillation signal is lead by light pipes to a number of photomultipliers mounted inside water tanks. Lower limits were set at $T_{1/2}^{0\nu\beta\beta} > 6.2 \times 10^{22}$ years [40].

Tracking-Calorimeter The most advanced non-homogeneous detector was the NEMO-3 detector studing 7 $\beta\beta$ emitters in the form of thin foils. The ^{100}Mo is used to study $0\nu\beta\beta$ decay with better sensitivity. The distinctive feature of NEMO-3 detection method is the full reconstruction of the decay topology using 3-dimensional tracking as well as calorimetric and timing information.

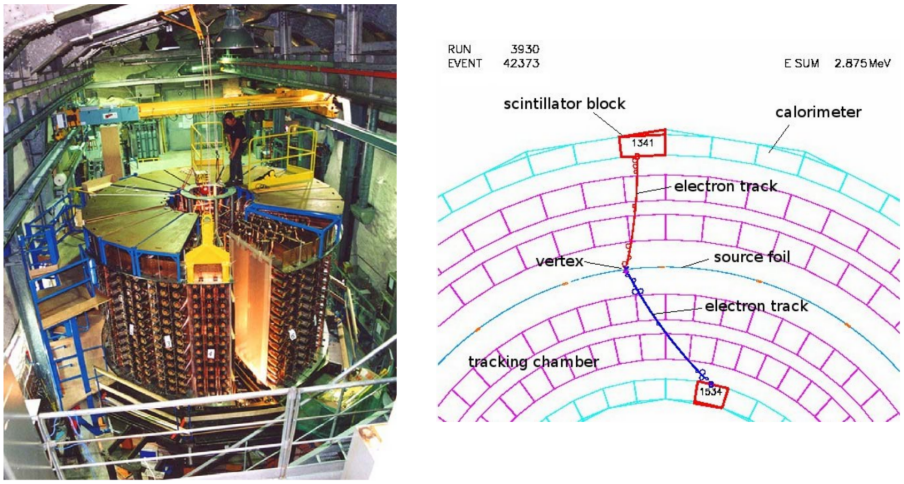

Figure 1.21 – To the left : Image of the detector installed at Laboratoire Souterrain de Modane (LSM). To the right : 2-D view of the NEMO-3 detector showing the source foil emitting two electrons, the calorimeter and tracker detectors.

From figure 1.21, the main principle of the detector can be summarized as :

- A $\beta\beta$ source is placed inside the detector which emits two electrons across the detector tracker.

- The electrons trigger the chamber wires running the Geiger mode. The trajectory of the electron is reconstructed in 3 dimensions.

- Under the influence of 25 G magnetic field, their tracks are curved, allowing a charge identification.

- Electrons then deposit energy within the plastic scintillators by emitting scintillation photons which are collected and measured by the photomultipliers.

One of the unique advantages of NEMO-3 detector is its ability to unambiguously identify electrons, positrons, gammas and delayed alpha particles. This permits a strong suppression of background by eliminating events that don't exhibit a $\beta\beta$ topology, achieving a background rate of $\sim 10^{-3}$ events/keV/kg/yr in the

region of interest around $Q_{\beta\beta}$. This detector has set limits on the $0\nu\beta\beta$ half-life of these 7 isotopes between 0.9×10^{19} years and 1.1×10^{24} years.

- SuperNEMO : This experiment inherits the detection technique from the precedent NEMO experiments. It is dedicated to search for the $0\nu\beta\beta$ signal and measure the half-life of several isotopes mainly ^{82}Se, and possibly ^{150}Nd and ^{96}Zr if enrichment is feasible. The final detector is intended to be made of 20 modules each having about 5 kg of source foils each, totally 100 kg of isotope mass. In case of signal detection, SuperNEMO will be able to identify the decaying mechanism using its full topological reconstruction advantages. The experiment started with a demonstrator to check the feasibility of scaling up to the full 20 modules detector, conserving the ultra low background levels. The demonstrator is in the commissioning phase with 6.23 kg of ^{82}Se as the double beta source.

Tables 1.2 and 1.3 summarize the limits that the experiments introduced above set on the $0\nu\beta\beta$ half-life, along with the isotope and detection method used.

Technology Name (Isotope)	Exposure [kg.y]	Energy resolution % FWHM at $Q_{\beta\beta}$	Background index 10^{-3} count/ keV.kg.yr
Semi-conductors **Ge-Diodes**			
GERDA (^{76}Ge)	127	0.15	0.5
Majorana (^{76}Ge)	65	0.12	6
LEGEND, Expected (^{76}Ge)	10000	0.12	0.03
Bolometers			
CUORE (^{130}Te)	288	0.31	15
CUPID-0 (^{82}Se)	16.6	0.67	3.5
CUPID-Mo (^{100}Mo)	2.7	0.24	3
AMORE, Expected (^{100}Mo)	500	0.53	0.1
TPC			
EXO-200 (^{136}Xe)	178	1.23	1.5
nEXO, Expected (^{136}Xe)	50000	0.8	0.183
NEXT-100 (^{136}Xe)	300	0.91	0.5
PandaX-III (^{136}Xe)	420		
Liquid Scintillator			
KamLand-Zen (^{136}Xe)	970	4.3	0.9
Tracking Calorimeter			
SuperNEMO, Expected (^{82}Se)	17.5	4.6	0.1

Table 1.2 – Summary of the major experiments in searching for $0\nu\beta\beta$, with their used isotopes [62] [63] [64] [65] [66] [67] [68] [69] [70] [71] [72] [73] [74] [75].

Technology	$T^{0\nu}_{1/2}$ 10^{25} [years]	$<m_{\beta\beta}>$ [meV]
Semi-conductors		
Ge-Diodes		
GERDA (^{76}Ge)	18	79-180
Majorana (^{76}Ge)	8.3	113-269
LEGEND, Expected (^{76}Ge)	1000	15-50
Bolometers		
CUORE (^{130}Te)	2.2	90-305
CUPID-0 (^{82}Se)	0.47	276-570
CUPID-Mo (^{100}Mo)	0.18	280-490
AMORE, Expected (^{100}Mo)	50	17-29
TPC		
EXO-200 (^{136}Xe)	3.7	103-278
nEXO, Expected (^{136}Xe)	0.0035	5-20
NEXT-100 (^{136}Xe)	6	80-160
PandaX-III (^{136}Xe)	9	
Liquid Scintillator		
KamLand-Zen (^{136}Xe)	230	36-156
Tracking Calorimeter		
SuperNEMO, Expected (^{82}Se)	0.5	260-500

Table 1.3 – Summary of the major experiments in searching for $0\nu\beta\beta$, and the lower limits (90% CL) that they set on the decay half-life and upper limits (90% CL) on Majorana mass $<m_{\beta\beta}>$ [62] [63] [64] [65] [66] [67] [68] [69] [70] [71] [72] [73] [74] [75].

2 - The SuperNEMO Experiment

SuperNEMO is a $0\nu\beta\beta$ experiment with the detector technology derived from the previous NEMO experiments. It is located at Modane at the French-Italian border, in the middle of the Frejus tunnel at a depth of 4800 meters water equivalent.

As mentioned before, the experiment is made of a non-homogeneous detector, the source is made of ^{82}Se double beta emitter distributed over radio-pure thin source foils. The foils are then surrounded by the tracker cells operating in Geiger mode. Then, they are surrounded by 6 calorimeter walls that measure individual particle energies and time of arrival. This setup allows a full topological reconstruction of the decaying particles. The whole structure is then enveloped by an anti-Radon tent to prevent Radon emanation from lab equipment and rocks diffusing into the tracker chamber, and finally an iron shielding to prevent gammas from entering and polyethylene water tanks and boron polyethylene plates to thermalize neutrons and stop them.

In this chapter, different detector parts will be reviewed, and eventually, the expected background will be presented.

2.1 . Detection Method

The scheme presented in figure 2.1 shows the source foils located in the middle of the detector that will undergo $2\nu\beta\beta$ decays emitting two electrons. They will then travel through the detector ionizing the tracker chamber gas allowing for reconstruction of the trajectories of the charged particles. The particles will be under the effect of a magnetic field that curves the tracks of charged particles and allows particle discrimination. Finally, they will reach the segmented calorimeter wall made of plastic scintillators coupled to low-radioactive photomultipliers where each particle energy will be measured individually.

This detection technique offers a lot of physics aspects and background rejection abilities :

- With the tracker, the experiment gains the ability to reject natural radioactivity background very efficiently as it is possible to identify the different particles and decay topologies. The detector is also able to identify crossing muons, external and internal backgrounds through dedicated channels.

- Detailed physics studies of the $2\nu\beta\beta$ decay can be carried out because the SuperNEMO detector allows a measurement of the individual energies, as well as the angular distribution between the electrons. This enables additional analysis :

1- The study of the quenching of the axial-vector coupling constant mentioned in 1.2.7 that goes into the calculation of both the half-life of the $2\nu\beta\beta$ and $0\nu\beta\beta$ decays.

2- Study whether the decay passes through higher state dominance (HSD) or single

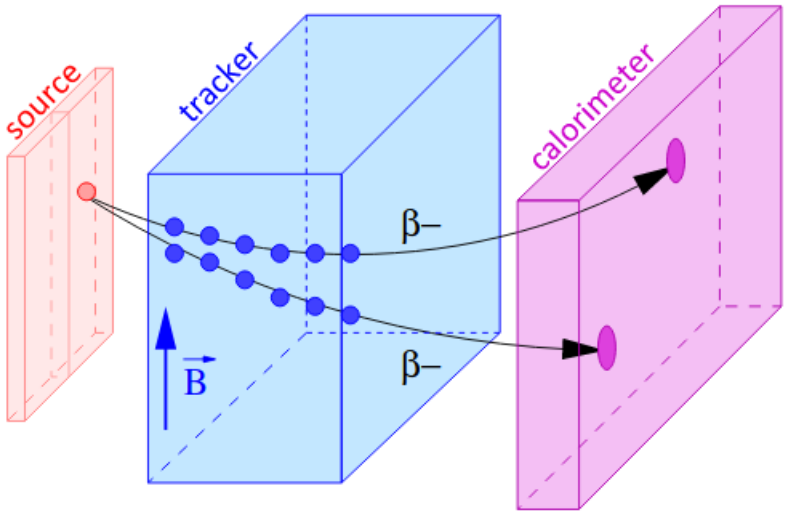

Figure 2.1 – Scheme showing the principle of detection of the SuperNEMO experiment. Two electrons are emitted from the source foils, their trajectories are then reconstructed by the tracker and finally their energies measured by the calorimeter.

state dominance (SSD), and this can be studied by looking at the low energy part of the spectrum of individual electron energies.

3- Study of possible exotic decay (Majoron emission, Lorentz violation, Bosonic neutrinos, ...) which would introduce a deformation in the spectrum of the energy sum of the two electrons.

4- In the case of detection of the $0\nu\beta\beta$, the experiment will be able to identify the decay mechanism by studying the kinematics of the decay (single electron particle energy and angular distributions).

- As the source is separated from the detector, we are able to study different isotopes by replacing the source foils.

2.2 . The SuperNEMO Demonstrator

The first module, called demonstrator, aims to check the ability of the full experiment to reach its ultra-low background specification. Moreover, it will also set limits on the half-life of the $0\nu\beta\beta$ decay. Figure 2.2 shows a schematic view of the detector with the two main calorimeter walls, the tracking module and the source module.

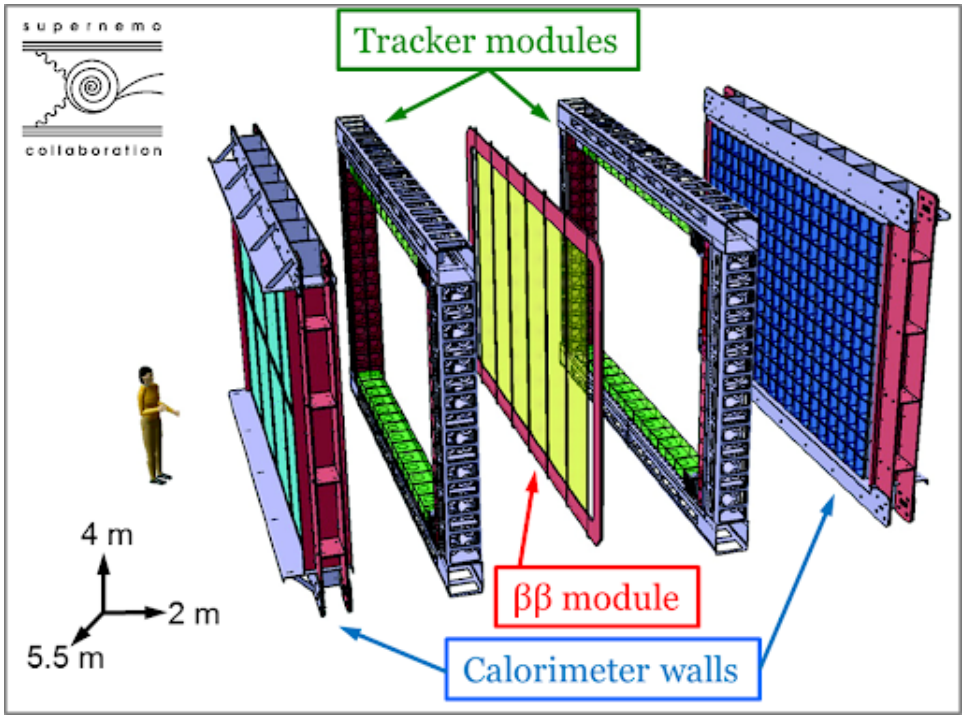

Figure 2.2 – Scheme showing the different components of the Super-NEMO demonstrator, human for scale. The numbers at the bottom left shows the dimensions of the demonstrator. The thin $\beta\beta$ source is in sandwich between the tracker and the calorimeter walls.

2.2.1 . Source

The demonstrator source is made of 6.23 kg of ^{82}Se separated into 34 ultra pure thin source foils. For the reasons mentioned in 1.3.1, the choice of ^{82}Se was made :

1- Having a relatively high $Q_{\beta\beta}$ value, which decreases the β and γ natural radioactive background effects.

2- Having a relatively high $2\nu\beta\beta$ half-life, which decreases the $2\nu\beta\beta$ background.

3- Having high natural abundance and enrichment techniques, which allows the production of the isotopes in large quantities.

4- Ability to reach high purification values through the available techniques.

The use of thin foils limits the energy loss of low energy electrons, which can produce fluctuations of the two electron energies and degrade the electron energy resolution of the detector.

The manufacturing of the foils was done by two methods depending on the laboratories where the preparation was made in.

LAPP Method

This purification method was developed and implemented at the Laboratoire d'Annecy De Physique Des Particules (LAPP). First, natural selenium is prepared by "reverse chromatography" at Dubna, Russia, over two batches in jars made of polyethylene, one with water and propanol and the other with water alone. Then the LAPP team used ultra-pure water to prepare the PVA, then mixed it with the selenium power and poured it on a raw mylar foil, closed the top with another mylar and let it dry. Eventually, each 8 pads were attached to each other to form several foils, see figure 2.3.

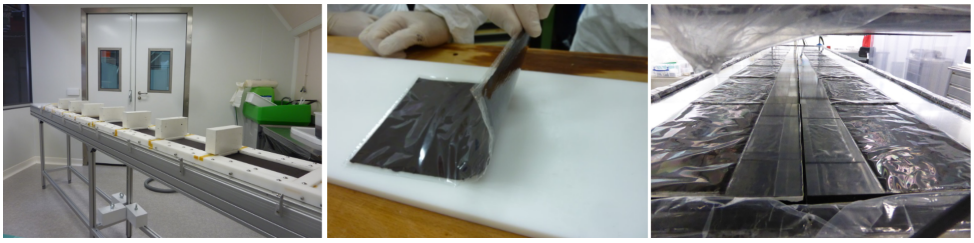

Figure 2.3 – To the left : The mylar pads that the selenium+PVA was poured on. In the middle : Selenium LAPP pad after it has dried, the edges are mylar. To the right : Selenium LAPP source foils after having 8 pads attached together.

ITEP Method

The production was developed and implemented at Institute for Theoretical and Experimental Physics (ITEP), Russia. The purification was done through distillation and then the sample was turned into powder and measured for its radiopurity using a high-purity germanium (HPGe) detector. Then as the LAPP foils, the selenium + PVA mixture was added between two mylar sheets and let dry, but now the full strip is made from a single part

The final source foils were made of 6.23 kg of ^{82}Se distributed over 34 foil strips of dimensions 135.5 $\times$ 2700 mm and a thickness of 300 μm.

To conclude, the LAPP method is more radiopure than the ITEP method, where one can find the measurements in [76]. The ITEP method was used because a portion of the ^{82}Se was grounded to very small grains and it was not possible to prepare the foils with the LAPP method. Geometry-wise, since this grounded ^{82}Se was difficult to work with, the ITEP foils became curved. The final form of the foils is presented in figure 2.4 after installation inside demonstrator in a frame measuring 4.857 meters large and 2.7 meters high. One can differentiate between

the ITEP and LAPP foils. Also, one can see that there is a slight curvature in the ITEP foils and this happened probably during the glue drying phase. The curvature of each foil was precisely measured with a high precision laser tracking system for a precise description of the foils geometry for analysis and implementation into the simulation software.

Figure 2.4 – Picture of the source foils (in dark grey) hanging inside the SuperNEMO demonstrator. One can spot the two types of foils : the LAPP (with foils pads attached together) and the ITEP foils.

2.2.2 . Tracker

The tracker is a wire chamber made of 2034 drift cells operating in Geiger mode. The source foils are placed in the middle of the chamber which is filled with a gas mixture (95% Helium, 4% ethylic alcohol and 1% Argon). The tracking chamber configuration was chosen to limit as much as possible the amount of materials crossed by electrons before reaching the calorimeter.

The tracker allows a highly efficient particle identification between different particles and performing high background rejection to select eventually only two e^- events. The goal of the tracker is to provide a three dimensional reconstruction of the charged particle trajectories, hence a good spatial resolution is required for a good vertex reconstruction. A correct reconstruction of the two electrons originating from the same vertex, or at the minimum, from the same source foil

is a key feature of the experiment. It also allows an identification of the so-called "hot spots", due to a local radioactive contamination of the source.

Cells Operating in Geiger Mode

The tracker cells are made of two copper rings on the top and bottom connected by an anodic wire in the middle with grounded wires surrounding it. The cells are fed with high voltage ($\sim$ 1500 V - 1700 V) creating a powerful electric field.

When a particle passes through the gas, it ionizes it along its path, creating heavy positive ions and electrons. The electrons will travel towards the anodic wire creating an anodic signal, and just as they get close enough to the wire, the electric field becomes very strong allowing the ionized electrons themselves to ionize the gas and start an avalanche. As the avalanche will mask the electric field, new created electrons will not be able to start new avalanches, but the emission of de-excitation and recombination UV photons will bring forth new avalanches that will create plasma and propagate along the wires to each side of the cells. The process is illustrated in figure 2.5.

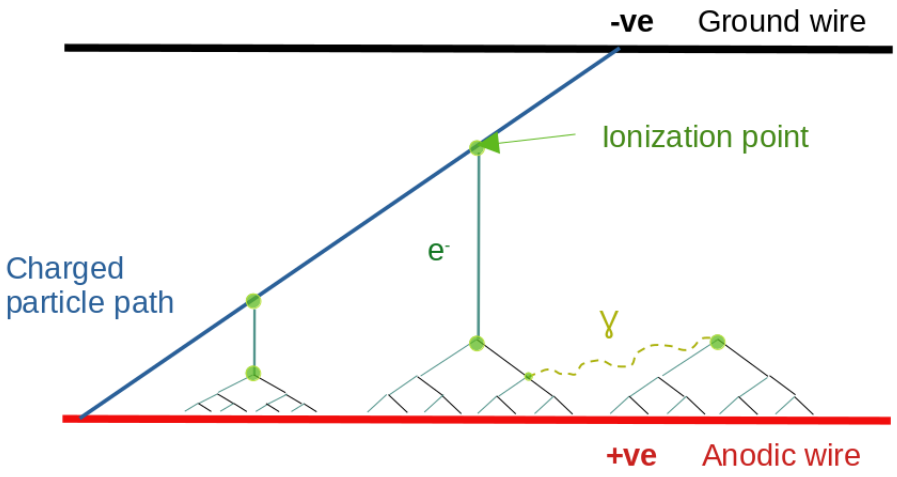

Figure 2.5 – Scheme showing how a charged particle passing through a cell operating in Geiger mode will ionize the surrounding gas and start an avalanche that propagates along the anodic wire by de-excitation and recombination UV photons.

To prevent the avalanche from being self sustaining which produce a continuous electric current that leaves the cells useless, a quenching agent is added to the gas mixture to absorb secondary photons. However, after the absorption process, polymer chains are created on the cell wires disrupting the electrical field and creating premature aging. This can be avoided by adding oxygen rich molecules, such as ethyl alcohol.

The anodic signal allows a measurement of the distance at which the electron passes with respect to the anode wire. On the other hand, the plasma propagation allows a pinpoint of the vertical position of the interaction by measuring the time the avalanche needed to travel to each cathodic ring, a registered signal is presented in figure 2.6.

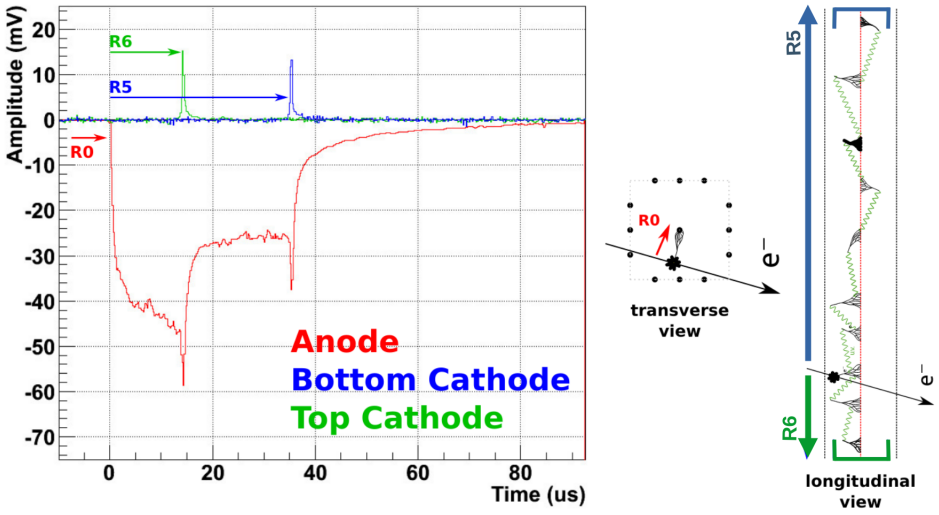

Figure 2.6 – To the Left : Registration of the signal of a passing particle by a tracker cell. R0 represents the time between the creation of the first electron-ion pair and the first cell signal. R5 and R6 represent the time the plasma needed to propagate to the bottom and top cathodic rings, respectively. A visualization of these registered times is presented to the right.

This whole process produces a dead time of the tracker cells of the order of ms ($\sim$ 5ms [45]), hence it is suited to a low-radioactivity experiment surrounded by shielding in an underground laboratory.

The operation of these cells depends greatly on the high voltage (HV) fed to them. Figure 2.7 presents how the charge collection varies with the voltage applied. At low energies, the charge collected is proportional to the voltage applied. With the increase of the voltage to a certain level, the cell reaches a saturation in charge in which the charge collection stays stable, this is the region that the cells should be working in and it is called the Geiger region or Geiger plateau, which provides a very high detection efficiency (>99%). The region is around 1500 V and about 300 V wide.

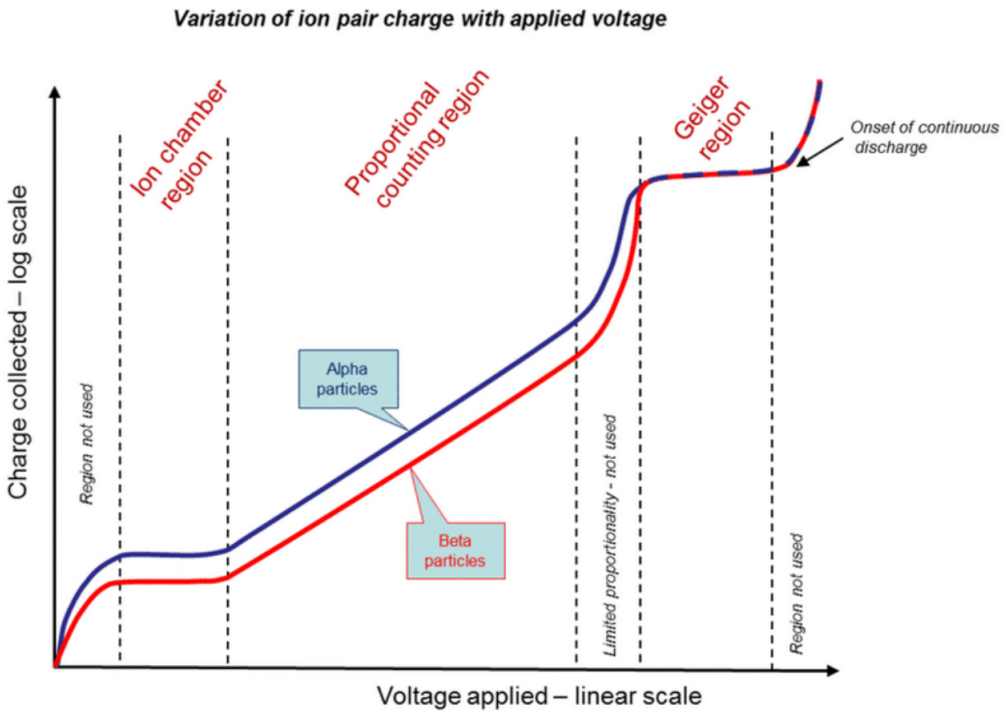

Figure 2.7 – Collected charge by the anodic wire of the cell in logarithmic scale as a function of the applied voltage. Different operation regimes are presented. We are interested in the Geiger regime, below that the charge collection is variant with the voltage and above it is unstable.

Gas Mixture

The tracker gas composition is a vital part of the detection process in the wire chamber, as choosing the components of the gas affects the ionization and energy loss of the passing charged particles. For the SuperNEMO demonstrator, the mixture is chosen to be :

- Helium as the main component, ionized by incident radiations. Being an inert gas, it does not react with the detector parts.

- Argon (1%) has low ionization energy and enhances the propagation of avalanches along the anode wires.

- Ethanol (4%), a quenching agent used to stop the successive discharges and preventing the breakdown of the detector.

This gas composition guarantees a medium with low Z number, minimizing energy losses and particle multiple scatterings.

SuperNEMO Cells

The dimension of tracker cells was chosen after compromising between the required spatial resolution and the resulting particle energy loss in the wires.

The cells of SuperNEMO were designed to have a diameter of 4.4 cm : two copper rings of 4 cm and an anodic wire of stainless steel with a 40μm diameter surrounded by 12 grounded wires of the same material with 50μm diameter. The whole tracker chamber is made of 2034 cells placed in arrays of 9$\times$113 parallel to the source foils.

Figure 2.8 – The tracker cathode cells, along with the anode wires with light reflected on them. The source foils can also be seen (grey, middle).

The voltage applied on each cell should be within the Geiger plateau as mentioned before. The actual voltage depends on intrinsic individual properties of each cell, and is determined during the tracker commissioning phase.

The intrinsic spatial transverse resolution is expected to be on the order of few millimeters, even if it can be enlarged by left-right ambiguities (w.r.t the central anodic wire). The longitudinal resolution is expected to be around 1 cm.

2.2.3 . Calorimeter

Neutrinoless double-beta decay experiments always aim to have a very good energy resolution coupled with high radio-purity and background rejection. The

high radio-purity is targeted in the manufacturing process for all the material of the detector as it greatly helps in reducing the background, especially in the energy region of interest of $0\nu\beta\beta$. Also, background can be due to external sources outside the detector, and this can be massively reduced by installing active and passive shields. Backgrounds are further detailed in 2.5.

But still, an irreducible background for $0\nu\beta\beta$ is the $2\nu\beta\beta$ decay, hence the great importance of having a very good energy resolution. The latter will allow a better discrimination between the $2\nu\beta\beta$ decay energy distribution tail and the $0\nu\beta\beta$ signal, separating the two and decreasing the $0\nu\beta\beta$ peak width. The requirement on the calorimeter energy resolution of the SuperNEMO demonstrator is 8% FWHM for 1 MeV electrons, for the optical modules (OM) designated for signal selection. In addition, a very good time resolution is expected for external background rejection, the resolution is required at $\sigma_t \leq 400$ ps for 1 MeV electrons for SuperNEMO. The scintillator blocks size took into account the need for an efficient γ detection efficiency of 50-80% (depending on the gamma energy) [42].

The whole setup of SuperNEMO (source + tracker) is enveloped with a calorimeter of 712 optical modules, of which 440 are 8" OMs of the required specifications, mentioned above. The rest are 5" OMs of 11-12 % FWHM for electrons at 1 MeV for the main walls. The Calorimeter is made of 6 OM walls separated into 3 categories depending on their designated work, see figures 2.9 and 2.10 :

- Main Walls : they are made of two walls standing in parallel to the source foils on the two opposing sides, they are named the French and Italian walls according to which country they side. Each wall is made of 13 $\times$ 20 blocks of OMs, totally 520 OM, all of which 8" OMs (440 OM) except the first and last rows which are 5" OMs, mainly used for background rejection. The 5" OMs have worse resolution (11-12% FWHM), but they are placed near cathode rings, so they offer a γ background rejection. These are the walls that will be used for signal detection.

The two other categories are concerned with background rejection and fully made of 5" OMs :

- X-Walls : They are two walls closing the two (other) sides of the detector, called tunnel and mountain sides (for the same naming reasons). Each wall is made of 2 identical columns each of 16 OMs, directed towards the tracking chamber with the source foils on the middle plane.

- G-Veto : Two walls closing the top and bottom of the detector, named, creatively, top and bottom walls. Also made of 2 $\times$ 16 blocks, they are used as active veto shieldings for γs.

The aim of the calorimeter walls is to measure each individual particle energy and register their detection time.

Figure 2.9 – Side view of a main calorimeter wall. Visible are the optical fibers, electric cables and signal cables, which deliver the high voltage and retrieve the PMT signals.

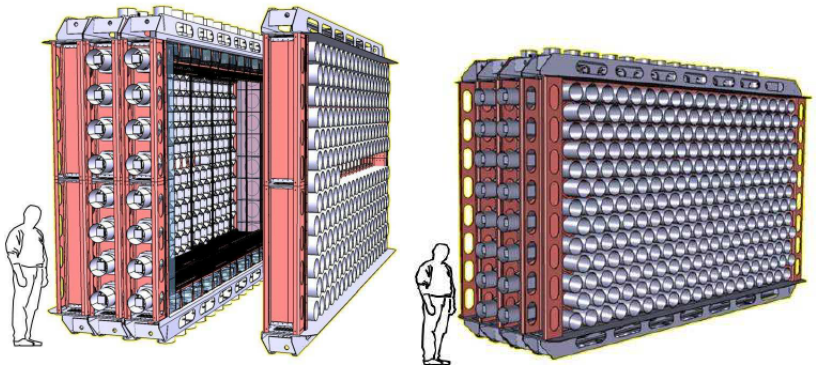

Figure 2.10 – The calorimeter of SuperNEMO. Each white tube represents an OM. To the left : One main wall separated from the rest detector module. Half of the X-Wall is shown with two columns of optical modules. The G-Veto walls are on the top and bottom of the module. To the right : A clearer view of the main wall, composed of 260 optical modules. Each wall has its symmetric part at the opposing side.

Energy Measurement Principle

Each individual optical module in the calorimeter is composed of two sub-detectors, a scintillator and a photomultiplier (PMT). The working principle of energy detection through OMs can be summarized as (see also figure 2.11) :

- An electron, an alpha particle, or a γ particle (through Compton scattering) interacts inside the scintillator, scintillation photons are emitted with an amount proportional to the energy of incoming particle (low energy particles undergo quenching [43]).

- The scintillation photons propagate through the scintillating medium until a fraction reaches the photomultipliers' photocathode, which can absorb the photons and emit photo-electrons via the photo-electric effect.

- Each photo-electron will move towards the first dynode of the PMT under the influence of a high electric potential difference. When an electron reaches the first dynode, it will create multiple other electrons by ionization. The number of electrons is further amplified as they cascade through several dynodes. The number of electrons created finally generates a measurable electric current at the anode.

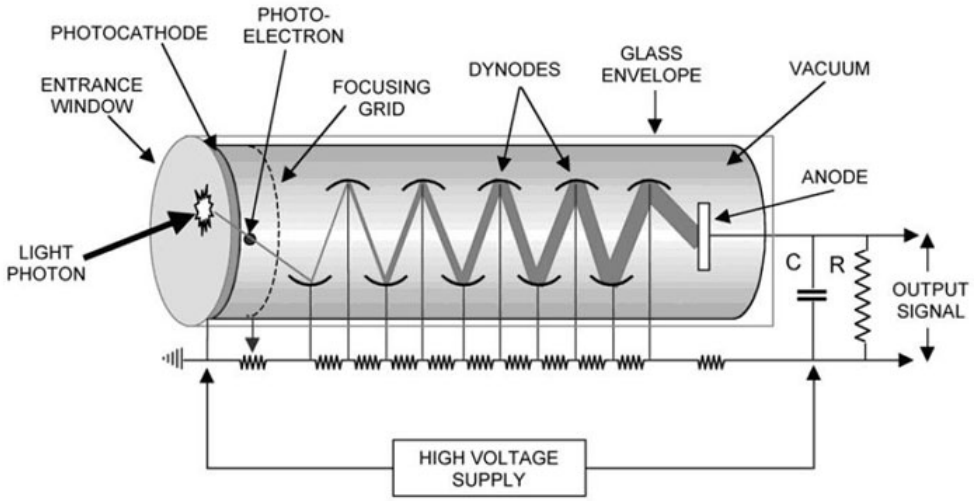

Figure 2.11 – Scheme showing principle of energy measurement inside an optical module. Scintillation photons can create electrons via photoelectric effect from the photocathode. These photoelectrons are accelerated by the PMT electric field, producing secondary electrons when crossing dynodes. Finally an electric current is detected at the anode, and finally is sent to the electronics acquisition.

Photomultiplier

A good PMT checklist for double beta decay searches would include a :

- High quantum efficiency (probability of conversion of the incident photons to an electrical signal).
- Good photo-electron collection efficiency.
- Linear gain with energy.
- High radio-purity.
- Good time resolution.
- Low dark currents.

For the SuperNEMO demonstrator, 8 inches PMTs (R5912-MOD Hamamatsu) were chosen because of the good number of electronic channels and the fit to the scintillator design, in addition to the improved energy measurement due to the increase of the photo-detection surface compared to the 5" PMTs, which were used in the previous NEMO-3 experiment, winning a factor of ~ 2 on the energy resolution for SuperNEMO (8%) compared to NEMO-3 (14%).

The quantum efficiency of the chosen photomultipliers was optimized for 400 nm wave-lengths and is equal to 35% (compared to the 25% for NEMO-3). The photo-electrons collection efficiency and linearity were also improved, increasing the number of photo-electrons to ~ 1000 for 1 MeV electrons in order to reach the 8% energy resolution at 1 MeV. The gain reached by the 8" PMTs of SuperNEMO is 10^6.

Scintillator

SuperNEMO scintillators are made of an organic polystyrene based material, doped with 0.05% of POPOP (1.4-bis(5-phenyloxazol-2-yl) benzene) and 1.5% of p-Terphenyl (p-TP) as primary and secondary wavelength shifters, respectively. This composition fulfills the requirements of high light yield, low electron back-scattering (low Z), good timing, high radio-purity and a relatively low cost.

In the R&D phase different scintillator block geometries were considered. After performing simulations and test, the best energy resolutions are reached for the geometry shown in figure 2.13, with the dimensions of the entrance face (i.e towards the tracker) of 256×256 mm.

The scintillator depth choice is motivated by the presence of a magnetic field (detailed in 2.2.5). A study showed that a magnetic shielding needs to extend at least 10 cm beyond the PMT photocathode for it to be efficient, otherwise, depending on the orientation of the dynode system with respect to the magnetic field, the gain would be noticeably reduced and the resolution worsened relatively by up to 50 $\%$. Therefore, 3 mm thick pure iron shielding have been designed to surround each optical module and protect it from the magnetic field, presented in figure 2.12 as the black iron box. In order to increase the light collection efficiency, each scintillator block is wrapped in radio-pure Teflon (on its sides) and aluminized

Mylar (on its sides and front face), see figure 2.12. The latter also protects against the UV photons coming from the tracker chamber and other surrounding optical modules.

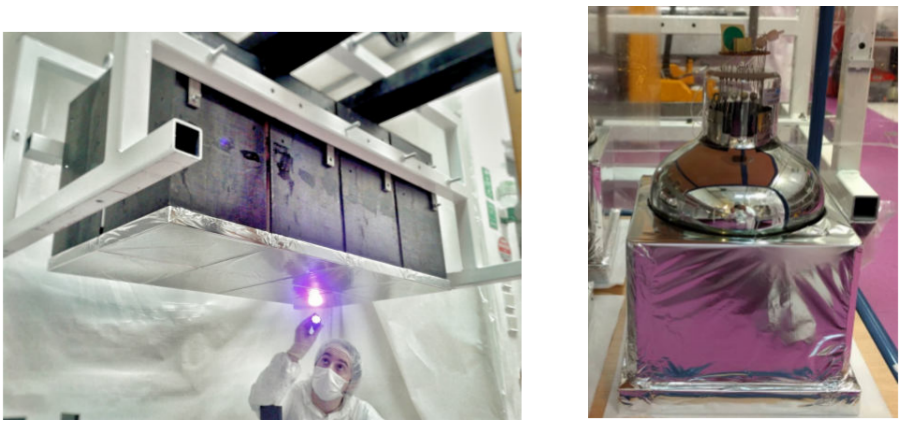

Figure 2.12 – Tp the left : 8" OMs are grouped together for ease of transportation. The black iron boxes are the iron shielding, inside is the OM. To the right : PMT on top of the scintillator block, which is covered by the aluminized mylar.

Figure 2.13 shows a 2D drawing of the scintillator geometry, and the shape of it. The scintillator is hollowed to fit the photomultiplier bulb. The SuperNEMO scintillators are designed thicker than the previous NEMO-3 design, improving background rejection by enhancing γ detection.

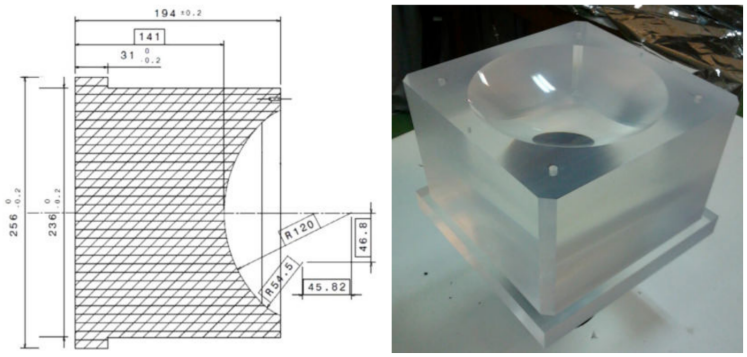

Figure 2.13 – To the left : A 2D drawing of the geometry of the scintillator block. To the right : The scintillator block hollowed to fit the PMT bulb.

Particle Interaction Inside Scintillator Block

The detector is mainly aimed at detecting electrons and gammas, so understanding their interaction point inside the polystyrene blocks is essential for correct analysis, especially timing analysis.

Electron Interaction Point

Electrons interact with matter through one of two processes : elastic scattering on a nucleus, or inelastic scattering on an atomic electron. For polystyrene scintillators, inelastic scatterings dominate and occur through two different forms : coherent scattering with the electron cloud, and radiative energy losses (Bremsstrahlung effect). Looking at figure 2.14, in our energy range of interest (50 keV to few MeVs), collision stopping power is dominating and in particular, a 1 MeV electron will stop just few millimeters inside the scintillating block, as seen in figure 2.16.

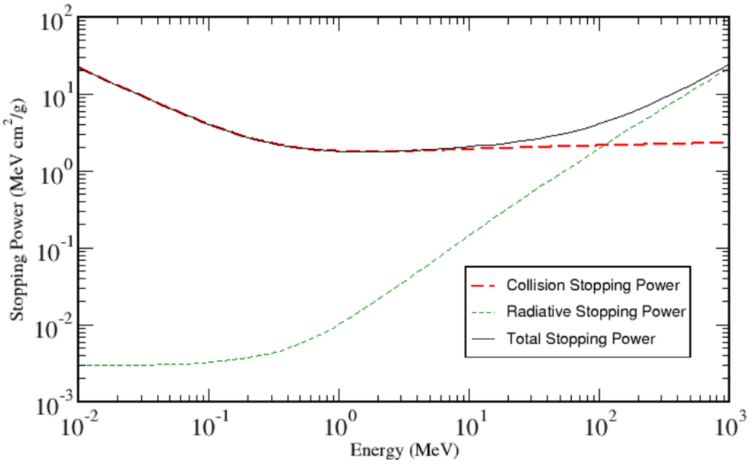

Figure 2.14 – The stopping power of electrons inside polystyrene according to their energies in MeV.

Photon Interaction Point

Photons traveling in matter can interact with the electronic cloud. Low-energy photons mainly interact with the electron cloud, either through photoelectric effect (γ radiation is fully absorbed by an electron of the cloud), or through coherent scattering (Rayleigh scattering). For higher energy photons the Compton inelastic scattering of a γ with an atomic electron dominates. Figure 2.15 shows the mean attenuation length of a γ radiation in polystyrene scintillators as a function of energy, and inferring that most of 1 MeV γ radiations will interact around 10 cm (10^{-2} cm^2/g) inside the scintillating material before stopping, as seen in figure 2.16.

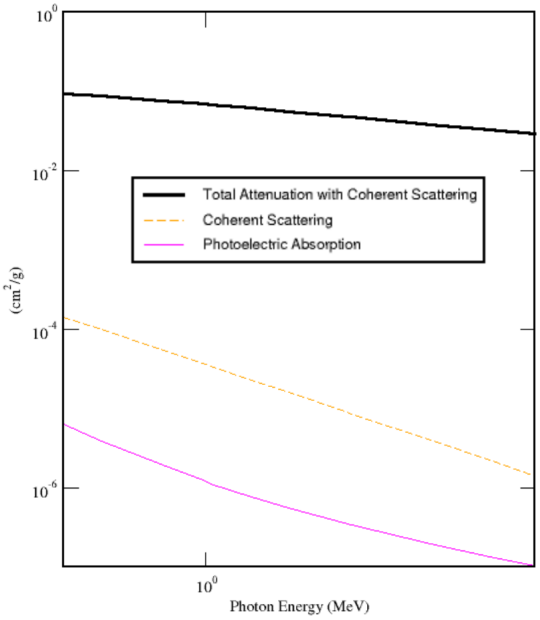

Figure 2.15 – The attenuation of photons inside polystyrene according to their energies in MeV.

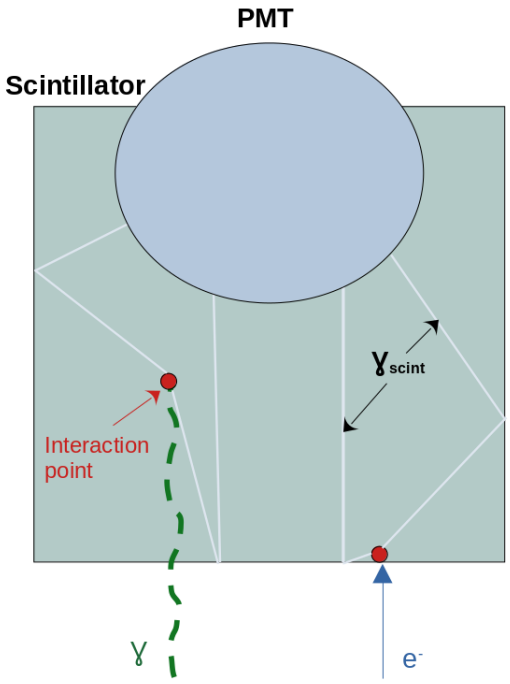

Figure 2.16 – Interaction point (red circle) of both gammas and electrons inside the scintillator block, where scintillation photons are created, and finally collected by the PMT glass.

Time Resolution

The timing information of a passing particle through the OM proceeds in a sequence, from the scintillation photons in the scintillator, converted to electrons at the photocathode, amplified and then transmitted to the PMT electronics and finally to the electronics board.

The uncertainty on the measured time is defined as :

$$\sigma_t = \sqrt{\frac{\tau_{sc}^2 + (FWHM_{transit\ time}/2\sqrt{2ln(2)})^2}{N_{PE}}} \tag{2.1}$$

Where :

- τ_{sc} is the de-excitation time of single atoms excited by the passage of an incoming particle in the scintillator.

- FWHM$_{transit\ time}$ is the transit time is defined as the time delay between the input light pulse at the PM tube and the appearance of the output pulse, this time delay is different between the input photons. The FWHM is linked to the transit time spread (due to the time delay difference) of photo-electron creation [44].

- N$_{PE}$ is the number of photo-electrons (PE) generated, and is defined as :

$$N_{PE} = E^2 \times (2\sqrt{2ln(2)}/FWHM_E)^2 \tag{2.2}$$

Where :

- E is the deposited energy of the particle inside the scintillator.

- FWHM$_E$ is the energy resolution of the OM which depends on the energy (taken for electrons at 1 MeV). It is linked to the PMT light collection of the scintillation photons and to the quantum efficiency of the PMT.

The difference in time resolution between 5" and 8" OMs is mainly linked to the energy resolution. The two have the same scintillation time, while the transit time is slightly worse for the larger 8" OM. The transit time is unique per OM, and is dependent on the point of creation of the photo-electrons, and as the photocathode increases in size, the larger the dispersion will be [44]. But, as the PMT glass of the 8" PMT is larger and more adapted to the scintillator geometry, the light collection is better, meaning that the energy resolution is better and hence the time resolution of 8" OMs is better than that of 5".

Time resolution also differs in case of detection of an electron or a gamma. The interaction point is different in the two cases for reasons presented in the previous paragraphs. As a consequence, for a gamma interaction the depth of interaction is larger than that of the electron (see figure 2.16), which induces an additional temporal enlargement of the light pulse.

The characterization of the resolution for the demonstrator calorimeter was performed, see further details in chapter 3.

2.2.4 . Gas Tightness

Ensuring that the tracker gas do not leak out and that outside air does not leak in is a major step that needs to be executed properly, it ensures that there are no contaminants entering the detector. Several measures were taken into account during installation and assembly of the module :

- The pre-assembled blocks of 8 optical modules were wrapped in a radio-pure nylon film. Additional patches of it were glued on the calorimeter back side on each gap between these groups of 8 optical modules.

- After the calorimeter walls assembly, copper bars have been installed on the back side at the gap between the calorimeter and the structure supporting the detector.

- A piece of nylon was mounted on the front side of each main wall before the detector was closed in order to prevent the Radon from emanating from the calorimeter to the tracker, see figure 2.17.

But even with these measures, leaks still existed mainly between the tracker and calorimeter frame, and from the calorimeter to the outside clean tent environment.

The detection of these leaks is done by injecting gas into the detector through the gas injection system, and search for gas leaks using a gas probe. Since Helium is known to cause damage to the PMTs, the gas used for these leak tests was Argon. Every leak was fixed using the proper leak seal depending on the leak size and location (Different leak-sealing radio-pure materials (SBR, RTV, Stycast and Black Mamba glues)).

Finally after many months taken to fix these leaks, the detector reached an over-pressure of 10 mbar, which is even above the desired pressure inside the gas chamber.

Figure 2.17 – A calorimeter wall covered with radio-pure nylon film. To avoid Radon diffusion from the calorimeter towards the tracker gas

2.2.5 . Magnetic Coils and Passive Shielding

The magnetic field is essential for the discrimination of charged particles, especially electrons and positrons. If a high energy gamma interacts through pair creation with the source, it can act as a background, if the charge of the positron is not identified. If it is not possible to efficiently discard these events it will affect the $0\nu\beta\beta$ signal energy region, which is problematic.

The magnetic field is generated by a copper coil, parallel to the tracker field wires, with an intensity of 25G, good for an appropriate discrimination of charged particles. The copper bars used are recycled from the NEMO-3 experiment and redesigned by the mechanical team at LAL (currently IJCLab). The coil is already installed at the experiment site as seen in figure 2.18. They surround the full structure of the demonstrator.

Figure 2.18 – Magnetic coil installed at the experiment site. The coil surrounds the detector. One side is shown in the figure.

The coil will then be surrounded by an anti-Radon tent, which prevents the Radon from emanating from lab materials and rocks diffusing into the demonstrator. The detector volume will then be flushed with Radon-free gas, then the flushed Helium will be purified by a dedicated factory which uses Radon trapping materials at low temperature to trap the Radon atoms until they decay. The mechanical

design of the anti-Radon tent is presented in figure 2.19.

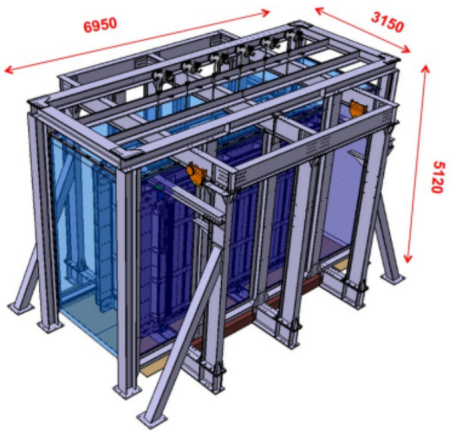

Figure 2.19 – Mechanical design of the anti-Radon tent. The structure of the tent is supported by stainless steel bars, while the panels of the tent are made of High Density Poly Ethylene (blue shaded areas).

The tent will then be surrounded by a 20 cm thick pure iron shielding to prevent external gammas from entering and interacting inside the detector. Then a neutron shielding will be installed constituting of polyethylene water tanks and boron polyethylene plates that will thermalize neutrons and stop them. The mechanical design of these two shields is presented in figure 2.20.

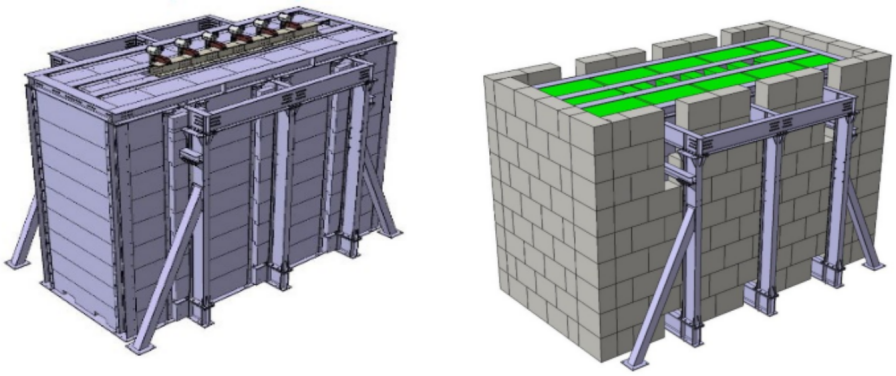

Figure 2.20 – Mechanical design of the iron shielding that stops gammas (to the left) and the neutron shielding made of polyethylene water tanks and boron polyethylene plate (to the right).

2.3 . Detector Real-Time Calibration

To control the detector equipment function during the long exposure time, monitored calibration over time intervals is necessary. For this, SuperNEMO is equipped with two systems : a ^{207}Bi source deployment system and a light injection system.

2.3.1 . ^{207}Bi Source Deployment System

^{207}Bi is used as the absolute energy calibration source. Each nucleus then decays dominantly through electron capture to the excited state of ^{207}Pb, where there are two dominant scenarios : two γs emitted nearly simultaneously (1063 keV and 570 keV), or the emission of a conversion electron at 976 keV followed by a γ at 570 keV, see decay scheme in figure 2.21. The scenario with electron emission is used to calibrate the detector in energy daily. The three possible electron peaks will be used to perform absolute energy calibration of the OMs.

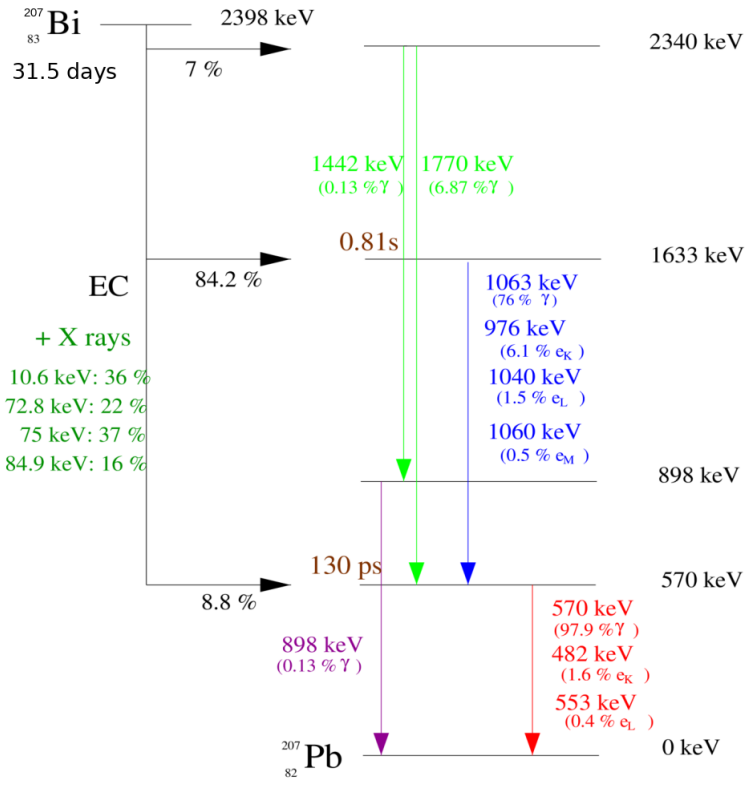

Figure 2.21 – The decay scheme of ^{207}Bi to the ground state of ^{207}Pb, dominantly through electron capture and gamma emission.

The system deploys 42 sources, with a mean activity for each source of 130 Bq, into the source frame between the foils. The sources should have a limited activity to keep the trigger rate of each tracker cell under 30 Hz to avoid damage or

premature aging of the wires [45]. Also the calorimeter walls should receive enough electrons to allow a fitting of the electron energy peak with a sufficient precision ($\sim 1\%$ [45]) with a reasonable data-taking time (on the order of $\sim$ 1 hour). To achieve these points, the ^{207}Bi sources are attached in 7 different positions to 6 steel wires, see figure 2.22.

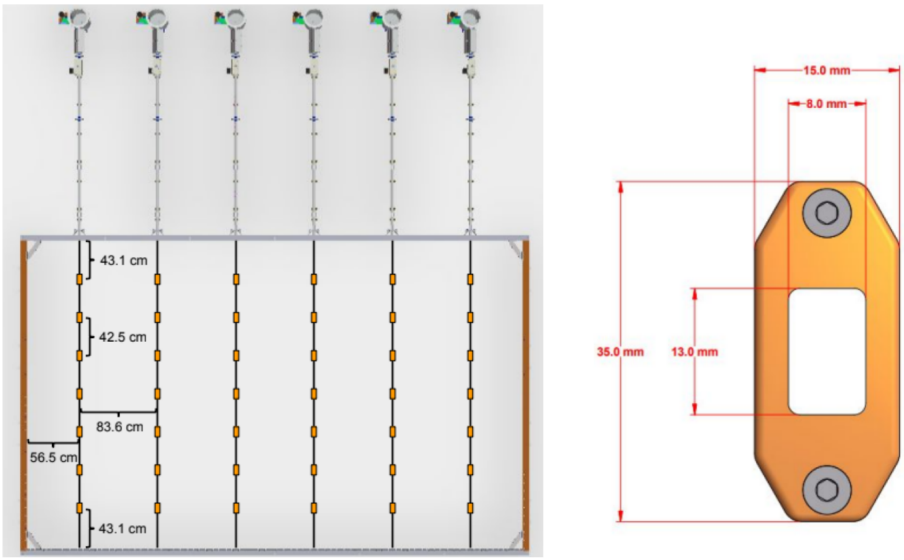

Figure 2.22 – ^{207}Bi deployment system. To the left : The deployment system of the sources inside the foils frame, each orange rectangle represents a ^{207}Bi source, 7 are held by a steel wire that can be deployed automatically. To the right : The sources are inserted into the middle of the white rectangle, which is then deployed as in the picture to the left.

2.3.2 . Light Injection System

This system should run in addition to the ^{207}Bi source deployment system during the full data taking time ($\sim$2.5 years). A scheme of the system is presented in figure 2.23. The system is made of 20 LEDs emitting light at a wavelength of 385 nm through optical fibers connected to the OMs. To keep the stability of the injected light at check, a reference OMs is kept aside that receives the same light as the calorimeter along with a ^{241}Am source used as a reference. The system is intended as a cross check and will allow a survey of the OMs, especially keeping the linearity of the OMs and compensating for any deviations created by HV and temperature variations.

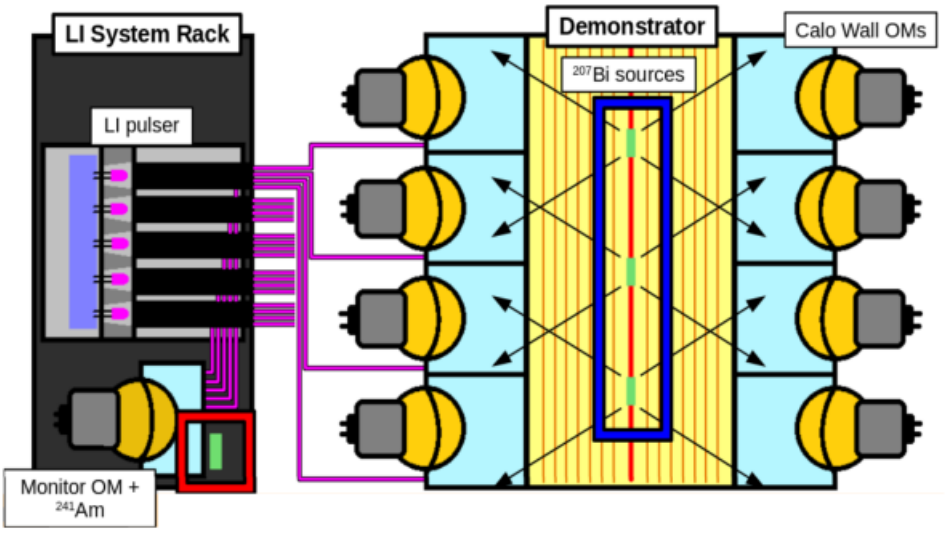

Figure 2.23 – the Light injection system setup. Inside the rack is shown the reference OM with the ^{241}Am source. Optical fibers (shown in purple) are connected between the LEDs (pink dots) and each OM.

2.4 . Detector Electronics

The detector electronics go through three stages :

1- The Front-End Boards (FEB) : They receive, process and digitize the OMs and tracker cells primary analog signal. The previous NEMO-3 experiment lacked this analog signal digitization. This signal is then sent to the control boards.

2- The Control Boards (CB) : They receive the signals from the different FEBs and forward them to the trigger board.

3- The Trigger Boards (TB) : They are in charge of taking the decision whether an event should be registered or not according to the selection criteria given by the user taking data. After the decision is taken, a command is sent to the tracker and calorimeter FEBs to register the event.

4- Data Acquisition System (DAQ) : After registering of the event is done (open for a certain time interval), all digitized data are sent to the DAQ.

For the calorimeter electronics, each main wall is connected to 20 FEBs, each FEB corresponds to 13 OM. The X-Walls are connected to 8 FEBs while the G-Veto walls have 4 FEBs, each FEB is connected to 16 OM. For the tracker, we have 19 FEBs each containing 108 electronic channels.

2.5 . SuperNEMO Expected Background

Due to the rarity of the $0\nu\beta\beta$ signal, an ultra-low background is required.

Background sources can be separated into three categories : internal, external and Radon backgrounds.

2.5.1 . Internal Background

This category concerns the background originating from the source foils, mainly from contaminants inside, mainly ^{214}Bi (Q_β = 3.27 MeV) and ^{208}Tl (Q_β = 4.99 MeV). These contaminations are naturally occurring inside the source through the decay chains of ^{232}Th and ^{238}U, and they can mimic the $\beta\beta$ signal through the following possible cases, also presented in figure 2.24 :

- The isotope undergoes β decay and emits an electron that undergoes Møller scattering, creating a second electron.

- The β decay is accompanied by an internal conversion electron of the daughter nucleus.

- The β decay along with a photon from the de-excitation of the daughter nucleus. A Compton scattering of this photon produces the second electron.

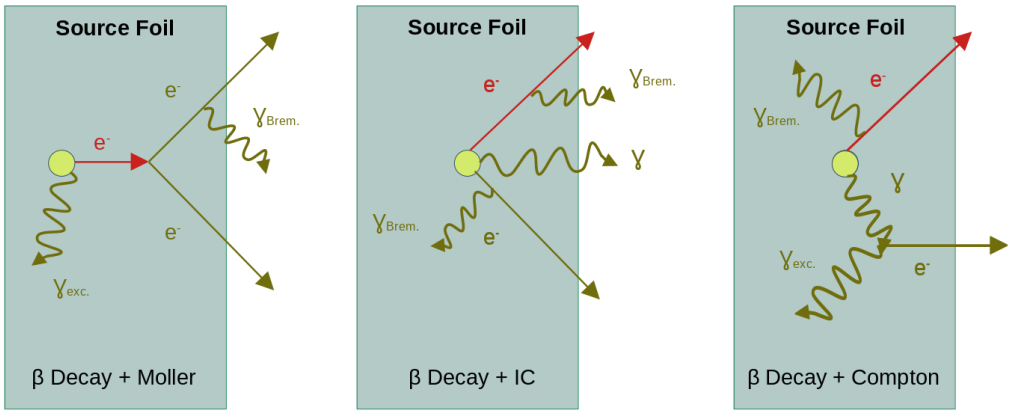

Figure 2.24 – The different processes by which a contamination of the source foils can mimic a $\beta\beta$ signal. To the left : Beta decay followed by a Møller. In the middle : Beta decay followed by internal conversion electron. To the right : Beta decay with Compton scattering.

Along with these events, one or more gamma emissions can take place following from either the de-excitation of the daughter nucleus after the decay, or from Bremsstrahlung effect. ^{208}Tl emits 1 to 3 γs and ^{214}Bi from 0 to 2 γs hence the channels of 1e and 0 to 3 γs are used to measure this background.

The contamination can already be present inside the source powder and not completely removed during the purification process. They can also be introduced during the production, transportation or installation of the foils. Hence, a great care was taken of the foils during these steps.

The contamination of the source foils was measured using a very sensitive detector developed by the collaboration called the BiPo-3 detector. It is specifically

designed to look for Bismuth-Polonium cascades, and hence its name [41]. The results are presented in the table below 2.1. The measured activity of ^{208}Tl has 5 times improvement from the NEMO-3 detector. Due to its sensitivity and accidental background, the detector was only able to set upper limits of the ^{214}Bi contamination, it should be measured more precisely with the demonstrator.

Contamination Isotope	Required Specification [μBq/kg]	BiPo-3 Measured Activity [μBq/kg]
^{208}Tl	< 2	20 ± 10
^{214}Bi	< 10	< 290 (90% CL)

Table 2.1 – Measured activity of the contaminating isotopes inside the $\beta\beta$ source foils. The measure ^{208}Tl activity was obtained for the source with the lowest activity measurements.

2.5.2 . External Background

External gammas are the main contributor for the external background. The gamma passes through the detector to interact inside the source foils. The origins of this gamma can be summarized into 3 contributors :

1- Radiative capture of thermal neutrons, induced by natural radio-activity from (α,n) reactions or spontaneous fission or Bremsstrahlung of cosmic muons, in the shielding and matter.

2- Natural radio-activity present in the laboratory, mainly in the surrounding rocks.

3- Contamination of the PMT glass, mainly by ^{208}Tl, ^{214}Bi and ^{40}K.

The main mechanisms for mimicking the $\beta\beta$ signal are as follows, also presented in figure 2.25 :

- Gammas producing an e^- e^+ pair, where the positron can be misidentified as an electron due to incorrect reconstruction of the curvature.

- Gammas inducing a double Compton scattering.

- Gammas inducing a Compton scattering followed by a Møller scattering.

Contamination Isotope	Measured Activity [Bq]
^{40}K	540
^{226}Ra	197
^{232}Th	124

Table 2.2 – Total measured activity combined for both 8" and 5" optical modules of the contaminating isotopes of PMT glass [47].

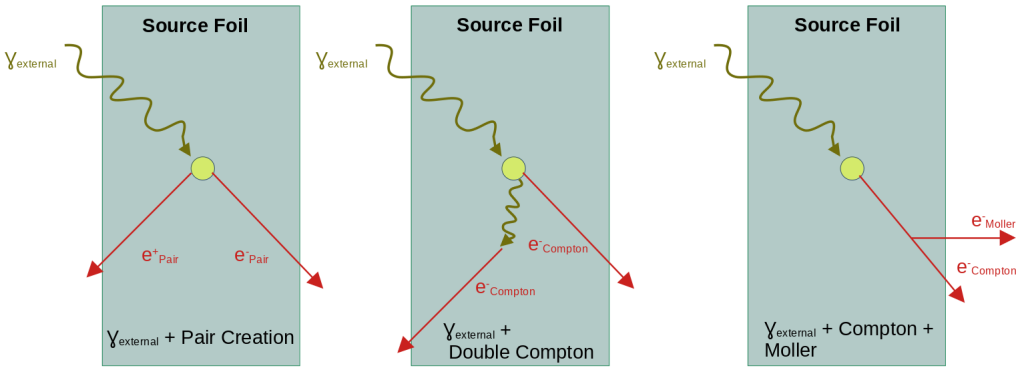

Figure 2.25 – The different processes by which an external gamma interaction with the source foil can mimic $\beta\beta$ signal. To the left : Pair creation . In the middle : Double Compton. To the right : Compton followed by a Møller effect.

The contamination level of the PMT glass was measured using high purity Germanium detector, and the results are presented in table 2.2. The total measured activity for ^{232}Th is 151% higher than the previous NEMO-3 detector, but for ^{226}Ra and ^{232}Th, we can see a total activity reduction by 35%. The main difference between the NEMO-3 and SuperNEMO concerning the effect of the radioactive contamination of the PMT glass, is that for SuperNEMO has thicker scintillator blocks, meaning that a gamma emitted from the PMT glass has more chance to interact with a scintillator before reaching the foil. In that case, this background can be rejected. Moreover, double Compton and Compton + Møller induce additional gammas, which are more likely to be detected with thicker scintillator blocks. This is also the case for pair creations, for which positron annihilation induce two 511 keV gammas, even if these gammas can be detected in the same scintillator blocks as the positrons. Hence, along with the fact that the calorimeter energy resolution is improved, a negligible increase in the background is expected.

2.5.3 . Radon Background

Another main and very important background source is the Radon. This gas is highly diffusive and exists naturally in the rock walls of the laboratory. Its long half-life (3.8 days) allows it to emanate from the rock walls of the laboratory, and to diffuse into the detector. Additional potential sources of Radon are :

- Emanation from tracker materials.
- Contamination of the tracker gas.
- Diffusion from detector materials to the tracker chamber.

^{222}Rn disintegrates into ^{214}Bi (see decay scheme in figure 2.27). If such a decay occurs close to the source foil it is indistinguishable (except if the α emitted by ^{214}Po disintegration is detected) from a $\beta\beta$ events as shown in figure 2.26.

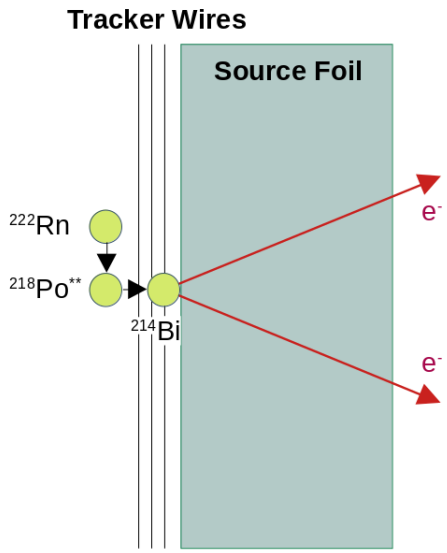

Figure 2.26 – Radon disintegration to ^{214}Bi, where it decays near the source foil mimics the $\beta\beta$ signal.

To achieve the desired sensitivity of SuperNEMO, Radon emanation inside the tracker chamber must not exceed 0.15 mBq/m^3. The latest measurement of the tracker parts, extrapolated to a gas flux of 2 m^3/h, gives an activity of 0.16 mBq/m^3.

2.5.4 . Background Reduction

The demonstrator is build under the Frejus mountain on a depth of 4800 meter water equivalent, reducing greatly the cosmic muons to $\sim$ 4 muons/m^2/day.

The passive shielding installed (mentioned in 2.2.5) offers a reduction to the external background.

To reduce the Radon background :

- The tracker chamber gas is intended to be recycled and re-injected to prevent Radon background.

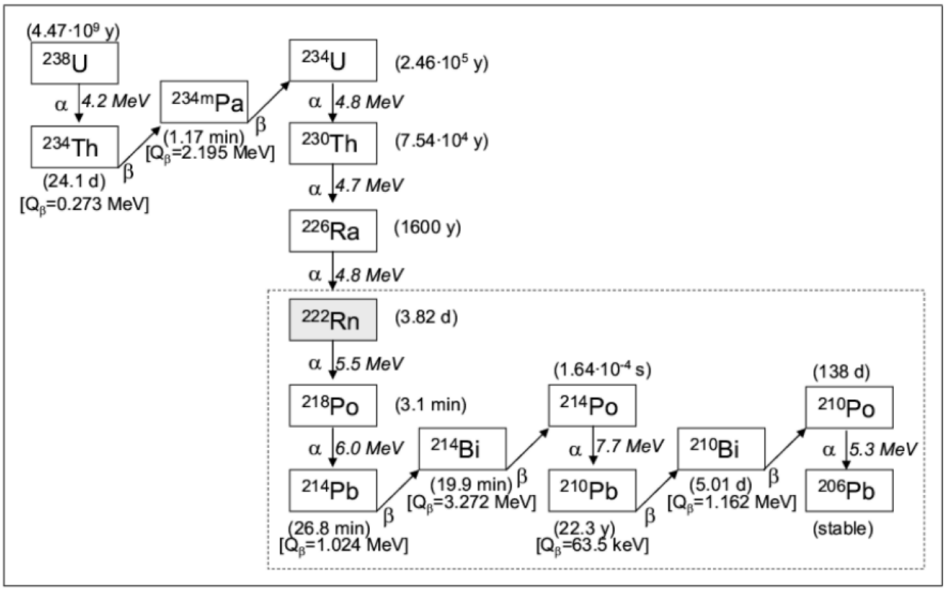

Figure 2.27 – ^{238}U natural radioactivity decay chain. This includes the Radon ^{222}Rn, which is relatively long-lived (3.8 days), emanates from or diffuses through materials. The disintegration of one daughter in the chain, ^{214}Bi, can mimic $0\nu\beta\beta$ decay, because of its high Q_β value (3.27 MeV).

- The emanation of the tracker materials was measured in emanation chambers developed at CENBG or UCL before installation.

- The purified gas flux can be increased to reach the specified emanation levels.

- The tracker is gas tight and leak proofed (protection against Radon diffusion : nylon films in front of the calorimeter walls, use of stycast for the seals which is tight to Radon).

2.6 . Falaise : SuperNEMO Simulation Software

The SuperNEMO collaboration has developed its own simulation software that simulates physics events inside the SuperNEMO environment. The simulation process is based on Decay0 [58] which simulates the radioactive decays and the corresponding emitted particles. The GEANT4 Monte-Carlo method takes into account the materials and the geometry of the demonstrator to simulate energy deposits by particles in different parts of the detector.

Then, the reconstruction software introduces the effect of the energy, time and spatial resolution of the detectors to simulate reconstructed signals. In details, the events then pass through reconstruction pipeline that accounts for particle energy loss and track tracing. It is formed of successive algorithms that reconstructs

particle tracks by grouping cell hits to form a continuous track to identify the passage of a particle. These hits are reconstructed either with a helix or a line, the former is best suited to identify electrons and positrons curved by the magnetic field, while the latter identifies muons and alpha particles. These tracks are then associated with a vertex and a hit in the calorimeter. As for gammas, they do not show any tracks inside the tracker, only a hit in the calorimeter wall, which could be followed by successive hits in the neighboring scintillators.

3 - Time Calibration and Time Resolution Calculations obtained for Gammas for the SuperNEMO Calorimeter

In this chapter, a time alignment and calibration of the calorimeter optical modules for SuperNEMO is performed and the time resolution is extracted for each module for γs.

This analysis was made using data runs performed with a ^{60}Co source which emits simultaneously two gammas. The source is placed behind the calorimeter walls (outside the detector). These gammas are then detected in coincidence at the calorimeter end, where time of flight analysis is performed.

The analysis is separated into two studies :
- Time calibration of the optical modules (OM) : time synchronization of all OMs with respect to a single arbitrary chosen OM, called later "reference OM". This allows a better rejection of background using time of flight calculations.
- Extraction of time resolution : time resolution per OM was determined using a dedicated method, which also depends on time coincidences between OMs.

3.1 . Presentation of Maps and Notations

A quick presentation of the calorimeter map, notations and general information is made.

The calorimeter data acquisition process, when these runs were taken, was only possible for each main wall separately, and for the X-Wall and G-Veto combined. The simultaneous data taking of all the walls was not possible.

The two maps shown in figures 3.1 and 3.2 are example of the maps used to introduce the design. Each square in the map is a PMT. The big rectangle in the middle is the main wall, the rectangles on the left and right sides are the X-Walls, and the rectangles on top and bottom are G-Veto walls. Each map has a label at the top indicating whether the map is for the French or Italian side of the detector, and which side of the map corresponds to the tunnel or mountain side.

Going up on the map you will start counting the rows of PMTs, and counting to the right of the map is the columns of PMTs.

The denomination of an OM will be in the form of : OM number [column number, row number], e.g : OM 40 [3,1].

Each **main wall** has 13 rows of PMTs and 20 columns. The first and last rows are made entirely of 5" PMTs, while the rest of rows are 8" PMTs.

For **X-Wall** there is one row per side (on a given side with respect to the source foil, and mountain or tunnel) and 20 columns. For **G-Veto**, there are two columns per side and 13 rows. These walls are made up entirely of 5" PMTs.

The colors in the maps start from blue to gradually reach red. Blue represents the lowest numbers in the map, and red the highest numbers, where numbers will present a certain quantity e.g : time shift, error, time resolution, number of hits, ...etc.

White boxes will represent dead optical modules (if the run should include them), or OMs that are not associated to the run. For example, main wall runs are taken separately from X-Wall and G-Veto, hence in the case of showing a main wall run, the OMs on the side are going to be white, but if an OM inside the main wall is white, this means that it's not functioning.

Extra details that are beneficent for those who will use this map in an analysis :

Each PMT has a designated number :

- For the main wall the PMTs are numbered as M :module :column :row. "M" for main, and module corresponds to whether it is French (1) or Italian (0) walls.

- For X-Walls the PMTs are numbered as X :module :side :column :row, where side corresponds to either tunnel(1) or mountain(0).

- For G-Vetos the PMTs are numbered as G :module :side :column, where side corresponds to either top (1) or bottom (0).

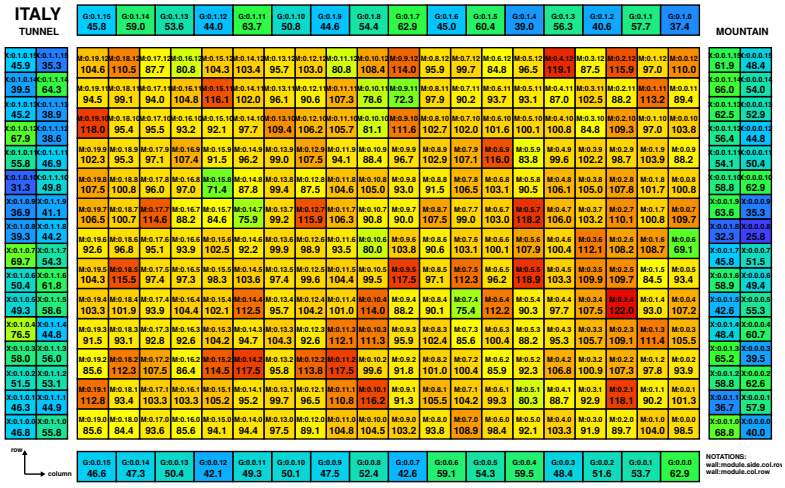

Figure 3.1 – Example map of the Italian calorimeter main wall. Filled with random numbers.

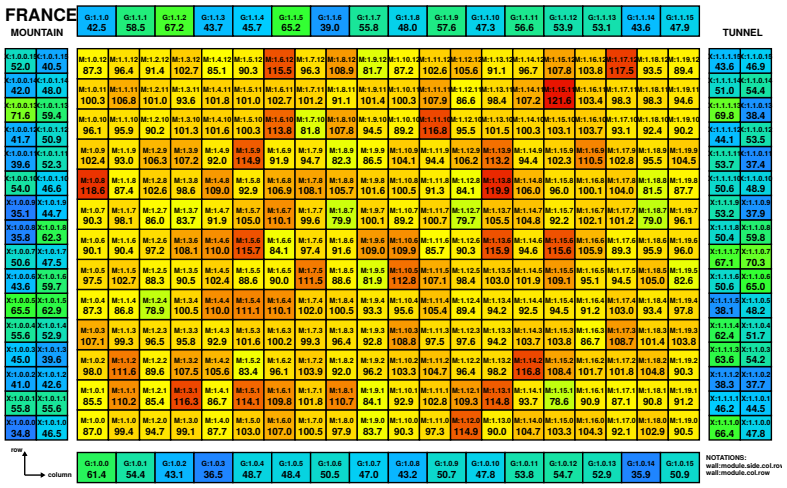

Figure 3.2 – Example map of the French calorimeter main wall. Filled with random numbers.

3.2 . The ^{60}Co Runs

At the time of performance of the analysis, the tracker was not yet commissioned, nor the light injection system (LIS) was fully studied, so the ^{207}Bi sources and LIS were not used for calibration. ^{60}Co runs are made using a cobalt source with an activity $\approx$ 184 kBq. At the moment of acquisition (October 2020). Also, It was not possible to take a global acquisition using the full detector, hence, acquisitions were performed separately for each main calorimeter wall (Italian and French sides, separately) and simultaneously for the X-Walls and G-veto (separated from the main walls).

The source was positioned in 9 different places behind each main wall and in 2 positions on each side of the X-Walls (Tunnel and Mountain) and G-Veto (Top and Bottom), totaling to 26 runs for the whole calorimeter. The runs were taken with a :

- Multiplicity = 2, meaning the electronics will take the first particle interaction, and wait in a time window of 62.5 ns, if another interaction happens in a different OM, then the time, energies and OM numbers of the event (2 particles) is registered.
- High threshold (HT) = low threshold (LT) = -100 mV, applied to the amplitude of the pulses, meaning a low energy threshold is set at 0.5 keV for the interacting particles.
- Acquisition time of each run is 30 minutes.

Background runs (i.e without the cobalt source) were also performed on each wall (one run per wall, taken between the cobalt runs). The runs are numbered from 421 to 463 on the SuperNEMO Wiki page.

Figure 3.3 shows the number of counts from several runs, it is shown to point

out the source positions, by looking at the OM with higher rate, in this case colored red. On the main walls to the left of the figure (Italian main wall is shown, the French wall is the same). To the right of the figure, is shown the count rate while the source is positioned on the X-Wall mountain side.

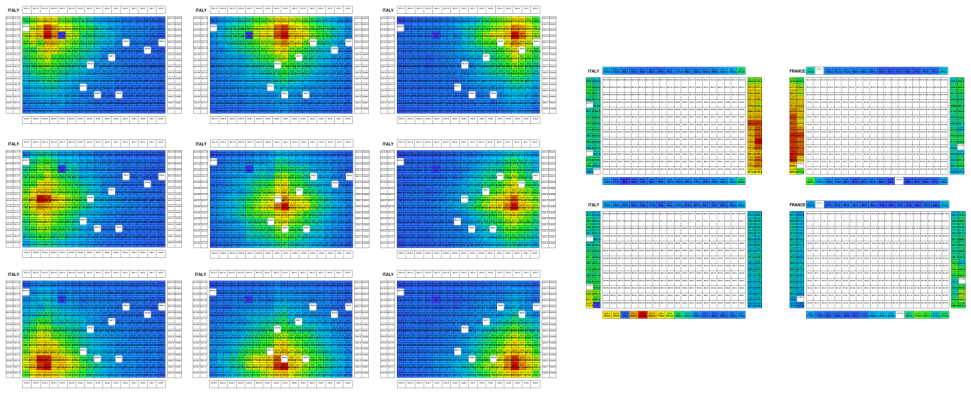

Figure 3.3 – Example of a hit map of the runs with the source located in different positions behind the Italian main wall. The images to the left represent a Main Wall, to the right the X-Wall and G-Veto.

3.2.1 . Method to Calibrate in Time and Extract the Time Resolution using the ^{60}Co Runs

^{60}Co is a source that emits two γs almost simultaneously with energies of 1.17 MeV and 1.33 MeV, the γs can interact with two different calorimeter OMs, a scheme is presented in figure 3.4. The time registered will be the "time to digital converter" (TDC) time.

Equation 3.1 is used to give the interaction time of the gamma with the optical module :

$$t = TDC \times 6.25 - 400 + t_{signal} \tag{3.1}$$

Where "t" is the time of the hit in [ns], "TDC" is the time to digital converter value registered by the electronics, "6.25" is used to convert "TDC" into [ns], "400" is the time window where the full pulse is integrated and t_{signal} is the constant fraction discriminator (CFD) time of the hit at 25% of the rising time of the pulse (in ns). The CFD is presented in figure 3.5.

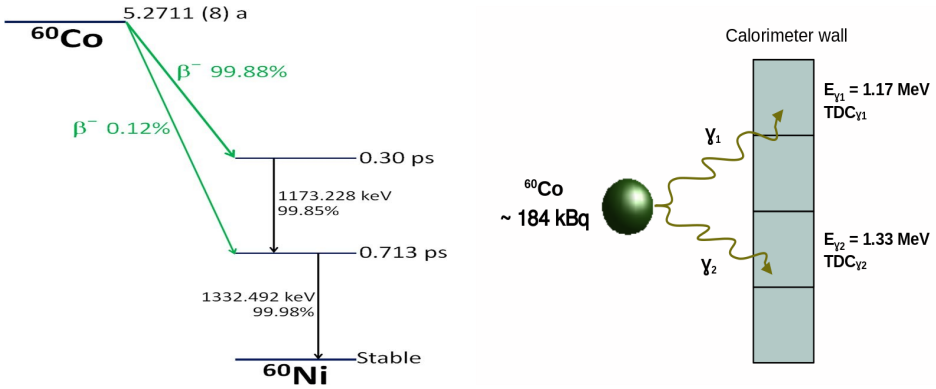

Figure 3.4 – To the left : The decay scheme of ^{60}Co through β^- process to the ground state of ^{60}Ni, emitting two γs with a time difference of the order of less than a picosecond. The γs are considered to be emitted simultaneously. To the right : A scheme showing the ^{60}Co source behind the calorimeter wall. The two arrows represent the two γs emitted from the source hitting the calorimeter blocks.

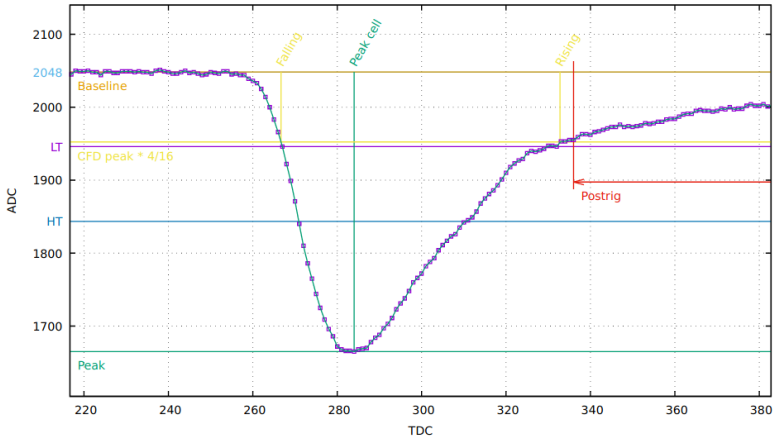

Figure 3.5 – The CFD calculation of a registered signal. The CFD time is taken at 25% of the falling time of the analog to digital converter (ADC) signal. It also shows the registration of the baseline of the signal, the peak cell, the rising and falling cells and the postrig where the signal falls below threshold.

After starting the acquisition, the registering of two hits in two different OMs each with time t_{γ_1} and t_{γ_2} in coincidence within a time window = 62.5 [ns], one can plot what will be called the Δ(t) distribution, where :

$$\Delta(t) = t_{\gamma_1} - t_{\gamma_2} \tag{3.2}$$

Δ(t) is the time difference between the two hits in the two OMs, in [ns]. One will

end up with the distribution in figure 3.6.

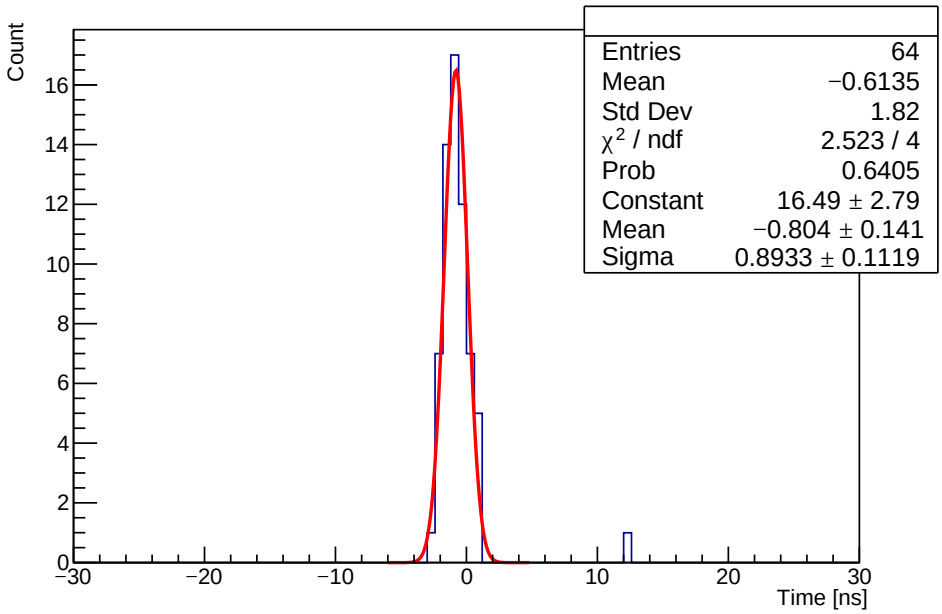

Figure 3.6 – Δ(t) distribution for the time coincidence between two OMs, in [ns]. The distribution is fitted with a Gaussian (shown in red).

After fitting this distribution with a Gaussian fit, the **mean** of this fit is used to determine the time offset per OM (calibrate in time). This time calibration takes into account all the possible offsets created by the time it takes for the signal to travel from the electronics board to the OMs and total offsets created by electronics, scintillation time, propagation of scintillation photons in the scintillators and the transit time in the PMT. The **sigma** given by the Gaussian fit is used to determine the time resolution per OM for γs @ 1MeV.

3.2.2 . Event Selection

Cuts are applied on the coincidence hits to reject effectively the random coincidences of background events :

The energy of each hit should be **larger than 0.7 MeV** and **less than 1.4 MeV**, this energy threshold ensures that we reject double Compton interactions from a single gamma emitted by a ^{60}Co disintegration, where in this case there is a time shift between the two registered hits. Figure 3.7 shows the change in the 2D energy distribution, after applying the low energy threshold at 0.7 [MeV] and upper threshold at 1.4 [MeV].

Another cut applied is on the number of coincidences between two OMs, which is set to be a **minimum of 50 coincidences**. This cut is to ensure that we have enough statistics to obtain a good Gaussian fit for the Δ(t) distribution.

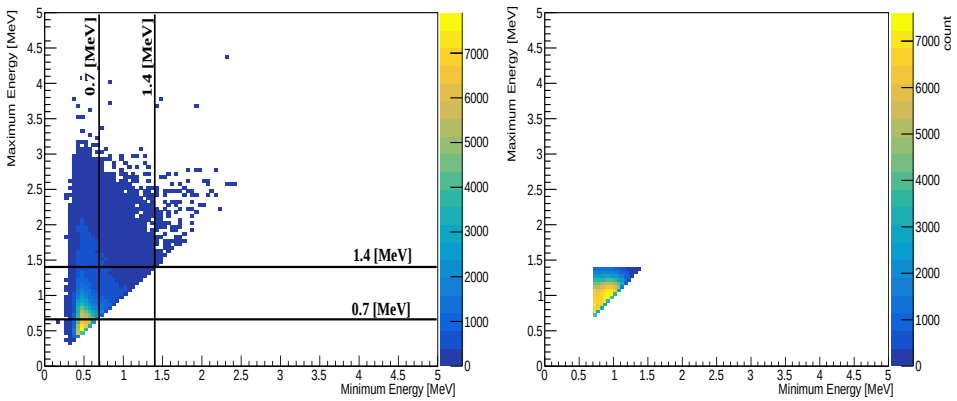

Figure 3.7 – 2D plots showing the maximum energy vs. the minimum energy for coincidences between two calorimeter hits, in [MeV]. On the left, no cuts applied : Most of the hits energies are concentrated on the low energy part due to the background from the lab, and the double Compton from the γs of the source. The bold black lines defines the energy at 0.7 [MeV] and 1.4 [MeV]. On the right, applying the cuts at 0.7 [MeV] and 1.4 [MeV] and having the number of coincidences between two OMs $>$ 50 coincidences, now the hits energies are concentrated around 1 [MeV].

The following analysis is going to have these cuts unless mentioned otherwise.

3.3 . Expected Background for ^{60}Co Events

Gammas emitted from the detector components, especially from the glass PMT can contribute as a background, and since the calorimeter is not shielded yet, particles coming from natural radioactivity of the laboratory walls and equipment can also mimic the ^{60}Co source events, as shown in figure 3.8.

3.4 . Signal Over Background

In this section, we will study the signal (S) over background (B), defined for a source at a given position, such that :

S = Coincidences between hits associated to the ^{60}Co source. But in principle, they could also be generated by a single gamma from ^{60}Co disintegration.

B = Coincidences between hits not associated to the ^{60}Co source. They are induced by gammas either from the detector components or from the laboratory.

In practice S cannot be determined directly, because runs with the source may also be affected by coincidences not generated by ^{60}Co source. Therefore I determined :

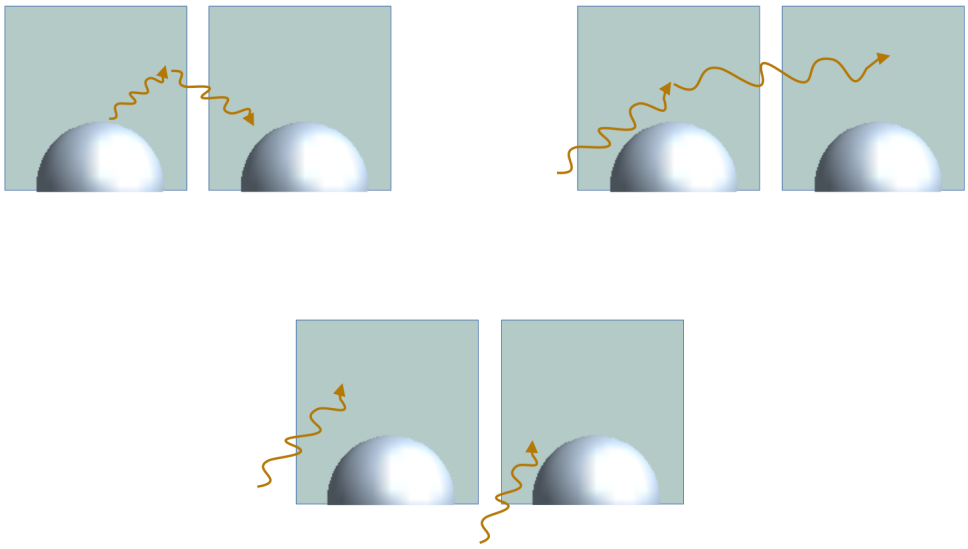

Figure 3.8 – The type of backgrounds expected for this analysis. Each box represents a scintillator block, the sphere a PMT glass and the orange arrows represent gammas. To the left : The case of the contamination of the photomultiplier glass, where a photon emitted undergoes a double Compton and is detected in two different scintillator blocks. To the right : The case of detection of a gamma from the source or laboratory which undergoes a double Compton to the neighboring OM. To the bottom : The case of detection of two uncorrelated γs from the laboratory in the trigger time window.

S+B : By counting the number of coincidences for a given OM, for the run with a ^{60}Co source at a given position.

B : By counting the number of coincidences for a given OM, for the run without the source.

Neighboring OMs will be concerned more with Double Compton of single gammas than random coincidences between two independent gammas. So, this study is going to give the lead to whether we should reject neighboring OMs, or not. In case of rejecting neighboring OMs, there exists a decreased chance of selecting random coincidences of events that are background.

3.4.1 . Main Walls

For this section we use two runs, run 421 and run 424. Run 421 is a background run (without the introduction of the ^{60}Co source) with multiplicity 2, and the same trigger options mentioned previously. Run 424 is a run with the source positioned in the middle of the main wall. For both runs the acquisition is performed for the optical modules of the Italian wall.

Figure 3.9 shows the rate per OM for the background run. Figure 3.10 shows

the rate per OM for the source run, where the ^{60}Co source is located behind the Italian calorimeter wall, in the middle position. Both maps have no cuts applied on them. Clearly, the rate is higher for the run source close to the source position. Far from the source, the rate decreases to become similar to that of the background run.

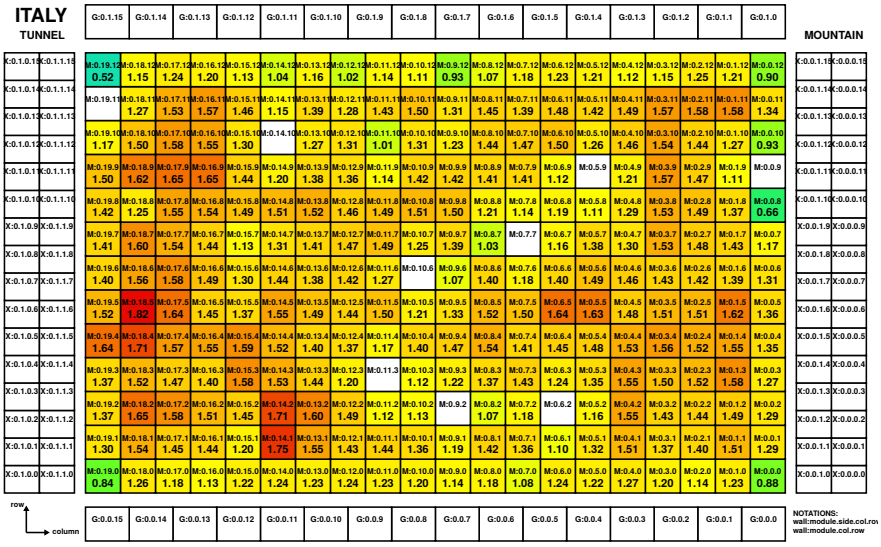

Figure 3.9 – The hit rate per OM [s^{-1}] from the background run, the color scale represents the rate per OM. No cuts applied. The multiplicity was set to 2 and LT = HT = -100 mV.

Shown in figures 3.11 and 3.12 are plots of the rate per OM maps but with energy threshold cut at 0.7 MeV and 13 MeV and taking more than 50 coincidences between two OMs. The rate per OM strongly decreases for the background run to less than 0.22 hits per second per OM compared to a typical value of 1.5 hits per second. For the source run, the hits in the source position are still elevated while far from the source the rate decreases to less than one.

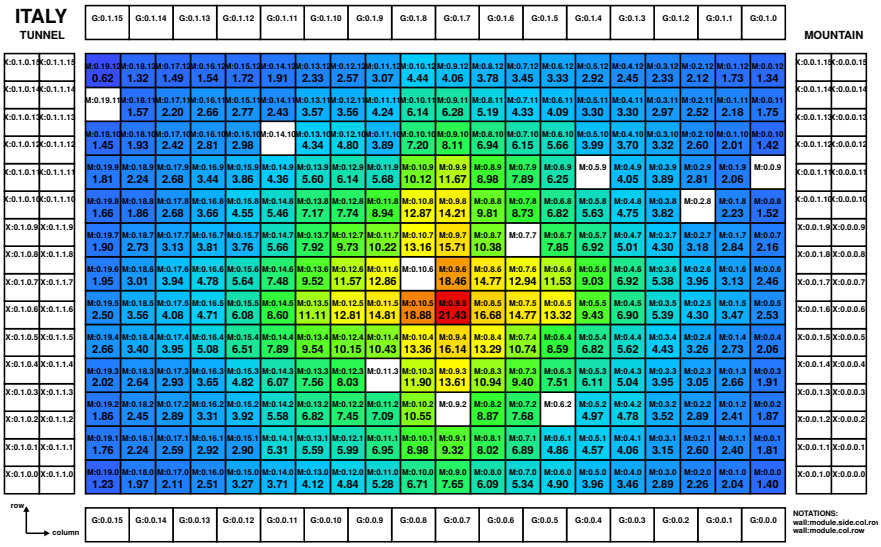

Figure 3.10 – The hit rate per OM [s^{-1}] from a run with the source in the center of the Italian wall, the color scale represents the rate of hits per OM. No cuts applied. The multiplicity was set to 2 and LT = HT = -100 mV.

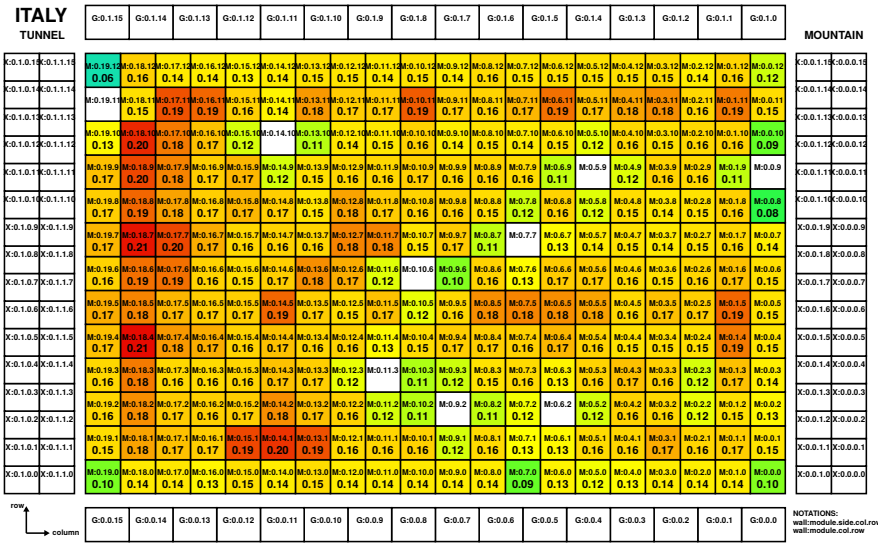

Figure 3.11 – The hit rate per OM [s^{-1}] from the background run, the color scale represents the rate. Cuts applied : energy greater than 0.7 MeV and less than 1.4 MeV and the number of coincidence $>$ 50 per OM. The multiplicity was set to 2 and LT = HT = -100 mV.

Figure 3.13 shows the (S+B)/B for the two runs, with an energy threshold

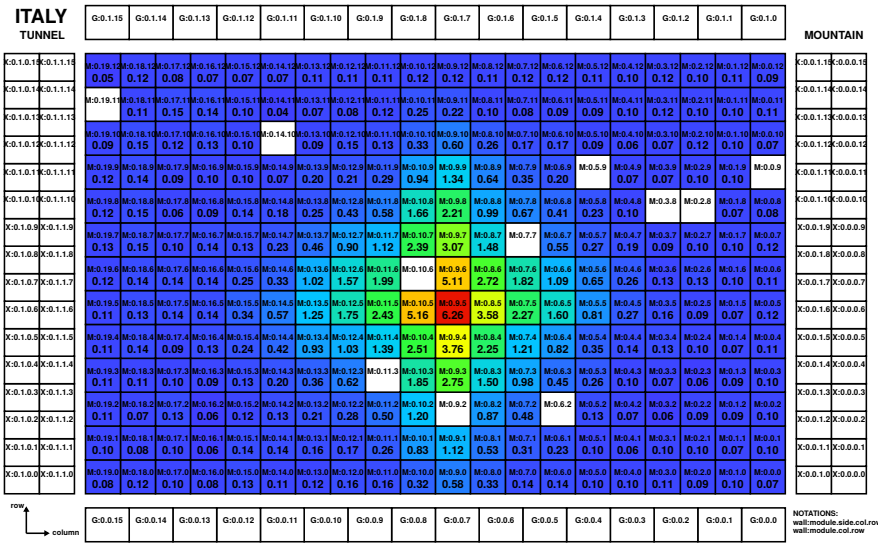

Figure 3.12 – The hit rate per OM [s^{-1}] from a run with the source in the center of the wall, the color scale represents the rate of hits per OM. Cuts applied : E $>$ 0.7 MeV and E $<$ 1.4 MeV and the number of coincidence larger than 50 coincidences.

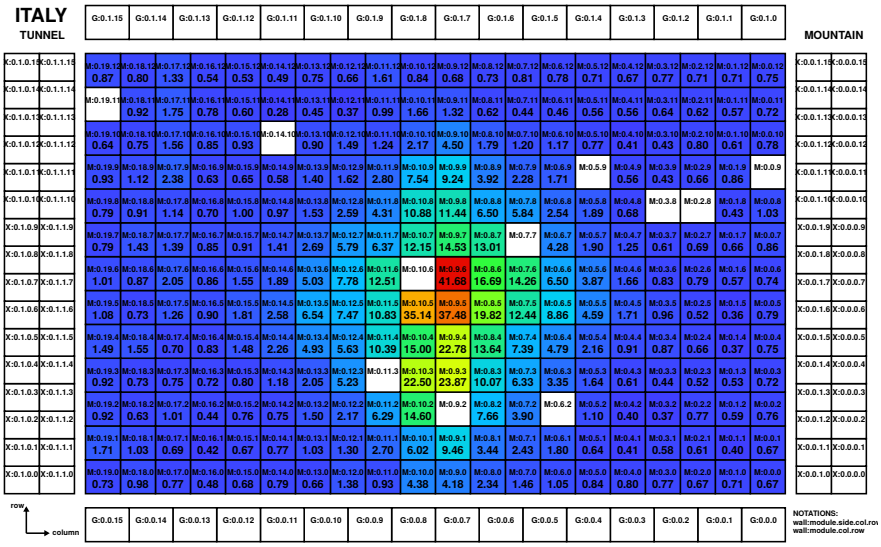

Figure 3.13 – (S+B)/B for a run with the source in the center of the wall, the color scale represents the (S+B)/B per OM. Cuts applied : energy larger than 0.7 MeV and less than 1.4 MeV and the number of coincidence greater than 50 coincidences. The neighboring OMs are kept.

cut at E $>$ 0.7 MeV and E $<$ 1.4 MeV and number of coincidence $>$ 50 between

two OMs. The source hits strongly dominate around the source position where (S+B)/B = 41 and this decreases gradually as you get far from the source until the background starts dominating.

Study of Neighboring OMs

I select events that have only two calorimeter hits, in both the background and source runs. I then study the number of coincidences between two arbitrary OMs. To check the effect of neighboring OMs on the selection of background events, we study the coincidences in the background run.

In figure 3.14, the maps to the left are the background run, while on the right the source run, with cuts applied at E $>$ 0.7 MeV, E $<$ 1.4 MeV and the number of coincidence $>$ 50.

Each red box represents a unique reference OM, which is the same in the maps facing each other. We can see, in some cases of the source run, the neighboring OMs have almost the same number of events as in the background run, while in others the source run events slightly dominates. These events are dominantly created by Double Compton induced by a single gamma in two neighboring OMS, other causes are mentioned in 3.3 page 83. Because of this, it was decided to remove the directly neighboring OMs, that have their sides fully in contact with another OM (diagonal OMs are not removed) for the main wall runs.

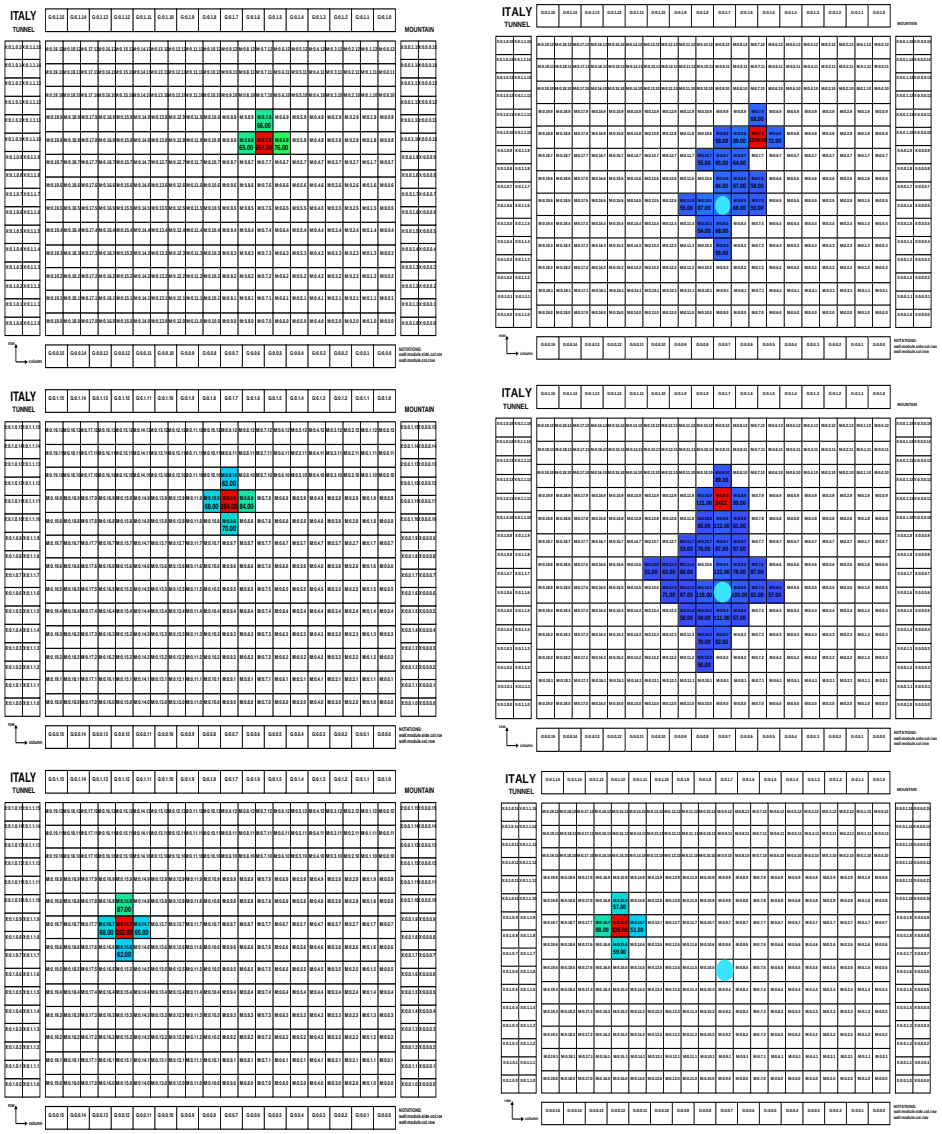

Figure 3.14 – Figures comparing between the coincidences of a given OM in both the background run (figures to the left) and the source run (figures to the right). For the considered source run, the source was place in front of OM [9,5] (highlighted with a light blue circle), i.e approximately in the middle of the wall. First, second and third row of figures represent the reference OM [7,8], OM [9,9] and OM [15,7], presented as red squares. Cuts applied : E $>$ 0.7 MeV, E $<$ 1.4 MeV and number of coincidences between two OMs $>$ 50

Figure 3.15 shows the map of the (S+B)/B after removing directly neighboring OMs (shown in figure 3.14), doing so will lead to no events in the background run, all background events are rejected. In order to calculate (S+B)/B we take, as a

limit, the number of background events per OM to be 2.3 events. Comparing with the previous map 3.13, the OMs where the background previously dominated (far from the source position) are now rejected in the analysis.

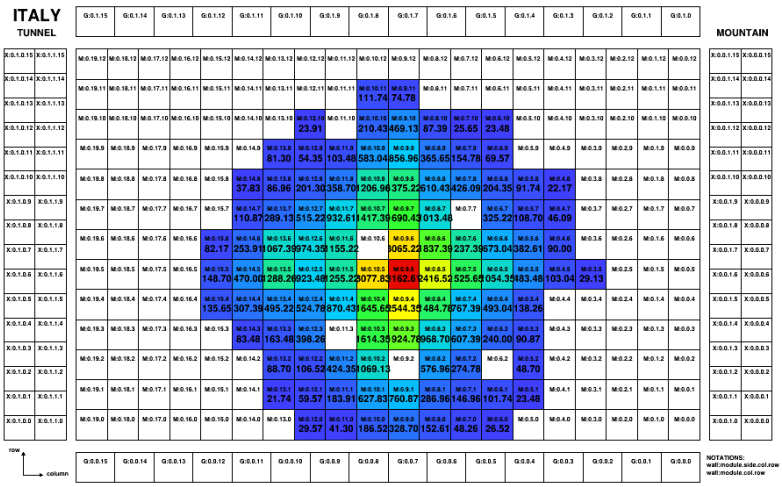

Figure 3.15 – Map showing the (S+B)/B from a run with the source in the center of the wall after removing directly neighboring OMs, also, E $>$ 0.7 MeV, E $<$ 1.4 MeV and the number of coincidence $>$ 50. The color scale represents the (S+B)/B per OM.

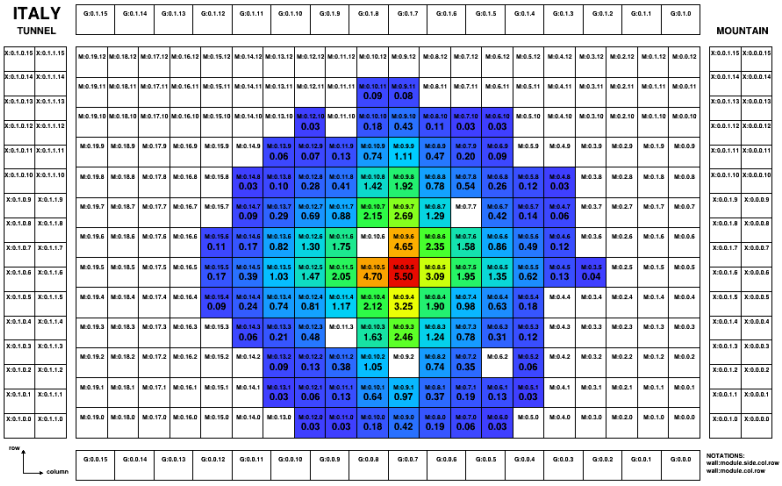

Figure 3.16 – Map showing the hit rate (or coincidence rate) per OM [s^{-1}] from a run with the source in the center of the wall, the color scale represents the rate of hits per OM. Cuts applied : Removing directly neighboring OMs, also,E $>$ 0.7 MeV, E $<$ 1.4 MeV and the number of coincidence $>$ 50.

So to finalize, the final cuts applied are : E $>$ 0.7 MeV, , E $<$ 1.4 MeV, number of coincidences between 2 OMs $>$ 50 and removing directly neighboring OMs.

3.4.2 . X-Walls and G-Veto

The X-Walls energy calibration was used but it was not available for the G-Veto walls. Hence no energy cuts were applied on the G-Veto walls . Initial cuts were made identical to the ones mentioned above, but without removing neighboring OMs. The hit map after time selection (finding time coincidences) is shown in figure 3.17, it shows a uniform number of hits for the X-Wall Mountain side which is not what is expected. In the run shown (run 452) the source is on the bottom mountain side of the X-Wall(the left and right sides of the main wall). The larger number of events for the G-Veto (top and bottom of the main wall) is due to the fact that no energy cuts were applied there.

The fact that we dont see the source on the X-Wall can be associated to the fact that the high voltage map was still not well equalized for this wall, which affects the energy calibration of the OMs. Also, not to forget that the OMs on the X-Walls and G-Vetos are 5" OMs and have decreased energy resolution compared to the 8" OMs on the main walls.

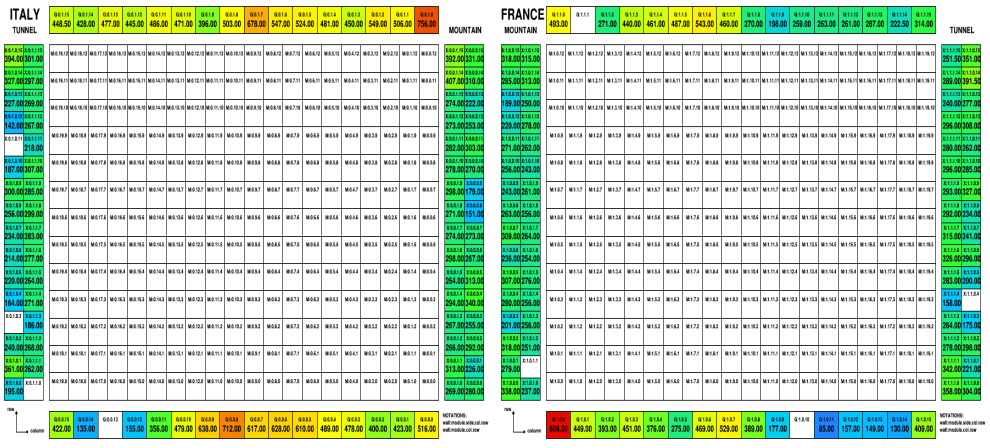

Figure 3.17 – Number of coincidences per OM for run 452 (source on the Bottom Mountain side of the X-Wall). The applied cuts were : energy larger than 0.7 MeV and less than 1.4 MeV (only for X-Wall) and number of coincidences between two OMs is larger than 50 coincidences. It is clear that the shown map is uniform and shows no existence of a source (which exists). The non uniformity of the G-Veto is due to the fact that there is no energy calibration and hence no energy cut applied.

From here on, no energy cuts are applied on the X-Walls and G-Veto unless mentioned otherwise. The cut on the minimal number of coincidences is still applied ($>$ 50).

We investigated the background run for these two walls. Run 448 was used as the background run with multiplicity 2 and the same trigger options mentioned above. The source run 452 is used with the source positioned on the bottom mountain side.

Figure 3.18 shows the (S+B)/B of the background run 448 and the source run 452 with the source being on the bottom mountain side. No strong dominance of the source events in the source position is observed.

We check the number of neighboring OMs in the background run to see how much we should cut to reject the background. Figure 3.19 shows a chosen OM from the X-Wall from the background run, we conclude that all the neighboring OMs (not just directly neighboring OMs with sides in full contact as in the Main Walls) should be removed to avoid adding background in the analysis.

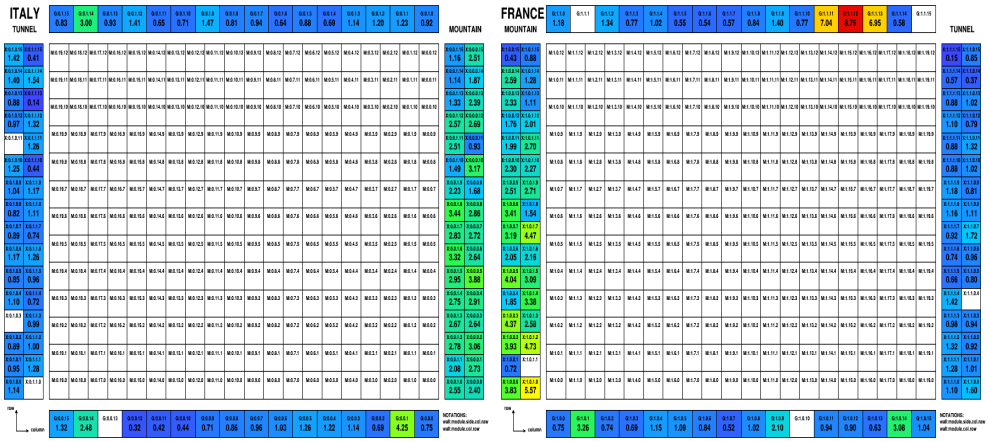

Figure 3.18 – (S+B)/B using the background run 448 and the source run 452 with the source being on the bottom mountain side. The color and text represent the (S+B)/B values. Cuts applied : Coincidences between OMs > 50

We remove the neighboring OMs from the source run, figure 3.20 show the maps before and after the cut on the neighboring OMs.

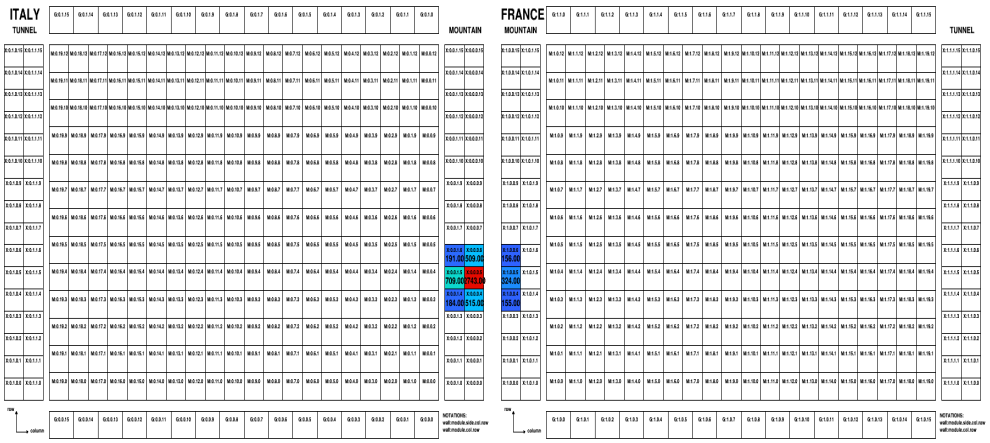

Figure 3.19 – The coincidence OMs with OM 525 using the background run.

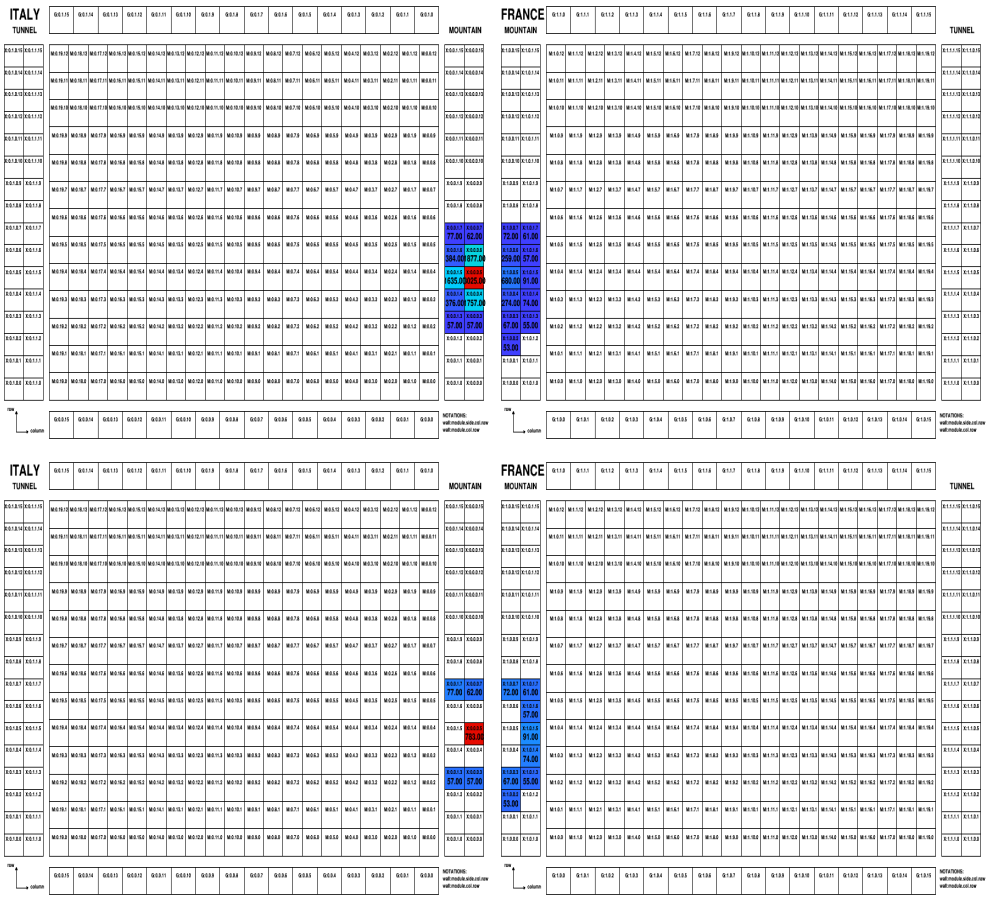

Figure 3.20 – The coincidence OMs with OM 525 using the source run. Top : Before removing neighboring OMs. Bottom : After removing neighboring OMs.

The (S+B)/B after removing the neighboring OMs is presented in figure 3.21. Now a visible dominance of the events at the source position is achieved.

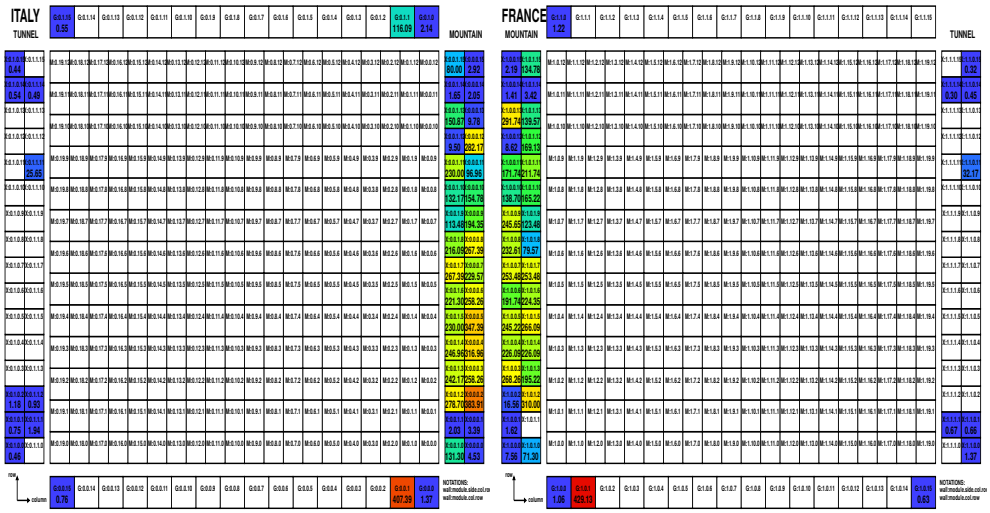

Figure 3.21 – (S+B)/B using the background run 448 and the source run 452 with the source being on the bottom mountain side, after removing neighboring OMs and setting the coincidences between OMs > 50. The color and text represent the (S+B)/B values.

So to finalize, the final cuts applied for X-Walls and G-Veto are number of coincidences between 2 OMs larger than 50 coincidences and removing all neighboring OMs.

3.5 . Interaction Point of Particles Inside the Scintillation Block

SuperNEMO calorimeter is made of plastic scintillators composed dominantly from polystyrene. Inside, the interaction point of gammas differs from the ones of the electrons. Presented previously in 2.2.3 (page 61), and inferring from the graphs, the 1 MeV electrons stop at the surface of the scintillation block (few mm inside), while 1 MeV gammas can travel up to 10 cm inside the block.

Since our study is performed with gammas, this kind of uncertainty on the time of flight of the γ will lead to a broadening of the Δ(t) distribution (presented in 3.2.1), hence, increasing the value of the sigma, which will decrease our calculated time resolution (see figure 2.16, page 62).

To be conservative about the interaction point of the γs, we will schematically assume that they will stop at exactly the center of the scintillation block. This will create a time delay of 1.25 ns for a scintillation gamma that traveled from the interaction point to the front surface of the block and then reflected back

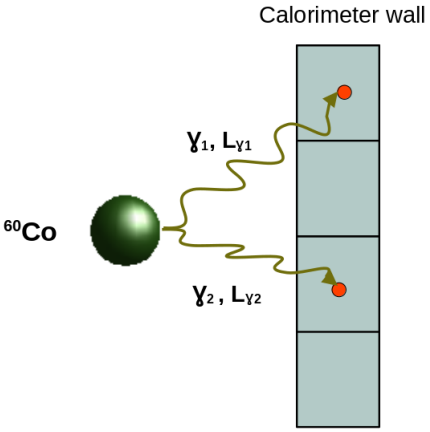

Figure 3.22 – Schematic representation of the source positioned behind the calorimeter wall. the source emits two gamma simultaneously, where they travel to the middle of the calorimeter block. The distance between the source position and each calorimeter is denoted by "L".

to the PMT. For electrons, this delay is negligible compared to the scintillator de-excitation time and the transit time spread in the PMT.

The integration of time of flight was taken into account in the time offsets calculation (time calibration) to take into account the different gamma flight time from the source to the OMs. But, it was not taken into account while calculating the time resolution to avoid unnecessary uncertainties on time (since there are several source positions included in the analysis).

3.6 . Calculation of Time of Flight

By default, we suppose that the interaction point of a gamma in an OM is in the middle of the scintillation block.

The $\Delta(t)$ equation is expressed as :

$$\Delta(t) = (t_{\gamma_1} - \frac{L_{\gamma_1}}{c}) - (t_{\gamma_2} - \frac{L_{\gamma_2}}{c}) \tag{3.3}$$

where L is the distance from the source position to the calorimeter hit position, and c is the speed of light. In figure 3.22 is a schematic representation of this distance.

The reason for the difference in time resolution between 8" and 5" OMs is presented in 2.2.3, page 63.

3.7 . Time Calibration of Optical Modules

If a source emits two particles simultaneously, it means for a perfect detector, the difference of their time of flight should be zero.

To calibrate in time means to synchronize all optical modules, such that the time delay created by the signal propagation through the cables, or the delay created by signal processing, is taken into account.

Once performed, this synchronization will optimize the rejection of background using time of flight criteria.

Reflectometry Tests : A step towards time calibration of the optical modules (OMs) was already taken before by performing reflectometry tests on the Main walls. These tests were as follows : a primary signal is sent from the electronics boards to the OMs, where it is reflected back, and the time offset between the initial and reflected pulses, which is proportional to the cable length between each OM and the electronics boards, was used for timing calibration. These tests only took into account the time offsets created by the cable length, but they were not 100% accurate. The signal is attenuated inside the cable and there is a signal shape difference between the sent and the reflected pulses, which was not taken into account during the analysis (see figure 3.23). The latter is also true for 5" and 8" OMs for which the signal shapes are different and should be treated differently. Further details about this test can be found in Cloé Girard-Carillo's PhD [46].

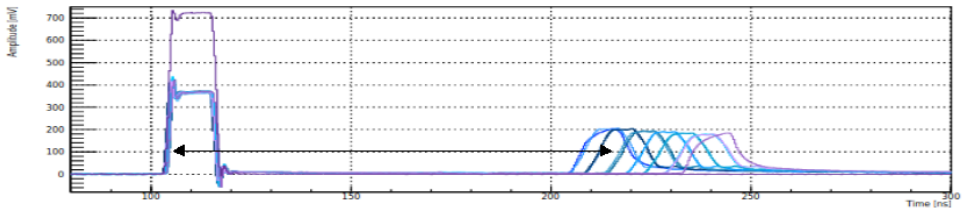

Figure 3.23 – The sent pulse from the electronics (left) and the reflected pulse at the OMs side (right), one can see the attenuation and the change of the shape. The black arrow shows that the time difference was taken between the signal rise of the sent signal and the signal fall of the reflected signal.

3.7.1 . Method to Determine the Time Offset Per OM

We will define what will be called the "absolute time of detection" as follows :

$$t_{absolute} = t_{[ns]} - ToF - \varepsilon \tag{3.4}$$

Where "$t_{[ns]}$" is the value obtained from equation 3.1, "ToF" is the time of flight of the particle from the known source position to the center of the calorimeter block, which is also known. "ε" is the time offset (shift) of the OM, it is unique per OM, fixed and unknown.

As the two γs are emitted simultaneously from the ^{60}Co source, the time difference between the two registered hits (i and j) should be equal to "0", if there are no errors on these measurements, such that :

$$t_{absolute_i} - t_{absolute_j} = 0 \tag{3.5}$$

Meaning

$$t_{[ns]_i} - ToF_i - \varepsilon_i = t_{[ns]_j} - ToF_j - \varepsilon_j \tag{3.6}$$

And eventually

$$\varepsilon_i - \varepsilon_j = \delta_{ij} \tag{3.7}$$

where $\delta_{ij} = t_{[ns]_i} - ToF_i - t_{[ns]_j} + ToF_j$ which all have known values.

Now, one can calibrate the offset of one OM with respect to (w.r.t) a single OM, called the "reference OM" or "OM$_{ref}$". To be noted again that the ε_{ref} is also unknown.

The method used to determine the offset values is as follows :

Step 1 : Get the OMs in coincidence with the OM$_{ref}$, called OM$_j$, and find their offsets, which are going to be the mean value of the Δ(t) distribution of the coincidences between OM$_{ref}$ and OMj :

$$\varepsilon_j = \varepsilon_{ref} - \delta_{ref,j} = \varepsilon_{ref} - mean(\Delta(t)_{ref,j}) \tag{3.8}$$

such that ε_{ref} = 0, as the offset values are going to be determined w.r.t this reference OM.

Step 2 : For OMs (OM$_k$) not characterized in Step 1 either because there are no coincidences between OM$_{ref}$ and OM$_k$ or the error of the offset obtained is larger than a certain value, we consider the coincidences between OM$_k$ and OMs already characterized in Step 1, OM$_j$:

$$\varepsilon_k = \varepsilon_j + \delta_{k,j} = \varepsilon_j + mean(\Delta(t)_{k,j}) \tag{3.9}$$

Using equations 3.8 & 3.9 we can obtain the offset of OM$_k$ w.r.t OM$_{ref}$

$$\varepsilon_k = \varepsilon_{ref} - \delta_{ref,j} - \delta_{k,j} \tag{3.10}$$

Since OM$_k$ is going to have several coincidences with the different optical modules OM$_j$, one will end up with several mean offset values per OM$_k$ (from equation 3.10), to obtain a single value, a weighted average is going to be applied, taking into account the uncorrelated coincidences :

$$\varepsilon^{final}_{ref,k} = \frac{\frac{\varepsilon_{k(1)}}{\sigma^2_{\varepsilon_{k(1)}}} + \frac{\varepsilon_{k(2)}}{\sigma^2_{\varepsilon_{k(2)}}} + \frac{\varepsilon_{k(3)}}{\sigma^2_{\varepsilon_{k(3)}}} + ...}{\frac{1}{\sigma^2_{\varepsilon_{k(1)}}} + \frac{1}{\sigma^2_{\varepsilon_{k(2)}}} + \frac{1}{\sigma^2_{\varepsilon_{k(3)}}} + ...} \tag{3.11}$$

And the error is calculated using propagation of errors :

$$\sigma(\varepsilon_{ref,k}^{final}) = \sqrt{\sigma(\delta_{ref,j})^2 + \sigma(\delta_{k,j})^2} \tag{3.12}$$

Steps 3, 4 : If OMs were not characterized in the previous steps, additional extrapolations are performed using the same method in Step 2 but w.r.t OM_k instead of OM_j.

Since several runs were taken, each with a different source position, we have to analyze each run on its own for accurate ToF calculations. So, eventually, we perform, again, a weighted average on the several obtained offset values for the same OM, from the different runs, to obtain the final offset value per OM w.r.t a reference OM.

3.7.2 . Calibrating the Full Calorimeter Wall w.r.t One OM

Since there are still no ^{60}Co runs that include both the main walls at the same time (Italian and French), a calibration of the calorimeter w.r.t one OM is not possible. So, a choice for a reference OM for each wall is made as follows : The middle of the two Main Walls, OM 122 for the main Italian wall and OM 396 for the main French wall (check figure 3.24). As for the X-Walls and G-Veto, the nature of data taking includes these walls at the same time and both are calibrated w.r.t OM 709. The choice of these OMs in particular is due to the minimization of extrapolations, errors and to the simplicity of coding.

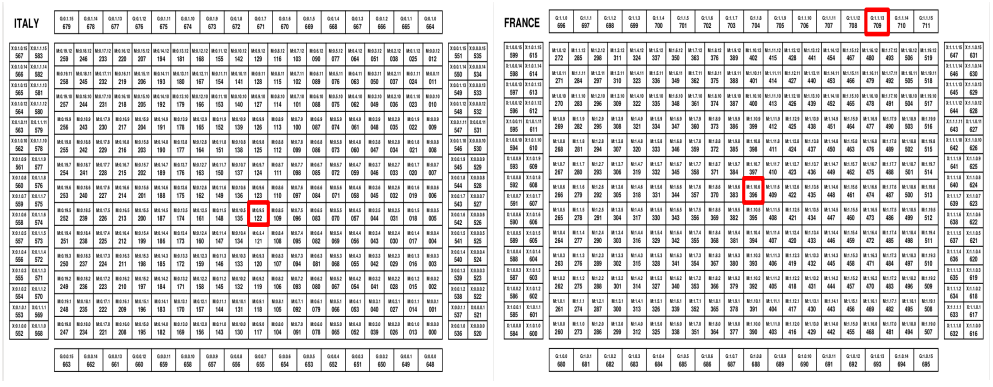

Figure 3.24 – Reference OM positions for each wall (red box). Middle of the Wall for Main Walls and on the top French side of the G-Veto for the X-Walls and G-Veto

3.7.3 . Illustration of the Calibration Method for the Italian Main Wall

For the sake of visualizing, the Italian main wall will be taken to explain the method.

Step 1 : Determine the offset of OMs in coincidence with OM 122 : Italian Main Wall

The offset values in the first plot (top left) in figure 3.25 are calculated using equation 3.8 and their errors are taken from the Gaussian fit. The reference OM is 122 and the colored squares are OMs "j".

Step 2 : Determine the Offset of OMs not Calibrated in Step 1

The offset values in the top right plot in figure 3.25 are calculated using equation 3.10 and their errors are calculated using equation 3.12. We illustrate the step by choosing the OMs "j" (colored squares) in coincidence with OM 40 ([3,1]) OMs, characterized in step 1, and find their offset.

Now, the bottom plots in figures 3.25 give a look on how the extrapolation steps work on a one run scale, where the source was placed at the bottom right of the plot (OM 40, [3,1]). Here, all the values for the intermediate OMs are calculated.

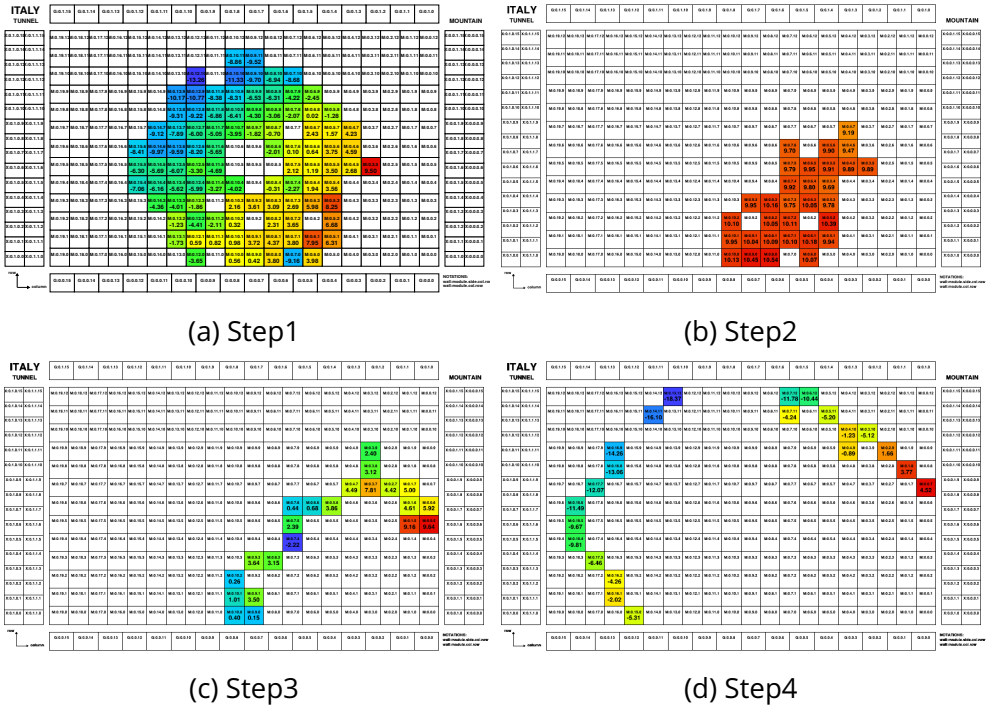

(a) Step1 (b) Step2

(c) Step3 (d) Step4

Figure 3.25 – Offset values [ns] calculated using : Top left : Step 1 w.r.t reference OM 122 ([9,5]). Top right : Step 2 using OM 40 ([3,1]). Bottom maps represent the extra extrapolation steps to retrieve the values for the full map. The run used is for the Italian main wall with the source being on the bottom right.

In order to get a calibration of all OMs of the calorimeter, a combination of all the runs per wall should be done, a weighted average is performed on the common OMs between runs to obtain a final map w.r.t the reference OM.

3.7.4 . Final Offset Values Per OM for the Main Walls

The maps in figures 3.26 and 3.27 show the offset values and their errors per OM for the Italian and French walls, respectively, w.r.t OM 122 and OM 396, respectively, after combining the runs (each wall separately). The white OMs shown on the Main Wall are dead OMs, i.e it ws not possible to take data through them.

One can clearly observe from the color gradient, which corresponds to the offset values, this effect is created by the cable length, the closer you are to the electronics board, the smaller this offset will be (bottom right for Italian wall, bottom left for French wall).

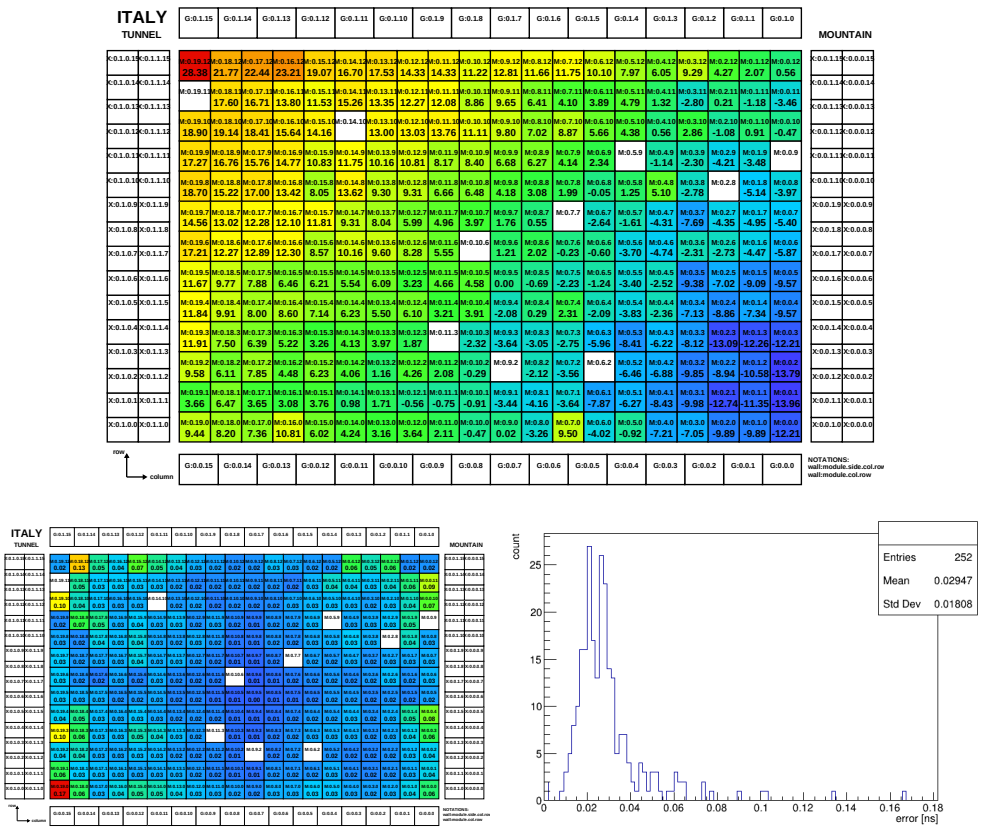

Figure 3.26 – Top : Time offset values per OM of the Italian Main Wall w.r.t OM 122. Bottom : To the left the final offset error values per OM of the Italian Main Wall w.r.t OM 122, on the right a 1 dimensional distribution of the error on time offset values. All in [ns].

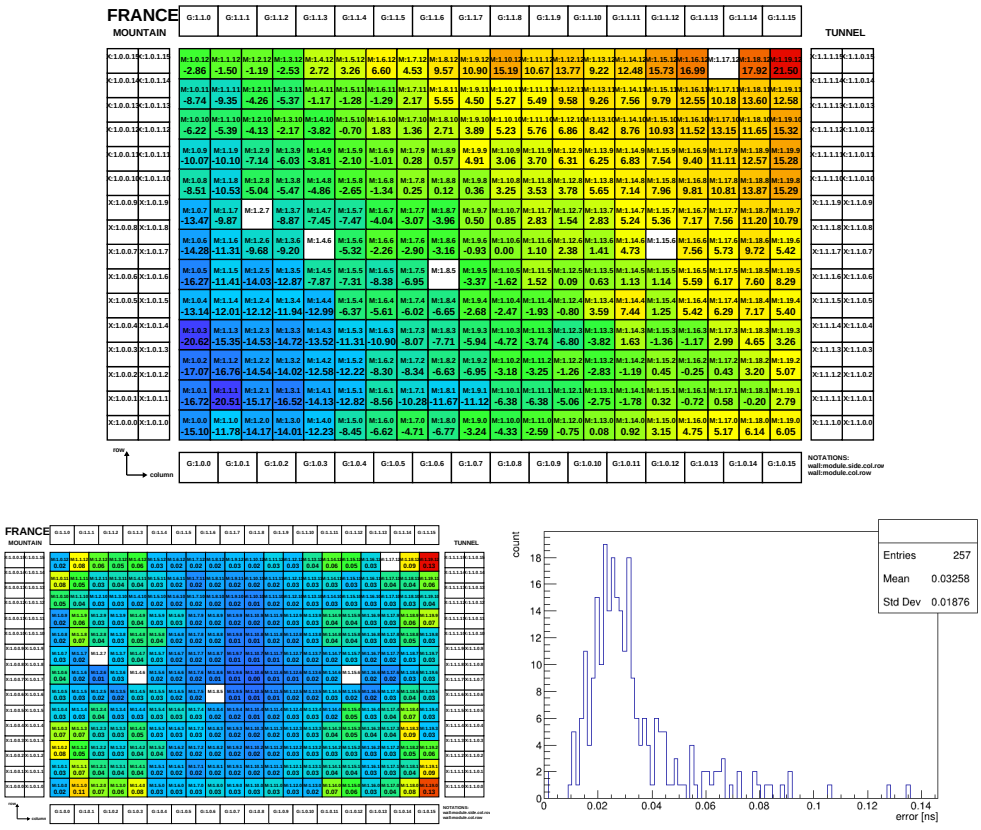

Figure 3.27 – Top : Time offset values per OM of the French Main Wall w.r.t OM 396. Bottom : to the left the final offset error values per OM of the French Main Wall w.r.t OM 396, on the right a 1 dimensional distribution of the error on time offset values. All in [ns].

Cross-Check of the Time Offsets Obtained with the Reflectometry Measurements

As mentioned before, reflectometry tests were made to check the time offset of OMs created by their cable length. The results of the comparison of the time offsets measured using either ^{60}Co runs or by reflectometry are shown in figures 3.28 and 3.29.

In the ^{60}Co runs results, you can clearly see the effect of time offset created by the cable length by just checking the color gradient. By looking at the plots on the bottom of the same figures, you can see the difference between the reflectometry results and the ^{60}Co run results, and this can be attributed to the fact the reflectometry have a different signal shape between reflected and sent that was not taken into account during the analysis. Moreover, the ^{60}Co runs includes also the delays created by the electronics. Even though 8" OMs show a peak at 0 of difference for the Italian wall, one can see that there is a large error on this value.

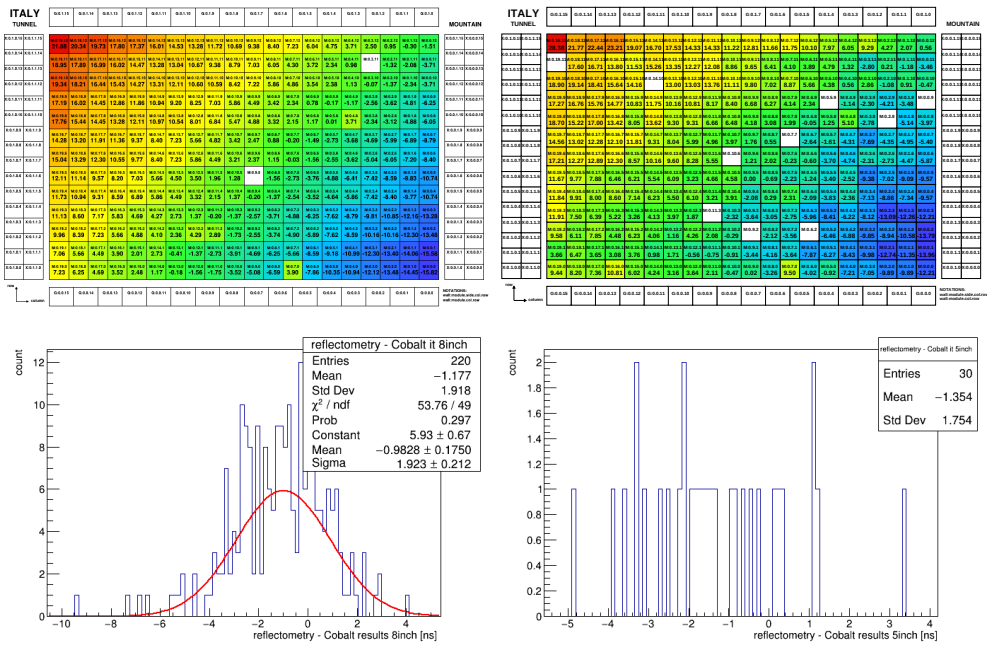

Figure 3.28 – Top left : Time offsets obtained from Reflectometry runs using cable length. Top right : Time offset using ^{60}Co runs. Bottom left : Difference between reflectometry results and ^{60}Co runs results for 8” OMs, bottom right : For 5” OMs. All in [ns]. All for the Italian main wall.

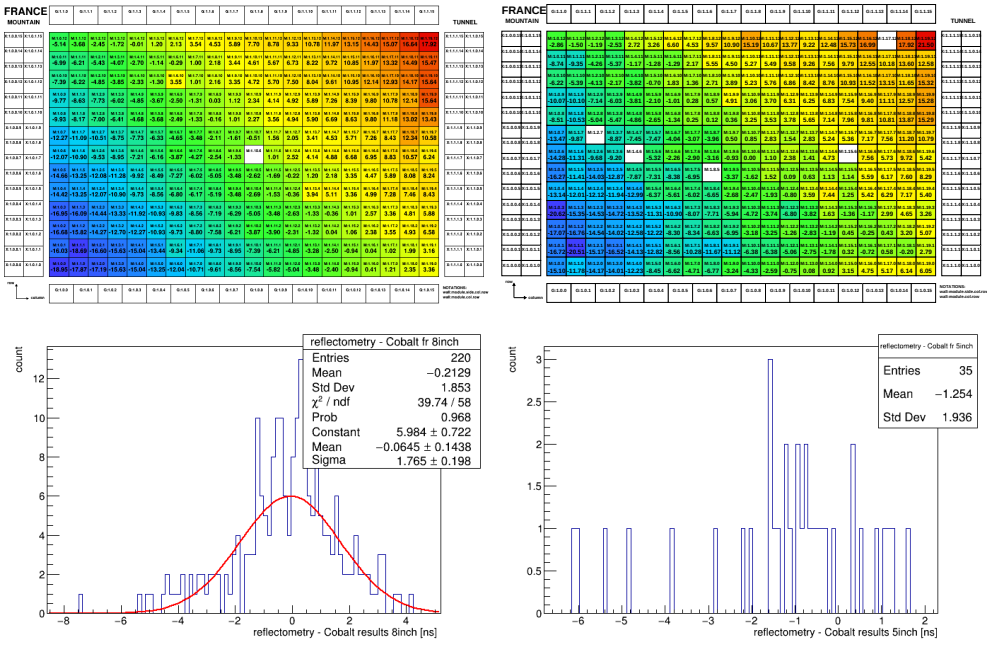

Figure 3.29 – Top left : Time offsets obtained from Reflectometry runs using cable length. Top right : Time offset using ^{60}Co runs. Bottom left : Difference between reflectometry results and ^{60}Co runs results for 8” OMs, bottom right : For 5” OMs. All in [ns]. All for the French Main Wall.

3.7.5 . Time Offset Values Per OM for the X-Walls and G-Veto

The creation of the final offset map of the X-Walls and G-Veto went through a process identical to that of the main walls except that these walls are separated into two different sides, "Top" and "Bottom" sides for the G-Veto and "Mountain" and "Tunnel" sides for the X-Walls. The calibration of each side was performed with respect to a reference OM that is different for each side of the walls, figures 3.30 and 3.31 offer a visual explanation. As a reminder, the cuts applied are : number of coincidences between two OMs > 50 and removing neighboring OMs.

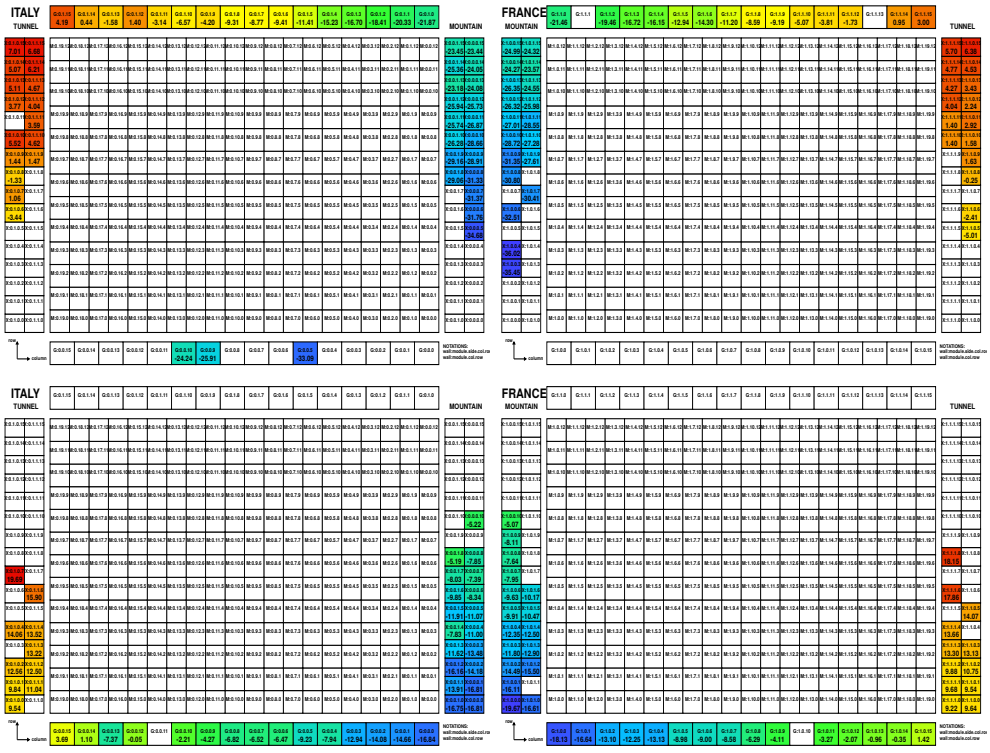

Figure 3.30 – Final offset values [ns] for the G-Veto sides. The Top side is calibrated w.r.t OM 709 (First row figures), the Bottom side w.r.t OM 659 (Second row figures).

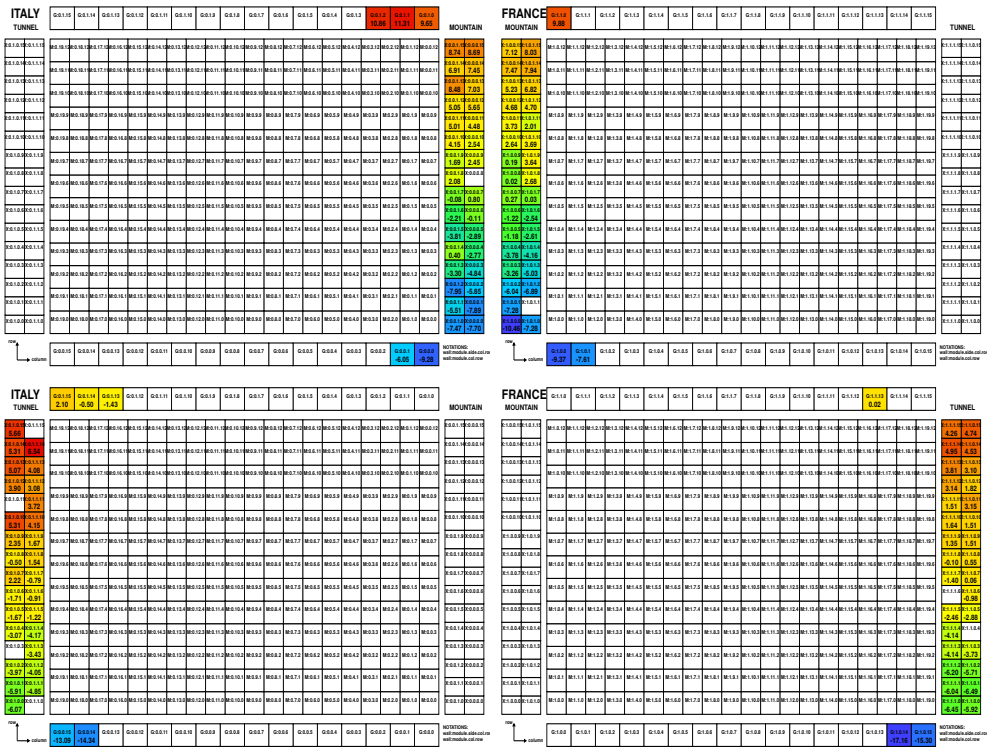

Figure 3.31 – Final offset values [ns] for the X-Wall sides.The mountain side w.r.t OM 528 (Third row figures) and the tunnel side w.r.t OM 638 (Last row figures).

A calibration of both the X-Walls and the G-Veto was done w.r.t OM 709 (this OM in particular to minimize the extrapolation from both the XWalls and Gveto OMs). Figure 3.32 shows the results of the full calibration and the error on the offset values obtained.

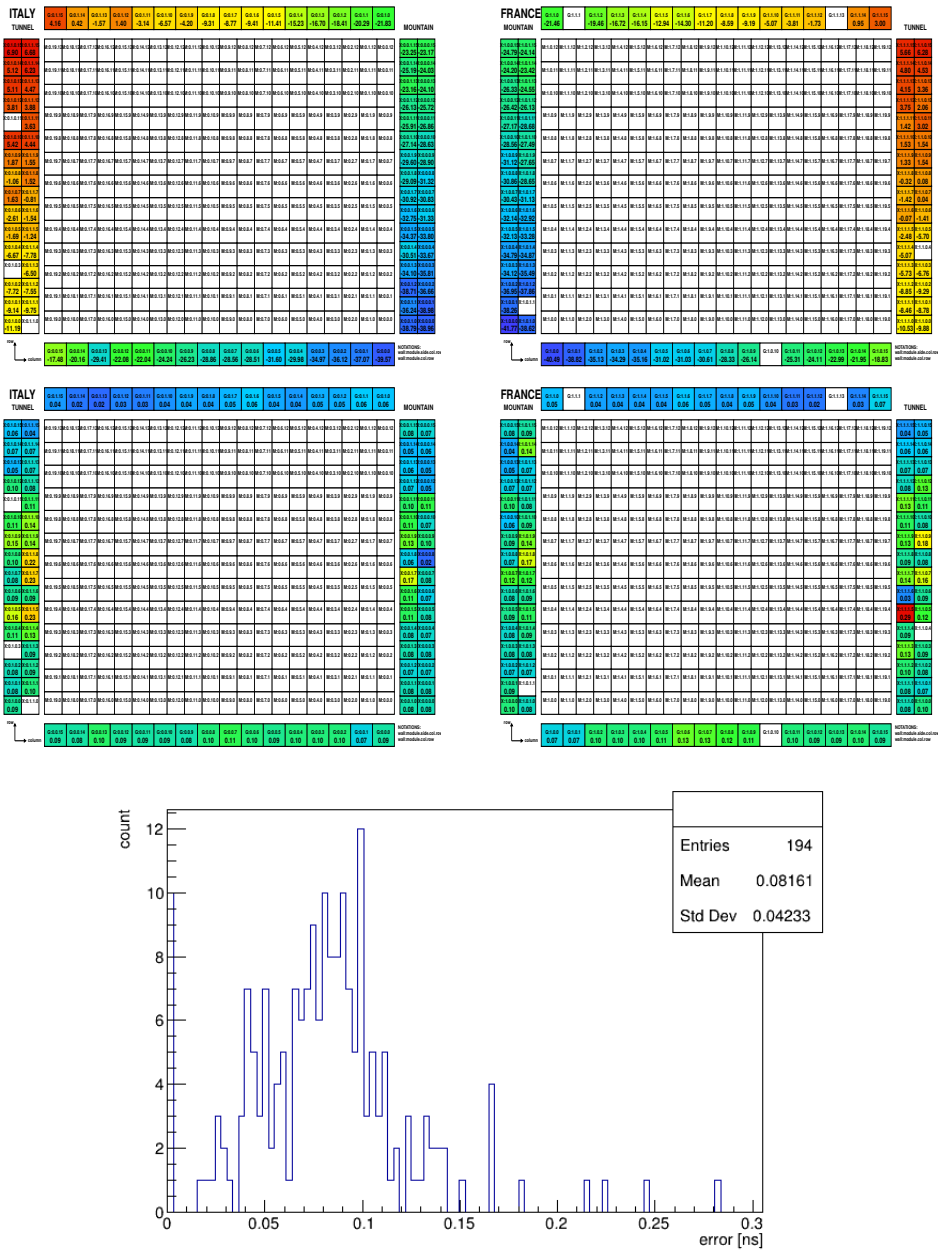

Figure 3.32 – Top plots show the final time offset values and on the bottom plots their error values per OM of the X-Walls and G-Veto w.r.t OM 709. On the right the Italian wall and on the left the French wall. The histogram on the bottom shows these errors in 1D.

Again, here you can see the color gradient corresponding to the offset values. It clearly shows the effect of time offset created by the cable length connected to the electronics board and the effect of the distance of the OMs from the reference OM.

3.7.6 . Results After Applying Offset Corrections

Main Walls

Figures 3.33 and 3.34 shows plots of the mean of the Gaussian fit of the Δ(t) distributions, before and after applying the offset corrections for a run on the Italian and French main wall, respectively. Clearly, after correction, the distribution is more centered at 0 and the mean is less dispersed, before : Mean = -2.7 [ns] error = 4.4 [ns] and after : mean = -0.01 [ns] error = 0.15 [ns]. The RMS is also well reduced by a factor of $\sim$ 30. Also, after correction, the sigma is nearly unchanged. This 0.1 [ns] precision will allow us to use the time of flight to reject backgrounds for our double beta signal studies.

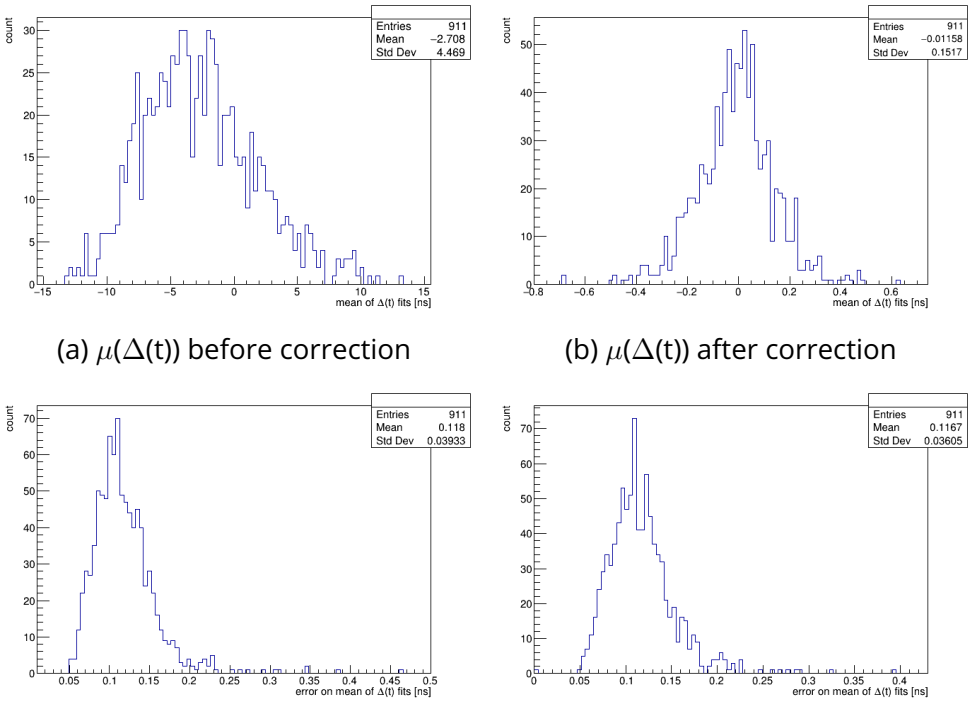

(a) $\mu(\Delta(t))$ before correction

(b) $\mu(\Delta(t))$ after correction

(c) $\sigma(\mu(\Delta(t)))$ before correction

(d) $\sigma(\mu(\Delta(t)))$ after correction

Figure 3.33 – Effect of offset correction on the mean and its error of Δ(t) distributions for the Italian main wall, in [ns]. To the left before the correction, to the right after the correction. On the top mean of the Δ(t) distributions and on the bottom the error on the mean of the Δ(t) distributions. One can clearly see that the interval of the distribution of the mean decreases significantly after correction, from approximately 15 [ns] to 0.8 [ns]. The error on these values are nearly unchanged.

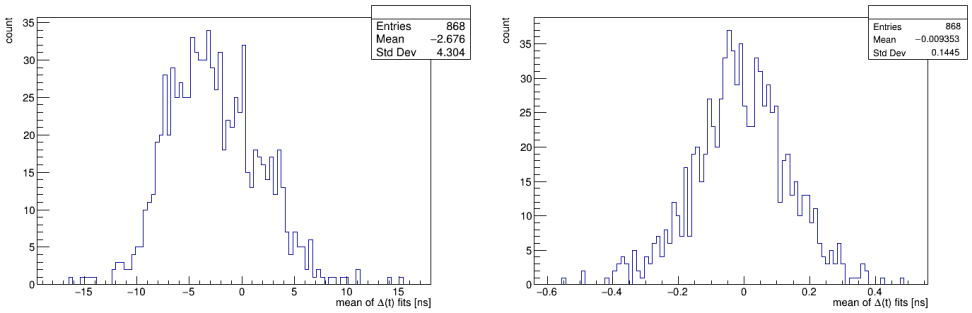

(a) $\mu(\Delta(t))$ before correction (b) $\mu(\Delta(t))$ after correction

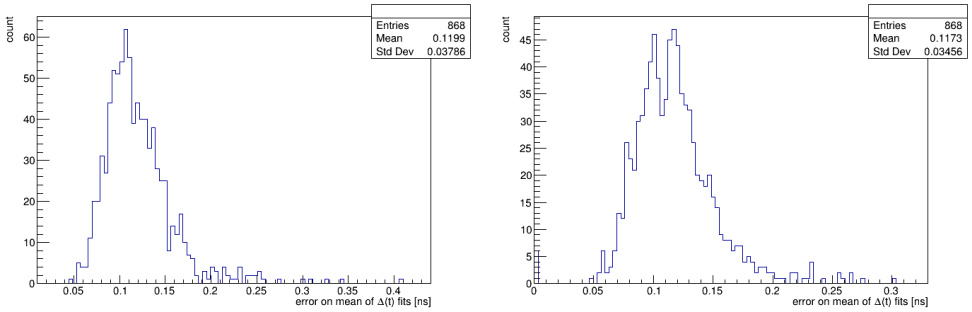

(c) $\sigma(\mu(\Delta(t)))$ before correction (d) $\sigma(\mu(\Delta(t)))$ after correction

Figure 3.34 – Effect of offset correction on the mean and its error of $\Delta(t)$ distributions for the French main wall, in [ns]. To the left before the correction, to the right after the correction. On the top mean of the $\Delta(t)$ distributions and on the bottom the error on the mean of the $\Delta(t)$ distributions. One can clearly see that the interval of the distribution of the mean decreases significantly after correction, from approximately 15 [ns] to 0.6 [ns]. The error on these values are nearly unchanged.

X-Walls and G-Veto

Looking at the figures 3.35 and 3.36, one would notice that after applying the offset correction the mean of the $\Delta(t)$ distribution has a nice peak around 0 and is less spread yet, but it is not as precise as the main wall corrections. Bad fits were removed from these plots (if existed). A discussion of a possible reason of why the distribution is spread will be presented in subsection 3.7.8 where different results are introduced.

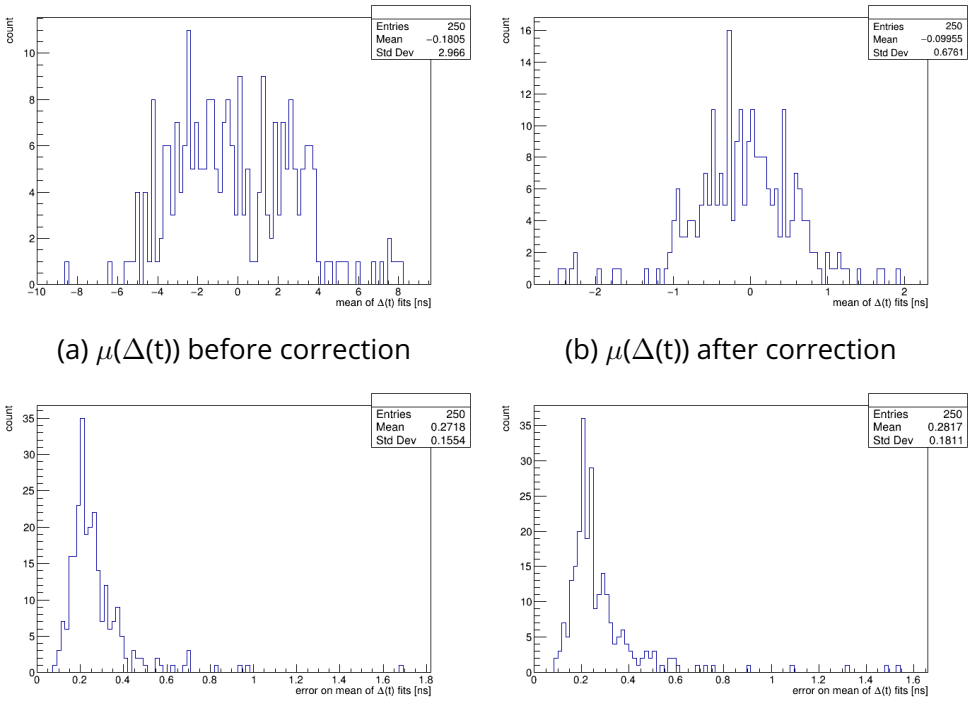

(a) $\mu(\Delta(t))$ before correction

(b) $\mu(\Delta(t))$ after correction

(c) $\sigma(\mu(\Delta(t)))$ before correction

(d) $\sigma(\mu(\Delta(t)))$ after correction

Figure 3.35 – Effect of offset correction on the mean and its error of Δ(t) distributions for the X-Wall run, in [ns]. To the left before the correction, to the right after the correction. On the top mean of the Δ(t) distributions and on the bottom the error on the mean of the Δ(t) distributions. One can clearly see that the interval of the distribution of the mean decreases after correction, from approximately 10 [ns] to 2.5 [ns]. The error on these values are nearly unchanged.

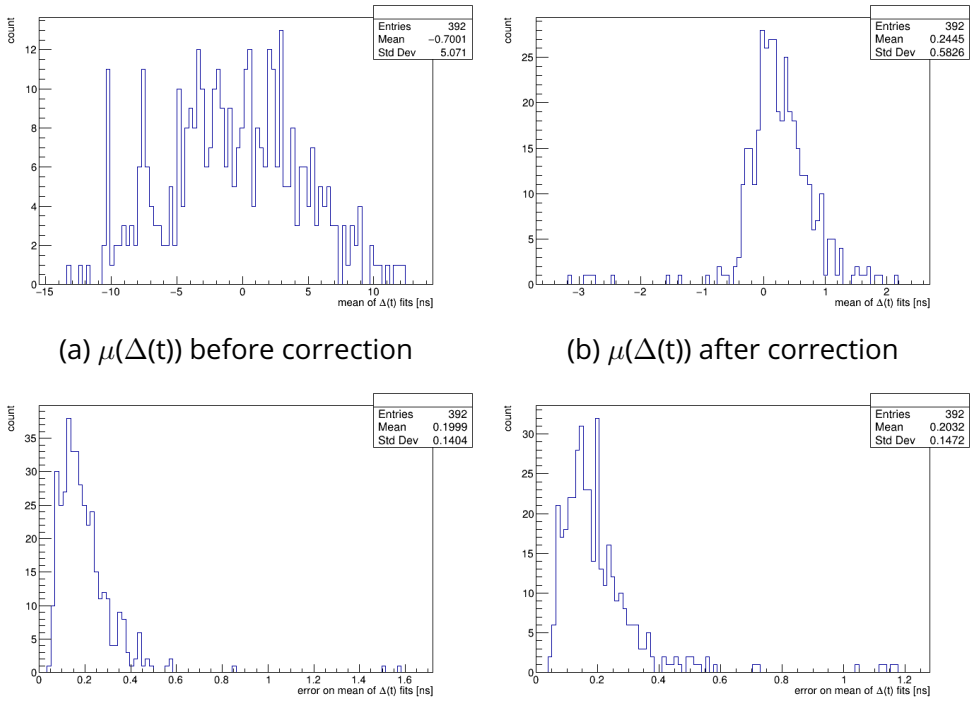

(a) $\mu(\Delta(t))$ before correction

(b) $\mu(\Delta(t))$ after correction

(c) $\sigma(\mu(\Delta(t)))$ before correction

(d) $\sigma(\mu(\Delta(t)))$ after correction

Figure 3.36 – Effect of offset correction on the mean and its error of $\Delta(t)$ distributions for the G-Veto run [ns]. To the left before the correction, to the right after the correction. On the top mean of the $\Delta(t)$ distributions and on the bottom the error on the mean of the $\Delta(t)$ distributions. One can clearly see that the interval of the distribution of the mean decreases significantly after correction, from approximately 15 [ns] to 3 [ns]. The error on these values are nearly unchanged.

3.7.7 . Effect of Cutting on Error of Offset Values

We study if a cut applied on the error on the time offset at each step of the calculation procedure can improve the precision on the time offset obtained. On one side, cutting at each step selects only OM calibrated with a small error on their $\Delta(t)$. While on the other side, the cutting induces more extrapolation steps to calibrate the full calorimeter (or the full calorimeter wall) producing larger extrapolation errors.

Main Walls :

Try cuts on the errors starting from 0.1 [ns] to 0.15 [ns], and then at each value plot the $\Delta(t)$ distribution of the results. Figures 3.37 and 3.38 shows the evolution of the mean of the mean of the $\Delta(t)$ distribution values and the error represents the error on the mean of the $\Delta(t)$ distribution, i.e $\mu(\mu(\Delta(t))$ and $\sigma(\mu(\mu(\Delta(t)))$.

There is a negligible improvement in the results after applying the cuts. The final offset file will include values with no cuts on error applied.

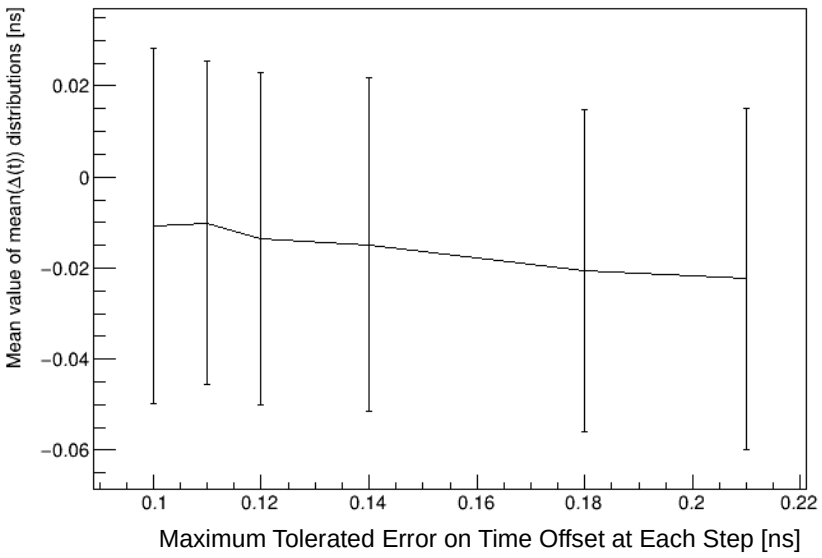

Figure 3.38 – Evolution of the $\mu(\mu(\Delta(t)))$ [ns] of the French Main Wall. The final point of each graph represents no cuts on time offset error applied.

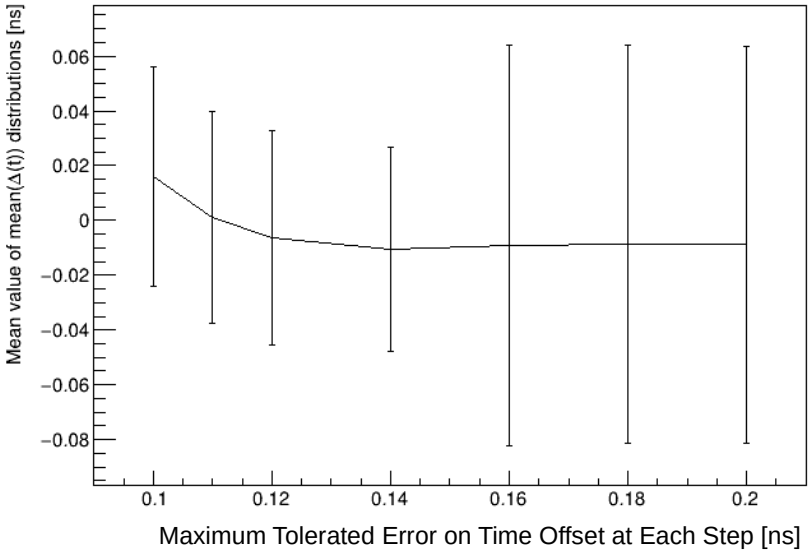

Figure 3.37 – Evolution of the $\mu(\mu(\Delta(t)))$ [ns] of the Italian Main wall. The final point of each graph represents no cuts on time offset error applied.

X-Walls and G-Veto :

Applying cuts on the error of the offset for the X-Walls and G-Veto would not allow a calibration of both walls w.r.t a single OM, so no cuts were made.

3.7.8 . X-Walls and G-Veto Source Position

A reason that the offset correction was not as good as expected *could* be associated to the following :
In the built code, the source position is determined automatically according to the OM with highest counting rate before applying any cuts. This approach should be correct if all the OMs are well calibrated in energy.
Looking at figure 3.39, the top and bottom plots are two different runs with the source position at the top (top map) and at the bottom (bottom map). You can see that there are two OMs that are always triggering at a higher rate than their surroundings, denoted by the bold black rectangle (on row 8). The bold black arrow is the source position determined by the code. Comparing with the measurement of the source position taken onsite, the top source position, if put at exactly the same marked spot, should be around row 11, the identified position is at row 8. If indeed the source position is misidentified by the code, there would be wrong measurements of the time of flight of the γs from the source position to the coinciding OMs, which would affect the offset correction that depends on it according to equation 3.7. As for the bottom plot, the source position is identified correctly comparing to the measurements onsite.

Figure 3.40 shows the hit count per OM for the tunnel side of the X-Wall. Again with the source identified according to the highest hit OM. But, then again, if you look at the map by eye, it is not very clear where the source is positioned.

Figure 3.41 shows the evolution of the hit count per OM map with each cut applied. To be noted : no energy cuts are applied here.
A possible reason for this kind of ambiguity in identifying the source position is because there is no gain equalization of the OMs, hence we do not know what kind of events we are detecting, and this, of course, affects the selection. Another possible reason is the position of the source. All sources are placed parallel to the wall, but at different distances depending on the wall. For the X-Wall, the source is placed at 1.6 [m], this will spread the detection angle of the source events compared to G-Veto (70 [cm]) and the main walls (1 [m]).

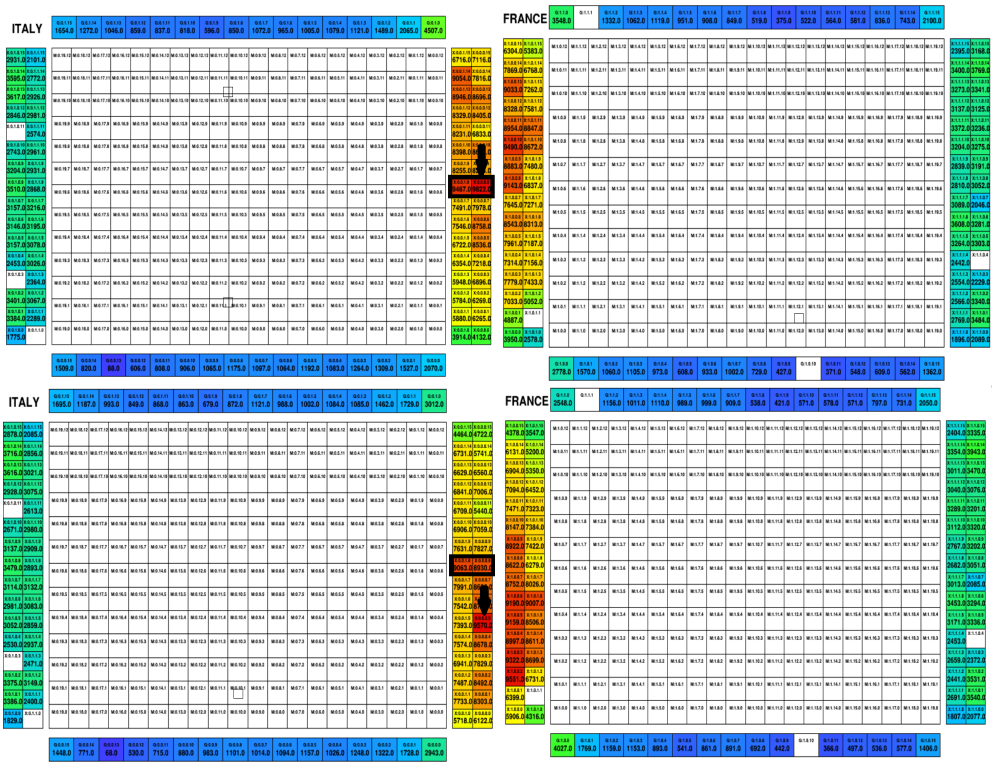

Figure 3.39 – X-Wall Mountain side hit count per OM map, no cuts applied. Top : Maps of run with source positioned at the top of the wall. Bottom : the source is positioned on the bottom of the wall. No cuts applied. The bold black arrows are the source position determined by the code. The bold black rectangles are OMs that are always triggering at a higher rate than their surroundings.

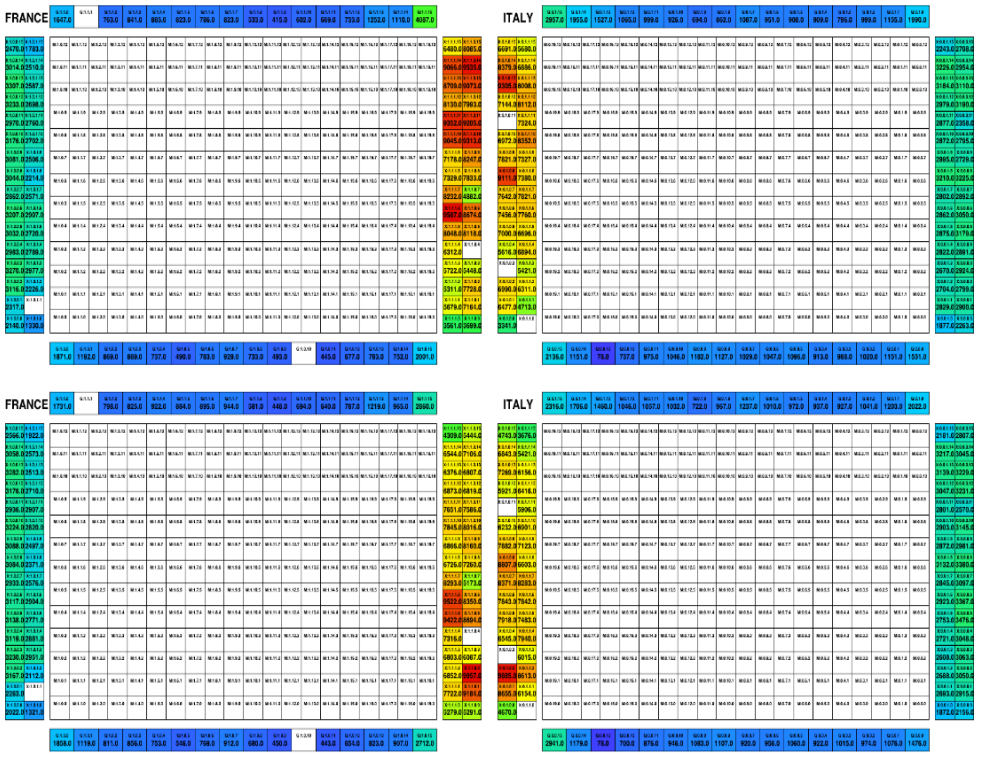

Figure 3.40 – X-Wall Tunnel side hit count per OM map, no cuts applied. Top : Maps of run with source positioned at the top of the wall. Bottom : the source is positioned on the bottom of the wall. No clear view of where the source is positioned.

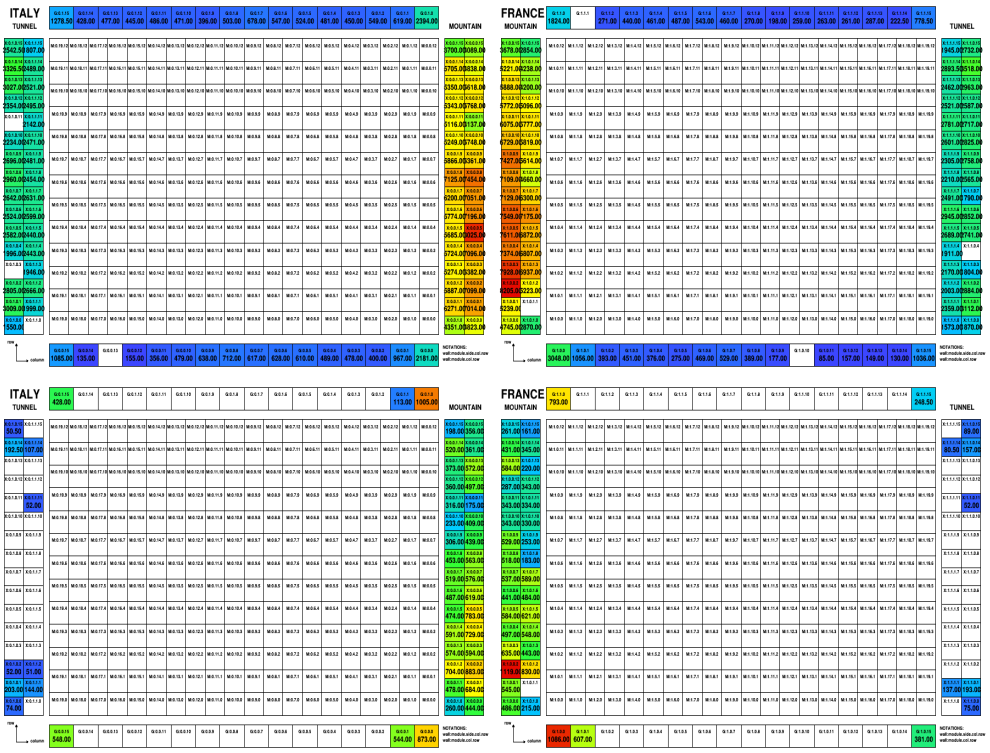

Figure 3.41 – X-Wall Mountain side hit count per OM map with the source on the bottom of the wall. Top : Cut applied : number of coincidences > 50. Bottom : Cut applied : number of coincidences > 50 and removing neighboring OMs.

3.7.9 . Results After Correcting Source Position to the Measurements on site

As mentioned in subsection 3.7.8, there is a possibility that the source position is misidentified due to PMT gain issues. So now we try to correct the source position to the one measured on site and check the results.

X-Walls and G-Veto

The histograms in figures 3.42 and 3.43 show the effect of changing the source position from code defined (OM with highest rate throughout the map, plots to the left of the figure) to on site defined position (measured onsite during the installation of the $^{6}0$Co source, plots to the right of the figure). There is an improvement for some runs (each row represents a run and a source position) where the range of the distribution narrows especially for the Tunnel side runs, except the Top Tunnel side of the G-Veto where the distribution increases its range. This could be explained by the fact that maybe the source may have not been placed at exactly the measured spot during data taking. Also for some runs the mean becomes closer to zero.

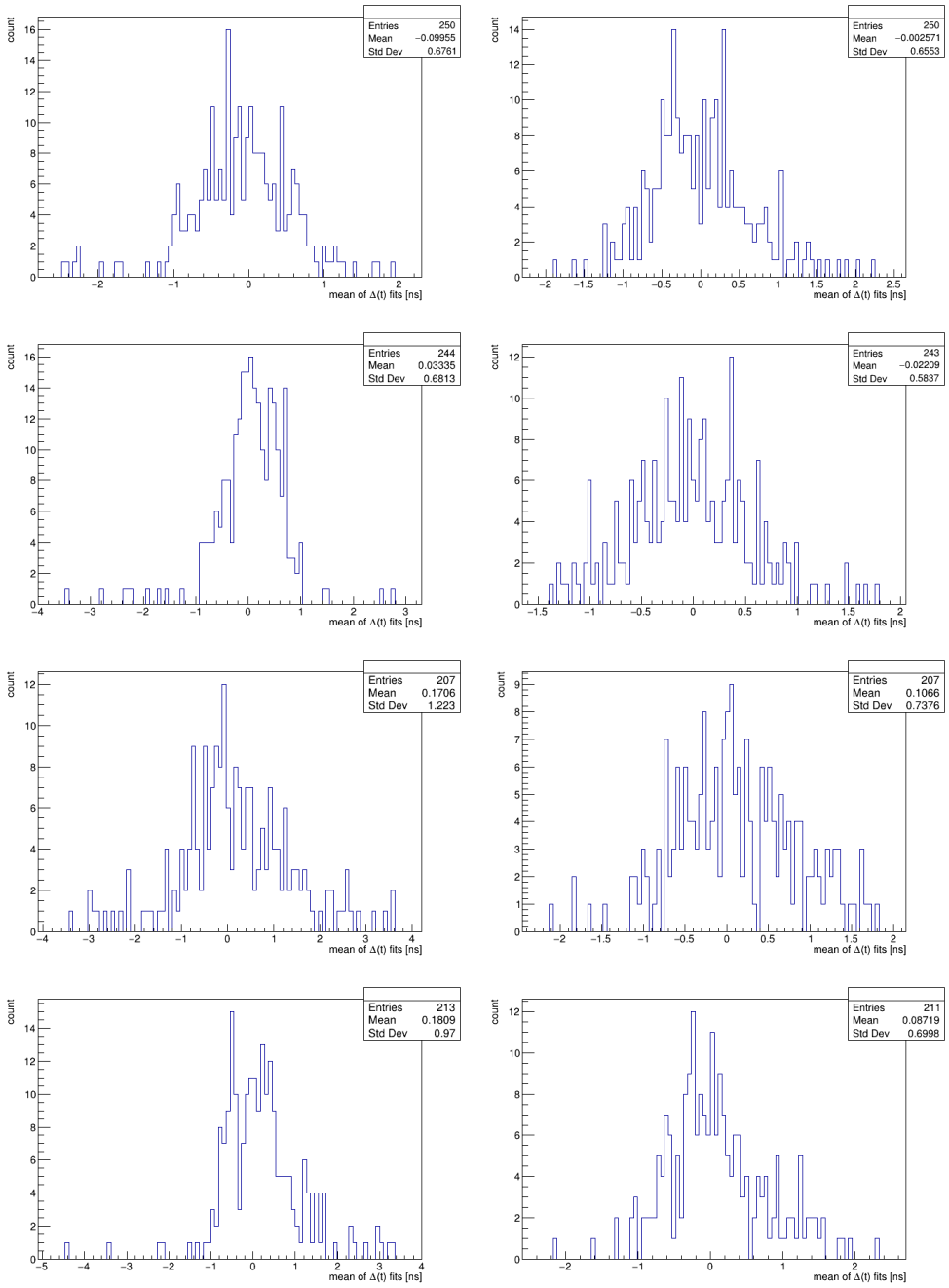

Figure 3.42 – Histograms showing the effect of changing the source position : Source is positioned according to the OM with highest counting rate (to the left) and source positioned according to the onsite measurements (to the right). Each row represents a unique run with a unique source position. The x-axis plots the mean of the Δ(t) distributions in [ns]. X-Wall runs from top to bottom : Bottom Mountain side, Top Mountain side, Bottom tunnel side, Top Tunnel side.

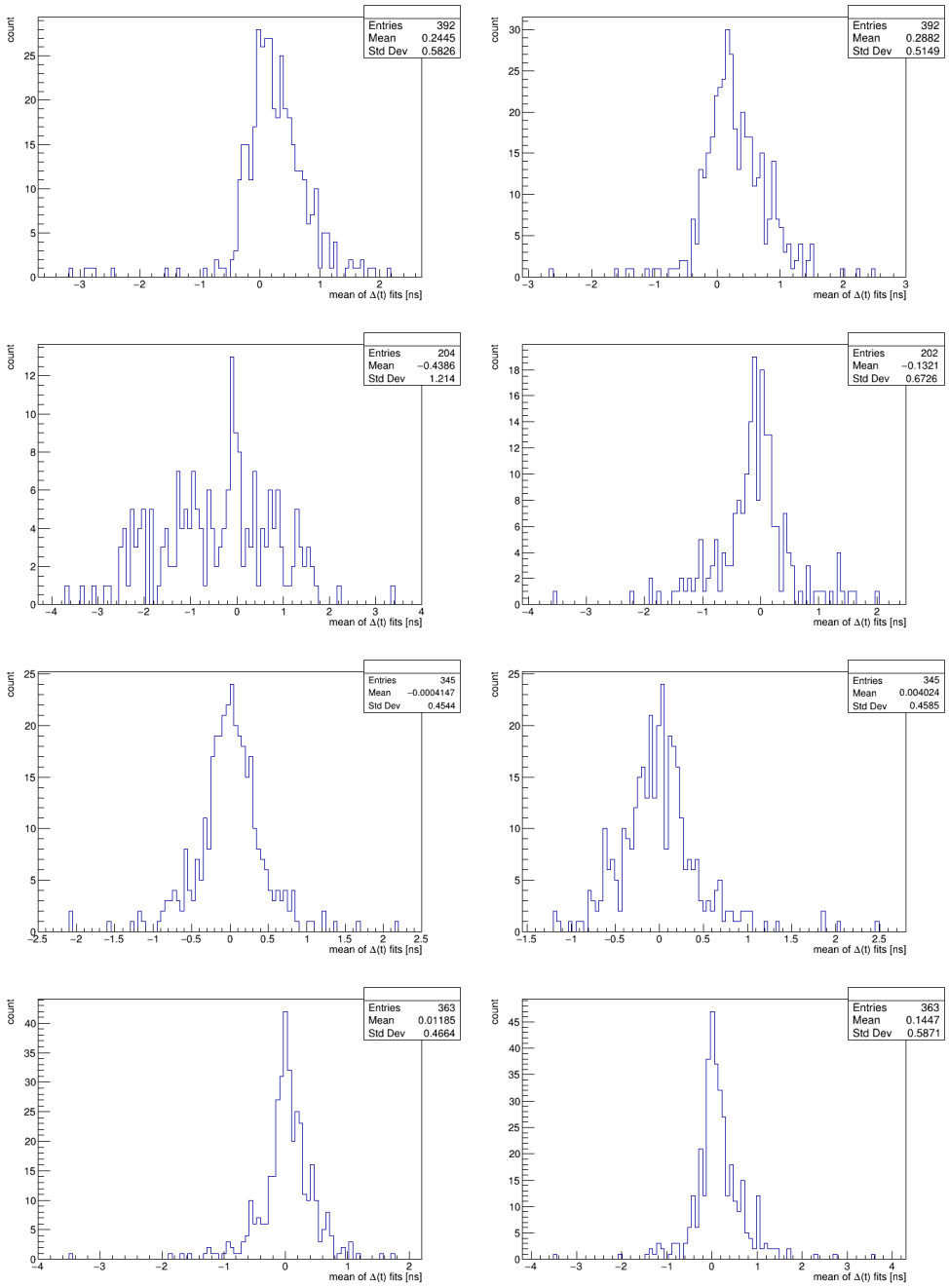

Figure 3.43 – Histograms showing the effect of changing the source position : Source is positioned according to the OM with highest counting rate (to the left) and source positioned according to the onsite measurements (to the right). Each row represents a unique run with a unique source position. The x-axis plots the mean of the Δ(t) distributions in [ns]. G-Veto Wall runs from top to bottom : Bottom Mountain, Bottom Tunnel, Top Mountain, Top Tunnel.

Main Walls

To be consistent in the choice of the source position, a change of it is also done for the main walls. The new offset values map is presented in figures 3.44 and 3.46 along with all the plots presented before. But with the new source position according to the new method used for the X-Walls and G-Veto, where the source is manually chosen from the measured position onsite. The change only appeared in the Italian wall where the reference OMs changed from OM 122 to 135. The results are shown in in figures 3.45 and 3.47. As for the effect of this cut on the mean of $\Delta(t)$ distribution, for the Italian wall the results got slightly worse and as for the french wall, it improved a bit for one or two runs and is worse for the rest. Also a comparison with the offset values from reflectometry runs is made and presented in figures 3.48 and 3.49, where there is a strong effect on the mean for the Italian main wall compared to previous positions of the source (in figures 3.29 and 3.28) and a small change for the French wall.

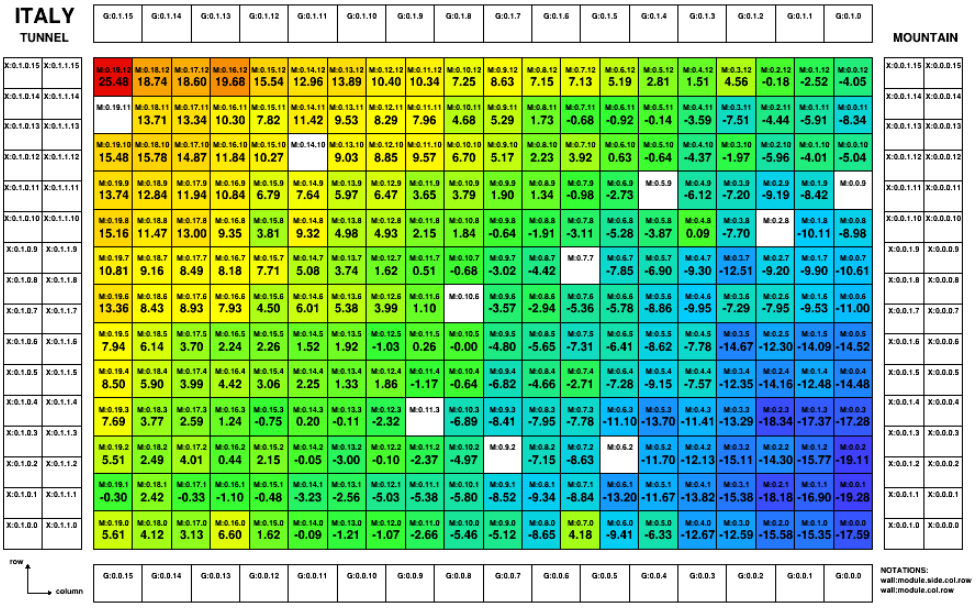

Figure 3.44 – Final offset values per OM of the Italian Main Wall w.r.t OM 135.

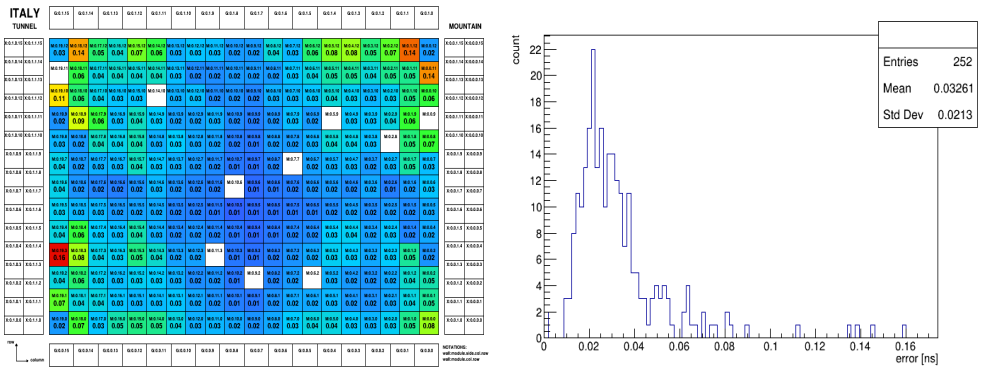

Figure 3.45 – Final offset error values per OM of the Italian Main Wall w.r.t OM 135, on the right you can find a 1D representation of the values in the map on the left.

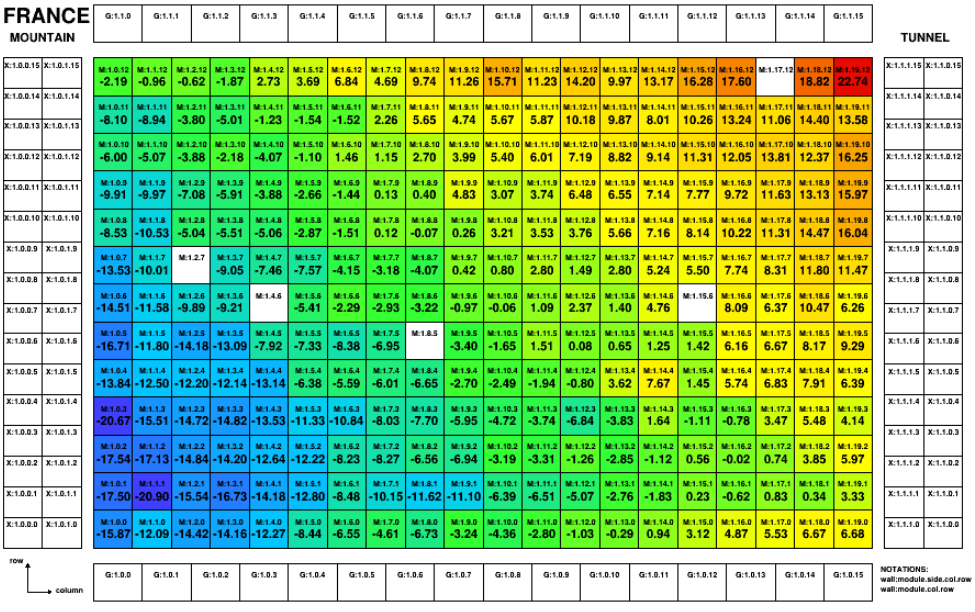

Figure 3.46 – Final offset values per OM of the French Main Wall w.r.t OM 396.

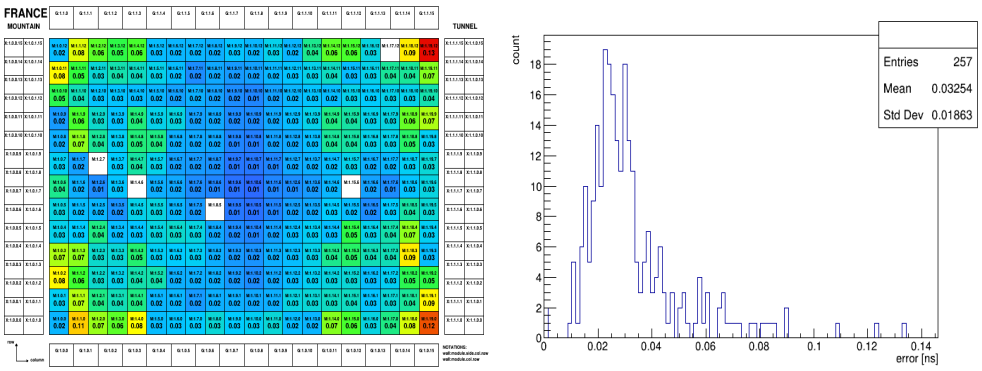

Figure 3.47 – Final offset error values per OM of the French Main Wall w.r.t OM 396, on the right you can find a 1D representation of the values in the map on the left.

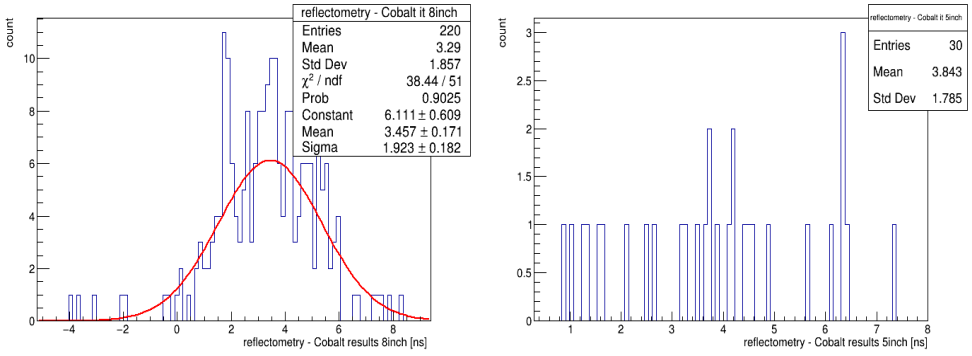

Figure 3.48 – Comparing between the results of reflectometry with the new results that use the source position measured on site for the Italian main wall.

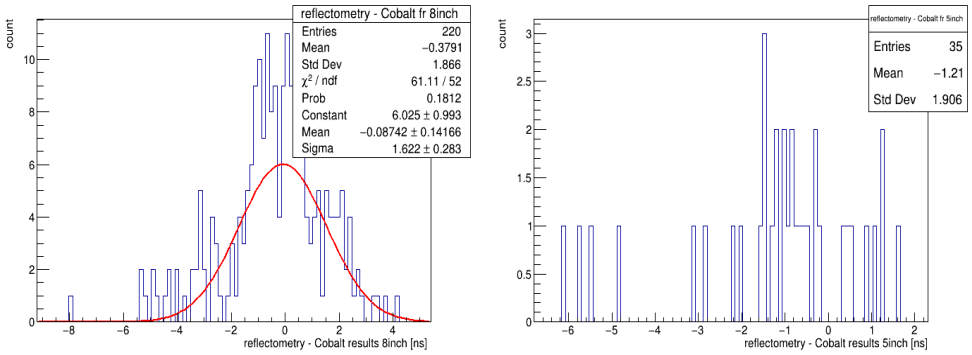

Figure 3.49 – Comparing between the results of reflectometry with the new results that use the source position measured on site for the French main wall.

3.8 . Time Resolution

To calculate the time resolution of the full calorimeter wall, the resolution should be extracted for each OM on its own.

Using the ^{60}Co source one can determine the time resolution for γs @ 1 MeV using the sigma of the Gaussian fit of the Δ(t) distributions.

3.8.1 . Method to Determine the Time Resolution Per OM

Step 1 : Fix an OM that will be called the reference OM or OM_0, this OM will have several coincidence OMs.

Step 2 : Get two of the coincidence OMs with OM_0, which will be called OM_1 and OM_2. The way to choose them is by checking their number of coincidences (N) with OM_0 and also between OM_1 and OM_2. Figure 3.50 shows a schematic view of coincidences between 3 optical modules, with the related parameters used to determined the sigma on time resolutions.

Using equation 3.13 the obtained number denoted by "A", should be the minimum between all the possible combinations of the different OM_1 and OM_2.

$$A = min_{ij}(\frac{1}{N_{0i}} + \frac{1}{N_{0j}} + \frac{1}{N_{ij}}) \tag{3.13}$$

Where N_{0i}, N_{0j} and N_{ij} are the number of coincidences between OM_0 and OM_i, OM_0 and OM_j & OM_i and OM_j, respectively. Where OM_i and OM_j are any two OMs in coincidence with OM_0. Each of these OMs will have the following :

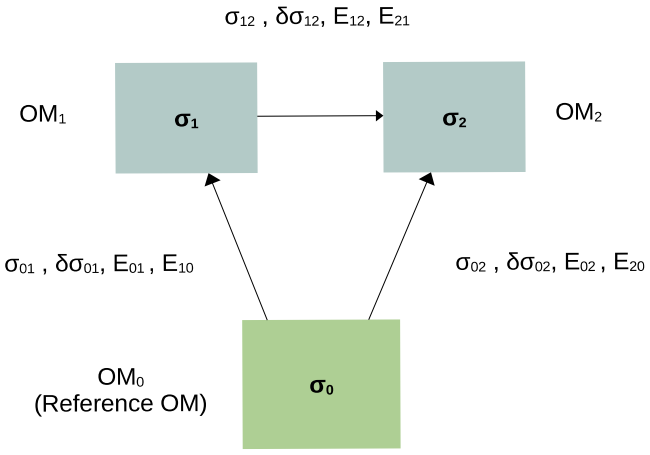

Figure 3.50 – Representation of OM_0 with its coincidences with OM_1 and OM_2. σ_0, σ_1 and σ_2 are the time resolutions of OM_0, OM_1 and OM_2 at 1 [MeV]. σ_{ij} is the uncertainty on the time distribution for coincidence events between OM_i and OM_j and $\delta\sigma_{ij}$ is its error. E_{ij} : Are the mean of the energy of the hits inside OM_i in coincidence with OM_j. Where i,j=0, 1, 2.

σ_0, σ_1 & σ_2 : Are the time resolutions at 1 MeV of OM_0, OM_1 and OM_2, respectively.
σ_{ij} : Are the sigma of the Gaussian fit of the Δ(t) distribution between OM_i and OM_j.
$\delta\sigma_{ij}$: Are the error on the sigma value.
E_{ij} : Are the mean of the energy of the hits inside OM_i in coincidence with OM_j.

Step 3 : In order to get the time resolution per OM, we inverse equations 3.14 to express σ_0, σ_1 and σ_2 as a function of σ_{01}, σ_{02}, σ_{12}, E_{01}, E_{02}, E_{10}, E_{12}, E_{20}, E_{21} and their associated errors

$$\begin{aligned} \sigma_{01}^2 &= \frac{\sigma_0^2}{E_{01}} + \frac{\sigma_1^2}{E_{10}} \\ \sigma_{02}^2 &= \frac{\sigma_0^2}{E_{02}} + \frac{\sigma_2^2}{E_{20}} \\ \sigma_{12}^2 &= \frac{\sigma_1^2}{E_{12}} + \frac{\sigma_2^2}{E_{21}} \end{aligned} \tag{3.14}$$

As there are several coincidences with OM_0, we will end up with several σ_0 values. The weighted average is used to get a final time resolution per OM.

Repeating steps from (1) to (3) one can get the time resolution for all OMs. The values per OM are presented in figures 3.51 and 3.52.

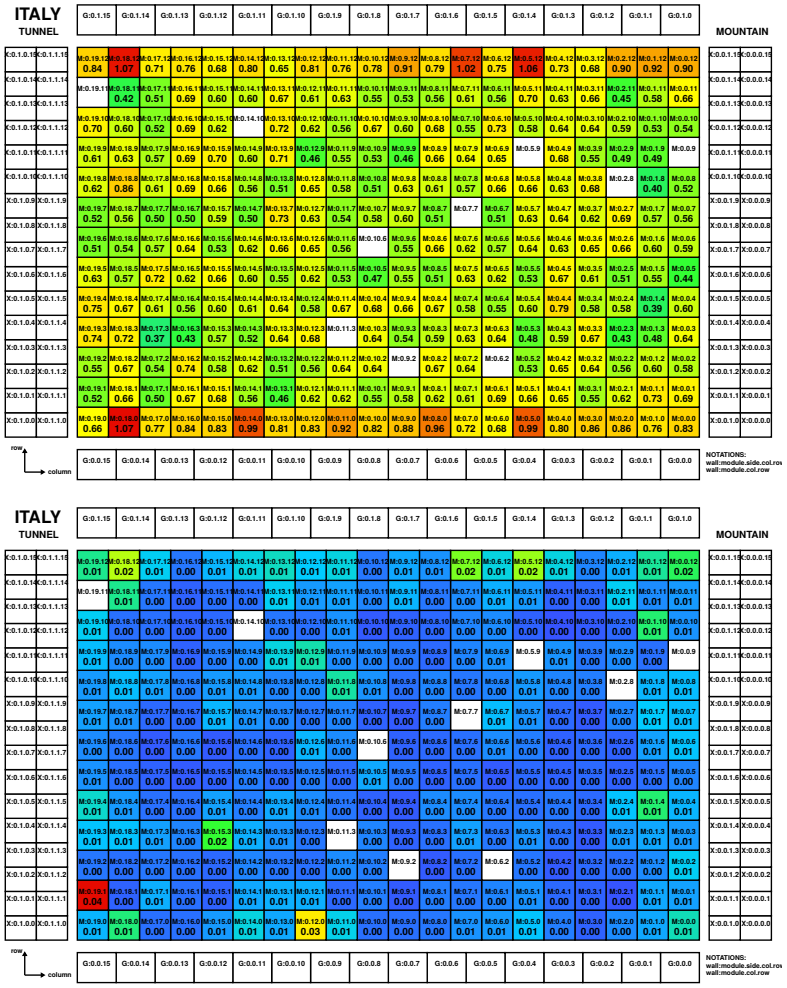

Figure 3.51 – Top : Time resolution, bottom : Error on time resolution, per OM for γs at 1 MeV for Italian main wall, calculated using ^{60}Co source runs with cuts applied being E > 0.7 [MeV] and minimum number of coincidences between 2 OMs is 50.

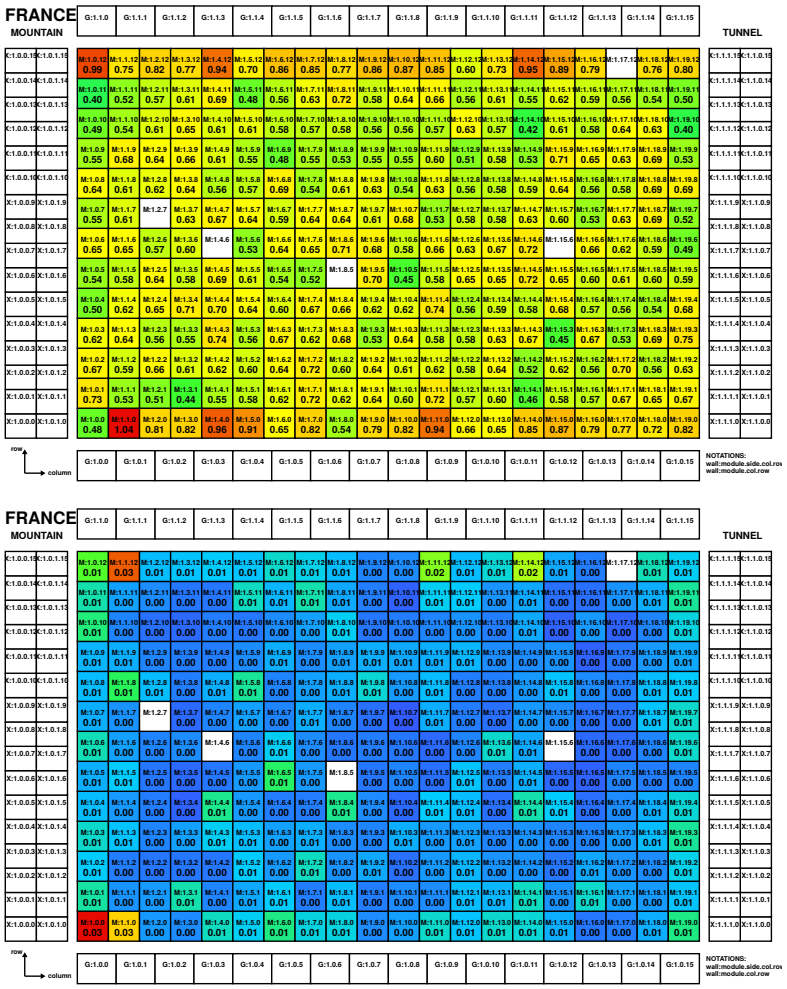

Figure 3.52 – Top : Time resolution, bottom : Error on time resolution, per OM for γs at 1 MeV for French main wall. calculated using ^{60}Co source runs with cuts applied being E > 0.7 [MeV] and minimum number of coincidences between 2 OMs is 50.

Perform weighted average, again, on all the OMs values per wall to obtain a time resolution for the full wall. Final results are shown in table 3.1.

	8" OMs	5" OMs
French Wall	0.619 ± 0.002 (stat)	0.814 ± 0.006 (stat)
Italian Wall	0.614 ± 0.002 (stat)	0.828 ± 0.005 (stat)

Table 3.1 – The calculated weighted average time resolution values for the main calorimeter walls including their statistical errors, in [ns].

A possible double check for the time resolution results is by comparing the

ratio of the time resolution results of 5" OMs to 8" OMs to their ratio of energy resolution. A quick reminder that the σ_t and energy resolution are both proportional to $1/\sqrt{number\ of\ photoelectrons\ at\ 1MeV}$ (more in 2.2.3, page 63), so we can compare the two ratios :

- Time resolution of 5" OMs / 8" OMs = 0.814/0.619 = 1.315
- Energy resolution of 5" OMs / 8" OMs = 11/8 = 1.375

The two ratios are compatible and we can consider the results as eligible.

Estimation of the Systematic Errors on the Time Resolution

To get the systematic errors on the time resolution, we vary the cuts applied. Reminding, the reference cut is $E_{min} > 0.7$ MeV and a number of coincidences between two OMs > 50.

Figures 3.53 and 3.54 show the resulting value of time resolution for the main wall while varying these cuts. N.B : The numbers in those figures are rounded to the nearest value.

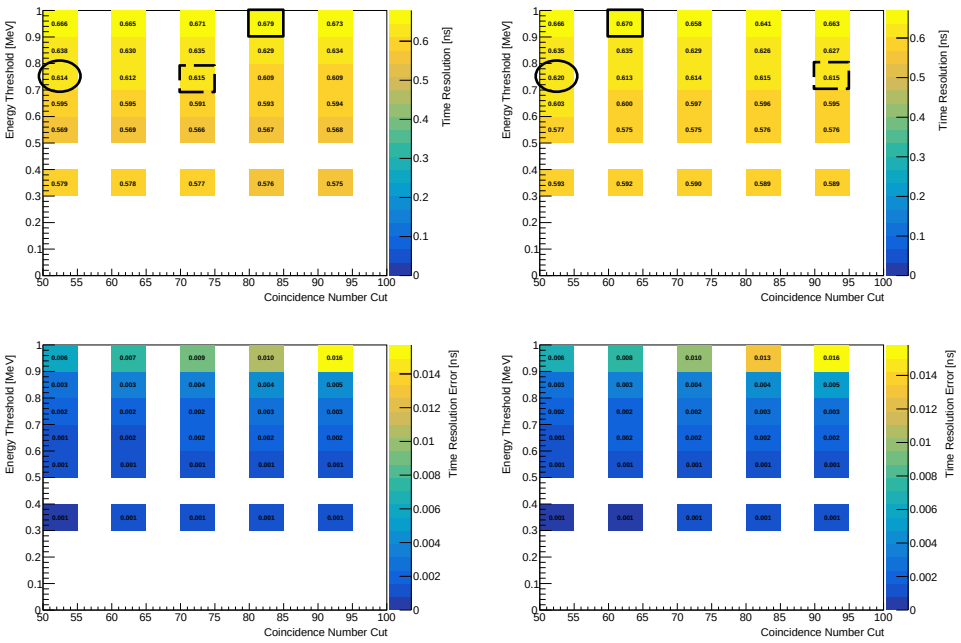

Figure 3.53 – For the main wall 8" OMS in [ns], Top : Time resolution values with each cut applied, the energy threshold cut on the vertical axis in [MeV] and the minimal number of coincidences between two OMs on the horizontal axis. Bottom : Error on Time resolution values. To the left Italian main wall, to the right French main wall. The ellipse represents the reference time resolution value with the typical cut, the full square represents the value that is most different from the reference value, while the dotted square represents the least different value.

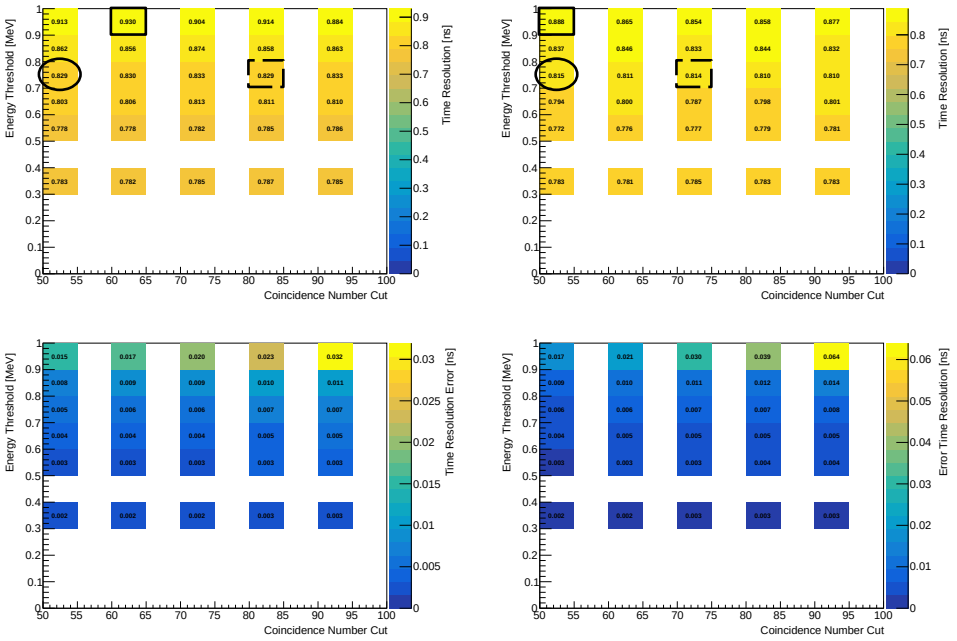

Figure 3.54 – For the main wall 5" OMS in [ns]. Top : Time resolution values with each cut applied, the energy threshold cut on the vertical axis in [MeV] and the minimal number of coincidences between two OMs on the horizontal axis. Bottom : Error on Time resolution values. To the left Italian main wall, to the right French main wall. The ellipse represents the reference time resolution value with the typical cuts, the full square represents the value that is most different from the reference value, while the dotted square represents the least different value.

The ellipse represents the reference time resolution value with the typical cut, the full square represents the value that is most different from the reference value while the dotted square represents the least different value. From the latter two values we get the systematic errors.

As there are no energy cuts on the G-Veto, no time resolution was calculated

3.8.2 . Results of Time Resolution

The time resolution in [ns] of the main calorimeter wall for γs @ 1 MeV is shown in table 3.2.

	8" OMs	5" OMs
French Wall	0.619 $\pm$ 0.002 (stat) + 0.049(sys) – 0.004(sys)	0.814 $\pm$ 0.006 (stat) + 0.073(sys) – 0.000(sys)
Italian Wall	0.614 $\pm$ 0.002 (stat) + 0.064 (sys) – 0.000 (sys)	0.828 $\pm$ 0.005 (stat) + 0.101 (sys) – 0.000 (sys)

Table 3.2 – The calculated time resolution values for the main calorimeter walls including their systematic and statistical errors, in [ns].

To conclude this chapter, I have aligned in time all the OMs with respect to three reference OMs, one for each main wall and one for both the X-Walls and G-Vetos. The precision of such alignment is better than 0.2 ns. Crossing electron events will allow us to align all OMs in all walls with respect to a single reference OM. I have also measured the time resolution of the main wall OMs using gammas at 1 MeV to be $\sim$600 ps, which is in an agreement with what is expected for gammas. An extra work should be performed using ^{207}Bi calibration source to check the time resolution for electrons at 1 MeV, which is better.

4 - Study of the Sensitivity of SuperNEMO to the Quenching of the Axial-Vector Coupling Constant "g_A"

This chapter presents the study of the constrains that the SuperNEMO demonstrator can set on the axial-vector coupling constant.

As mentioned in chapter 1 in subsection 1.2.7 page 29, the axial-vector coupling constant undergoes quenching because of the many nucleon-nucleon interactions inside the nucleus, which are not taken into account in the theoretical calculations in the first order approach.

At the free-nucleon level, the value of g_A is calculated from the decay of a free neutron to be $g_A^{free} = 1.2723$ [48]. At the nuclear level we find a quenched value called g_A^{eff}, which is the effective value of g_A^{free}, such that :

$$g_A^{eff} = q g_A^{free} \tag{4.1}$$

where "q" is called the quenching factor.

A good theoretical approximation to the effective g_A value should take into account many effects including [23] :

1- Nuclear medium effects such as non-nucleonic degrees of freedom (e.g : Δ resonances).

2- Many-body currents : Meson-exchange currents, that are beyond the one nucleon impulse approximation (where only one nucleon experience the weak decay without interference from the surrounding nuclear medium).

3- Deficiencies in nuclear many-body approaches like : restricted valence space, lacking many-body configurations or emission of three-body nuclear forces, all of which worsens the quality of the wave functions of the decay process.

First I will present the interest in determining the axial-vector coupling constant, and how its value strongly affects the $\beta\beta$ decays half-lives. Then, I will describe the work performed to implement the required physics processes in the simulations from calculations results provided by theoreticians and how this implementation was validated. Finally, I will describe the method used to constrain the axial-vector coupling constant, giving the most sensitive observable to this quenching and the expected sensitivity that could be reached.

4.1 . The Importance of Determining the Axial-Vector Coupling Constant

Considering the **contribution of g_A^{eff} to the fourth power inside the half-life calculations** of the $\beta\beta$ decay (as seen in equation 5.2), an uncertain g_A value

will have a strong influence on the double beta rate and change dramatically the predictions for $0\nu\beta\beta$ observation. Hence, it is very important to determine its value.

Moreover, There are some tensions between the theoretical calculations and experimental measurements, the new results from Cupid-0 has favored the single state dominance (SSD) for ^{82}Se [59], and similarly (but less significantly) the NEMO-3 has also favored SSD [53]. As is it going to be shown later, SSD is not compatible with different theoretical models calculations, so the constrain on the quenching using SuperNEMO demonstrator data could help to test if this tension will persist or not.

4.2 . Constraining g_A Using Accurate Measurement of the $2\nu\beta\beta$ Decay

The decay rate of the $2\nu\beta\beta$ decay is commonly presented as :

$$(T^{2\nu}_{1/2})^{-1} = (g_A^{eff})^4 |M^{2\nu}_{GT}|^2 G^{2\nu} \tag{4.2}$$

where $M^{2\nu}_{GT}$ is the Gamow-Teller nuclear matrix element, and $G^{2\nu}$ is a phase-space factor.

But a more accurate theoretical description is provided in [56], where they take into account in the calculations the dependence on lepton energies from the energy denominators of the NME. The equation of the decay rate becomes :

$$(T^{2\nu}_{1/2})^{-1} = (g_A^{eff})^4 |M^{2\nu}_{GT}|^2 (G^{2\nu}_0 + \xi^{2\nu}_{31} G^{2\nu}_2 + \frac{1}{3}(\xi^{2\nu}_{31})^2 G^{2\nu}_{22} + (\frac{1}{3}(\xi^{2\nu}_{31})^2 + \xi^{2\nu}_{51}) G^{2\nu}_4) \tag{4.3}$$

where $\xi^{2\nu}_{31}$ and $\xi^{2\nu}_{51}$ are two ratios of NMEs, where :

$$\xi_{31} = \frac{M^{2\nu}_{GT-3}}{M^{2\nu}_{GT-1}} \ , \ \xi_{51} = \frac{M^{2\nu}_{GT-5}}{M^{2\nu}_{GT-1}} \tag{4.4}$$

and

$$M^{2\nu}_{GT-3} = \sum_n M_n \frac{4m_e^3}{[E_n - (E_i + E_f)/2]^3} \tag{4.5}$$

$$M^{2\nu}_{GT-5} = \sum_n M_n \frac{16m_e^5}{[E_n - (E_i + E_f)/2]^5} \tag{4.6}$$

where m_e is the mass of the electron. E_i and E_f are the energies of the initial and the final nuclei, E_n is the energy of the intermediate nucleus and M_n describes the transition from the initial to final state of the decay through all the possible intermediate states (see figure 4.1) [56].

$G^{2\nu}_0$, $G^{2\nu}_2$, $G^{2\nu}_{22}$ and $G^{2\nu}_4$ are phase space factors that depend on different kinematics (energy and angular distribution) and can be calculated with good accuracy [56].

The above equation can be re-written with a dependence on the NME $M^{2\nu}_{GT-3}$, which can be calculated more reliably using Shell Model techniques, due to its dependence on the low-energy states of the intermediate nucleus (see more in 1.2.7, page 29). The equation is then written as equation 5.2 where the higher order terms of $\xi^{2\nu}_{31}$ and $\xi^{2\nu}_{51}$ are neglected in the development. This equation is going to be used in this analysis, and equation 4.3 will be ignored unless mentioned otherwise.
From here on we use the notation ξ_{31} instead of $\xi^{2\nu}_{31}$.

$$(T^{2\nu}_{1/2})^{-1} \simeq (g^{eff}_A)^4 |M^{2\nu}_{GT-3}|^2 \frac{1}{|\xi_{31}|^2}(G^{2\nu}_0 + \xi_{31} G^{2\nu}_2) \tag{4.7}$$

The use of a tracker-calorimeter detector, like SuperNEMO, allows a reconstruction of the full kinematics of the final state electrons, and therefore allowing a determination of the ξ_{31} parameter with several observables. Then, comparing the experimental constraints with the theoretical models, we can constrain the quenching of the axial-vector coupling constant.

4.2.1 . HSD and SSD ξ_{31} Value

There are two models that govern the double beta decay, a decay through higher state dominance (HSD) or through single state dominance (SSD) (introduced in 1.2.7, page 29). In figures 4.1 and 4.2, we present a schematic view of the decay of ^{82}Se, if the decay proceeds through one dominating 1^+ fundamental energy state of ^{82}Br, then it is said to be SSD (figure 4.1), otherwise, if it proceeds through the excited states then it is said to be HSD (figure 4.2), where only the G_0 process plays a role.

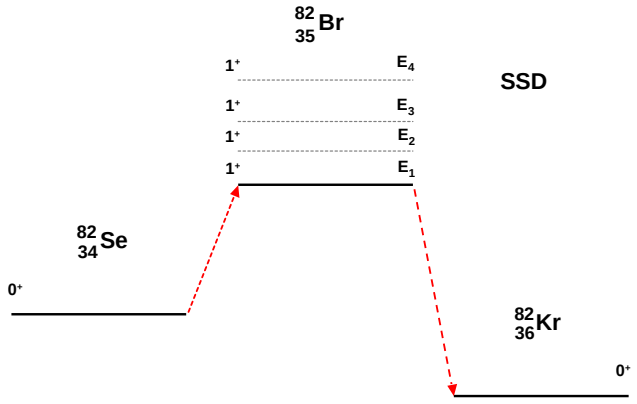

Figure 4.1 – Schematic sketch of the double beta decay of ^{82}Se through the SSD model.

The value of the parameter ξ_{31} changes depending on the governing model. In

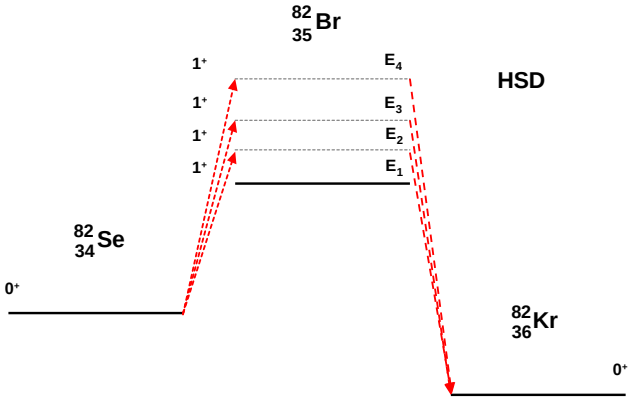

Figure 4.2 – Schematic sketch of the double beta decay of ^{82}Se through the HSD model.

the SSD case the parameter is calculated for ^{82}Se to be 0.3738, while for HSD ξ_{31} = 0 [49].

4.2.2 . Theoretical Calculations from QRPA and Shell Model to Constrain the Value of g_A

Two commonly used theoretical calculation methods are the interacting shell model (ISM/SM) and the quasi-particle random-phase approximations (QRPA), mentioned in 1.2.7, page 28.

QRPA calculations have a "free" parameter, usually called g_{pp} (the strength of the proton-neutron interaction) and it represents the isoscalar pairing (pairs having an angular momentum J=1 and isospin I=0 [51]). In the case of shell model, isoscalar pairing for each nuclear interaction is fixed, so the calculations have point like results and differ in the case of using different ISM interactions between nucleons. Adding that M_{GT-3} is sensitive to contributions from lowest-energy states in the intermediate odd-odd nucleus due to rapid suppression in the energy denominator [24], and hence this NME is easier to calculate with the ISM.

4.2.3 . Determining ξ_{31} by Fitting Energy Distributions

The phase space factors $G_0^{2\nu}$ and $G_2^{2\nu}$ have different leptonic energy dependencies, and they can be calculated with good precision. Knowing their spectral shape, and then fitting the $\beta\beta$ decay spectrum to extract the contribution of each process, one can then determine the ξ_{31} value, knowing that :

$$\xi_{31} = \frac{Contribution\ of\ G_2\ term}{Contribution\ of\ G_0\ term} \tag{4.8}$$

$G_0^{2\nu}$ and $G_2^{2\nu}$ also have different angular distributions, but the calculations were not available when I started this work. Recent work on the matter has been

published [49] and it is more complicated to analyze than using the energy distributions. With the latter, one is able to simulate $G_0^{2\nu}$ and $G_2^{2\nu}$ separately, while for angular distribution a separate simulation for the two processes is not possible and a separate simulation of each ξ_{31} value is needed, see article [49], equation 26.

4.2.4 . Constraining g_A from ξ_{31} Values

The constraints on g_A^{eff} and M_{GT-3} are already set by theoretical calculations, presented in figure 4.3, where it shows in dashed blue the SSD calculations using equation 5.2 where $\xi_{31} = 0.3738$. The two distributions for QRPA and 3 dots for Shell Model are also shown, each QRPA and SM value correspond to calculations with different interactions between nucleons used.

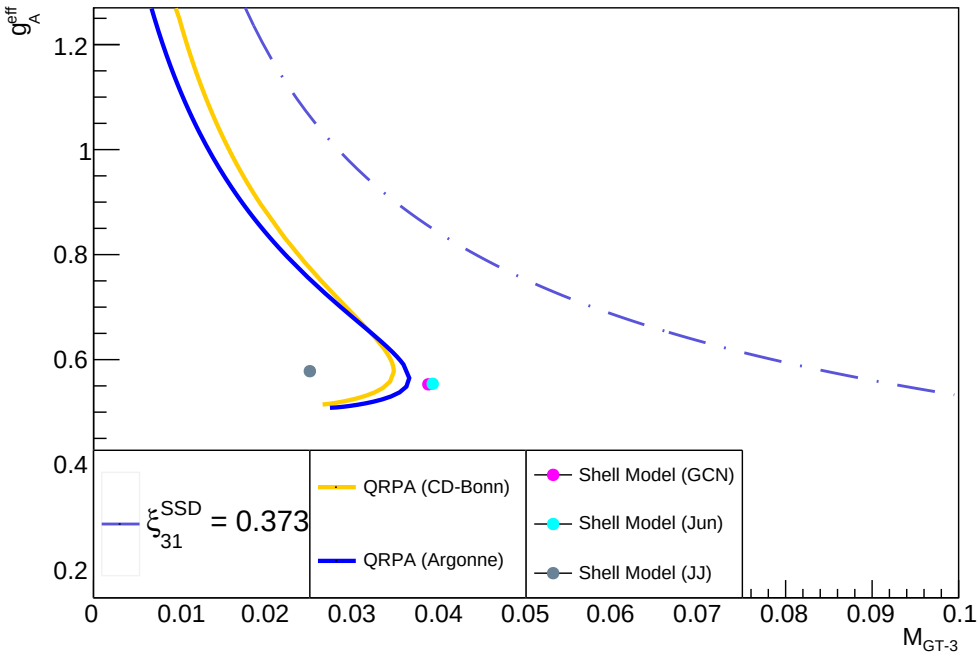

Figure 4.3 – Constrain plane for the values of g_A^{eff} and M_{GT-3} using theoretical calculations. The SSD model is obtained for the value ξ_{31} = 0.3738 and using equation 5.2. QRPA and SM are also shown with calculations provided by Fedor Šimkovic for QRPA and Javier Menéndez for Shell Model [60]. The QRPA calculations show a curve due to the variation of the pseudo-particle continuous coupling constant in the calculations.

4.3 . Implementation of the different Phase-Space Factors into

The implementation of the different phase space factors was needed in order to simulate these physics processes into the SuperNEMO environment.

The accurate expression of the half-life equation of the $2\nu\beta\beta$ decay is given in equation 4.3, where G_0, G_2, G_{22} and G_4 are the phase space factors to be implemented.

4.3.1 . Implementation

As the equation which generates the energy distribution of each factor is very complicated to implement, theoreticians (R. Dvornicki and F. Simkovic) have provided us with numerical files that contain the single energy of the two electrons along with the probability of their emission. The calculations were performed for ^{100}Mo, ^{82}Se, ^{116}Cd and ^{150}Nd. ^{82}Se is the isotope used for the detector and the rest are possible isotopes that could be used for physics studies in the future.

The implementation of the generation of the energy distributions of the four phase-space processes into the SuperNEMO software was performed.

In figures 4.4 (for G_0 process) and 4.5 (for G_2 process), we present both the generated electron energy from the SuperNEMO simulations, after implementing the theoreticians calculations (in blue), compared to the electron energies predicted by the calculations (in red).

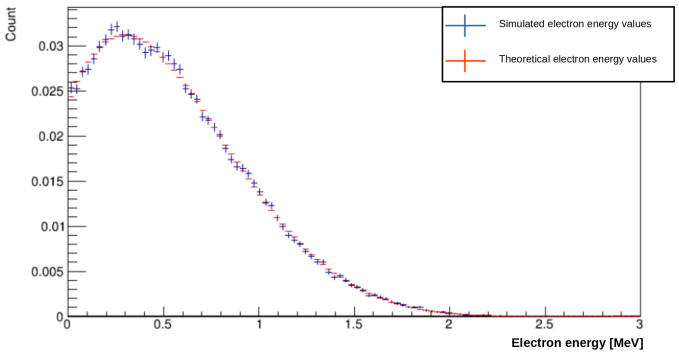

Figure 4.4 – Electron energy distribution for the G_0 process. The distribution after implementing this process into the SuperNEMO simulation (shown in blue) is compared to the results of the theoretical calculations (shown in red).

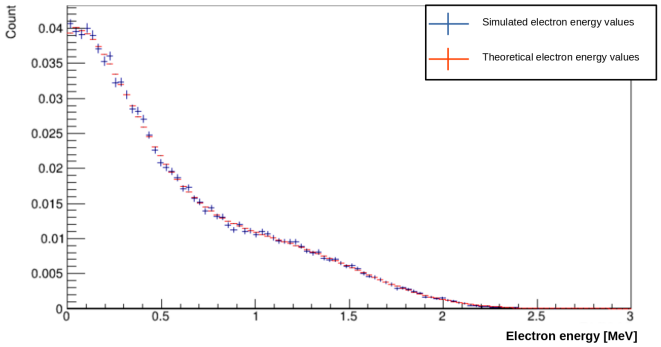

Figure 4.5 – One electron energy distribution for the G_2 process. The distribution after implementing this process into the SuperNEMO simulation (shown in blue) is compared to the results of the theoretical calculations (shown in red.

4.3.2 . Test and Validation

After simulating the energy distributions, pull distributions were calculated to check the level of agreement between the generated events and theoretical data.

Pull values of pull distributions are defined as :

$$Pull\ value = \frac{Extracted\ Value - Expected\ Value}{Error\ on\ Extracted\ Value} \tag{4.9}$$

Following from equation 4.9, the extracted values will be the values simulated in each bin of the energy distribution, whereas the expected values are the values derived from each energy bin from theoretical calculations. The pull distribution are then be fitted with a Gaussian, the fit should have a mean = 0 and the sigma = 1, any deviation in the mean means that there is a bias in the event generation and any deviation of the sigma means that there is an underestimation or overestimation of the statistical uncertainty.

Figure 4.6 shows the pull distribution of the electron energy distribution shown in figure 4.4, the distribution is then fitted with a Gaussian.

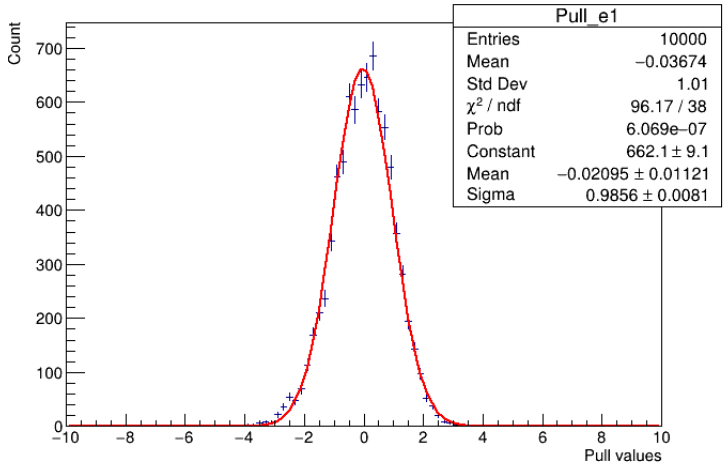

Figure 4.6 – Pull distribution of simulated energies of G0 process, fitted with a Gaussian. The ideal simulated data should have fit mean =0 and sigma = 1.

The results of the pull distributions for the 4 isotopes mentioned above, and the 4 processes, is done for simulation samples with 10^5 events. Then, the mean of the pull values (per simulations) is then taken and compared to zero, where this value represents the case of no bias in results. The same comparison is performed for the fitted sigma of the pull distribution, which is expected to be one. The comparisons are made in the form of another pull where the expected value is 0 or 1 and the extracted value is the mean and sigma values of the Gaussian fit made, respectively, the error is the error on each values from the fit.

The pull distributions were performed twice : one with the full energy distribution, and the other when rejecting energy bins with less than 30 events. The latter introduces incorrect error calculations, since by default they are considered to follow a Gaussian probability low. Figure 4.7 shows the final results, to the right when using the full distribution and to the left while cutting the tail (bins with too few statistics). The two marker colors represent the deviation of the mean of the fitted pull distribution from 0 (green) and the deviation of the sigma from 1 (blue). The division error (sigma_error) is the error on each mean and sigma values from the fit. The error bars represent the RMS of the 10 samples used. Most of the pulls fall inside a 2 σ value, which provides a good basis for simulation inside the SuperNEMO software Falaise.

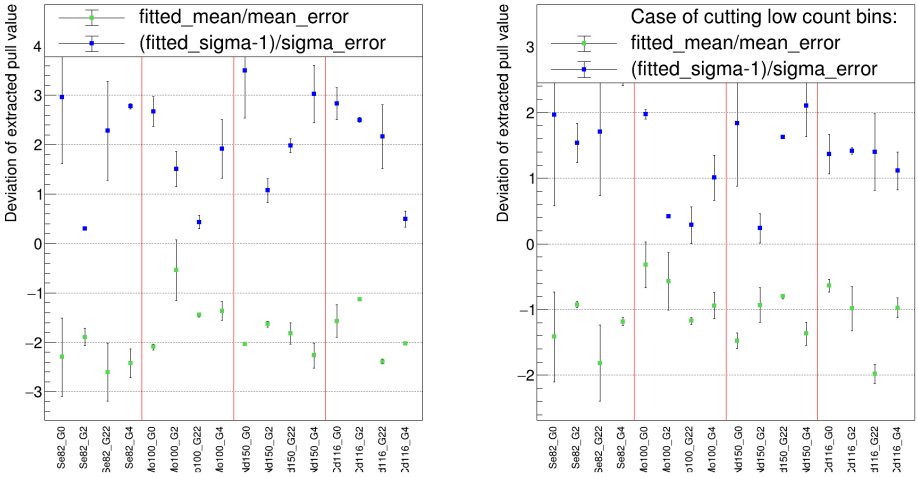

Figure 4.7 – Mean and sigma deviation from 0 and 1, respectively, for the fitted pull distribution of the simulated samples. Blue represents the deviation of the sigma from 1 and green the deviation of mean from 0. The error bars represent the RMS of the samples. To the left : Including the full energy distribution. To the right : not considering the energy bins with less than 30 events

4.3.3 . General Approach to Study the ξ_{31} Value and Find the Sensitivity

The sensitivity of SuperNEMO demonstrator to constrain the quenching was obtained using pseudo-data samples, corresponding to the expected exposure (17.5 kg.y). The first study was to determine which energy observable (minimum, maximum, single or total energies), or combination of these observables, would give the best precision with the least bias to determine the ξ_{31} value.

Then, using the best observable determined, and using the results from the theoretical calculations, we determine the sensitivity of ξ_{31} and then find the constrain that SuperNEMO sets on the quenching of the coupling constant g_A^{eff}.

4.4 . Determination of the Sensitivity of the SuperNEMO Demonstrator to the Quenching of g_A

To study the sensitivity of SuperNEMO to the different possible ξ_{31} values, pseudo-data samples were created. Different fitting procedures were applied on them to find the most discriminating method, and extract the sensitivity.

4.4.1 . Pseudo-Data Samples : Creation and Fitting Procedure

Samples corresponding to the exposure of the demonstrator, containing G_0 and G_2 processes events with and without background (internal + external) were created after simulating, reconstructing and applying selection conditions. Then, by fitting and studying the energy distributions (elaborated in 4.4.1) of selected events, we choose the most discriminant distribution to find the sensitivity.

There are 100 studied values of ξ_{31}, ranging from $\xi_{31} = 0.00$ to $\xi_{31} = 1.00$ with a step of 0.01. For each ξ_{31} value, 20 samples were made, each sample contains different, independent events (except for external background), allowing a study taking into account the statistical fluctuations of events for the considered energy distributions.

Each sample had two versions : one containing only $2\nu\beta\beta$ events from G_0 and G_2 processes, and the other contained the same events but adding background events (internal + external).

Events from the $2\nu\beta\beta$ Decay

The total expected number of events from the $2\nu\beta\beta$ decay is calculated such that :

$$N_{events} = (T_{1/2}^{2\nu})^{-1} \times M^{-1} \times ln(2) \times N_A \times m \times t \tag{4.10}$$

with the half-life of the decay is taken from the previous NEMO-3 measurment :

- $T_{1/2}^{2\nu\beta\beta} = 9.39 \times 10^{19}$ years [25]

m is the mass of the ^{82}Se isotope used and t is the exposure time of SuperNEMO :

- m = 6.23 kg
- t = 2.8 years, corresponding to the expected 17.5 kg.y exposure

This leads to an expected number of events for $2\nu\beta\beta$ decay of :

- N_{events} = 946639 events

The total number of $2\nu\beta\beta$ events can be generated by either G_0 or G_2 contributions. Defining N_0 as the number of events contributed by the G_0 process, and N_2 as the number of events contributed by the G_2 process, we can then write from equations 5.2 :

$$N_0 + N_2 = N_{events} \tag{4.11}$$

ξ_{31} is defined as :

$$\xi_{31} = \frac{N_2}{N_0} \tag{4.12}$$

And finally finding N_0 and N_2 to be :

$$N_0 = \frac{N_{events}}{1 + \xi_{31}} \tag{4.13}$$

$$N_2 = \xi_{31} \frac{N_{events}}{1 + \xi_{31}} \tag{4.14}$$

for a given value of ξ_{31}, the equations 4.13 and 4.14 fix the number of events to be simulated for each process, G_0 and G_2.

In the case where the value of $\xi_{31} = 0$, there would be no events generated by the G_2 process (HSD case).

Expected Background for the $\beta\beta$ Decay

The different backgrounds are detailed in 2.5, page 69.

External Background The external background considered come from the radioactive contamination of the PMT glass, which were measured by Germanium spectroscopy at CENBG (France) and Hamamatsu (Japan), and they are separated into the contamination introduced in the 5" PMTs and the 8" PMTs. The results are presented in table 4.1.

Isotope	Activity level [Bq]
8" PMT Glass	
^{214}Bi	141
^{208}Tl	115
^{40}K	417
5" PMT Glass	
^{214}Bi	56
^{208}Tl	9
^{40}K	123

Table 4.1 – Activities of the 8"and 5" PMT glass of the SuperNEMO demonstrator, measured by Germanium spectroscopy [61].

Internal Background Internal background is generated by the presence of contamination isotopes inside the ^{82}Se source. The activity of ^{214}Bi and ^{208}Tl were taken from the specifications of SuperNEMO [54]. As there are no measurement for the SuperNEMO sources for ^{40}K and ^{234m}Pa, the activity values were taken from the previous NEMO-3 measurements [53]. The activities and expected number of events are presented in table 4.2.

Isotope	Activity level [mBq/kg]
^{214}Bi	10×10^{-3}
^{208}Tl	2×10^{-3}
^{40}K	58.6 ± 0.1
^{234m}Pa	17.5 ± 0.1

Table 4.2 – Activities used for the sources of the SuperNEMO demonstrator. The first two activities are from the experiment specifications [54]. The other two activities come from the NEMO-3 measurements [53].

Radon Background The Radon background activity is also taken from the specifications of SuperNEMO [54], and presented in table 4.3.

Isotope	Activity level [mBq/m^3]
^{222}Rn	0.15

Table 4.3 – Expected Radon background activity from the experiment specifications [54].

Simulated Event Number

The simulation of the above mentioned backgrounds, and separately the G0 and G2 processes, was done in the SuperNEMO environment through Falaise (the experiment simulation software).

The simulation was done in the presence of a magnetic field to be able to separate electrons from positrons. Iron shielding was also added.

Table 4.4 summarizes the number of expected and simulated events, and the number of pseudo-data samples that can be created from them.

The limitation on the number of simulated events for the external background is due to the CPU time, because of the huge number of decays to be simulated.

Isotope	Expected number of disintegrations for SuperNEMO data-taking time of 2.8 years	Simulated number of disintegrations	Number of independent pseudo-data samples
External background			
8" PMT Glass			
^{214}Bi	1.24503×10^{10}	10^{10}	0.8
^{208}Tl	1.01545×10^{10}	10^{10}	0.9
^{40}K	3.68211×10^{10}	10^{10}	0.2
5" PMT Glass			
^{214}Bi	4.9448×10^{9}	10^{10}	2.0
^{208}Tl	7.947×10^{8}	4×10^{9}	5.0
^{40}K	1.08609×10^{10}	10^{10}	0.9
Internal background			
^{214}Bi	5501	1.09×10^{7}	1981
^{208}Tl	1100	1.9×10^{6}	1727
^{40}K	3.22364×10^{7}	6.8×10^{8}	21
^{234m}Pa	9.62691×10^{6}	2.5×10^{8}	26
Radon background			
^{222}Rn	202648	9.1×10^{6}	44
$2\nu\beta\beta$ Events			
G_0 , $\xi_{31} = 0$	946639	3.3×10^{7}	34
G_2 , $\xi_{31} = 0$	0	0	0
G_0 , $\xi_{31} = 1$	473320	1.9×10^{7}	40
G_2 , $\xi_{31} = 1$	473319	1.9×10^{7}	40

Table 4.4 – The expected number of disintegrations for the demonstrator exposure of 17.5 kg.year and simulated number of events for each background and for the two G_0 and G_2 processes, in the case of no G_2 process involved and in the case where ξ_{31} = 1 where the number of events for the G_0 and G_2 processes is equal. The number of independent pseudo-data samples that can be created for analysis is also given.

Event Reconstruction

The Falaise program (the collaboration simulation software) reconstructs simulated events to take into account the different physics processes that happen due to the structure of the detector (energy loss, multiple scattering, ...). The reconstructed data files are what will be used in the analysis. Figure 4.8 shows the

difference in single energy distribution between simulated and reconstructed events of G_0 and G_2 processes.

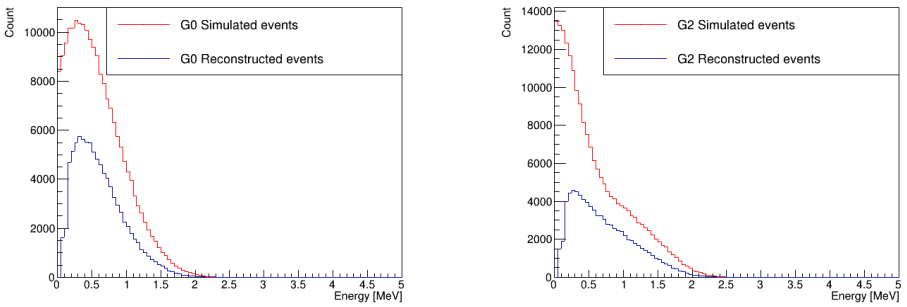

Figure 4.8 – Plots showing the single energy distribution of all simulated events before (red distribution) and after (blue distribution) energy reconstruction. To the left, the case of G_0 process. right, the case of G_2 process.

Selection Conditions

We are interested in two electron events. Selection conditions are used to select $2\nu\beta\beta$ events and reject internal, Radon and external backgrounds. The applied conditions are similar to previous analysis carried out with NEMO-3 data.

- The two electrons are selected by requiring two tracks, with associated calorimeter hits. The two tracks should have a curvature compatible with the one from an electron originating from the source foil and stopping in the calorimeter wall.

- The electron energy threshold is set to optimize the sensitivity and can vary from 100 keV to 400 keV with a 50 keV step. The standard energy threshold cut for the upcoming plots will be at **300 keV**, unless mentioned otherwise.

- The event should have exactly two calorimeter hits.

- The calorimeter hits should be associated with exactly two distinct tracks, originating from the source foil.

- The internal probability is the probability that the tracks are emitted simultaneously from the source foil, depending on the time of flight of the particles. This probability should be larger than 0.04.

- The external probability is the probability for one of the two particles in an event to have already deposited energy inside a calorimeter before traveling to the source foils and then to another calorimeter. This parameter also depends on the time of flight measurements of the particles and is required to be less than 0.01.

The two vertices should originate from the source foils :

- The x-ordinate difference between the two tracks vertices should be less than 20 mm

- The y-ordinate difference between the two tracks vertices should be less than 20 mm

- The z-ordinate difference between the two tracks vertices should be less than 40 mm

- The track length of each electron should greater than 432 mm, which is the distance between the source foils and each calorimeter walls.

- The electron tracks should have at least one hit in two first Geiger planes near the foils, and at least 2 hits in first 4 Geiger planes near the foils.

Selection Efficiency The efficiency of selection is determined by the remaining number of events after applying the selection conditions, the efficiency value is calculated as :

$$\epsilon = \frac{Number\ of\ events\ after\ applying\ selection\ conditions}{Total\ number\ of\ simulated\ number\ of\ events} \tag{4.15}$$

The error on efficiency value is defined as :

$$Efficiency\ error = \sqrt{\frac{\epsilon\ (1-\epsilon)}{Simulated\ number\ of\ events}} \tag{4.16}$$

The efficiency value of both the G_0 and G_2 processes, along with the values for internal and external background isotopes are presented in figure 4.9.

As expected, the efficiency presented in the three figures decreases with the energy cut. For G_2 process, there is a higher probability to emit low energy electrons, and hence it is more affected by these energy cuts especially when cutting above 300 keV.

For external background, after an energy cut at 300 keV, the efficiency seems to become constant.

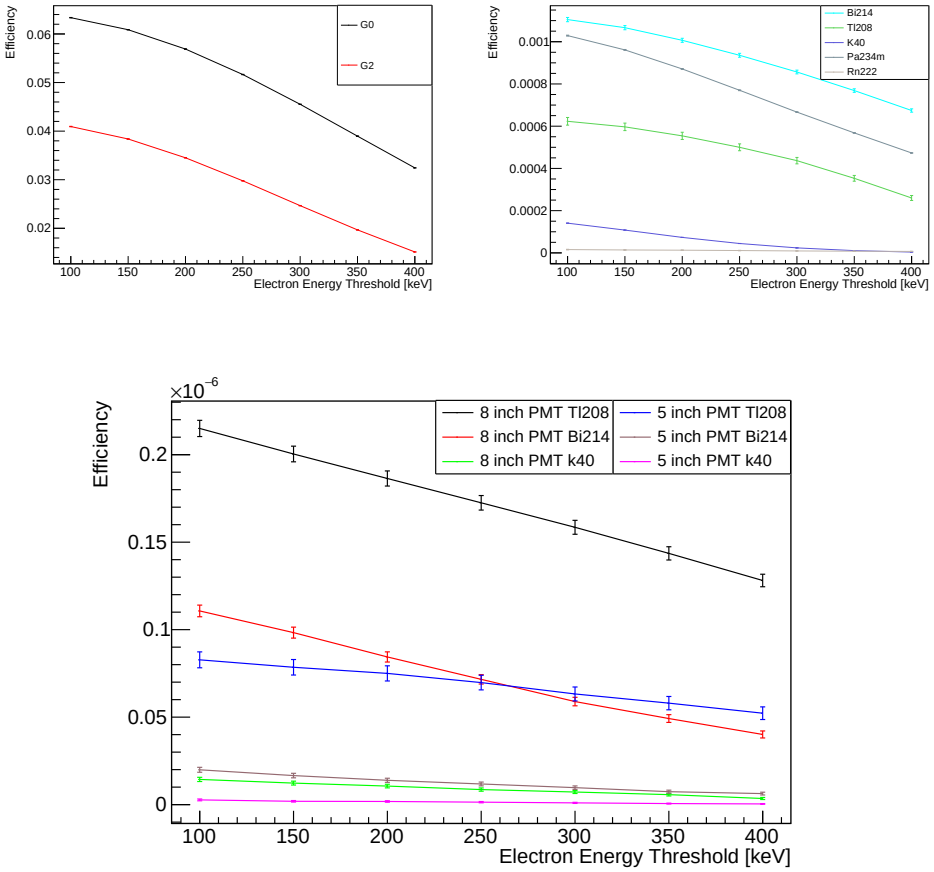

Figure 4.9 – Selection efficiency for G_0 and G_2 processes (top), internal background contamination isotopes (middle) and external background contamination isotopes (bottom), versus the energy threshold cut applied in [keV].

Pseudo-Data Sample Creation

For the G_0 and G_2 processes and internal background, the reconstructed number of events are enough to create 20 samples per process or isotope (see table 4.4). So, reconstructed events were separated into 20 samples with number of events corresponding to the exposure of the demonstrator (17.5 kg.y), and then selection conditions were applied.

For external background, as seen in table 4.4, there are not enough number of simulated events to create 20 samples. All 20 samples of the different ξ_{31} values were created with the same events for external background, where the number of events is normalized to the expected exposure time of the demonstrator at 2.8

years. Because the external events are shared across all the samples, the samples are not completely independent.

The single energy distribution of a sample is shown in figure 4.10. The input ξ_{31} is 0.37 (which corresponds to approximately the SSD value), the energy threshold cut is at 300 keV. The number of events for each isotope corresponds to the number of expected disintegrations for the demonstrator exposure, after applying selection conditions.

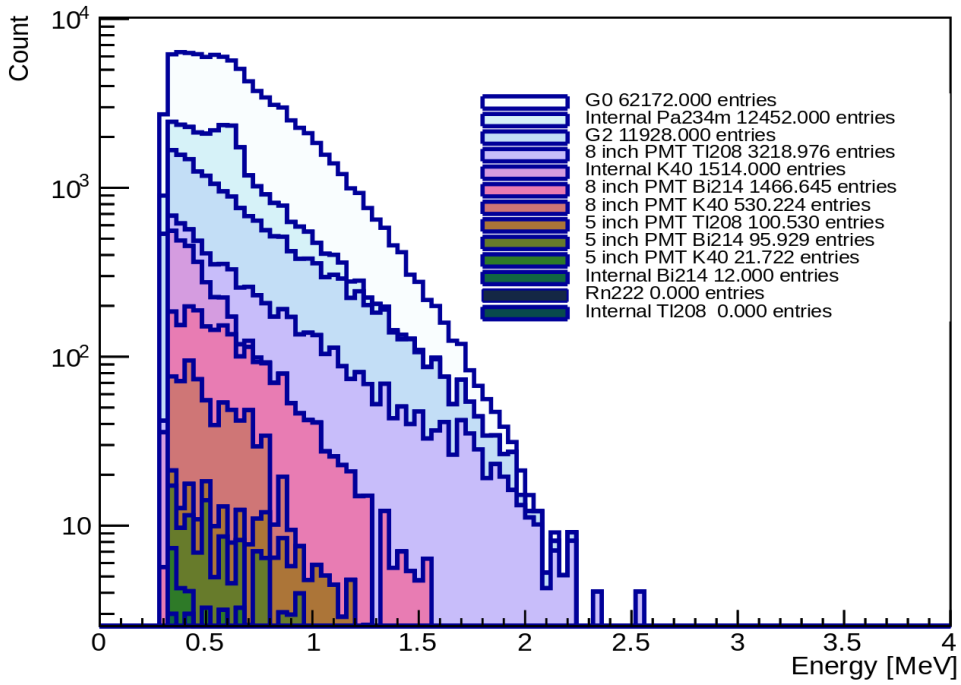

Figure 4.10 – Stacked histogram of the single energy distribution for a sample containing $2\nu\beta\beta$ events corresponding to ξ_{31} = 0.37, internal and external background events. The exposure considered for the demonstrator exposure at 17.5 keg.y. Selection conditions are applied with energy cut at 300 keV.

After applying the selection conditions, there remains no Radon and internal ^{208}Tl events. The dominating backgrounds are from internal contamination of ^{234m}Pa and ^{208}Tl from the 8" PMTs glass. A reminder is that ^{234m}Pa is taken from measurements from NEMO-3 [53] as there is no current measurement for SuperNEMO. Still, this dominance of ^{234m}Pa is expected. Also, the 8" PMT contamination with ^{208}Tl is increased by 151% compared to NEMO-3 measurements; this shouldn't pose a problem for the future $0\nu\beta\beta$ analysis since the 2.614 MeV gamma from the ^{208}Tl decay will not contribute to the region of interest of $0\nu\beta\beta$, taking into account the improvement of the calorimeter energy resolution.

After creation of samples, we begin to analyze their energy distributions to measure the amount of contribution of G_0 and G_2, and extracting ξ_{31}.

Method : Pseudo-Data Samples to extract ξ_{31}

Root Fitting Tool : RooFit

Roofit is a fitting tool implemented into ROOT, the data analysis framework made by CERN. It is a toolkit for modeling distributions of events in a physics analysis [55], it serves an easy to use but more sophisticated mathematical modeling tool to better perform analysis. It can provide probability density functions (PDF) of given binned or unbinned distributions. It also allows a summing of these PDFs in order to fit several distributions inside a single distribution.

The fitting tool provides two kinds of fitting :

- The usual fitting procedure of a distribution, which can be also done without using RooFit, I will call it in the future as "single 1D fit", where 1D represents the fact that the fitted distributions are one dimensional.

- Simultaneous fits, which are fits in which you provide a RooFit function with two (or more) distributions along side their PDFs, in such a way the PDFs depend on the same fitting parameters (one or more). RooFit will then perform the fitting of the two distributions simultaneously and converge the common fitting parameters to obtain the best value from the information of the distributions provided. This method is to be called "simultaneous 1D fit".

These two fitting procedures are going to be used and compared, to finally choose the one that is most sensitive to the different ξ_{31} values studied.

The Observables Used in the Fit

This analysis is going to use the energy observables of the two processes G_0 and G_2 as well as the ones from the backgrounds, meaning the study of :

- Single energy, i.e. made of both electron energies.
- Minimum energy, i.e the electron with lowest energy .
- Maximum energy, i.e the electron with highest energy.
- Total energy, i.e the sum of the two electron energies.

In figure 4.11, we see the minimum (minimum energy electron of the two emitted electrons), maximum (maximum energy electron), single (each electron energy is an input) and total (sum of the two electron energies) reconstructed energy distributions (no selection conditions applied), of both G_0 and G_2, normalized to their integrals. A distinguishing feature of the G_2 process is the low energy electron emission, which is more probable than that of G_0, mostly observed in minimum and single energy distributions. Total energy distribution is not a discriminating observable between the two distributions, but we still study this observable to be demonstrate the SuperNEMO capability of measuring single energy distributions.

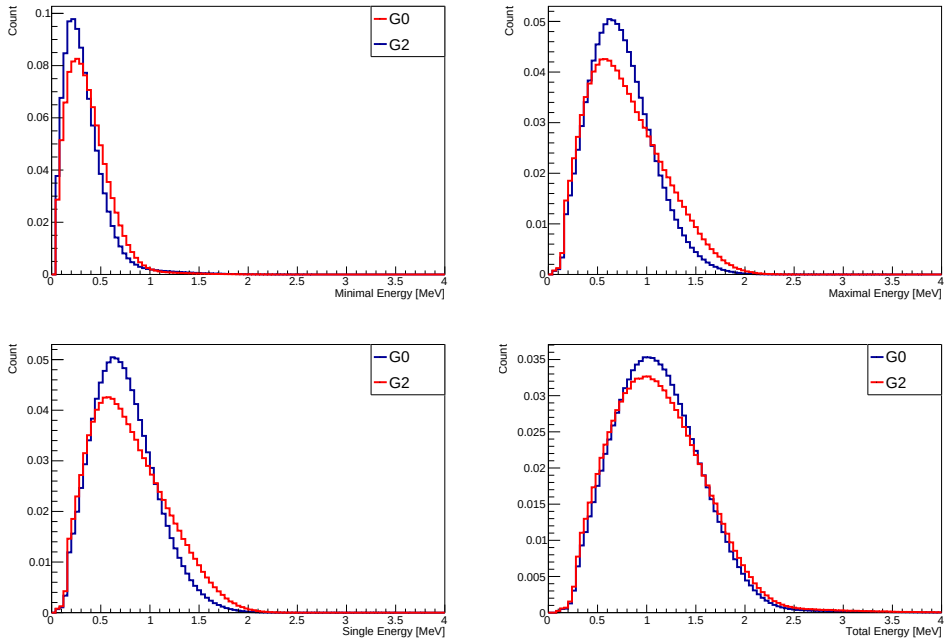

Figure 4.11 – From top left to bottom right : Reconstructed energy distribution of the two $2\nu\beta\beta$ processes G_0 and G_2 for the minimum, single, maximum, total energies. The distributions have been normalized to their integrals to better see their shape differences. No selection conditions applied.

Fitting Procedure : G_0, G_2 Processes and Background PDFs

RooFit is provided with the full number of reconstructed events, after applying selection conditions, in the form of binned energy distribution (i.e a histogram). Roofit then extracts the PDF of each supplied histogram.

Unfortunately, RooFit had a bug in the PDF extraction procedure for binned data, which was not stated in the documentation. The bug was corrected in a new function used specifically in this situation, the function is **RooBinSamplingPDF()**. But eventually, it was corrected for this work.

The PDF of each G_0, G_2 and background is presented in figure 4.12

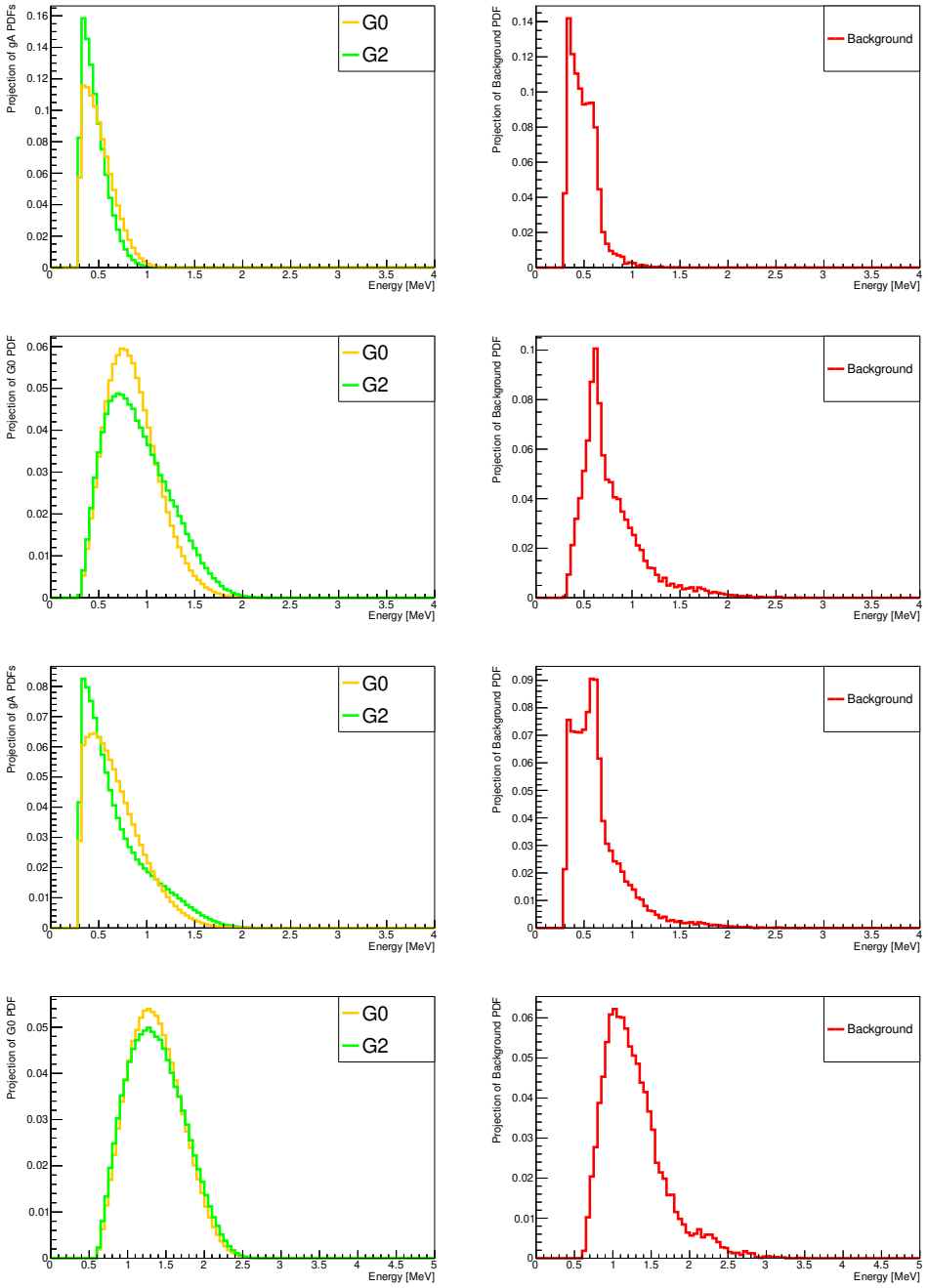

Figure 4.12 – Extracted PDF of G_0, G_2 and background for minimum, maximum, single and total energy distributions, from top to bottom. The energy threshold applied is 300 keV.

We provide the G_0 and G2 PDFs to RooFit, and if the sample contains background, and if needed, we add the background PDF using the function **RooAddPdf()**. In the case of adding only 2 PDFs (background is subtracted, only G_0 and G_2 contri-

bute), the resulting PDF will depend on only one fitting parameter. In the case of adding the 3 PDFs (background is included in the fitting procedure), the resulting PDF will then depend on 2 fitting parameters.

RooFit Fitting Options

Several options were set in the fitting function :

- **Minos(true)** : This option is designed to have a more accurate calculation of the error. It's also designed to have correct calculations in the case where there is a non-parabolic chi-square. A summary on the advantage of using Minos can be found in [57]

- **IntegrateBins(1)** : Improves accuracy for binned fits by integrating the PDF over bins.

- **Range()** : Ranges were set for every energy distribution studied (minimal, maximum, single, total), they were chosen to decrease the bias created in the fits.

Pseudo-Data sample Fitting

The binned data of a sample with a specific input ξ_{31} value is provided to RooFit, along with the PDFs of G_0, G_2 and the background (if the sample includes the background). We are then able to extract the contribution of each PDF component from the sample provided, see figure 4.13.

In case of one parameter fitting, we retrieve the contribution of G_2 in the sample along with the error on this contribution. The contribution of G_0 will then be *(1 - contribution of G_2)* and the error on it will be calculated using propagation of error where :

If the function f is dependent on two parameters A and B such that :

$$f(A, B) = aA + bB \tag{4.17}$$

where "a" and "b" are two numbers, then the error on the function f(A,B) is calculated as :

$$\sigma_f^2 = a^2\sigma_A^2 + b^2\sigma_B^2 + 2ab\rho_{AB}\sigma_A\sigma_B \tag{4.18}$$

where σ_A and σ_B are the error on the two parameters A and B, respectively. ρ_{AB} is the correlation between the two parameters. If the parameters are fully correlated, anti-correlated or uncorrelated then ρ_{AB} = 1, -1 or 0, respectively. This coefficient is taken from the calculations of roofit of correlation matrix and embedded into error calculations.

Then, the ξ_{31} value is calculated as :

$$\xi_{31} = \frac{G_2\, contribution}{G_0 contribution} \times \frac{G_0\, selection\, efficiency}{G_2\, selection\, efficiency} \tag{4.19}$$

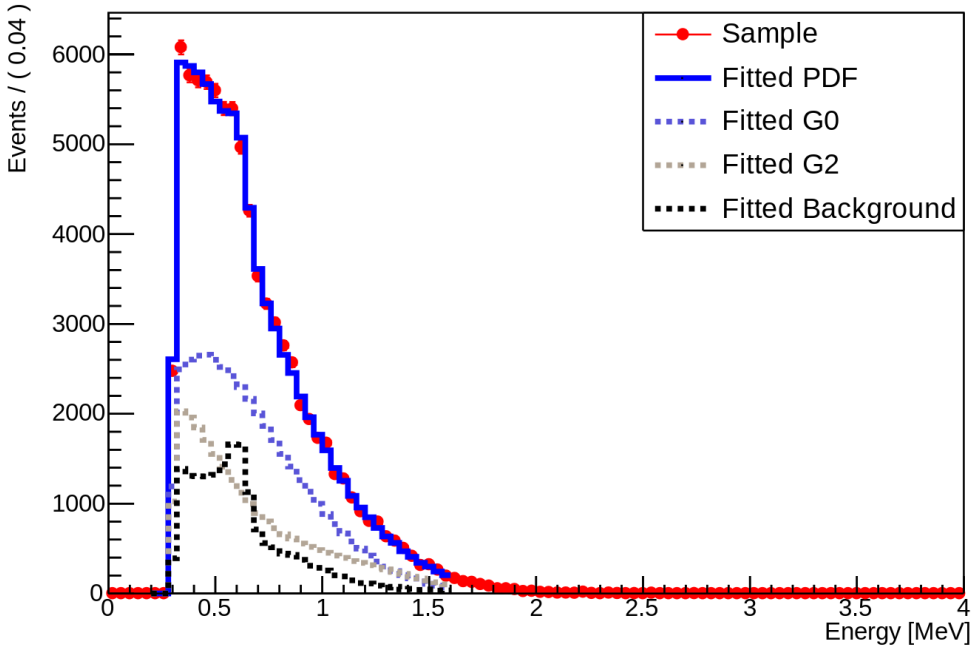

Figure 4.13 – Extracted PDF of G_0, G_2 and background single energy distributions of a sample chosen with ξ_{31} = 0.37. The fit is performed inside a chosen range where we exclude low count bins. The energy threshold applied is 300 keV.

Background Fitting Method Two methods were tested in the process of fitting samples with background : background subtraction and including background into the fitting PDF.

- **Background Subtraction :** It is done by subtracting the background contribution from the sample using the full statistics of the background normalized to the exposure (17.5 kg.y). The use of full statistics allows to reduce statistical fluctuations.

- **Including Background in the Fitting PDF :** The background energy distribution, normalized to the full reconstructed events statistics after applying selection conditions, is used as an additional PDF, after the PDF of G_0 and G_2.

4.4.2 . Determining the Best Observable(s) to Optimize the Sensitivity

As mentioned before, for each value of ξ_{31} 20 samples of nearly independent events were produced. To find a final contribution of the two processes. I perform a weighted average (see equation 4.20) on the extracted ξ_{31} value from each samples, after it passes a condition that the χ^2/(number of degrees of freedom (NDF)) of the fit should be less than 5. The errors were calculated as in equation 4.21. Where in equations 4.20 and 4.21, x_i represent the extracted value from each

sample where i<21, and σ_i is the error on the extracted value.

$$\bar{x} = \frac{\sum_{i=1}^{n} \frac{x_i}{\sigma_i^2}}{\sum_{i=1}^{n} \frac{1}{\sigma_i^2}} \tag{4.20}$$

$$\sigma_{\bar{x}} = \sqrt{\frac{1}{\sum_{i=1}^{n} \sigma_i^{-2}}} \tag{4.21}$$

It is to be noted that the contribution of each process is bounded, between a minimal value which is zero and a maximal value which 1 (100%), respectively. The values cannot exceed these two limits, hence a bias can be created near them.

In the following analysis I introduce two kinds of plots :

- The result of the weighted average extracted value of ξ_{31} versus the input ξ_{31} (the value which was initially input to create the samples). A violet straight line is added which represents the case if the extracted values were exactly equal to the input ξ_{31} values. The error bars represent the error on the weighted average extracted ξ_{31} values.

- The pull values (defined in equation 4.9) for each individual extracted ξ_{31} value is presented. These values are fitted for each observable with a Gaussian. In the case this fit succeeds, the mean and sigma will give an idea of how much the results correspond to reality : a mean at 0 and sigma of 1 would be the ideal case. The deviation of the fitted mean from 0 would mean that the results are biased, and for sigma (from 1) would mean that there is an underestimation or overestimation of the errors calculated. By finding the mean of the pull of the 20 fitted samples, I plot the final pulls to show the results for all the energy cuts.

Fitting the Distribution of One Observable

We start first by using the usual single 1D fits, with only one observable. I apply the fits for two sets of samples : with and without background. I also study the effect of applying a fitting range on the bias. The default energy threshold cut applied on the plots shown and detailed is at 300 keV, later on I will show the final results for all the energy cuts to be able to find the best sensitivity.

Single 1D Fitting : Samples without Background and without Fitting Range Applied As a start, I have worked with samples that contain only G_0 and G_2 events, as to see how the fitting process would act. As mentioned before, the samples are created and then we fit them using the PDF of both G_0 and G_2. I then extract the contribution of each process.

First, I check the results of the fit of the 20 samples created for a ξ_{31} value, which I choose to be $\xi_{31} = 0.37$. The one dimensional (1D) distributions of the extracted ξ_{31} values, error on the extracted value, the χ^2/NDF and pull values of the fit are presented in figures 4.14, 4.15 and 4.16 and 4.17 respectively.

In figure 4.14, we see the spread of the results of ξ_{31} of each sample. this spread is most notably observed for total energy fits. For minimum energy we observe a spread, but most results are concentrated in the region around the input ξ_{31}.

Looking at figure 4.16 the χ^2/NDF in most cases are well around, or less than 1. Like for the case of minimum energy, where there is a slight overestimation of the errors.

For figure 4.17, due to the low number of statistics (20 samples), we are not able to perform a Gaussian fit of the pull values. For this reason, I plot the 2020 samples (20 samples for each input ξ_{31} value $\times$ 101 input ξ_{31} values), for minimum energy they are near zero (mean = 0.126) and the standard deviation is 1.053. For total energy, we observe a very large bias at mean = 2.48.

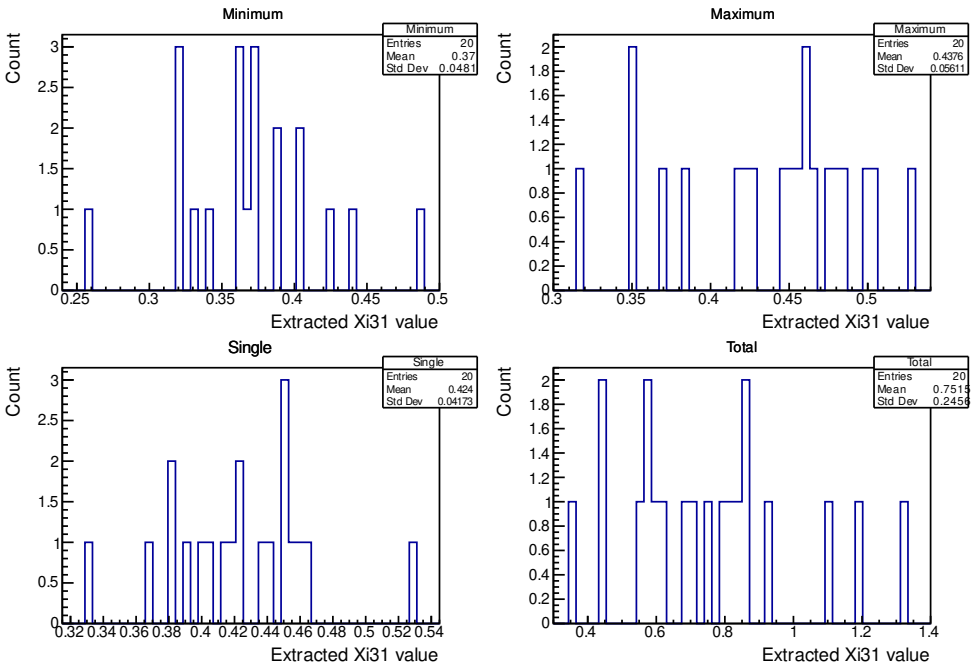

Figure 4.14 – Extracted ξ_{31} values from the fitted samples that passed the χ^2/NDF < 5 condition, with an input ξ_{31} = 0.37. Samples with **only G_0 and G_2**.

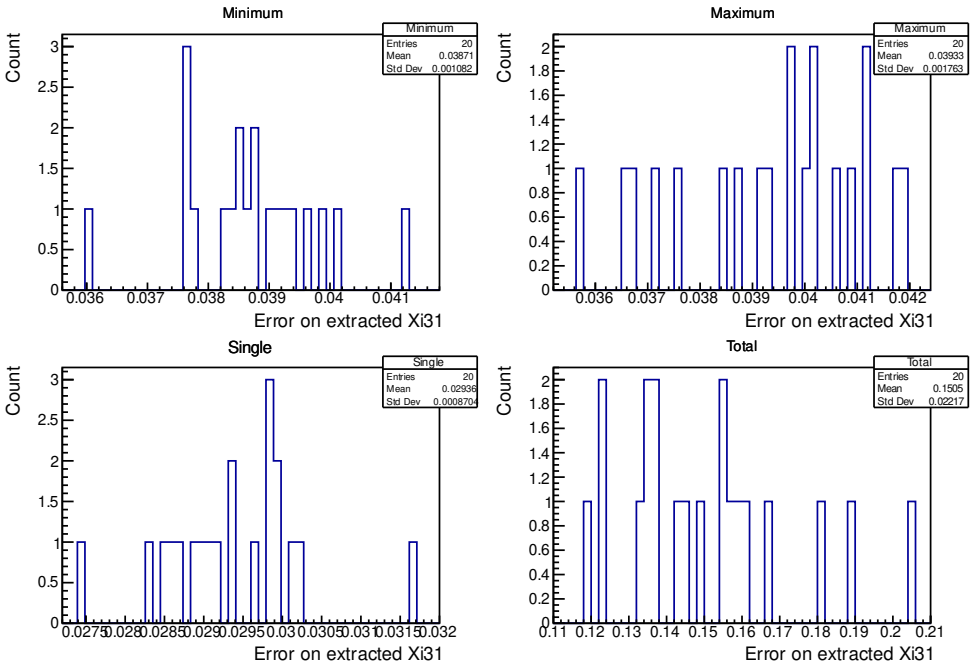

Figure 4.15 – Error on extracted ξ_{31} values from the fitted samples that passed the χ^2/NDF < 5 condition, with an input ξ_{31} = 0.37. Samples with **only G_0 and G_2**.

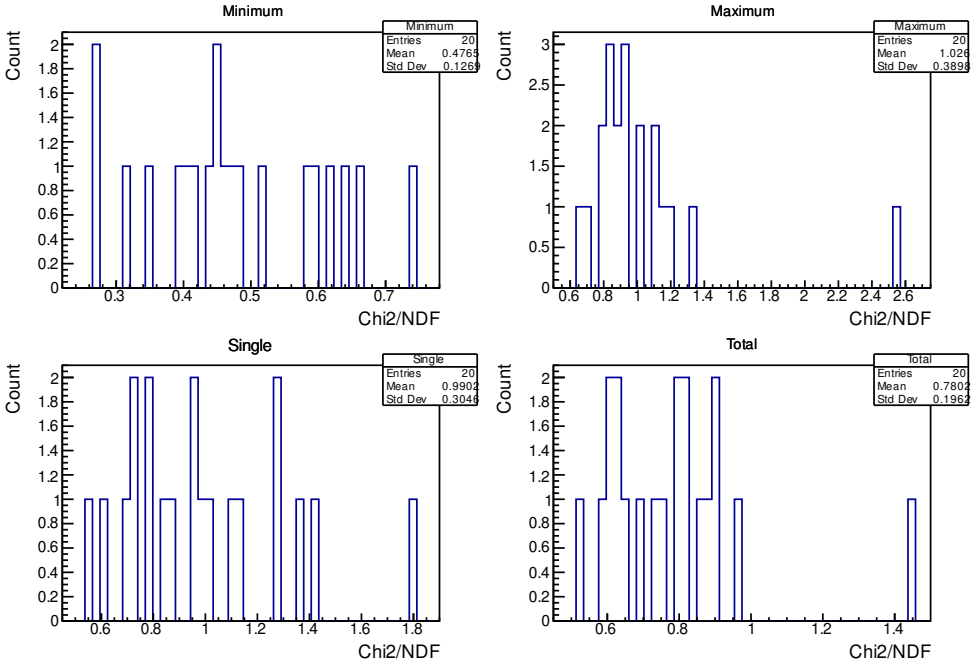

Figure 4.16 – The χ^2/NDF values of the fitter samples with an input ξ_{31} = 0.37. Samples with **only G_0 and G_2**.

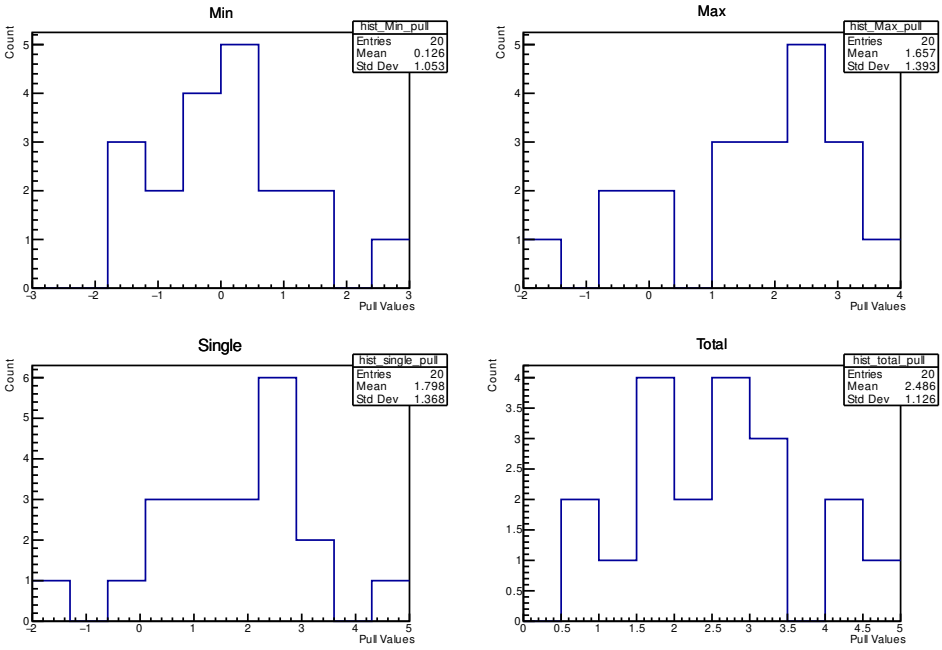

Figure 4.17 – The pull values of the fitted samples with an input ξ_{31} = 0.37, where pull = (extracted ξ_{31} - input ξ_{31})/error. Samples with **only G_0 and G_2**.

The results are plotted in figures 4.18 and 4.19. For minimum energy results, one can observe an insignificant bias from the input values where the pull mean is at 0.05 and the sigma is 1.13, taken from the pull distribution. To the left, we see the weighted average of the 20 samples, where a slight positive bias is observed at very low input ξ_{31} values (< 0.05). These biases can be explained by the fact that the fit doesn't allow negative contributions of the fitting PDFs.

For maximum energy, one can observe a large bias of the values, which are larger than the input values that are not included inside the error bars. As for the pull the mean quantize the bias with 1.77. We observe a similar behavior for single energy fit results.

A very large bias is observed for total energy fit results, and the notably larger error bars are associated to the fact that the total energy distribution of G_0 and G_2 are very similar as seen in 4.11, page 147, hence there is a larger range of values that the fit could take for the contribution of each process, so it enlarges the error bars to take into account all these possibilities.

These biases can be understood from the energy distributions shapes. For minimum energy, G_2 emphasizes itself better at lower energy and hence a good discrimination can be established, similarly for single and maximum energies where some discrimination can be established at the tail. For maximum energy there is an alignment of the peaks of the two distributions, which could confuse the fitting

procedure. These reasons **may** give an idea of why there are biases, but they explain more the behavior of the error bars.

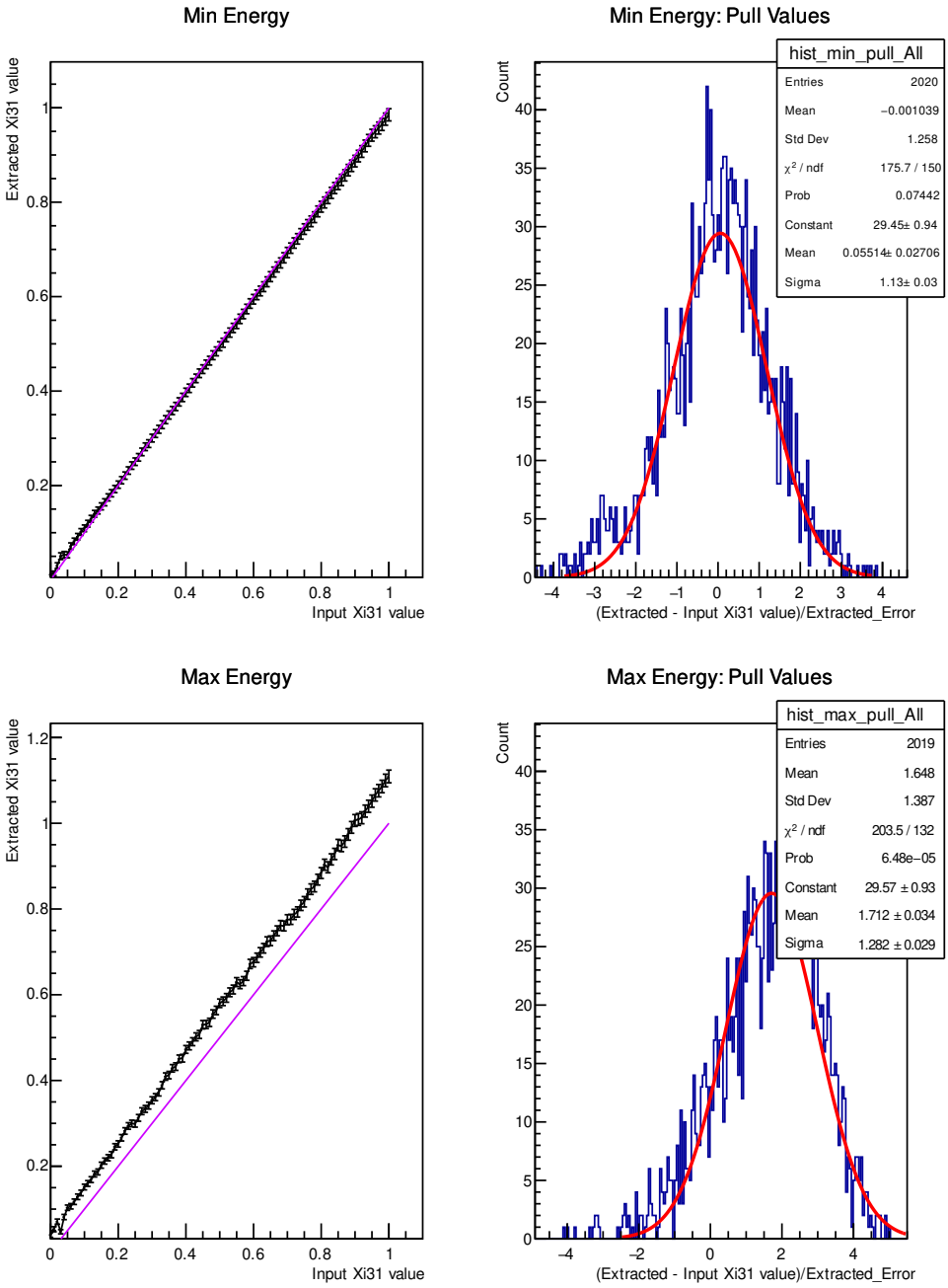

Figure 4.18 – Results of the fits of samples with **only G_0 and G_2**. To the left : Results of the average extracted ξ_{31} values (of 20 fitted samples) versus the input ξ_{31}. The error bars represent the error on the average extracted values. The violet line represents the case if these values are identical to the input values. To the right : pull distribution of the extracted results (i.e each point presents the mean of the pull of the 20 samples), fitted with a Gaussian, where the mean and sigma would represent the correctness of the fit. To the top, results of the fits of the minimum energy ; to the bottom for the maximum energy. Energy threshold cut at 300 keV.

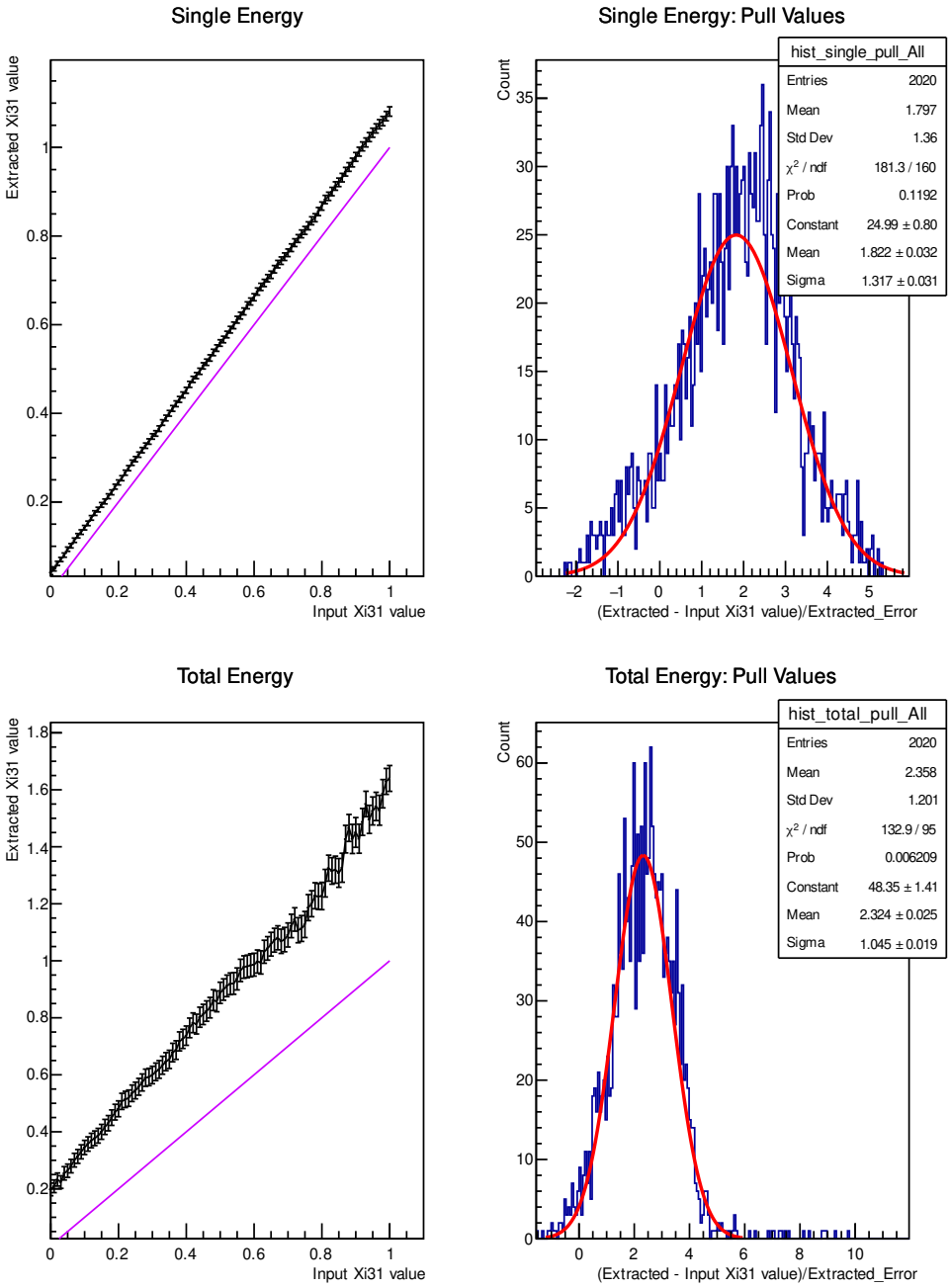

Figure 4.19 – Results of the fits of samples with **only G_0 and G_2**. To the left : Results of the average extracted ξ_{31} values (of 20 fitted samples) versus the input ξ_{31}. The error bars represent the error on the average extracted values. The violet line represents the case if these values are identical to the input values. To the right : pull distribution of the extracted results (i.e each point presents the mean of the pull of the 20 samples), fitted with a Gaussian, where the mean and sigma would represent the correctness of the fit. To the top, results of the fits of the single energy; to the bottom for the total energy. Energy threshold cut at 300 keV.

I will now introduce a fit range to see its effect on the bias and results.

Effect of Choosing a Fitting Range on the Bias The fitting range used for each distribution is chosen after trying several intervals. The best interval that gave the least bias is then chosen for the analysis. The reference energy threshold cut used when choosing these ranges is 300 keV, these ranges are then applied to all energy threshold cuts. The chosen ranges are shown in figure 4.20 and table 4.5.

Observable	Energy Fit Range
Minimum energy	[Energy Threshold - 100 keV , 1 MeV]
Single energy	[Energy Threshold - 100 keV , 1.6 MeV]
Maximum energy	[Energy Threshold - 100 keV , 2 MeV]
Total energy	[2*Energy Threshold + 100 keV , 1.7 MeV]

Table 4.5 – The ranges chosen to perform the fitting of each sample to extract the least biased results. "Energy threshold" represents the energy threshold cut applied to the distribution.

If one compares these ranges to the energy distributions in figure 4.11 page 147, one would especially see that for total energy distribution, the range with least bias avoids the areas where the two G_0 and G_2 distributions are least discriminant from each other. For the other ranges, they avoid low count bins, which would enhance the error calculations.

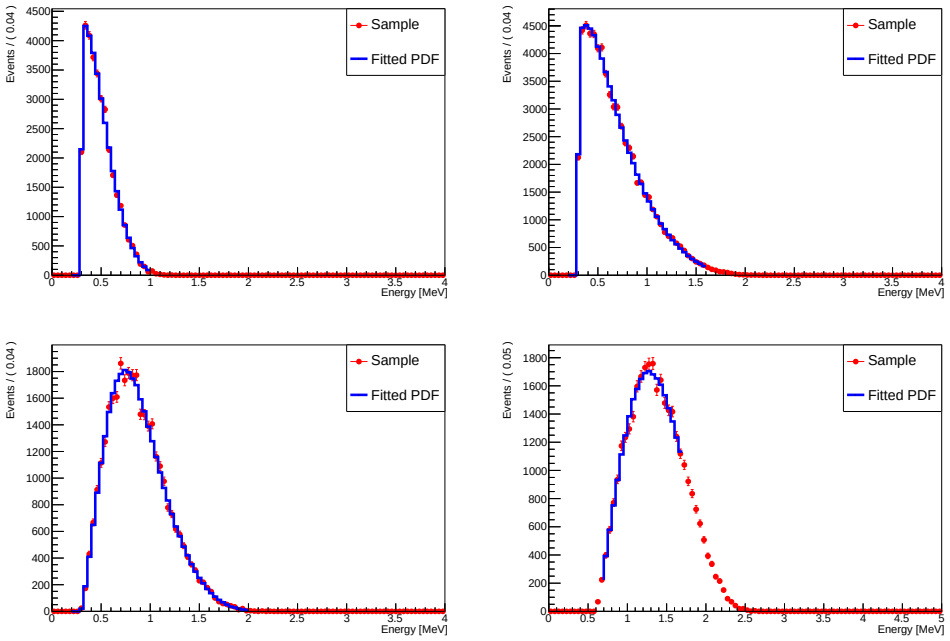

Figure 4.20 – Plots showing the fitting ranges of the PDF (highlighted in blue) for minimum (top left), single (top right), maximum (bottom left) and total (bottom right) energy distributions. The red distribution represents the distribution of a particular sample with only G_0 and G_2, the blue distribution is the fitted PDF (G_0 and G_2) in the chosen range.

Single 1D Fitting : Samples without Background and with Fitting Range Applied The fitting range applied can affect the bias observed in the results. So we apply the ranges specified in table 4.5 and check again our final results.

Similarly to above, I introduce the behavior of the 20 samples with $\xi_{31} = 0.37$. The 1D distributions of the extracted ξ_{31} values, error on the extracted value, the χ^2/NDF and pull values of the fit, are presented in figures 4.14, 4.15, 4.16 and 4.24, respectively.

For the results in figure 4.21, we see an improvement in the total energy extracted ξ_{31} values, where they now move to lower values. And looking at the pull distribution in 4.24, we see an improvement in the mean of the plot for total (from 2.32 to 0.02) energy fits.

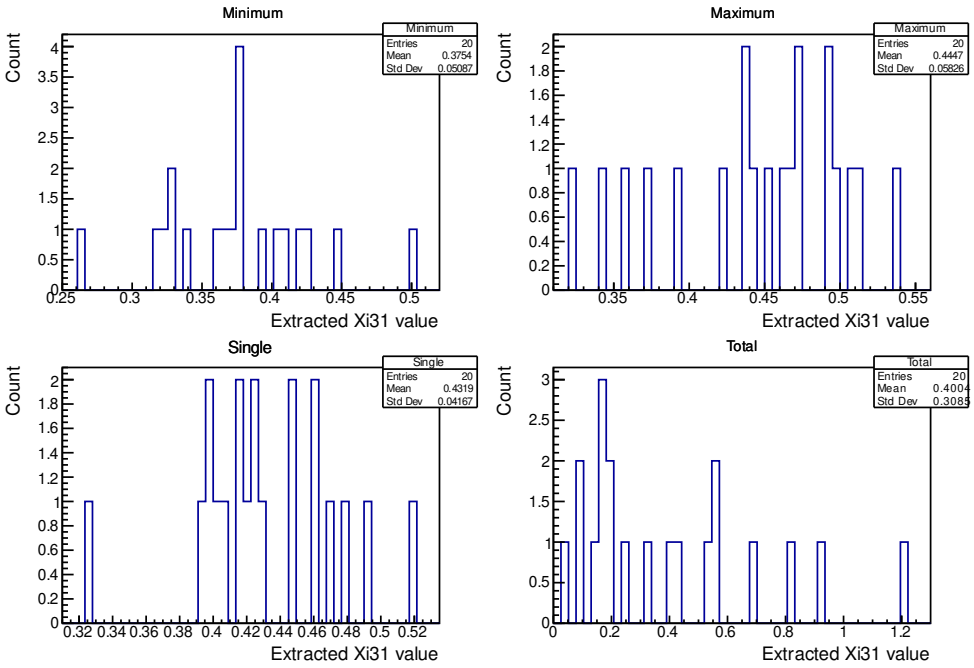

Figure 4.21 – Extracted ξ_{31} values from the fitted samples that passed the χ^2/NDF < 5 condition, with an input ξ_{31} = 0.37. **Fitting range is applied**.

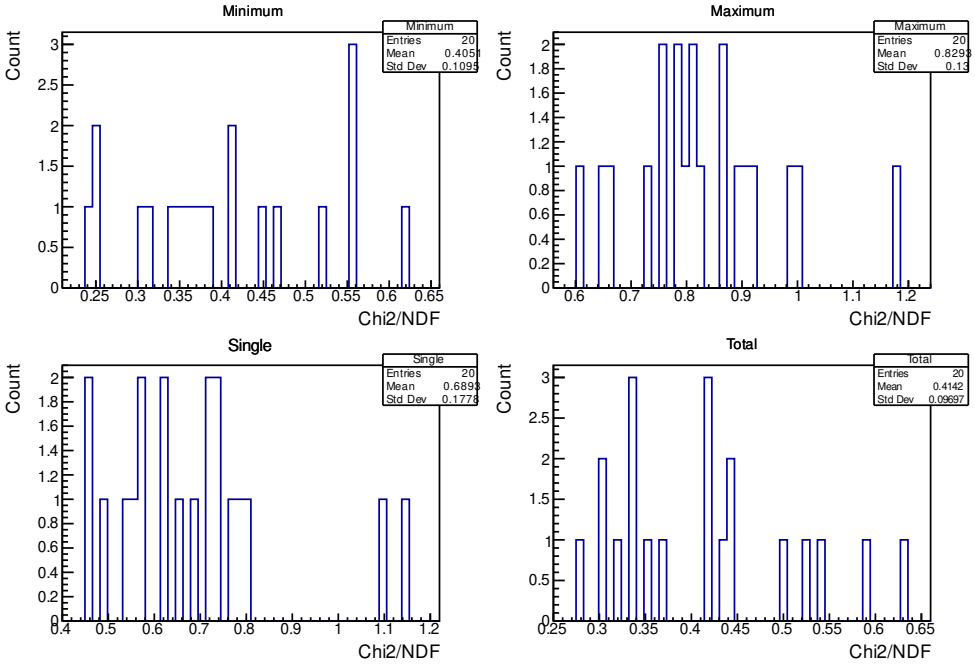

Figure 4.23 – The χ^2 values of the fitted samples with an input ξ_{31} = 0.37. **Fitting range is applied**.

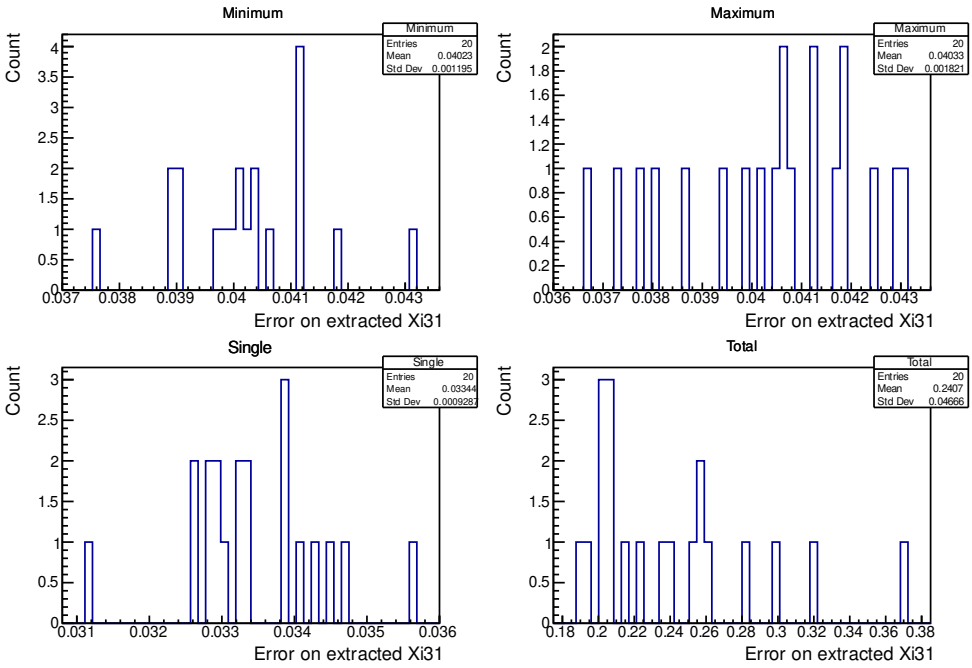

Figure 4.22 – Error on extracted ξ_{31} values from the fitted samples that passed the χ^2/NDF < 5 condition, with an input ξ_{31} = 0.37. **Fitting range is applied**.

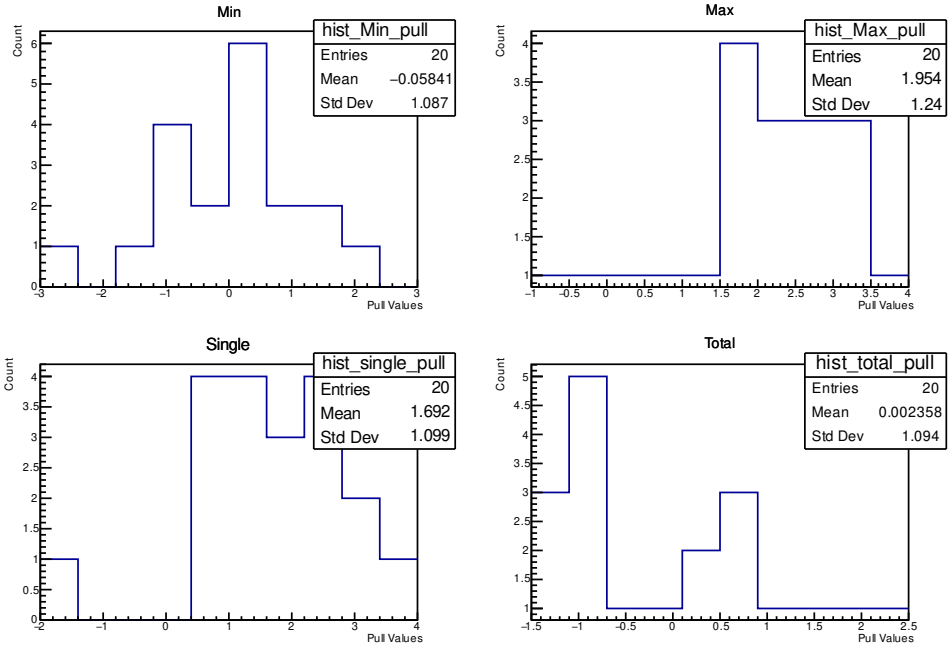

Figure 4.24 – The pull values of the fitted samples with an input ξ_{31} = 0.37. **Fitting range is applied**.

We observe a decrease in the bias notably for the results of total energy fits, where the pulls decrease from 2.32 $\pm$ 1.04 (figure 4.19) to 0.02 (pull mean) $\pm$ 1.04 (pull sigma) (figure 4.26). Also now, we observe more significantly the effect of constraining the contribution of both processes to be larger than (or equal to) zero, where a significant positive bias appears for low input ξ_{31} (<0.3) and a negative bias for large values (>0.5). A table summarizes the differences between the different methods and observables is presented in table 4.6.

Fitted energy spectra	Mean of Pull	Sigma of Pull	Comment
No Fitting Range			
Minimum	0.05 ± 0.02	1.13 ± 0.03	
Maximum	1.71 ± 0.03	1.28 ± 0.02	
Single	1.82 ± 0.03	1.31 ± 0.03	
Total	2.32 ± 0.02	1.04 ± 0.02	
Fitting Range Applied			
Minimum	0.20 ± 0.03	1.17 ± 0.03	
Maximum	1.97 ± 0.03	1.26 ± 0.03	
Single	1.87 ± 0.03	1.30 ± 0.03	
Total	0.02 ± 0.03	1.04 ± 0.02	Large bias

Table 4.6 – The different Pull distribution "mean" and "sigma" obtained using different fitted energy spectra of sample with only G_0 and G_2, with, and without, applying a fitting range in the fitting process.

Looking at figures 4.25 and 4.26, for minimum energy there is an improvement in the bias at large input ξ_{31}, but an increase of it at the low values (ξ_{31} input $<$ 0.05). While for maximum and single energy results, we don't have a noticeable change.

From here on, these energy ranges will be applied to all the fits that are going to be shown, unless mentioned otherwise.

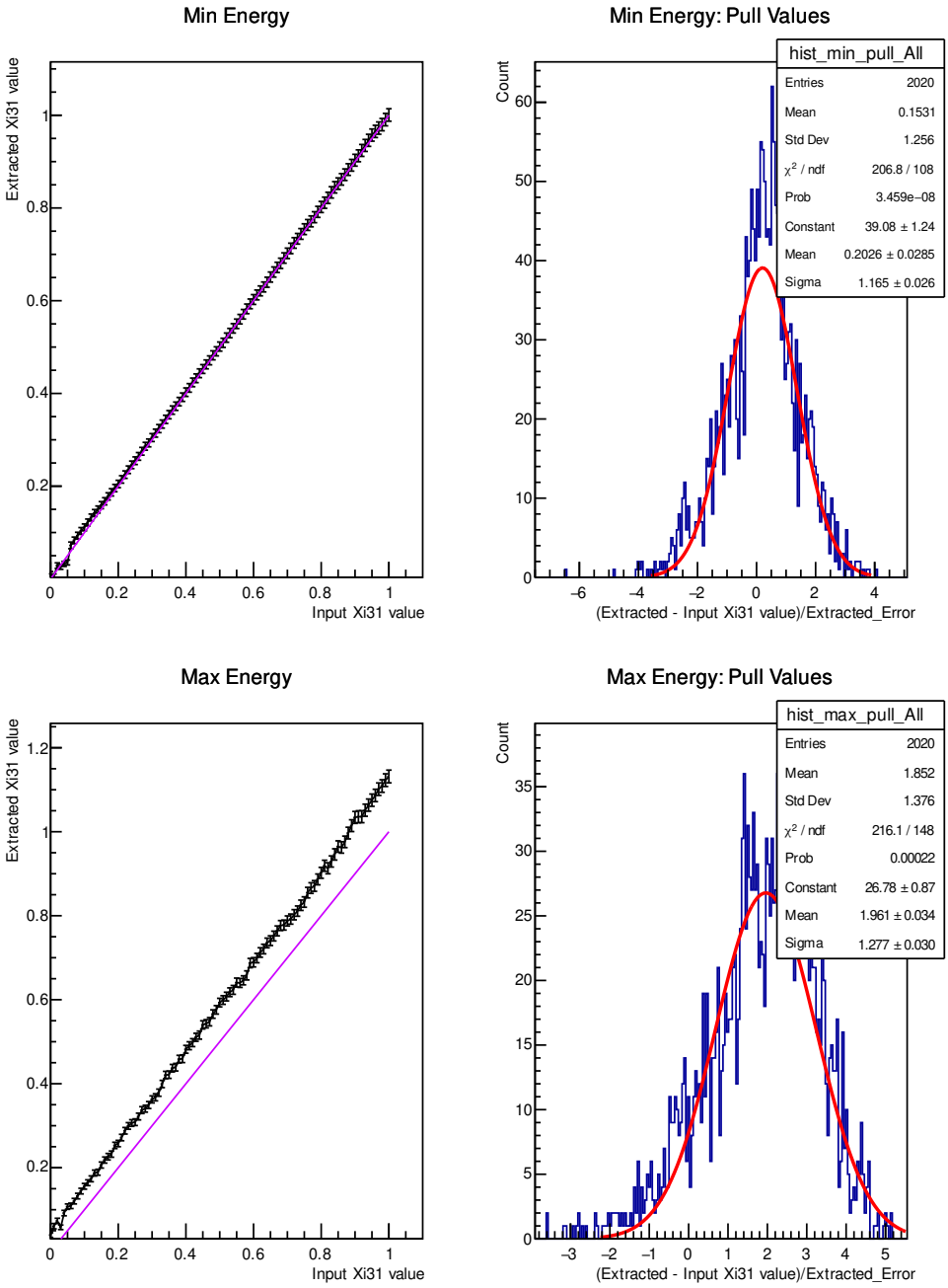

Figure 4.25 – Results of the fits of the samples with **only G_0 and G_2, applying a fitting range** according to table 4.5. To the left : Results of the average extracted ξ_{31} values (of 20 fitted samples) versus the input ξ_{31}. The error bars represent the error on the average extracted values. The violet line represents the case if the extracted values are identical to the input values. To the right : The pull distribution of the extracted results (i.e each point presents the mean of the pull of the 20 samples), fitted with a Gaussian, where the mean and sigma would represent the correctness of the fit. To the top, results of the fits of minimum energy; to the bottom for maximum energy. Energy threshold cut at 300 keV.

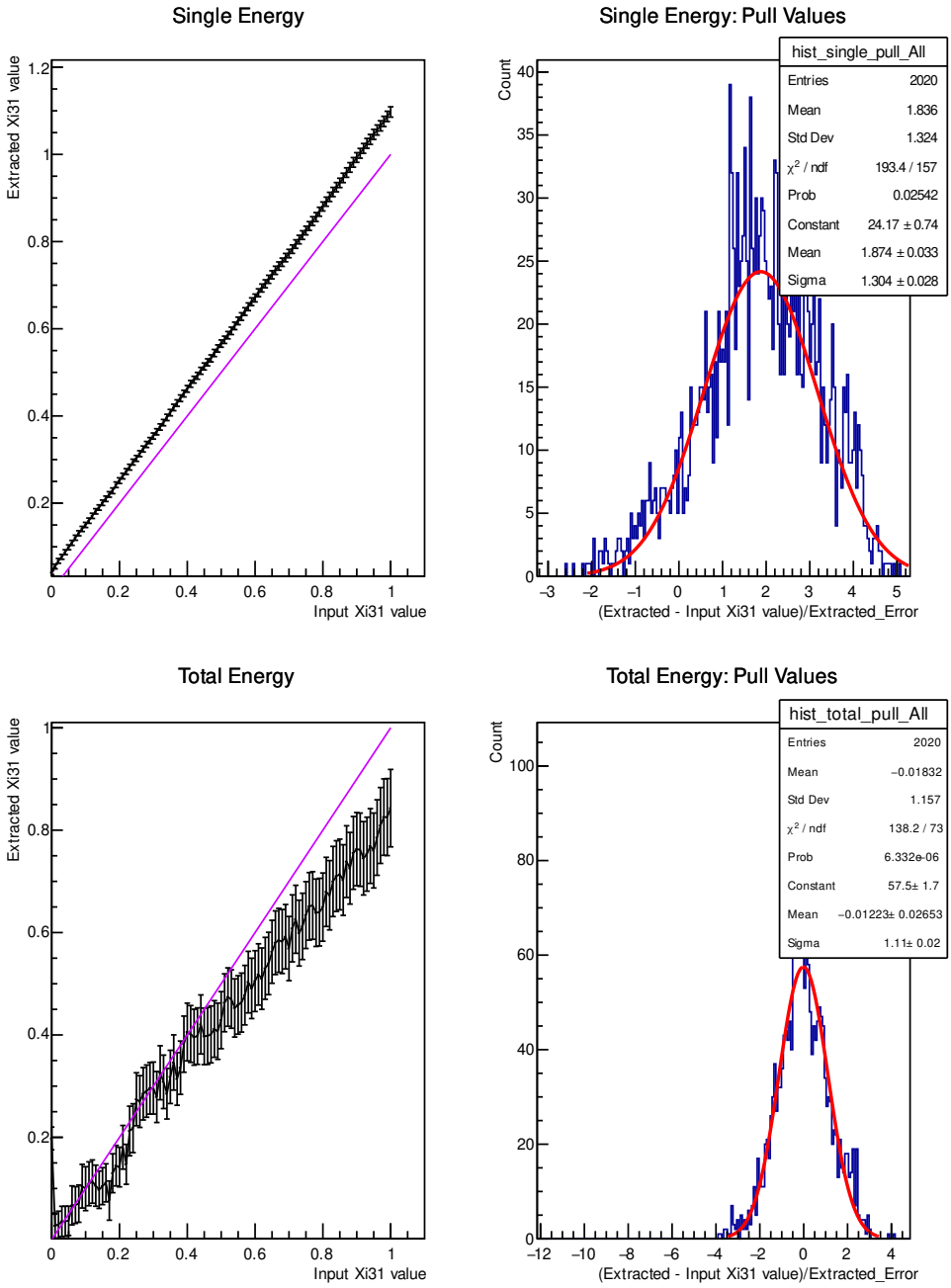

Figure 4.26 – Results of the fits of the samples with **only G_0 and G_2, applying a fitting range** according to table 4.5. To the left : Results of the average extracted ξ_{31} values (of 20 fitted samples) versus the input ξ_{31}. The error bars represent the error on the average extracted values. The violet line represents the case if the extracted values are identical to the input values. To the right : The pull distribution of the extracted results (i.e each point presents the mean of the pull of the 20 samples), fitted with a Gaussian, where the mean and sigma would represent the correctness of the fit. To the top, results of the fits of single energy; to the bottom for total energy. Energy threshold cut at 300 keV.

Single 1D Fitting : Samples with Background After understanding the distributions and fitting process, to better describe reality I now add the background components into the same samples as before. As mentioned in 4.4.1, page 144, every sample contains the same external background events. While the internal background has different independent events for each sample.

I study the samples using the two methods described before in 4.4.1, page 150.

- **Background Subtraction**

In this method I subtract the background from the samples and then perform the fit using only G_0 and G_2 PDFs.

First I show in figures 4.27 and 4.28 a 1D distribution of the extracted ξ_{31} values for input of 0.37 and their errors. It is expected for total energy to have a larger spread of the results. In figure 4.29, the 1D distribution of the χ^2/NDF of the fitted samples; these values are either around 1 or a bit less, where it signifies that there is an overestimation of the errors.

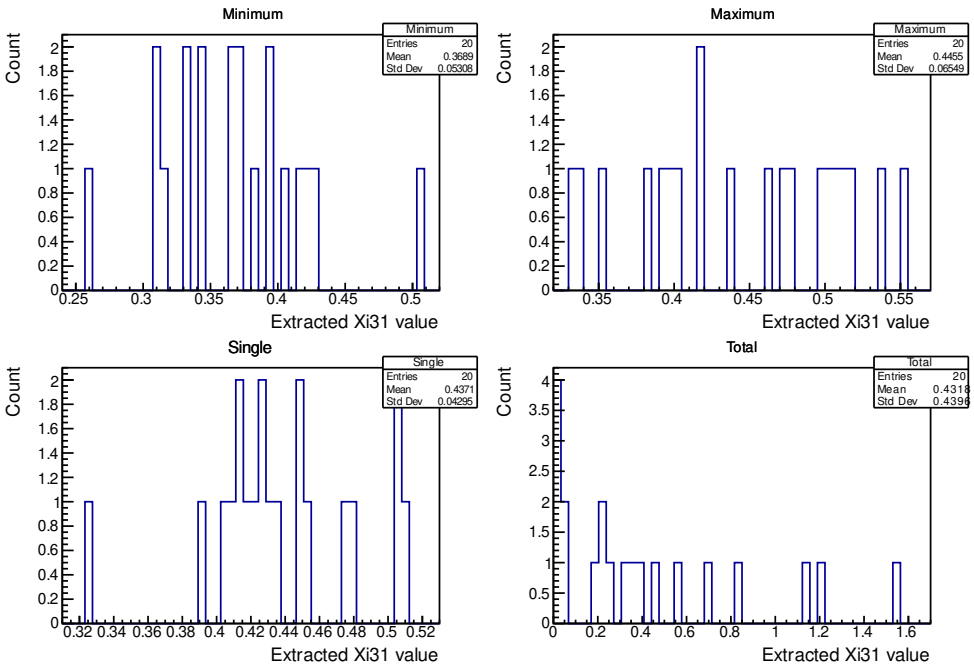

Figure 4.27 – Extracted ξ_{31} values from the fitted samples that passed the χ^2/NDF < 5 condition, with an input ξ_{31} = 0.37. Single observable fit while subtracting the background.

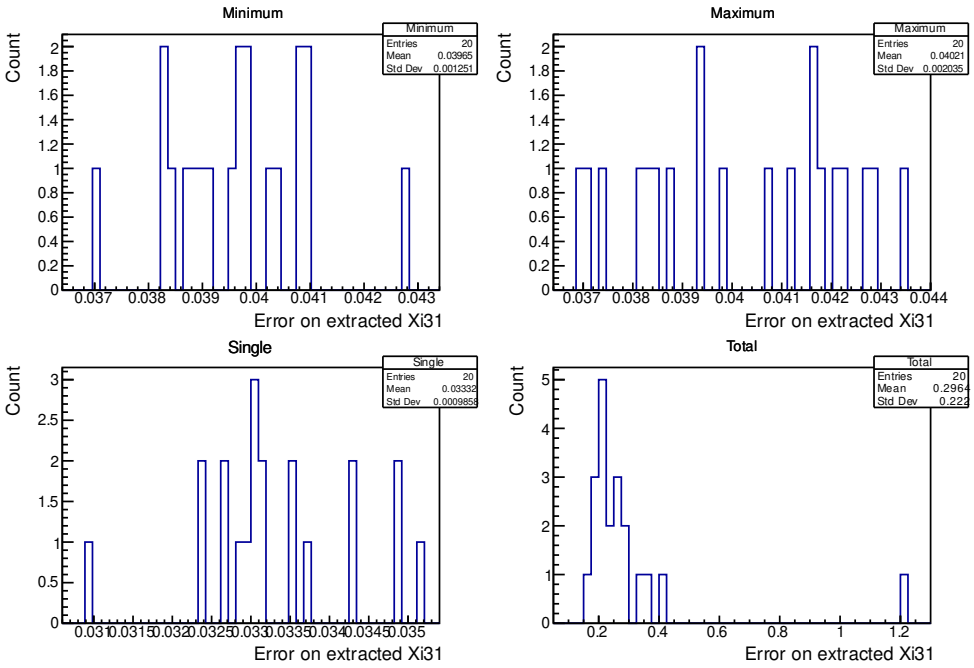

Figure 4.28 – Error on extracted ξ_{31} values from the fitted samples that passed the χ^2/NDF < 5 condition, with an input ξ_{31} = 0.37. Single observable fit while subtracting the background.

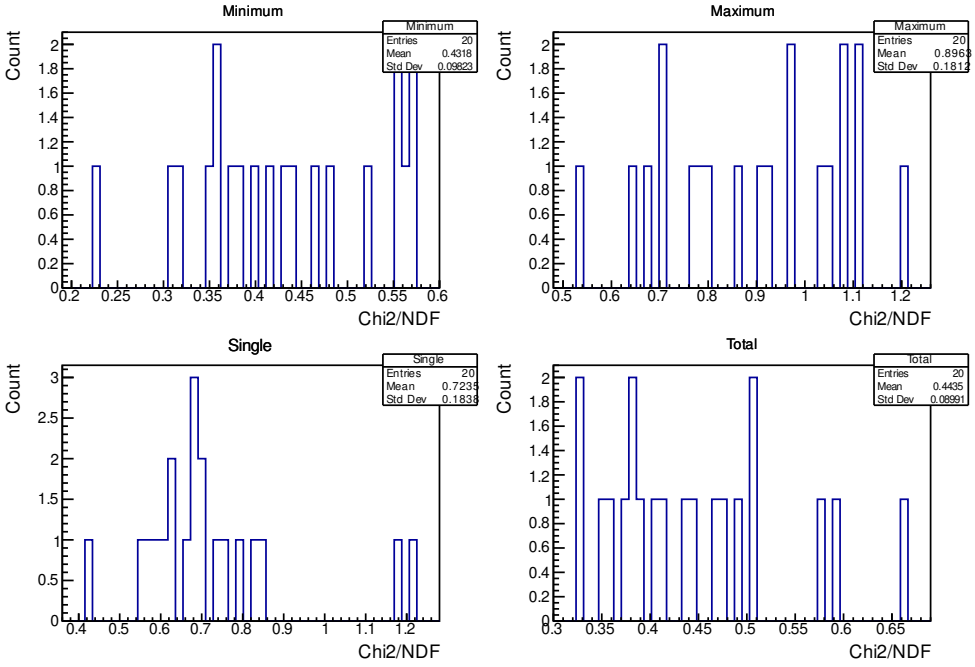

Figure 4.29 – The χ^2/NDF values of the fitted samples with an input ξ_{31} = 0.37. Single observable fit while subtracting the background.

Looking at figures 4.30 and 4.31, for minimum energy fits, there a slight decrease in the bias which existed before at input $\xi_{31} < 0.05$. But on the other side, an insignificant negative bias appeared. Maximum and single energy fits showed no significant difference comparing to the samples with only G_0 and G_2. While for total energy fit results, we observe a change in the shape of the distribution : we now have a negative bias especially for low input ξ_{31}, which could mean that we subtract more background events than what there is in the sample.

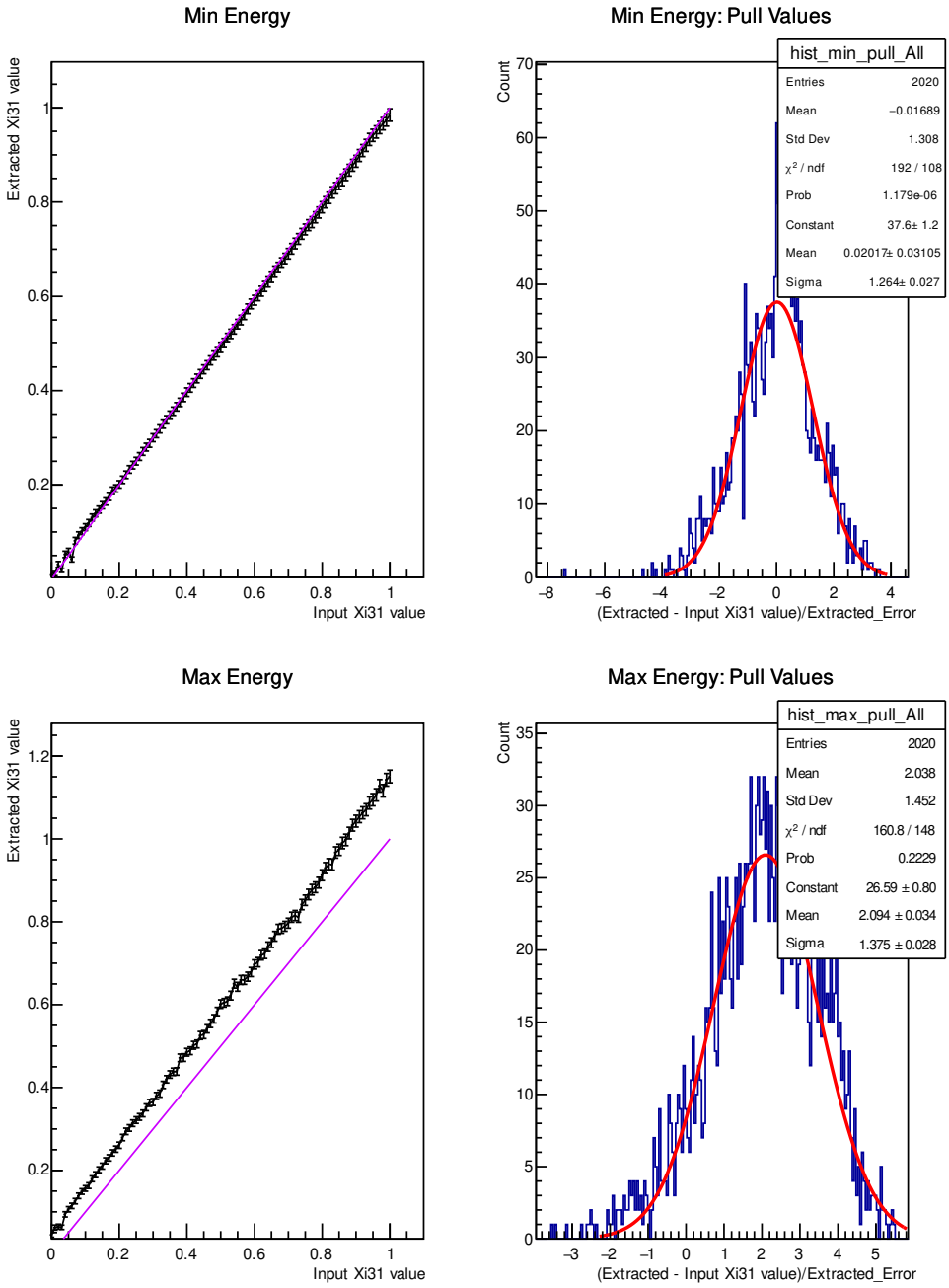

Figure 4.30 – Results of the fits of the samples with **G_0, G_2 and background**, the latter is **subtracted** from the sample. To the left : Results of the average extracted ξ_{31} values (of 20 fitted samples) versus the input ξ_{31}. The error bars represent the error on the average extracted values. The violet line represents the case if the extracted values are identical to the input values. To the right : The pull distribution of the extracted results (i.e each point presents the mean of the pull of the 20 samples), fitted with a Gaussian, where the mean and sigma would represent the correctness of the fit. To the top, results of the fits of minimum energy; to the bottom for maximum energy. Energy threshold cut at 300 keV.

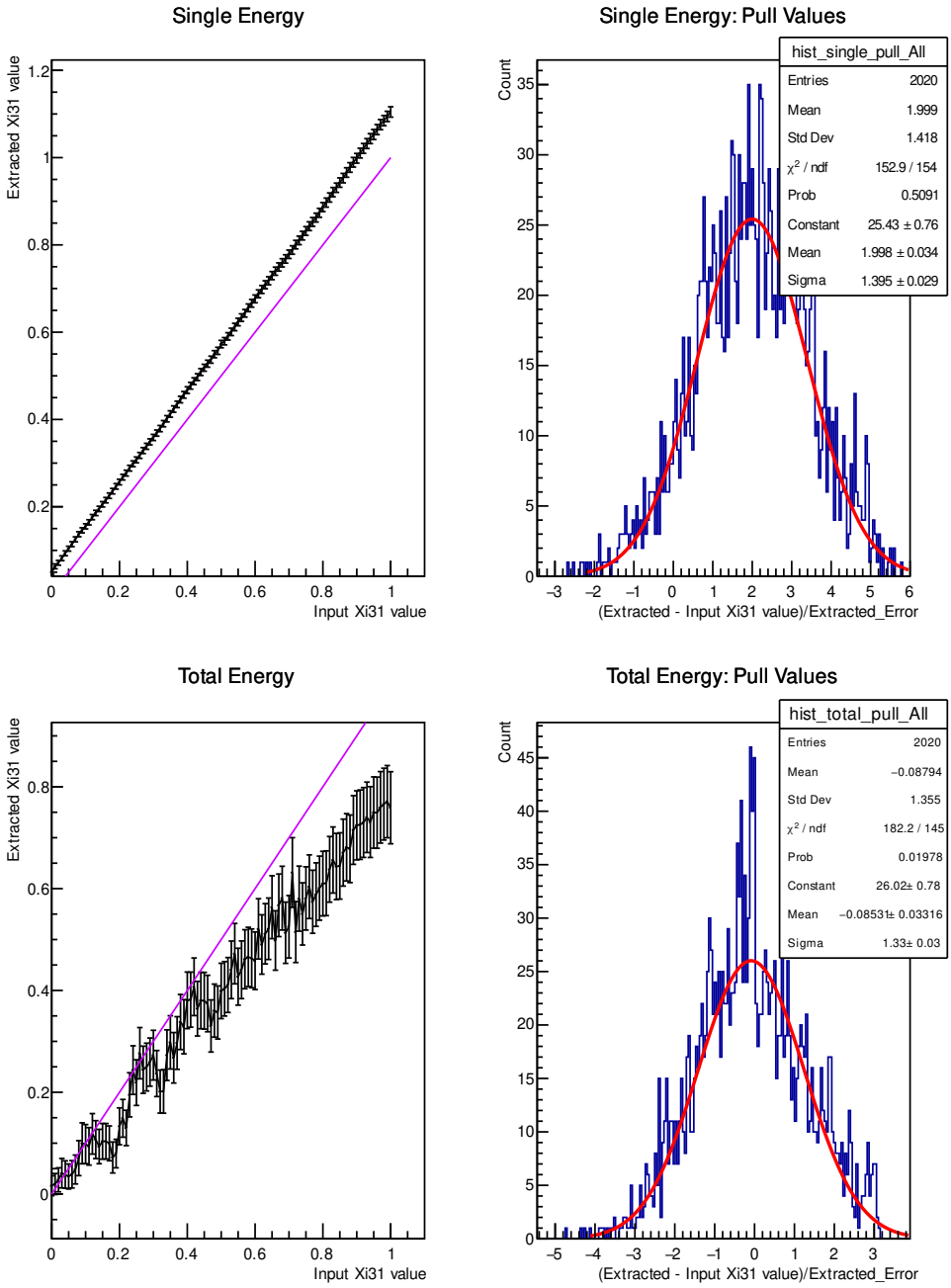

Figure 4.31 – Results of the fits of the samples with **G_0, G_2 and background**, the latter is **subtracted** from the sample. To the left : Results of the average extracted ξ_{31} values (of 20 fitted samples) versus the input ξ_{31}. The error bars represent the error on the average extracted values. The violet line represents the case if the extracted values are identical to the input values. To the right : The pull distribution of the extracted results (i.e each point presents the mean of the pull of the 20 samples), fitted with a Gaussian, where the mean and sigma would represent the correctness of fit. To the top, results of the fits of single energy ; to the bottom for total energy. Energy threshold cut at 300 keV.

- **Background PDF added to fitting PDF**

For the same samples, I check whether fitting the background component of the sample instead of subtracting it from the sample, then fitting the G0 and G2 components could improve the results (bias and errors).

First I show in figures 4.32 and 4.33 a 1D distribution of the extracted ξ_{31} values for input of 0.37 and their errors. It is expected for total energy to have a larger spread of the results. In figure 4.34, the 1D distribution of the χ^2/NDF of the fitted samples; these values are either around 1 or a bit less, where it signifies that there is an overestimation of the errors.

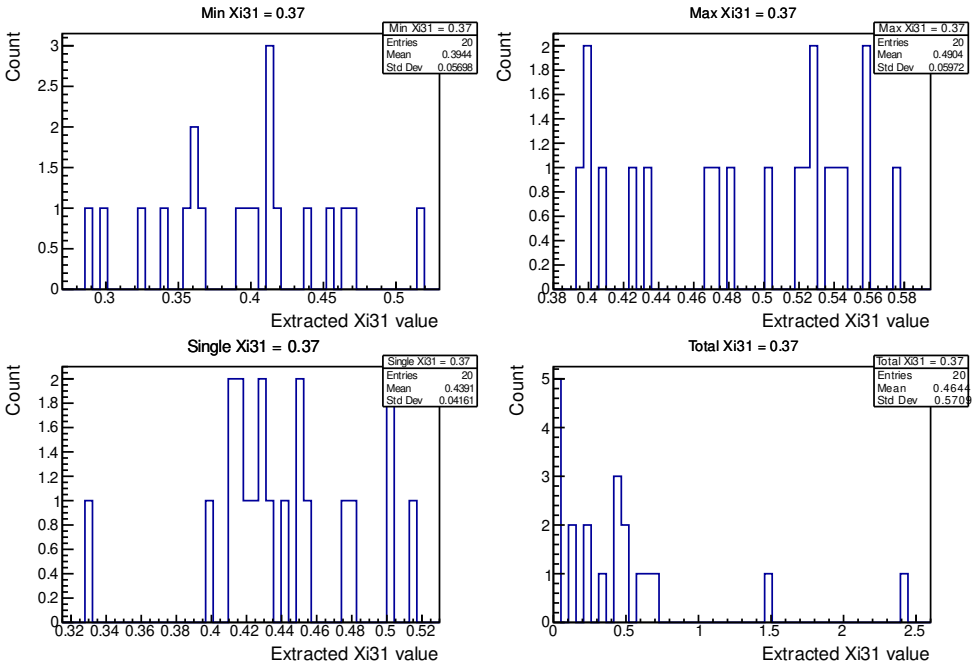

Figure 4.32 – Extracted ξ_{31} values from the fitted samples that passed the χ^2/NDF < 5 condition, with an input ξ_{31} = 0.37. **Single observable fit while fitting the background contribution**.

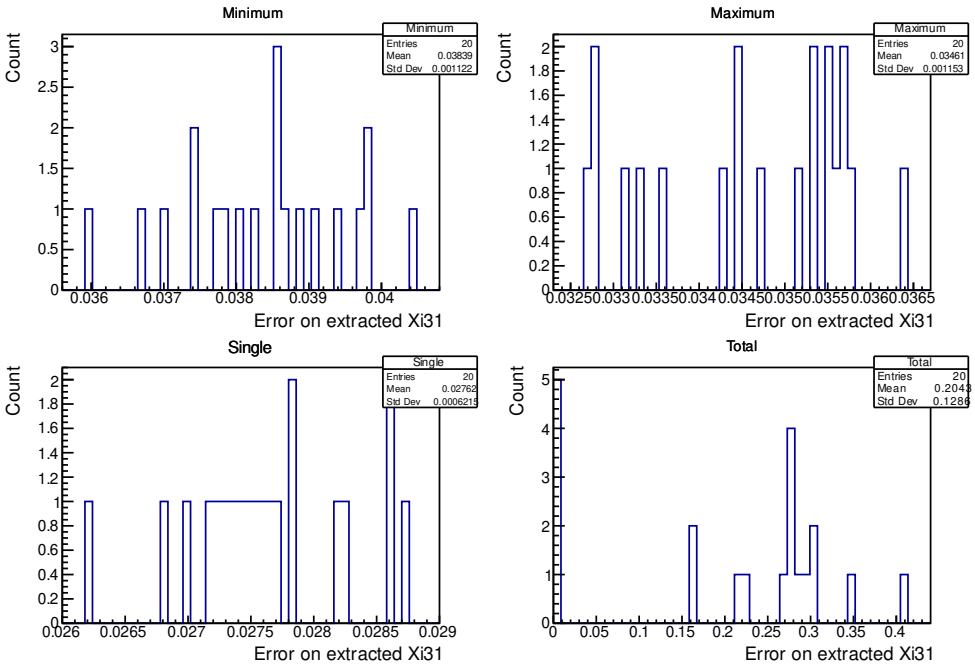

Figure 4.33 – Error on extracted ξ_{31} values from the fitted samples that passed the χ^2/NDF < 5 condition, with an input ξ_{31} = 0.37. **Single observable fit while fitting the background contribution**.

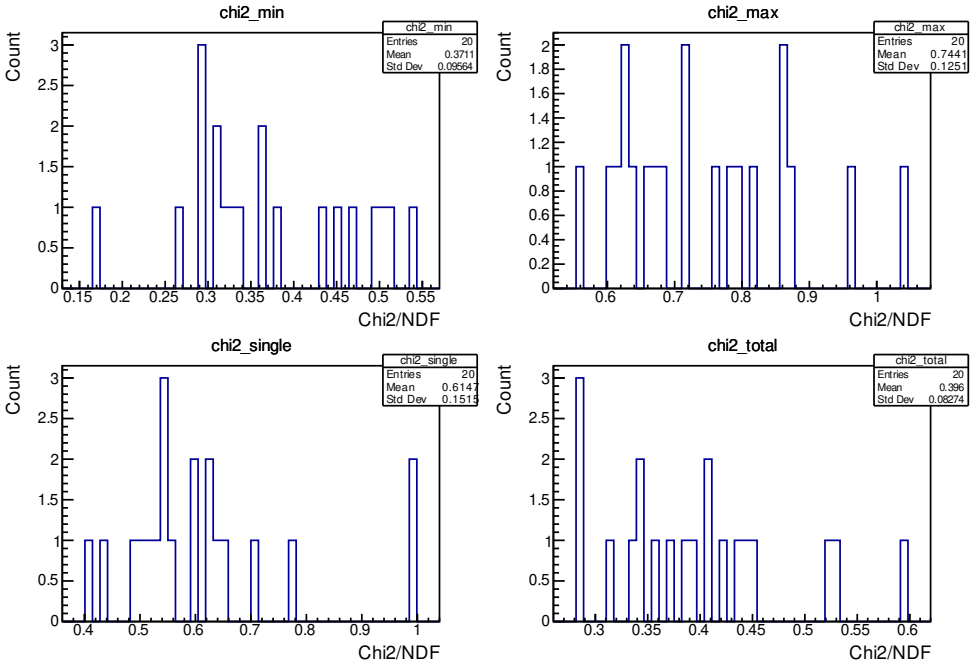

Figure 4.34 – The χ^2/NDF values of the fitted samples with an input ξ_{31} = 0.37. **Single observable fit while fitting the background contribution**.

Looking at figures 4.35 and 4.36, for minimum energy the bias increases compared to the method where I subtract the background contribution from the sample. We also observe a behavior for low input ξ_{31} values, where the weighted average gives very small values ($\sim$0). This is associated to the very small extracted ξ_{31} values with tiny errors associated for these inputs, which is also seen in the pull in the right plot.

Fitted energy spectra	Mean of Pull	Sigma of Pull	Comment
No Background			
Minimum	0.20 ± 0.03	1.17 ± 0.03	
Maximum	1.97 ± 0.03	1.26 ± 0.03	
Single	1.87 ± 0.03	1.30 ± 0.03	
Total	0.02 ± 0.03	1.04 ± 0.02	Large bias
Background Subtracted			
Minimum	0.02 ± 0.03	1.26 ± 0.03	
Maximum	2.09 ± 0.03	1.37 ± 0.03	
Single	1.00 ± 0.03	1.39 ± 0.03	
Total	-0.08 ± 0.03	1.33 ± 0.03	Large bias
Background in the fitting PDF			
Minimum	0.52 ± 0.04	1.62 ± 0.03	
Maximum	3.63 ± 0.04	1.61 ± 0.03	
Single	2.51 ± 0.04	1.65 ± 0.04	
Total	0.003 ± 0.040	1.71 ± 0.06	Large fluctuations

Table 4.7 – The different Pull distribution "mean" and "sigma" obtained using different fitted energy spectra of samples with background, in the case of subtracting the background and adding it to the fitting PDF.

For single and maximum energies where we observe an increase in the bias. While for total energy fits, we see that now the weighted average values are very small, but surprisingly the pull of all the fitted samples gives acceptable values for the mean (0.003) and a too large sigma (1.71). I compare between the different results in table 4.7, where it show the mean and sigma of the Gaussian fit of the pull distributions, for the two methods where I subtract the background contribution from the sample, and when I add the background contribution to the fitting PDF. Total energy fits present larger errors, so even with quite large input ξ_{31} values the fit can give an extracted value close to the boundary, so $\xi_{31} \sim 0$ with a very small error. This explains the mean of extracted ξ_{31} observed at ~ 0, for several input ξ_{31} values.

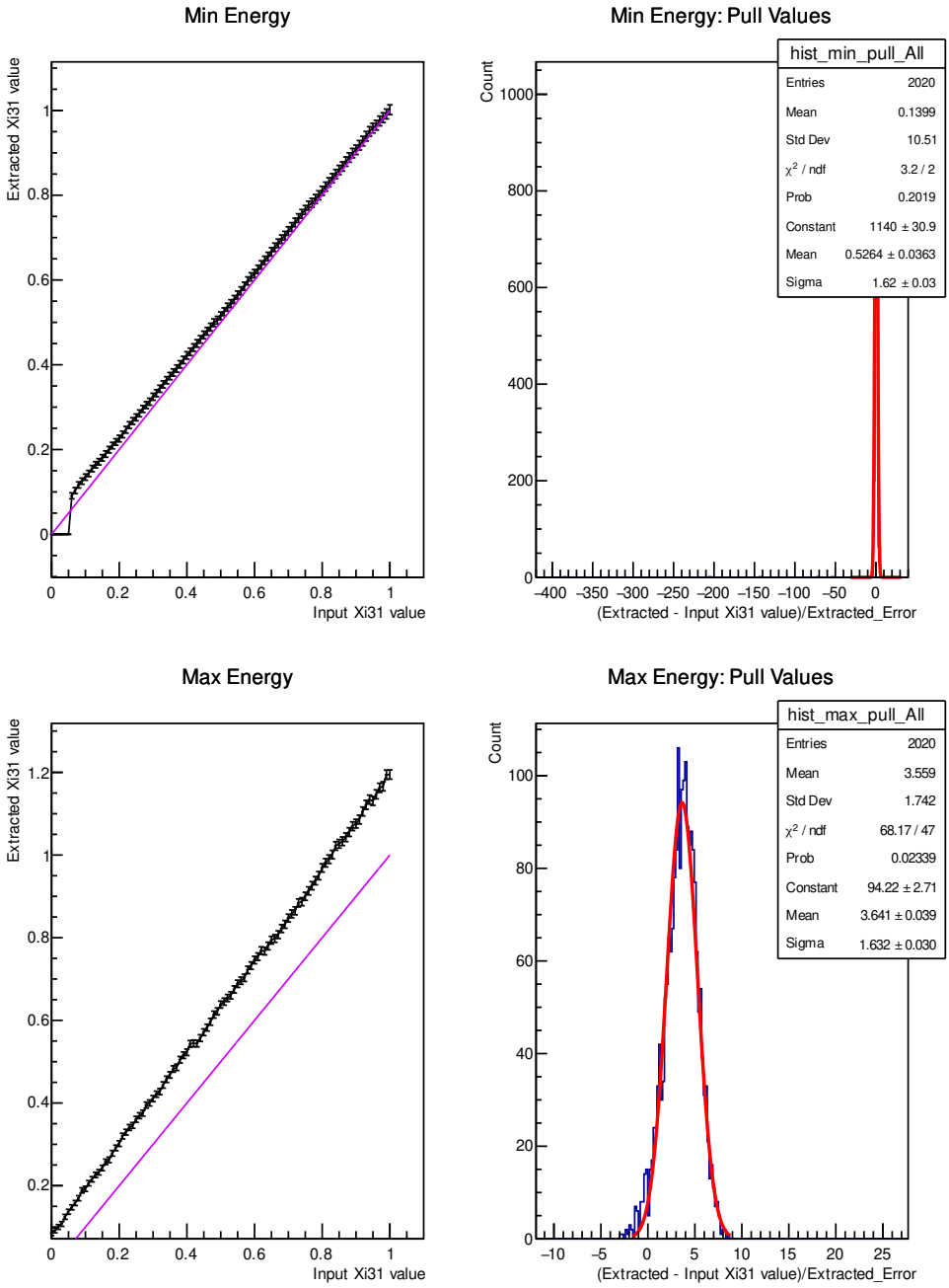

Figure 4.35 – Results of the fits of the samples with **G_0, G_2 and background**, the **background PDF is added to the fitting PDF**. To the left : Results of the average extracted ξ_{31} values (of 20 fitted samples) versus the input ξ_{31}. The error bars represent the error on the average extracted values. The violet line represents the case if the extracted values are identical to the input values. To the right : The pull distribution of the extracted results (i.e each point presents the mean of the pull of the 20 samples), fitted with a Gaussian, where the mean and sigma would represent the correctness of the fit. To the top, results of the fits of minimum energy; to the bottom for maximum energy. Energy threshold cut at 300 keV.

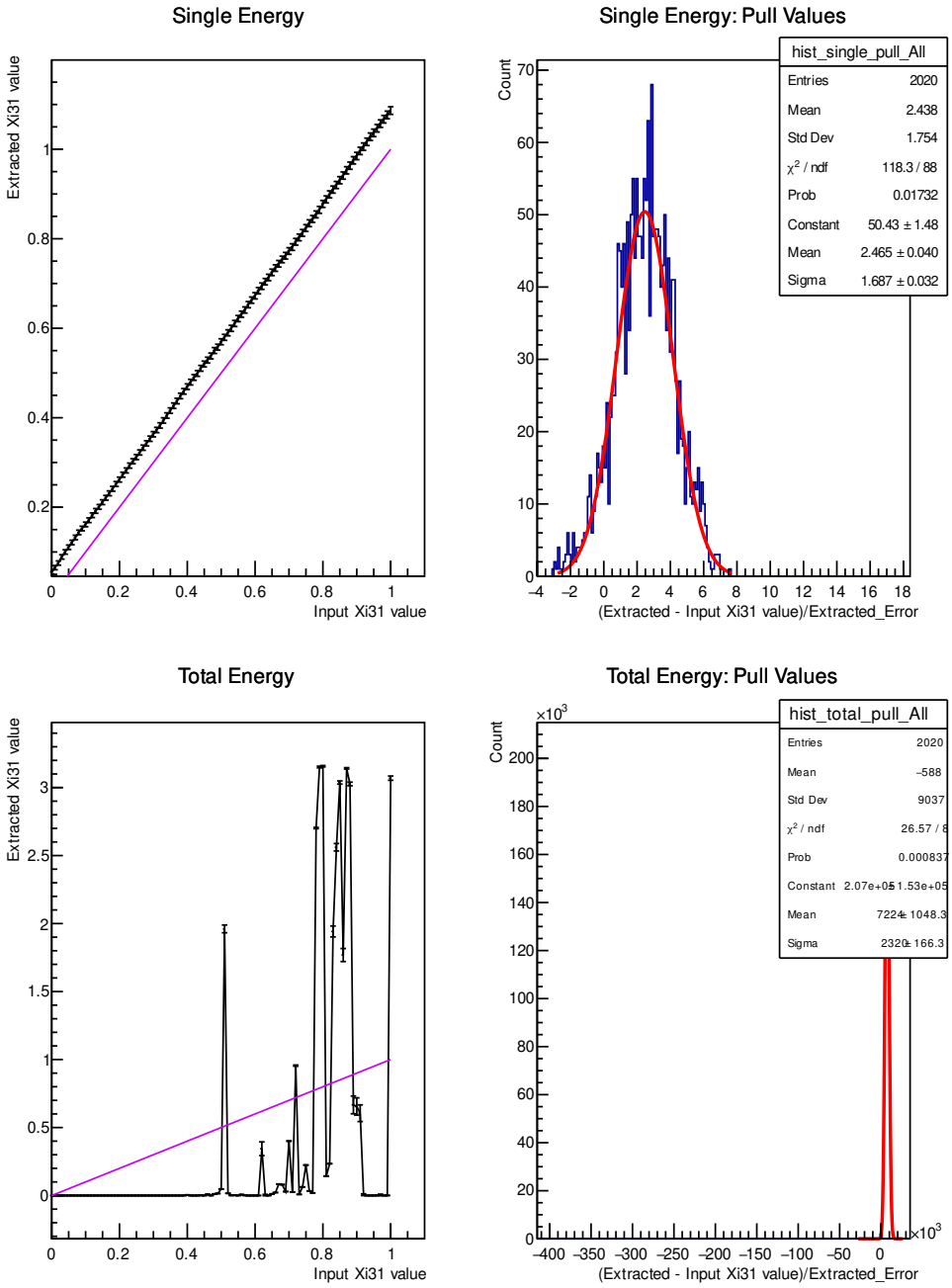

Figure 4.36 – Results of the fits of the samples with **G_0, G_2 and background**, the **background PDF is added to the fitting PDF**. To the left : Results of the average extracted ξ_{31} values (of 20 fitted samples) versus the input ξ_{31}. The error bars represent the error on the average extracted values. The violet line represents the case if the extracted values are identical to the input values. To the right : The pull distribution of the extracted results (i.e each point presents the mean of the pull of the 20 samples), fitted with a Gaussian, where the mean and sigma would represent the correctness of the fit. To the top, results of the fits of single energy; to the bottom for total energy. Energy threshold cut at 300 keV.

We now see if we can improve our result using fitting of several observables simultaneously, as described in 4.4.1 page 146.

Simultaneous 1D Fitting

Simultaneous fitting is done by adding two or more energy distributions (observables) to be fitted simultaneously and converging the common fitting parameter to the best value to obtain the ξ_{31} value.

The fits performed in this analysis uses simultaneously the shape of the following observables :

- Maximal and minimal energy, referred to as Maximum-Minimum (or max-min)

- Minimal and total energy, referred to as Minimum-Total (or min-total)

- Single and total energy, referred to as Single-Total

- Maximal, minimal, single and total energy, will be referred to as "all energy fits".

Some distributions fitted simultaneously are correlated, e.g : the total energy is the sum of the maximal and minimal energy.. In the calculations, this correlation between observables for a given event is not taken into account.

Simultaneous 1D Fitting : Samples without Background I present the results of simultaneous fits in figures 4.37 and 4.38, and I compare similar fits, e.g maximum-minimum energy fits with single energy distribution fit. the pull values have changed from mean = 1.82 and sigma = 1.31 (for single energy, figure 4.19 page 157) to mean = -0.27 and sigma = 1.66 (for maximum-minimum energy fit, figure 4.37), where the mean decreases but the sigma value increases. A small bias is observed with minimum-total energy simultaneous fit (mean = 0.24 sigma = 1.67), while for the single-total and all energy distribution simultaneous fit there is a bias in the values by an overestimation of the ξ_{31} values extracted.

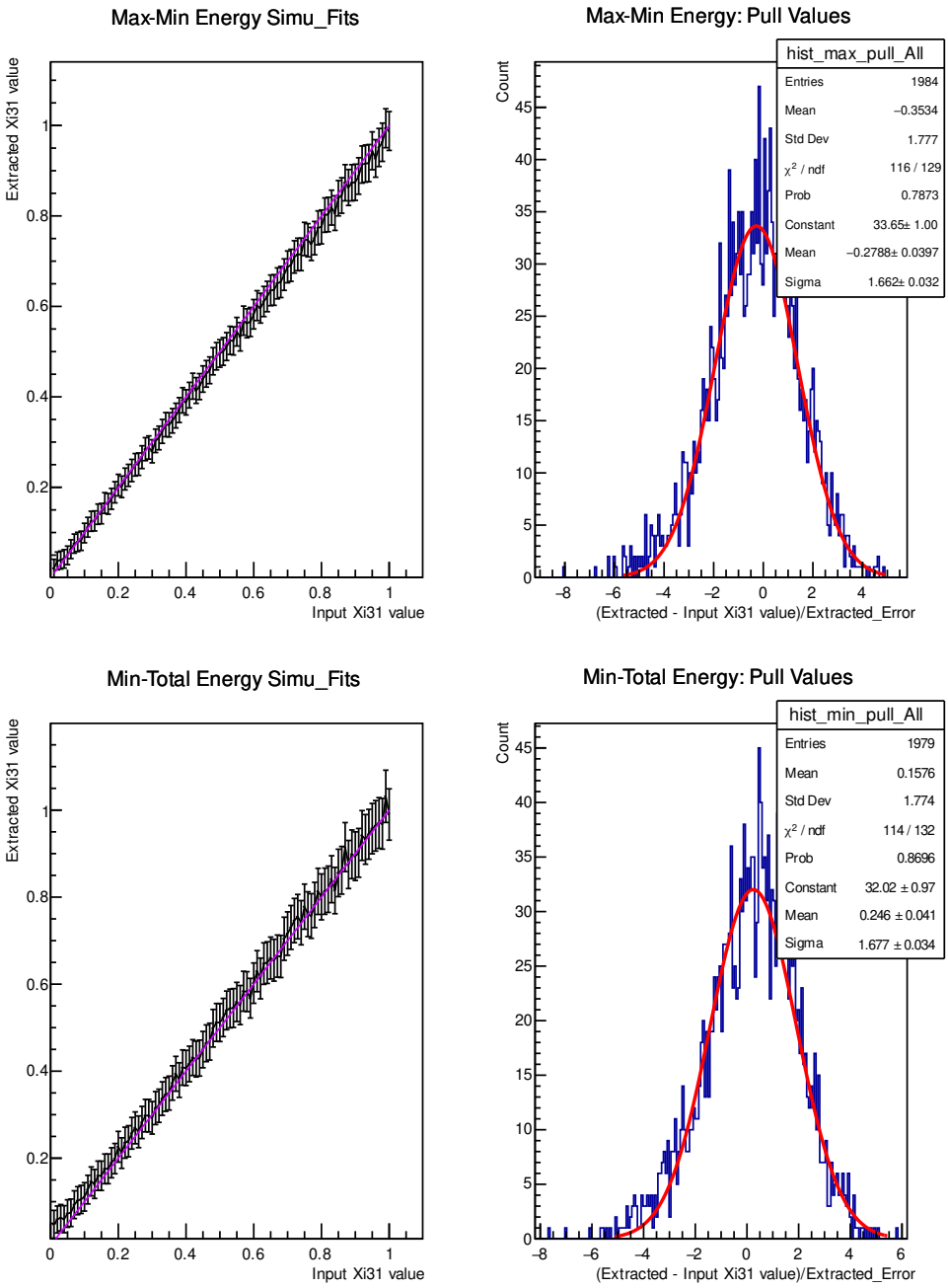

Figure 4.37 – Results of the **simultaneous** fits of the samples with **only G_0 and G_2**. To the left : Results of the average extracted ξ_{31} values (of 20 fitted samples) versus the input ξ_{31}. The error bars represent the error on the average extracted values. The violet line represents the case if the extracted values are identical to the input values. To the right : The pull distribution of the extracted results (i.e each point presents the mean of the pull of the 20 samples), fitted with a Gaussian, where the mean and sigma would represent the correctness of the fit. To the top, results of the fits of maximum-minimum energy ; to the bottom for minimum-total energy. Energy threshold cut at 300 keV.

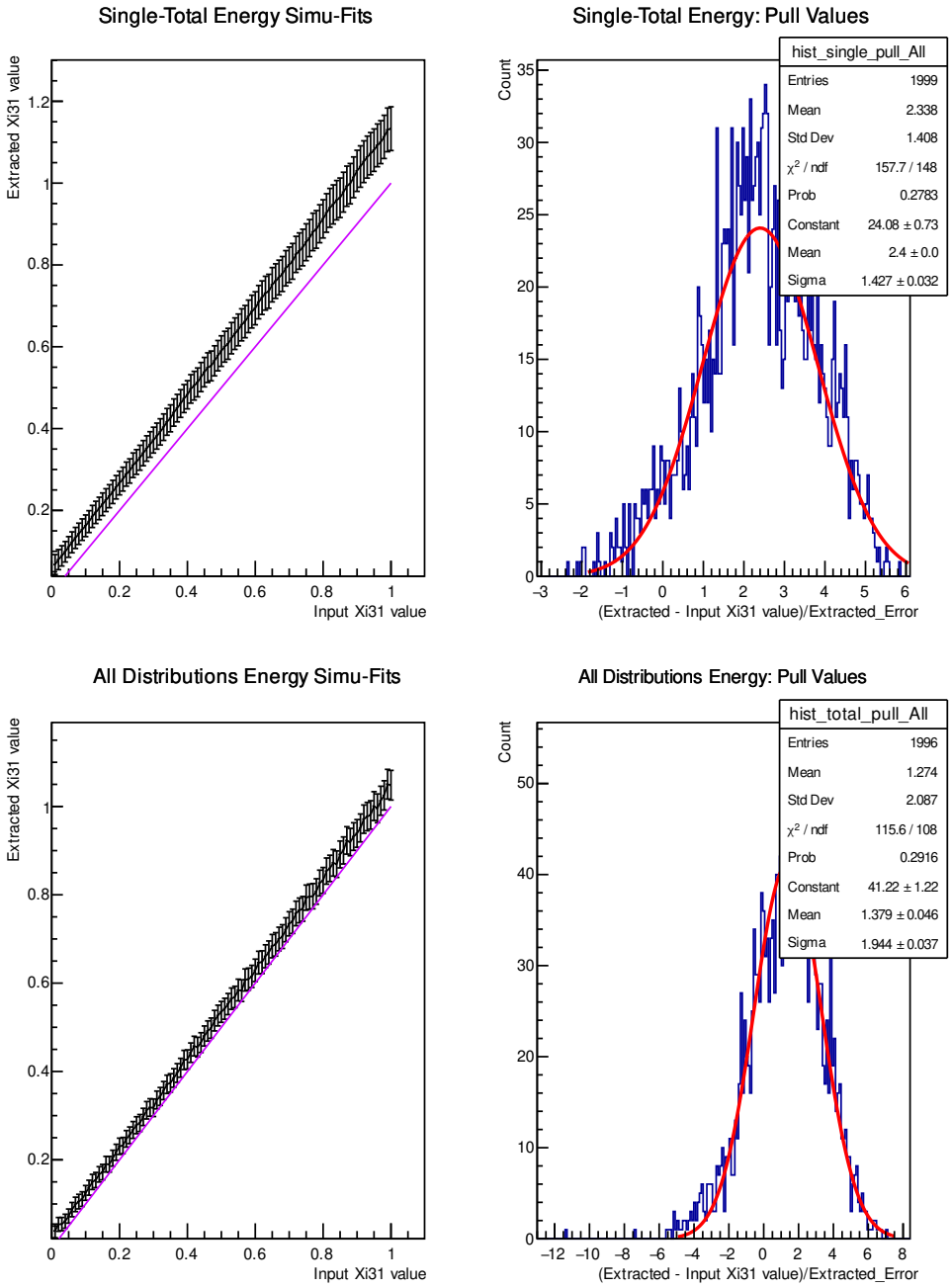

Figure 4.38 – Results of the **simultaneous** fits of the samples with **only G_0 and G_2**. To the left : Results of the average extracted ξ_{31} values (of 20 fitted samples) versus the input ξ_{31}. The error bars represent the error on the average extracted values. The violet line represents the case if the extracted values are identical to the input values. To the right : The pull distribution of the extracted results (i.e each point presents the mean of the pull of the 20 samples), fitted with a Gaussian, where the mean and sigma would represent the correctness of the fit. To the top, results of the fits of total-single energy; to the bottom for all energy distributions. Energy threshold cut at 300 keV.

Simultaneous 1D Fitting : Samples with Background - Background Subtraction

I now use simultaneous fit of several observables for the samples with background and in the case of background subtraction.

First I show in figures 4.39 and 4.40 a 1D distribution of the extracted ξ_{31} values for input of 0.37 and their errors, where the extracted values have a significant bias. All fits have similar extracted value spread.

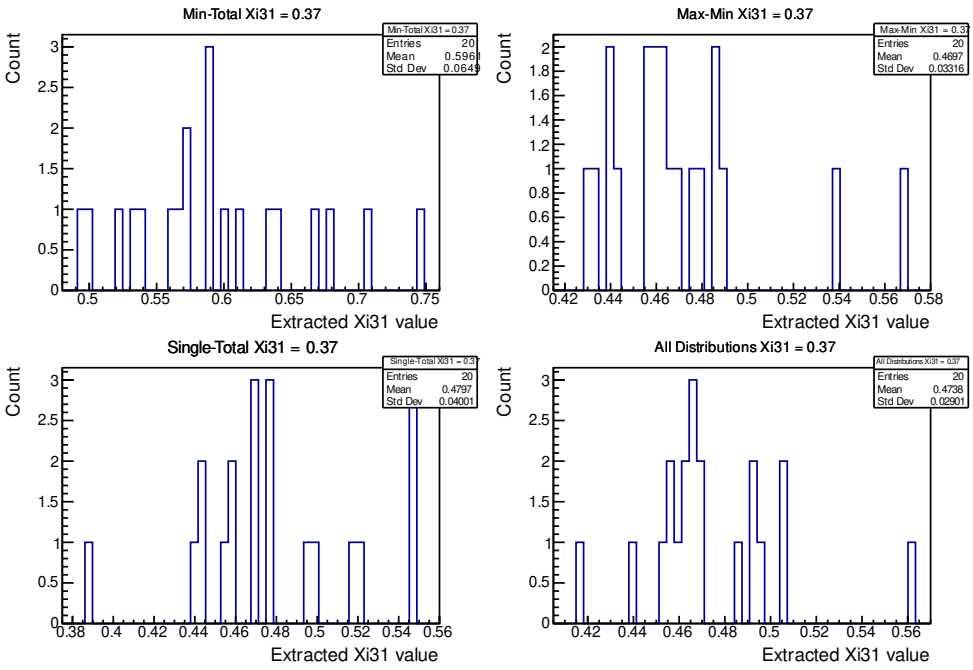

Figure 4.39 – Extracted ξ_{31} values from the fitted samples that passed the χ^2/NDF < 5 condition, with an input ξ_{31} = 0.37. Simultaneous observable fit while subtracting the background.

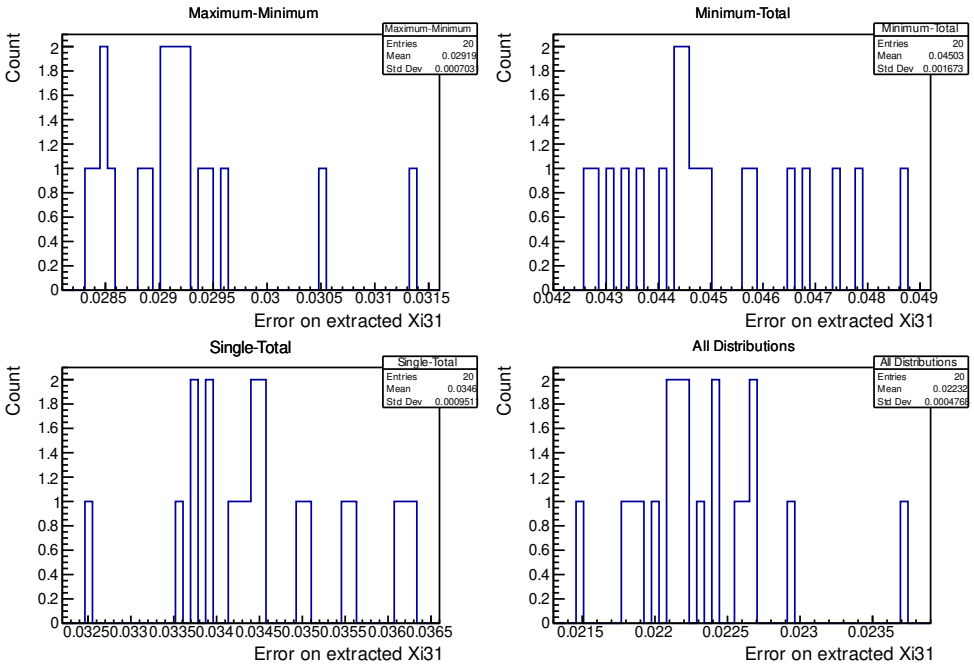

Figure 4.40 – Error on extracted ξ_{31} values from the fitted samples that passed the χ^2/NDF < 5 condition, with an input ξ_{31} = 0.37. Simultaneous observable fit while subtracting the background.

The results are presented in figures 4.41 and 4.42. One can see in all the fit cases there is an overestimation of the extracted value, i.e an overestimation of the contribution of the G_2 process. By looking back at the same method but using samples with no background, this bias did not exist, meaning that the subtraction of the background is affecting the spectrum shape in such a way that the process is overestimating the G_2 contribution. In some cases, this overestimation decreases to include the input values in its error bars, usually for ξ_{31} values above 0.8, where the G_2 contribution is more significant. But still, this method of fitting doesn't provide the good accuracy for the ξ_{31} value.

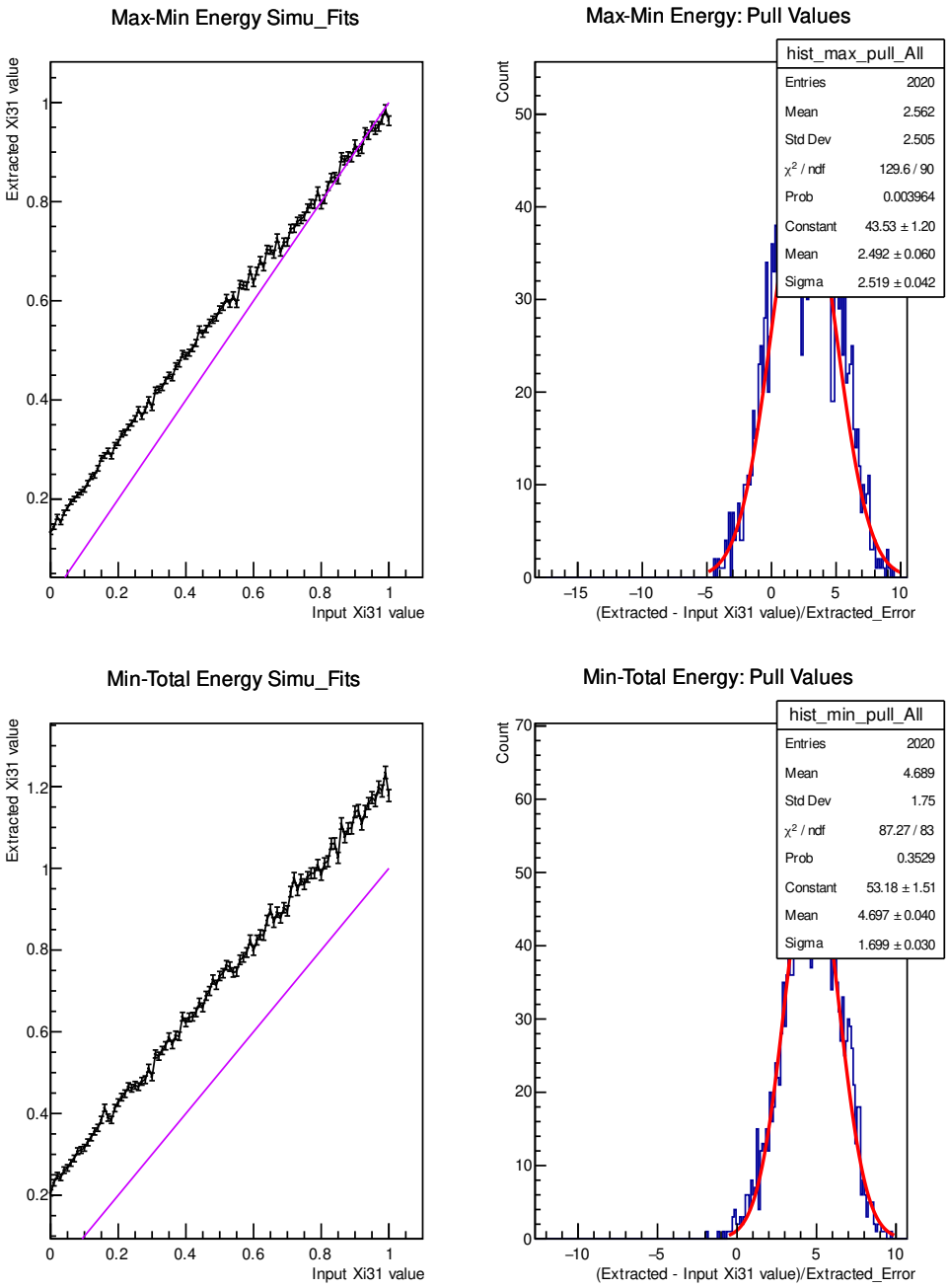

Figure 4.41 – Results of the simultaneous fits of the samples with **G_0, G_2 and background**, where the **background is subtracted** from the sample. To the left : Results of the average extracted ξ_{31} values (of 20 fitted samples) versus the input ξ_{31}. The error bars represent the error on the average extracted values. The violet line represents the case if the extracted values are identical to the input values. To the right : The pull distribution of the extracted results (i.e each point presents the mean of the pull of the 20 samples), fitted with a Gaussian, where the mean and sigma would represent the correctness of the fit. To the top, results of the fits of maximum-minimum energy ; to the bottom for minimum-total energy. Energy threshold cut at 300 keV.

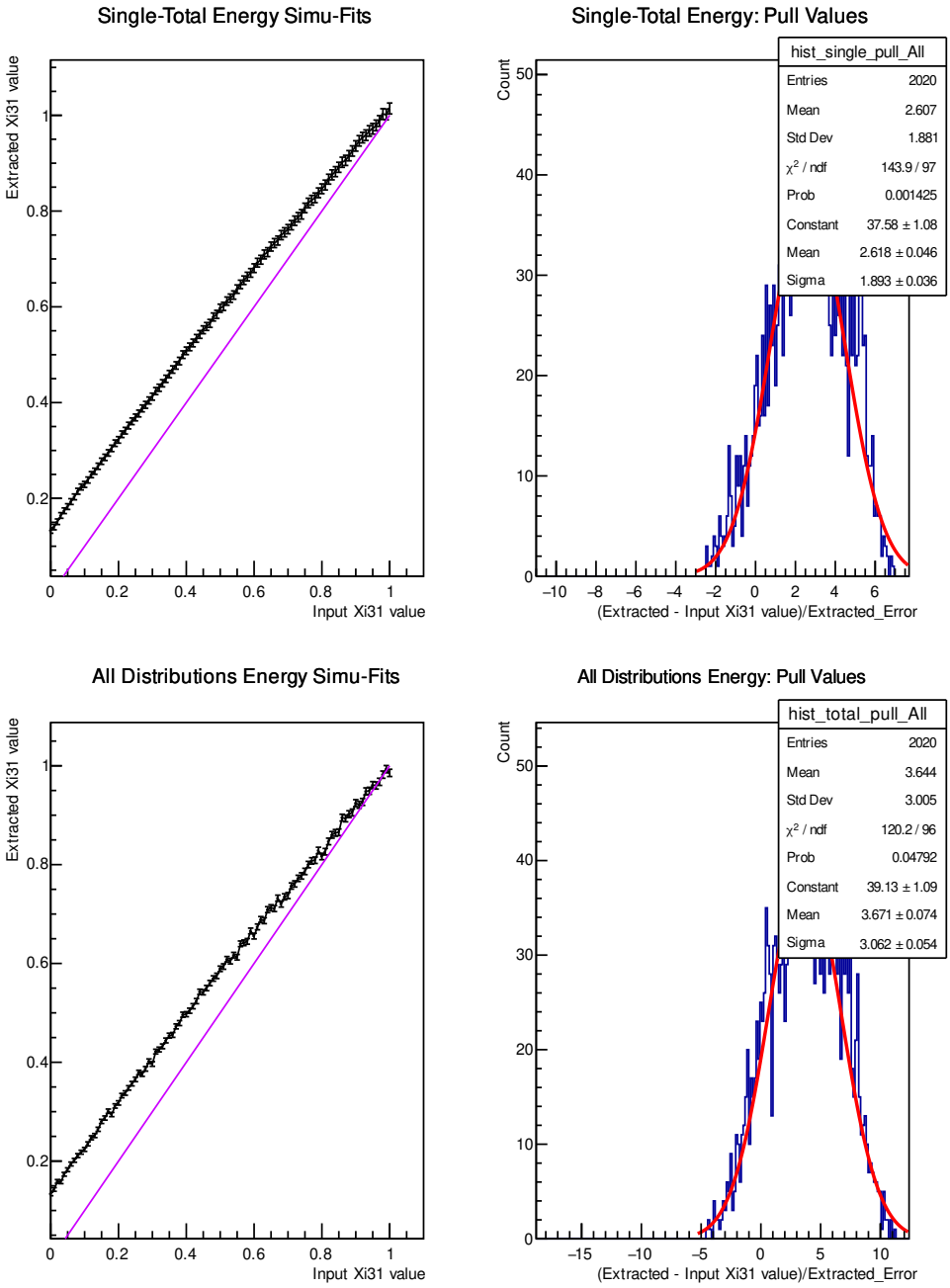

Figure 4.42 – Results of the **simultaneous** fits of the samples with **G_0, G_2 and background**, where the **background is subtracted** from the sample. To the left : Results of the average extracted ξ_{31} values (of 20 fitted samples) versus the input ξ_{31}. The error bars represent the error on the average extracted values. The violet line represents the case if the extracted values are identical to the input values. To the right : The pull distribution of the extracted results (i.e each point presents the mean of the pull of the 20 samples), fitted with a Gaussian, where the mean and sigma would represent the correctness of the fit. To the top, results of the fits of total-single energy; to the bottom for all energy distributions. Energy threshold cut at 300 keV.

- **Background PDF added to fitting PDF**

For this method, simultaneous fitting of several observables are used while including the PDF of background into the fitting PDF (fitting PDF = G_0, G_2 and background).

First I show in figures 4.43 and 4.44 a 1D distribution of the extracted ξ_{31} values for input of 0.37 and their errors, the results are less biased compared to the method where I subtract the background contribution from the samples. All fits have similar extracted value spread.

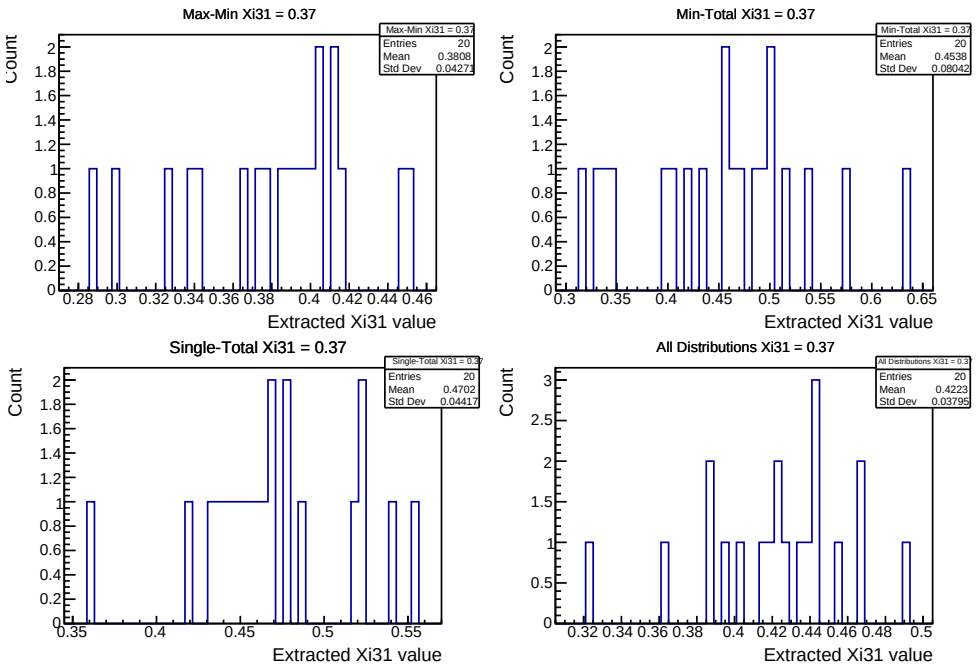

Figure 4.43 – Extracted ξ_{31} values from the fitted samples that passed the χ^2/NDF < 5 condition, with an input ξ_{31} = 0.37. Simultaneous observable fit while fitting the background.

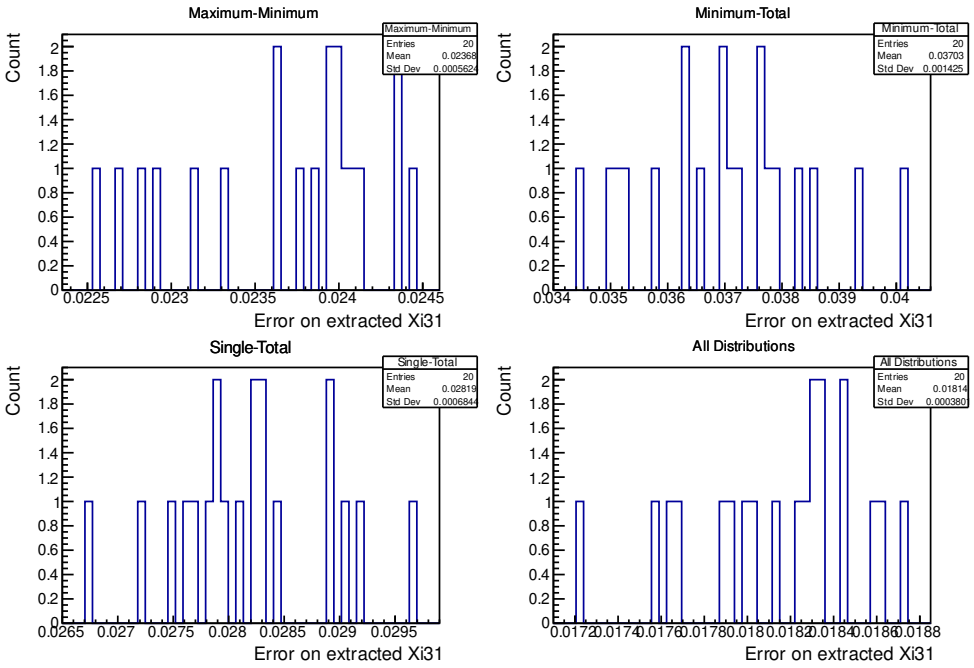

Figure 4.44 – Error on extracted ξ_{31} values from the fitted samples that passed the χ^2/NDF < 5 condition, with an input ξ_{31} = 0.37. Simultaneous observable fit while fitting the background.

The results are shown in figures 4.45 and 4.46. For maximum-minimum distribution simultaneous fits, and looking at the pull distribution (figure 4.45) we notice that there is a fitted sample that resulted in a ξ_{31} that is very far away from the input value. For this, the fit of the pull resulted in a largely biased mean and a huge sigma. Again, the behavior observed at low input ξ_{31} values is associated to the very low extracted values of the fits, with very small associated errors. For the rest of the fits, we observe a significant bias, which doesn't provide a good tool to extract ξ_{31}.

In table 4.8 I compare the results of simultaneous fitting with background subtracted and background PDF added to the fitting PDF.

Fitted energy spectra	Mean of Pull	Sigma of Pull	Comment
Background Subtracted			
Maximum-Minimum	2.49 $\pm$ 0.06	2.52 $\pm$ 0.04	
Minimum-Total	4.69 $\pm$ 0.04	1.69 $\pm$ 0.03	
Single-Total	2.61 $\pm$ 0.05	1.89 $\pm$ 0.04	
All distribtuions	3.67 $\pm$ 0.07	3.06 $\pm$ 0.05	
Background in the fitting PDF			
Maximum-Minimum	-3.51 $\pm$ 0.92	49.1 $\pm$ 2.7	very large pull
Minimum-Total	1.80 $\pm$ 0.05	2.00 $\pm$ 0.04	
Single-Total	3.43 $\pm$ 0.04	1.80 $\pm$ 0.03	
All distribtuions	2.23 $\pm$ 0.06	2.74 $\pm$ 0.05	very large pull

Table 4.8 – The different Pull distributions "mean" and "sigma" obtained using different simultaneously fitted energy spectra of samples with background, in the case of subtracting the background and in the case of adding the background to the fitting PDF.

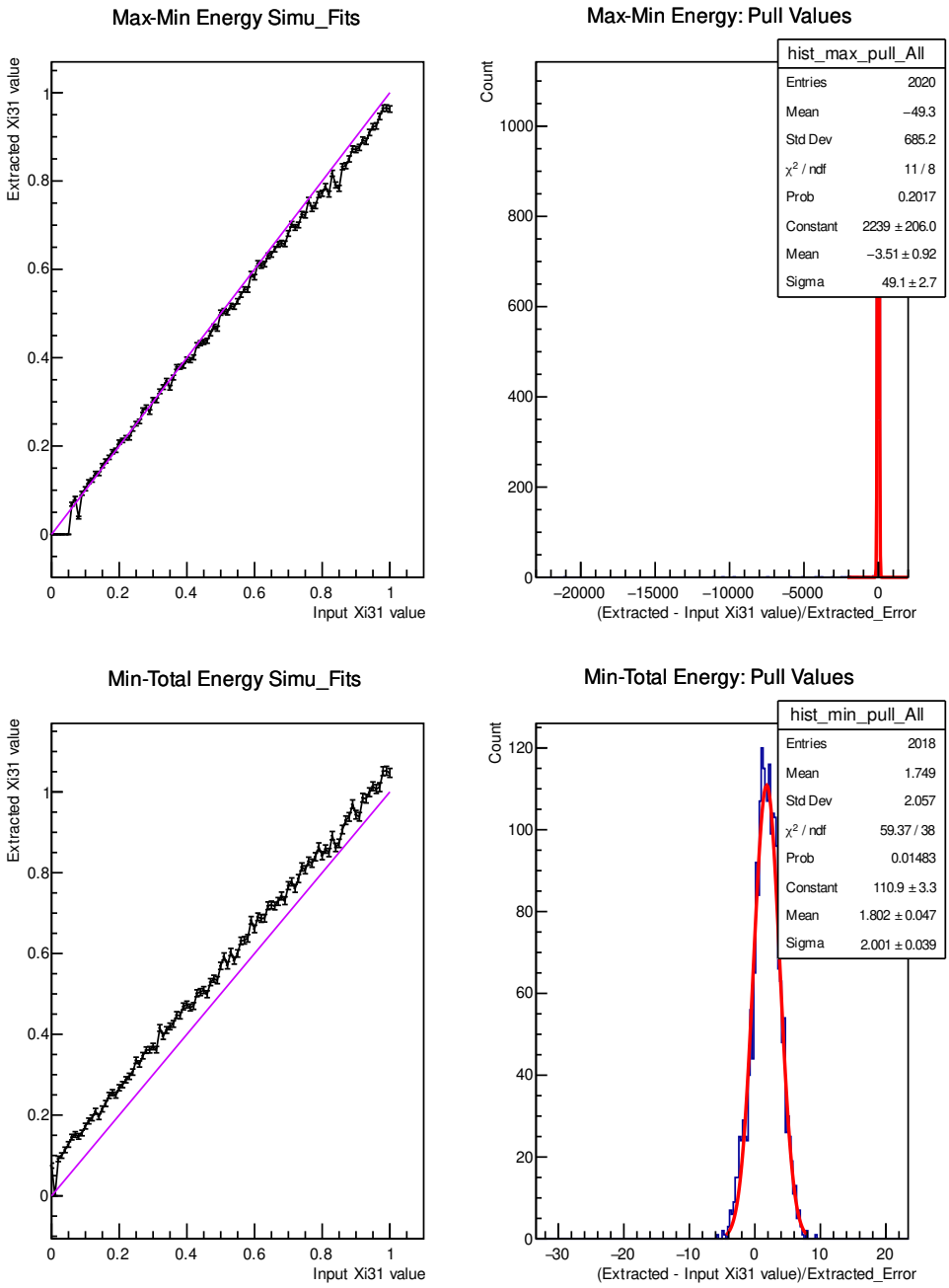

Figure 4.45 – Results of the simultaneous fits of the samples with $\mathbf{G_0}$, $\mathbf{G_2}$ **and background**, where the **PDF of the background is added to the fitting PDF**. To the left : Results of the average extracted ξ_{31} values (of 20 fitted samples) versus the input ξ_{31}. The error bars represent the error on the average extracted values. The violet line represents the case if the extracted values are identical to the input values. To the right : The pull distribution of the extracted results (i.e each point presents the mean of the pull of the 20 samples), fitted with a Gaussian, where the mean and sigma would represent the correctness of the fit. To the top, results of the fits of maximum-minimum energy ; to the bottom for minimum-total energy. Energy threshold cut at 300 keV.

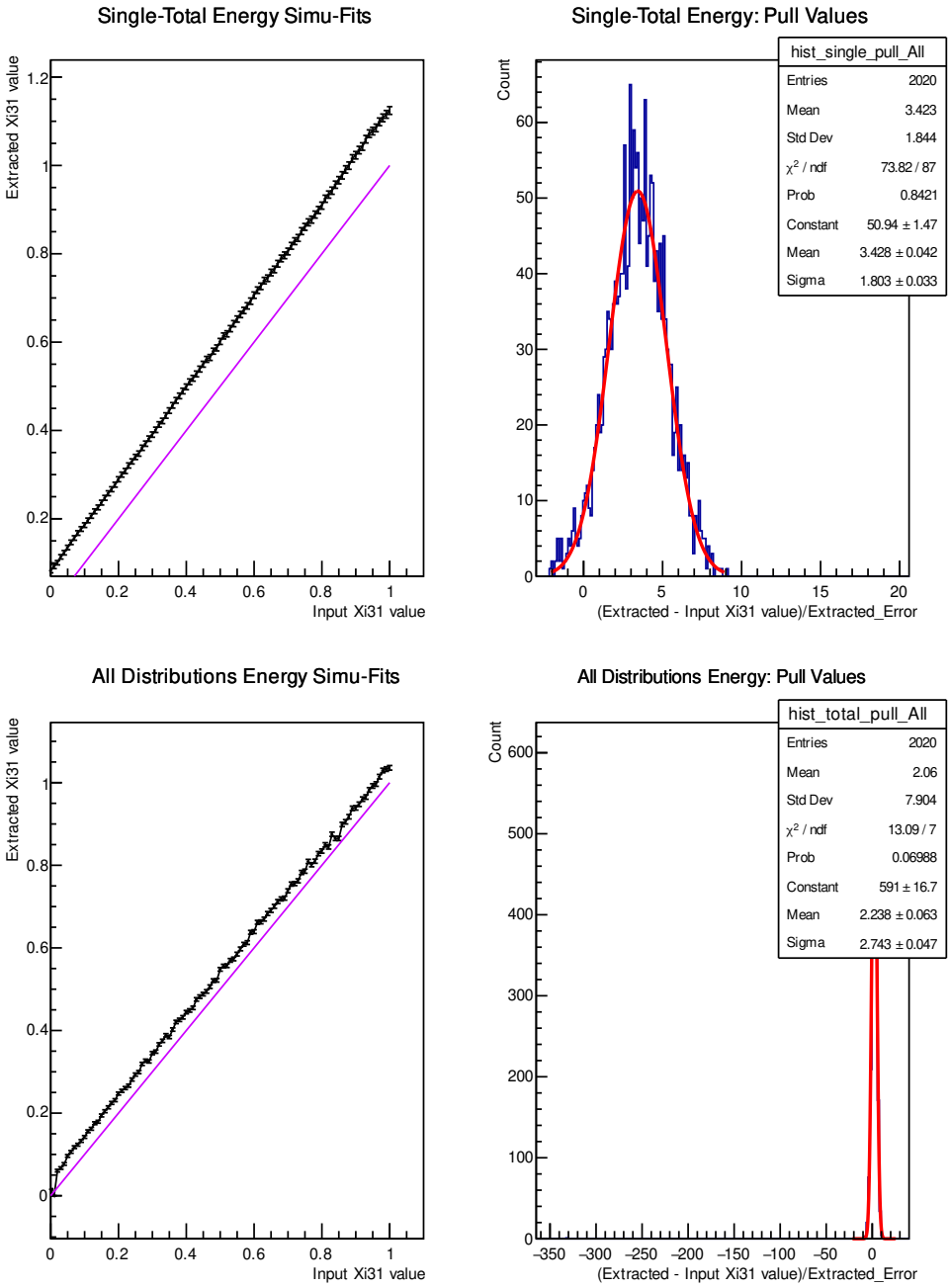

Figure 4.46 – Results of the **simultaneous** fits of the **samples with G_0, G_2 and background**, where the **PDF of the background is added to the fitting PDF**. To the left : Results of the average extracted ξ_{31} values (of 20 fitted samples) versus the input ξ_{31}. The error bars represent the error on the average extracted values. The violet line represents the case if the extracted values are identical to the input values. To the right : The pull distribution of the extracted results (i.e each point presents the mean of the pull of the 20 samples), fitted with a Gaussian, where the mean and sigma would represent the correctness of the fit. To the top, results of the fits of total-single energy; to the bottom for all energy distributions. Energy threshold cut at 300 keV.

This method doesn't provide better results than the previously introduced method, where we fit single distributions (in particular minimum energy) and subtract the background from the sample before fitting with only G_0 and G_2 PDFs. But in the case where we fit maximum-minimum energy distributions, the results can be acceptable if we remove the cases where we extract small values with very small errors.

Results from Different Energy Cuts To better observe the effect of the energy threshold cut on the sensitivity, I plot the pulls values of the extracted ξ_{31} (the weighted average of the pull values of the 20 fitted samples, as in figure 4.24), versus the input ξ_{31} value, introduced in figures 4.47, 4.48, 4.49 and 4.50. These plots are shown for the method where the background is subtracted from the sample and when the background contribution is added to the fitting PDF. Each color represents an energy threshold cut applied on the samples, from 100 keV to 400 keV.

In the case of single observable fit, and as previously mentioned, the minimum energy fit gives the best results, where the pull values have similar behavior for all the energy cuts, and vary between -0.5 and 0.5 for the standard energy threshold cut at 300 keV.

I also show the pull values from the different methods. In the case of simultaneous fit with background subtraction we see a decrease in the pull values as a function of the input ξ_{31} values, the behavior is the same for all the energy threshold cuts. In the other methods where the background PDF is added to the fitting PDF, we observe large spikes in the pull values. These spikes (mean of the pull values of the 20 samples) can be associated to one of the samples having a fit that extracted a value very far from the input value, and hence this creates the deviation. But in general, the pulls in these methods are larger than what consider as good values.

To conclude, the best method to find the sensitivity is using fit of minimum energy distribution and subtracting the background contribution from the sample.

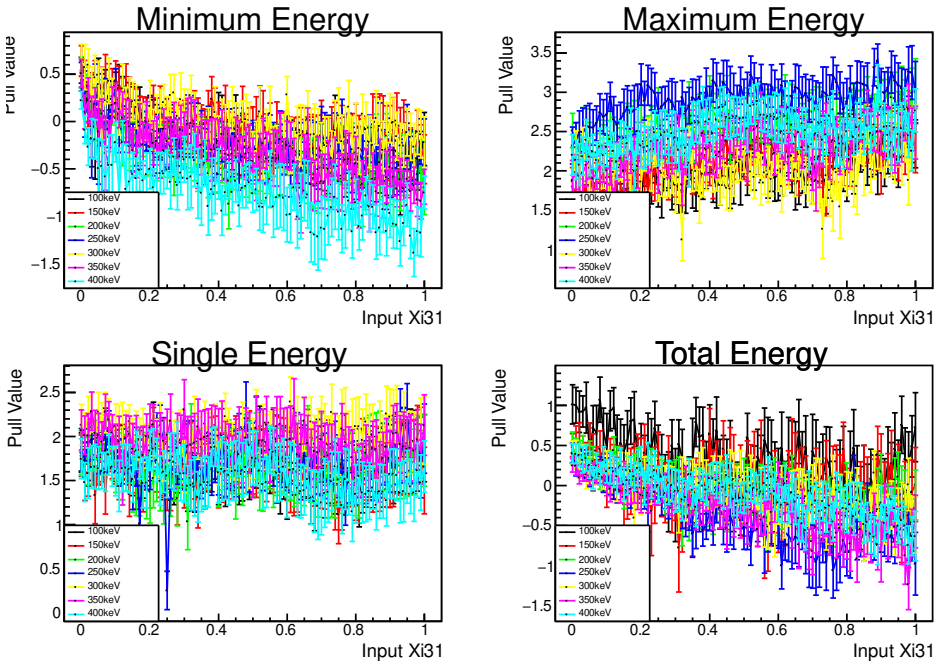

Figure 4.47 – Pull value of each average extracted ξ_{31} value versus the input ξ_{31} value. Each color presents and energy threshold cut applied on the samples. The results are for **single observable fit** with the **background subtracted**.

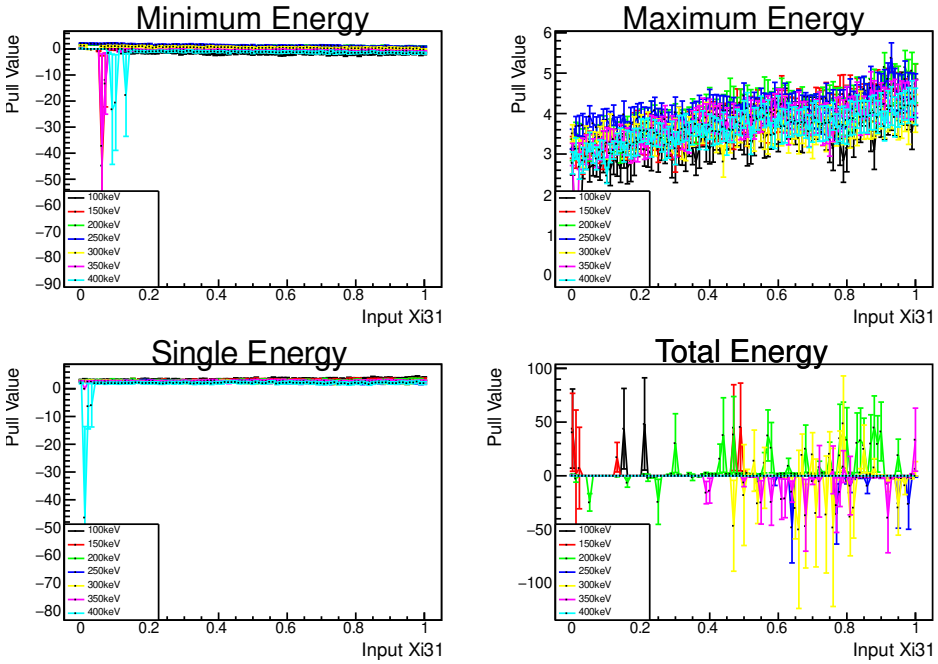

Figure 4.49 – Pull value of each average extracted ξ_{31} value versus the input ξ_{31} value. Each color presents and energy threshold cut applied on the samples. The results are for **single observable fit** with the **background PDF added** to the fitting PDF. Values with straight line at 0 value (or values at exactly 0), are fits that did not pass the χ^2/NDF less than 5 condition.

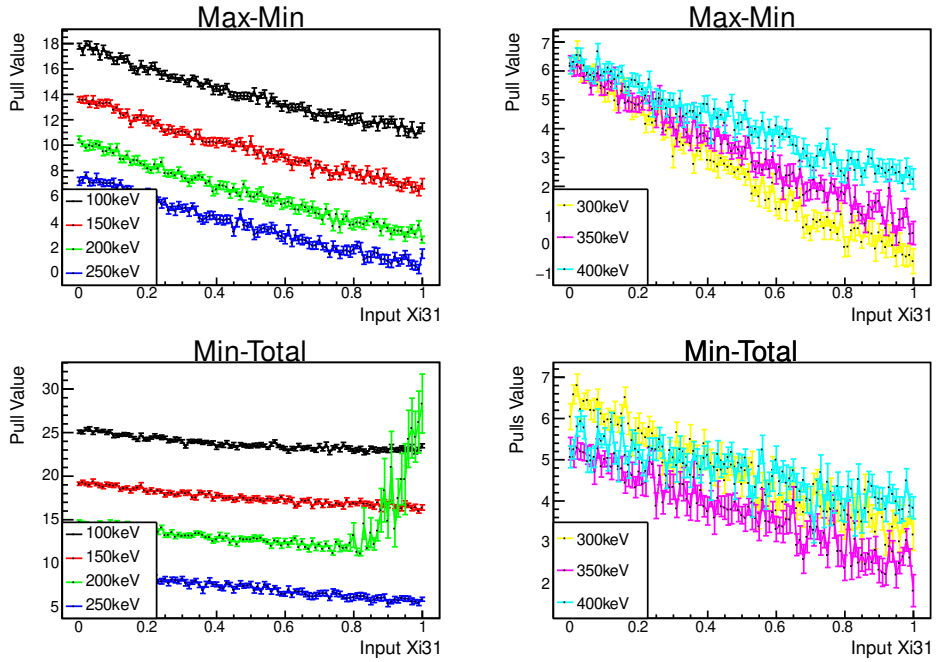

Figure 4.48 – Pull value of each average extracted ξ_{31} value versus the input ξ_{31} value. Each color presents and energy threshold cut applied on the samples. The results are for **simultaneous observable fit** with the **background subtracted**.

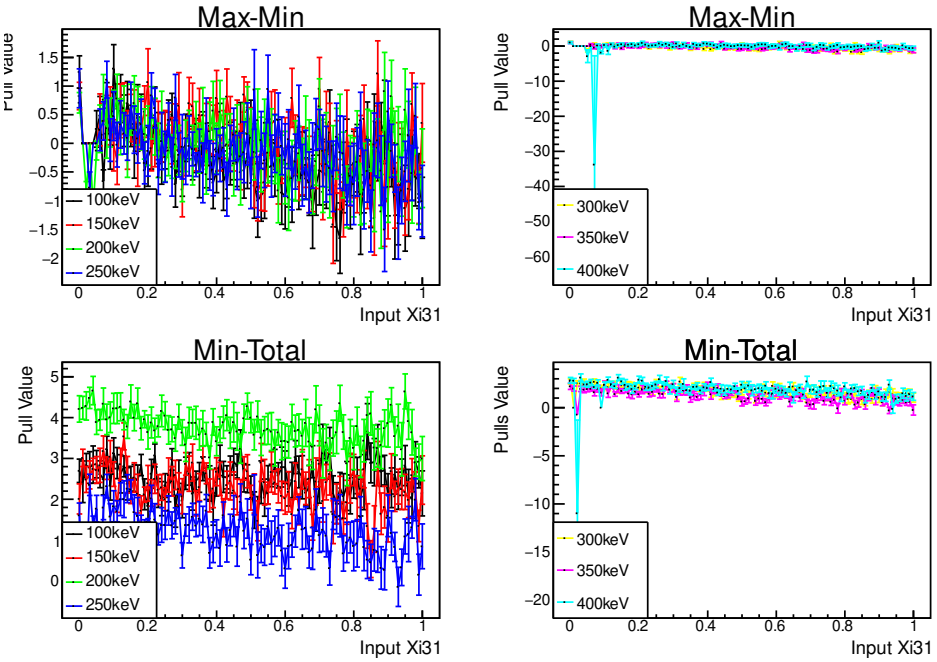

Figure 4.50 – Pull value of each average extracted ξ_{31} value versus the input ξ_{31} value. Each color presents and energy threshold cut applied on the samples. The results are for **simultaneous observable fit** with the **background PDF added** to the fitting PDF.

I extract the sensitivity of SuperNEMO using the single observable fit for minimum energy distribution, with an energy threshold cut at 300 keV. The choice is made because this method gives the least bias with the smallest errors, adding the good pull distribution ranging from -0.5 to 0.5.

The sensitivity result is presented for SSD (ξ_{31} = 0.373) and HSD (ξ_{31} = 0) values. The statistical errors are taken from the fits and the systematic from energy threshold cut variation. A visualization of the results is shown in figure 4.51, and they are :

- **SSD (ξ_{31} = 0.373) at 300 keV :** ξ_{31} = 0.365 $\pm$ 0.039 (stat) - 0.037 (sys) + 0.001 (sys)

- **HSD (ξ_{31} = 0.00) at 300 keV :** ξ_{31} = 0.0085 $\pm$ 0.029 (stat) - 0.0047 (sys)

The SSD results are presented in figure 4.52, where I plot the effective value of g_A versus the M_{GT-3} nuclear matrix elements calculations. The curve for the case of SSD value at 0.373 is plotted in dashed green. For the QRPA calculations, it is in solid blue for Argonne and solid yellow for CD-Bonn. Plotted also is the Shell model calculations for the different methods(GCN, JUN and JJ). The result of this study is plotted in solid black color, with the 2σ error in dashed red color. we can see that the extracted value using the SuperNEMO setup in the SSD case is in a good agreement with the SSD input value.

We see that within a 2σ band, if the SSD model is confirmed by the SuperNEMO measurements, this could lead to seeing incompatibilities with the nuclear models, whether Shell Model or QRPA.

The same measurement was performed by a calorimeter detector, where they measure only the total energy of the decay. I present the result in case of using the same method but with total energy distribution fit in figure 4.53. Such measurements will not be able to exclude these different nuclear models if the SSD is confirmed experimentally.

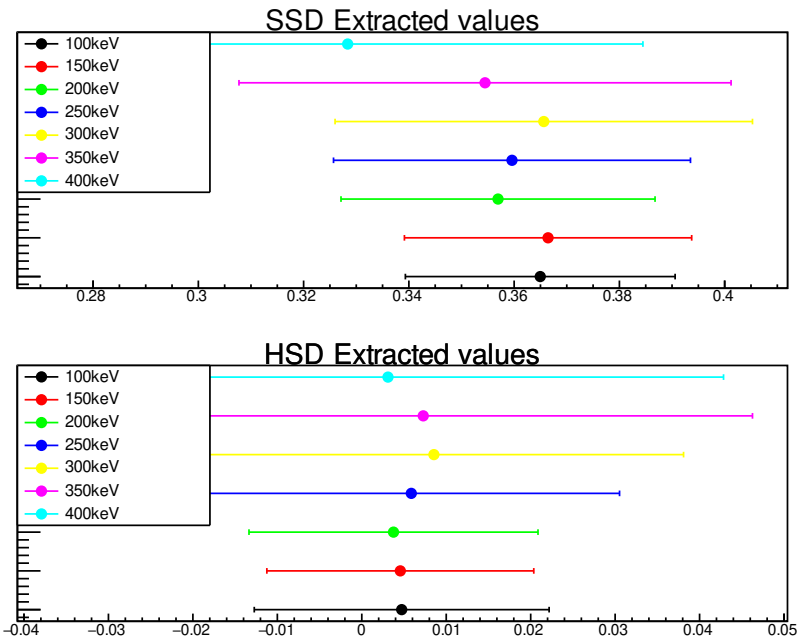

Figure 4.51 – Extracted value of ξ_{31} for an input of, to the top : 0.37 (SSD = 0.373) and to the bottom 0.0 (HSD). The different point represent the different energy threshold cuts applied, the errors shown are the statistical errors from averaged error value.

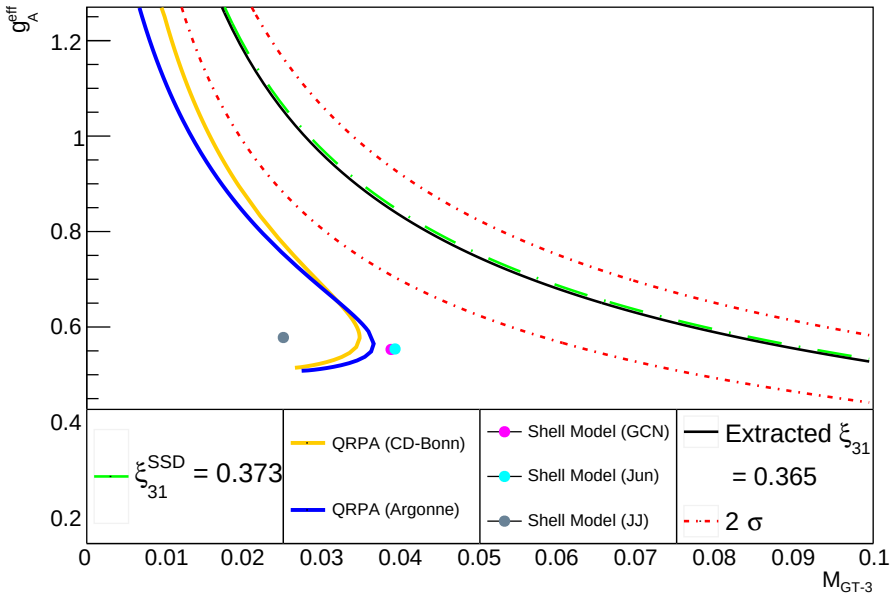

Figure 4.52 – Possible values of g_A^{eff} versus M_{GT-3}. The SSD value for ^{82}Se is plotted in the plane in bright green. The theoretical models of QRPA and shell model are presented. The curve corresponding to the results extracted for an input ξ_{31} = 0.37 is shown in solid black line, for which the fitted ξ_{31} using minimum energy distribution fit gives the value is ξ_{31} = 0.365 $\pm$ 0.039 (stat) - 0.037 (sys) + 0.001 (sys). The statistical + systematic errors are also shown in pointed red curve. The statistical errors are multiplied by 1.264 which is the value of the sigma of the pull distribution in 4.30; which represents the underestimation of the errors extracted.

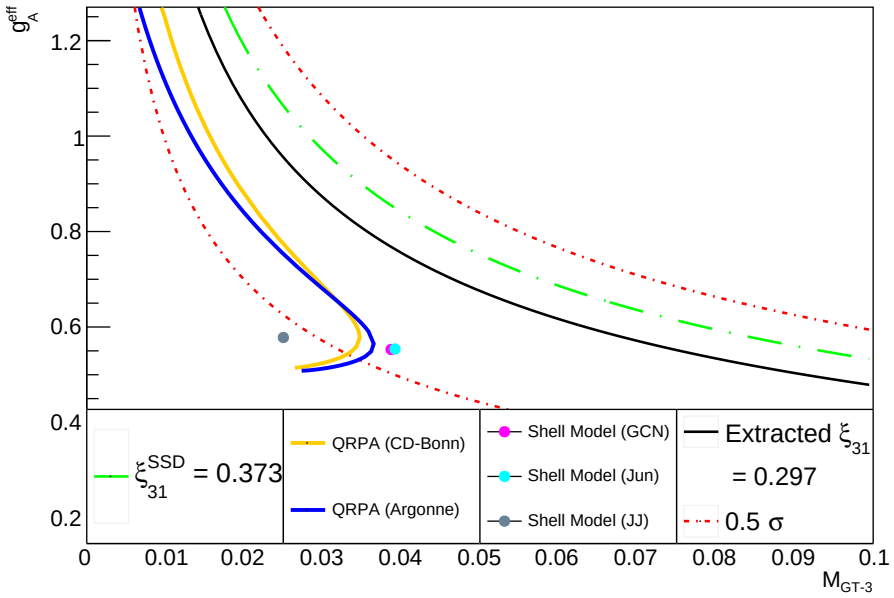

Figure 4.53 – Possible values of g_A^{eff} versus M_{GT-3}. The SSD value for ^{82}Se is plotted in the plane in bright green. The theoretical models of QRPA and shell model are presented. The curve corresponding to a sample generated with ξ_{31} = 0.37 is shown in solid black line, for which the fitted ξ_{31} value using the most sensitive method but with the total energy distribution fit is 0.2967 $\pm$ 0.2969 (stat) + 0.0815 (sys) - 0.06127 (sys). The statistical + systematic errors are also shown in pointed red curve.The statistical errors are multiplied by 1.33 which is the value of the sigma of the pull distribution in 4.31 ; which represents the underestimation of the errors extracted.

4.4.3 . Scintillation Energy Quenching

The previous analysis weren't exactly realistic as they didn't take into account the light quenching that occurs in the scintillators. The phenomena appears for low energy electrons, where the high ionization density induces a saturation of molecules capable of emitting scintillation light and this decreases the detected compared to the real energy. So, spectrum distortion is expected by this light non-linearity. The quenching follows Birks scintillation quenching [77] [43], where detector-specific suppression of the "visible" energy with respect to the local "deposited" energy by ionizing particles. this is due to intrinsic saturation effects in light-emitting scintillators or electron-ion recombination effects. The higher the local deposited ionization density (lower energy particles) the larger the quenching.

In addition to this light quenching, additional light induced by Cherenkov can be produced for electrons above a given energy : electromagnetic radiation emitted

when an electron passes through a dielectric medium at a speed greater than the phase velocity of light in that medium. This leads to an excess of detected light compared to light expected by scintillation, and an overestimation of the energy.

The effect of quenching correction depends on the calibration points. These points are the energies of the calibration source used. We take the non-linearity curve from the NEMO-3 calculations, with the calibration points at 0.482 and 0.976 MeV, which are the energies of the internal conversion electrons of the ^{207}Bi calibration source. Between these two points the non-linearity curve, strongly constrained by the energy calibration, is almost flat to achieve a linearity in correction. Below 0.482 MeV or above 0.976 MeV, the non-linearity slightly increases the energies of the particles : below 0.482 MeV up to $\sim 4\%$ at 150 keV and above 0.976 MeV up to $\sim 2\%$ at 3 MeV, see figure 4.54.

In Figure 4.54 three graphs are presented : Blue represents the mean value of the correction of energy, the other two represent the correction shifted to its upper error (red) and the correction shifted to its lower error (green). The energy quenching correction is applied on the individual energies of the electrons of the events of the samples. Then the analysis is performed three times on the same samples with the mean correction, applying a fitting PDF with either the mean correction or the correction shifted by its upper or lower errors. This will be performed for the different fitting methods mentioned before : with background subtraction or background fitting, using single observable fit or simultaneous fits. Also, I will study the effect of applying this quenching to the samples and not the fitting PDF and then to both, to finally be able to find the best method to extract the sensitivity.

Different Methods Used with Energy Quenched Samples with the Mean Value

From here on, the mean energy quenching correciton value is applied to the individual electron energies of the events in the samples. I will apply the different previously defined fitting methods on the samples, in the two cases of taking and not taking into account the quenching in the fitting PDF, to see the effect on the sensitivity. After doing so, I will see what values I obtain with the same chosen method for the samples with upper and lower errors applied on them, to finally extract the systematics introduced by the quenching correction.

Without Adding Quenching to the Fitting PDF In the case where we don't include the quenching factor to the fitting PDF, the final results of the fits in most cases doesn't pass the $\chi^2/\text{NDF} < 5$ condition, or if it passes it produces a pattern with large bias. So this approach is not considered. I only show the plots for the method that was chosen in the case of non-quenched energy, in figure 4.55.

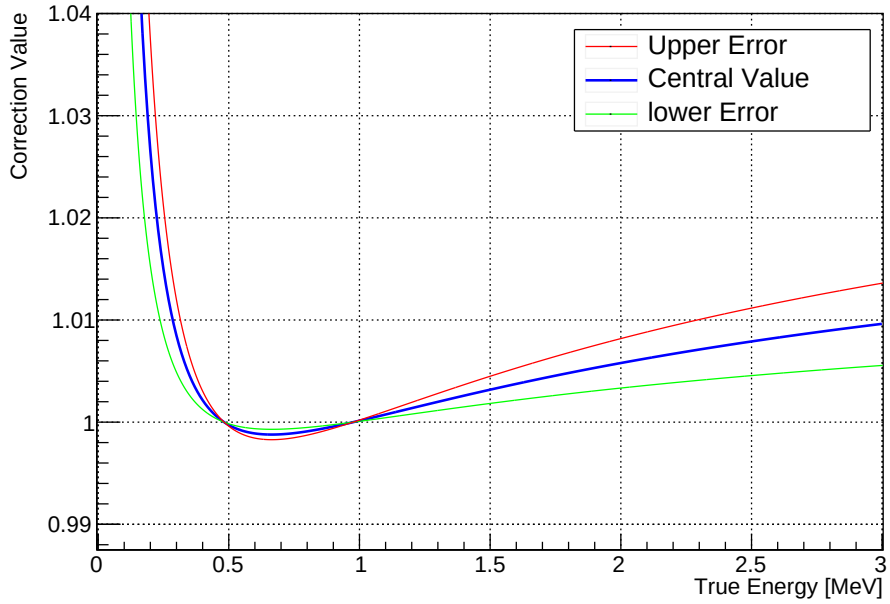

Figure 4.54 – Correction function which should be applied to the electron energy spectrum to take into account the quenching of the scintillation light. This correction takes into account the two calibration points of ^{207}Bi, ensuring a good linearity between the two points at 0.482 MeV and 0.976 MeV.

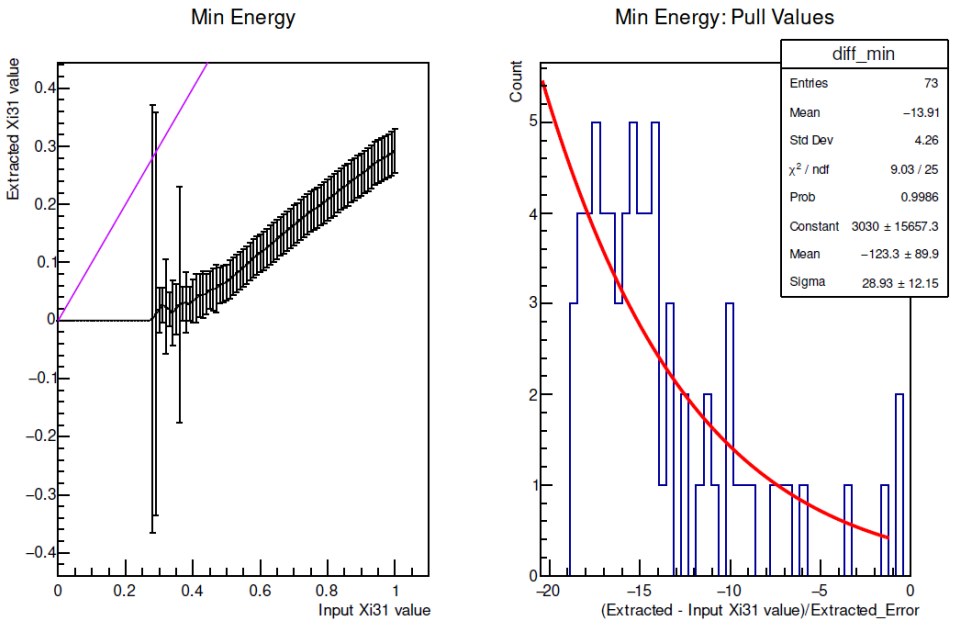

Figure 4.55 – Results of the fits of the samples with **G_0, G_2 and background**, with **mean energy quenching correction applied to sample events but not to the fitting PDF**; the **background is subtracted** from the sample. To the left : Results of the average extracted ξ_{31} values (of 20 fitted samples) versus the input ξ_{31}. The error bars represent the error on the average extracted values. The violet line represents the case if the extracted values are identical to the input values. To the right : The pull distribution of the extracted results (i.e each point presents the mean of the pull of the 20 samples), fitted with a Gaussian, where the mean and sigma would represent the correctness of the fit. To the top, results of the fits of minimum energy; to the bottom for maximum energy. Energy threshold cut at 300 keV.

Adding Quenching to the Fitting PDF Here we apply the energy quenching factor to the fitting PDF and proceed with the usual fitting methods we introduced.

- Figures 4.56 and 4.57 use the single distribution fit while subtracting the background from the sample. The minimum energy fits seem to have a positive bias at low input ξ_{31} and a slight negative bias for input values above 0.6. Looking at the pull distribution, the mean of the Gaussian fit is at 0.047 and the sigma is at 1.37, showing an acceptable agreement with the expected value for mean at "zero" and a slightly underestimation of the errors by an increase of the sigma from the ideal value at "one". The other obseravables give biased values, so they are not optimal for our work.

- Figures 4.58 and 4.59 use the single distribution fit while adding the back-

ground PDF to the fitting function. All observables have a bias, either positive (maximum and single energies) or negative (minimum energy), or mixed bias as in total energy. As there is large bias, this method is not taken into account.

- 4.60 and 4.61 are simultaneous fits of energy distributions, while subtracting the background from the samples. For max-min and all distributions fit, the fits did not pass the χ^2/NDF < 5 condition, hence there are no plots in this case. For minimum-total and single-total fits, there exists a negative (underestimation of G_2 contribution) bias and positive (overestimation of G_2 contribution) bias, respectively. Because of the reasons mentioned, this method is not considered for calculation of the sensitivity.

- 4.62 and 4.63 are results for the simultaneous fits while including the background PDF into the fitting PDF. The results are similar to those of samples with no quenching applied. In max-min distribution we observe a bias for input values < 0.1, this was explained before : roofit extracts very small values and applying a weighted average creates this bias. Results from this method have bias, and hence this method was also not considered.

Summarizing, table 4.9 compares, the different results. The method using single observable fits while subtracting background events from the sample gave the best results in the case of minimum energy fit. So this is going to be used to calculate the sensitivity of SuperNEMO.

Fitted energy spectra	Mean of Pull	Sigma of Pull	Comment
Single Observable Fit			
Background Subtracted			
Minimum	0.05 ± 0.03	1.3 ± 0.03	
Maximum	2.47 ± 0.03	1.36 ± 0.02	
Single	1.95 ± 0.03	1.46 ± 0.03	
Total	-0.13 ± 0.03	1.25 ± 0.03	large bias
Background in the fitting PDF			
Minimum	-1.58 ± 0.05	2.05 ± 0.04	
Maximum	4.74 ± 0.04	1.83 ± 0.05	
Single	3.30 ± 0.00	1.83 ± 0.04	
Total	0.45 ± 0.04	1.65 ± 0.04	large fluctuations
Simultaneous Observable Fit			
Background Subtracted			
Maximum-Minimum	-	-	no results
Minimum-Total	-5.21 ± 0.08	3.24 ± 0.06	
Single-Total	9.92 ± 0.05	1.64 ± 0.04	
All distributions	-	-	no results
Background in the fitting PDF			
Maximum-Minimum	66.52 ± 48.45	95.98 ± 12.10	very large pull value
Minimum-Total	-0.49 ± 0.06	2.71 ± 0.05	
Single-Total	4.80 ± 0.04	1.80 ± 0.03	
All distributions	6.63 ± 3.49	11.19 ± 2.73	very large pull value

Table 4.9 – The different Pull distribution "mean" and "sigma" obtained using different single parameter, or simultaneously, fitted quenched energy spectra with mean quenching value, of samples with background, in the case of subtracting the background and in the case of adding the background to the fitting PDF.

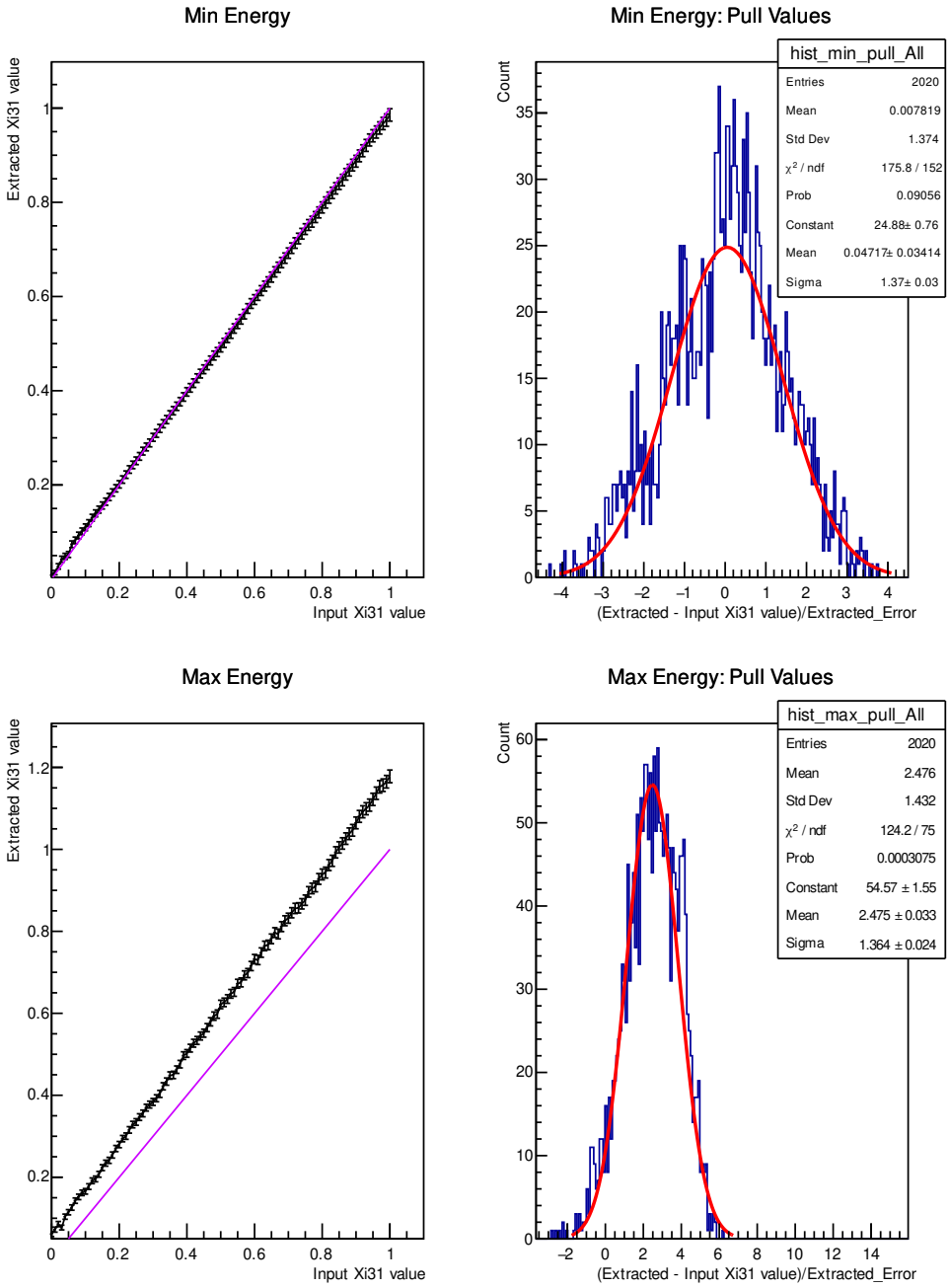

Figure 4.56 – Results of the **single observable fits** of the **energy quenched samples and fitting PDF with the mean value** with G_0, G_2 and **quenched background subtracted** from the sample. To the left : Results of the average extracted ξ_{31} values (of 20 fitted samples) versus the input ξ_{31}. The error bars represent the error on the average extracted values. The violet line represents the case if the extracted values are identical to the input values. To the right : The pull distribution of the extracted results (i.e each point presents the mean of the pull of the 20 samples), fitted with a Gaussian, where the mean and sigma would represent the correctness of the fit. To the top, results of the fits of minimum energy; to the bottom for maximum distributions. Energy threshold cut at 300 keV.

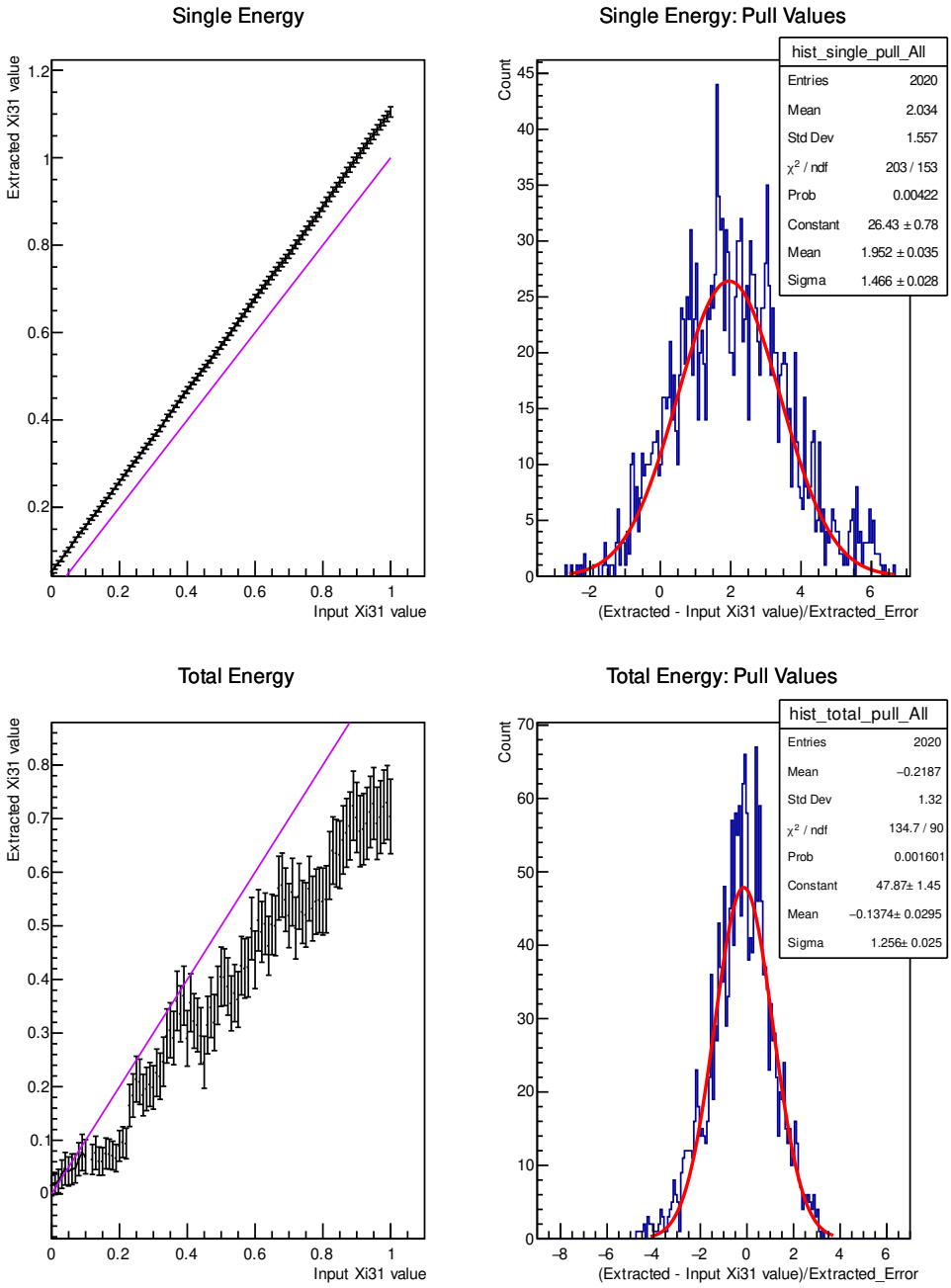

Figure 4.57 – Results of the **single observable fits** of the **energy quenched samples and fitting PDF with the mean value** with G_0, G_2 and **quenched background subtracted** from the sample. To the left : Results of the average extracted ξ_{31} values (of 20 fitted samples) versus the input ξ_{31}. The error bars represent the error on the average extracted values. The violet line represents the case if the extracted values are identical to the input values. To the right : The pull distribution of the extracted results (i.e each point presents the mean of the pull of the 20 samples), fitted with a Gaussian, where the mean and sigma would represent the correctness of the fit. To the top, results of the fits of single energy; to the bottom for total distributions. Energy threshold cut at 300 keV.

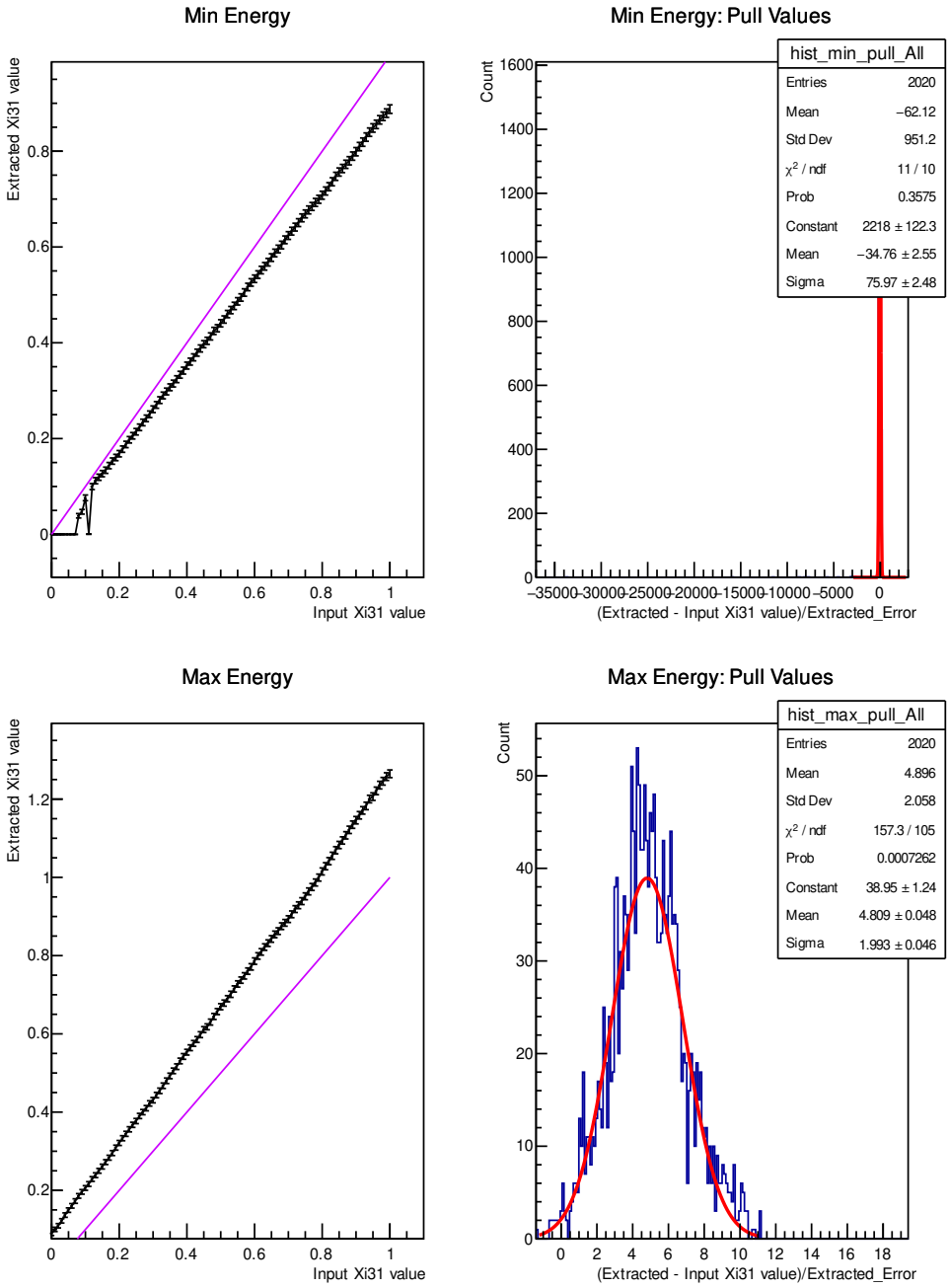

Figure 4.58 – Results of the **single observable fits** of the **energy quenched samples and fitting PDF with the mean value** with G_0, G_2 and **quenched background PDF added** to fitting PDF. To the left : Results of the average extracted ξ_{31} values (of 20 fitted samples) versus the input ξ_{31}. The error bars represent the error on the average extracted values. The violet line represents the case if the extracted values are identical to the input values. To the right : The pull distribution of the extracted results (i.e each point presents the mean of the pull of the 20 samples), fitted with a Gaussian, where the mean and sigma would represent the correctness of the fit. To the top, results of the fits of minimum energy; to the bottom for maximum distributions. Energy threshold cut at 300 keV.

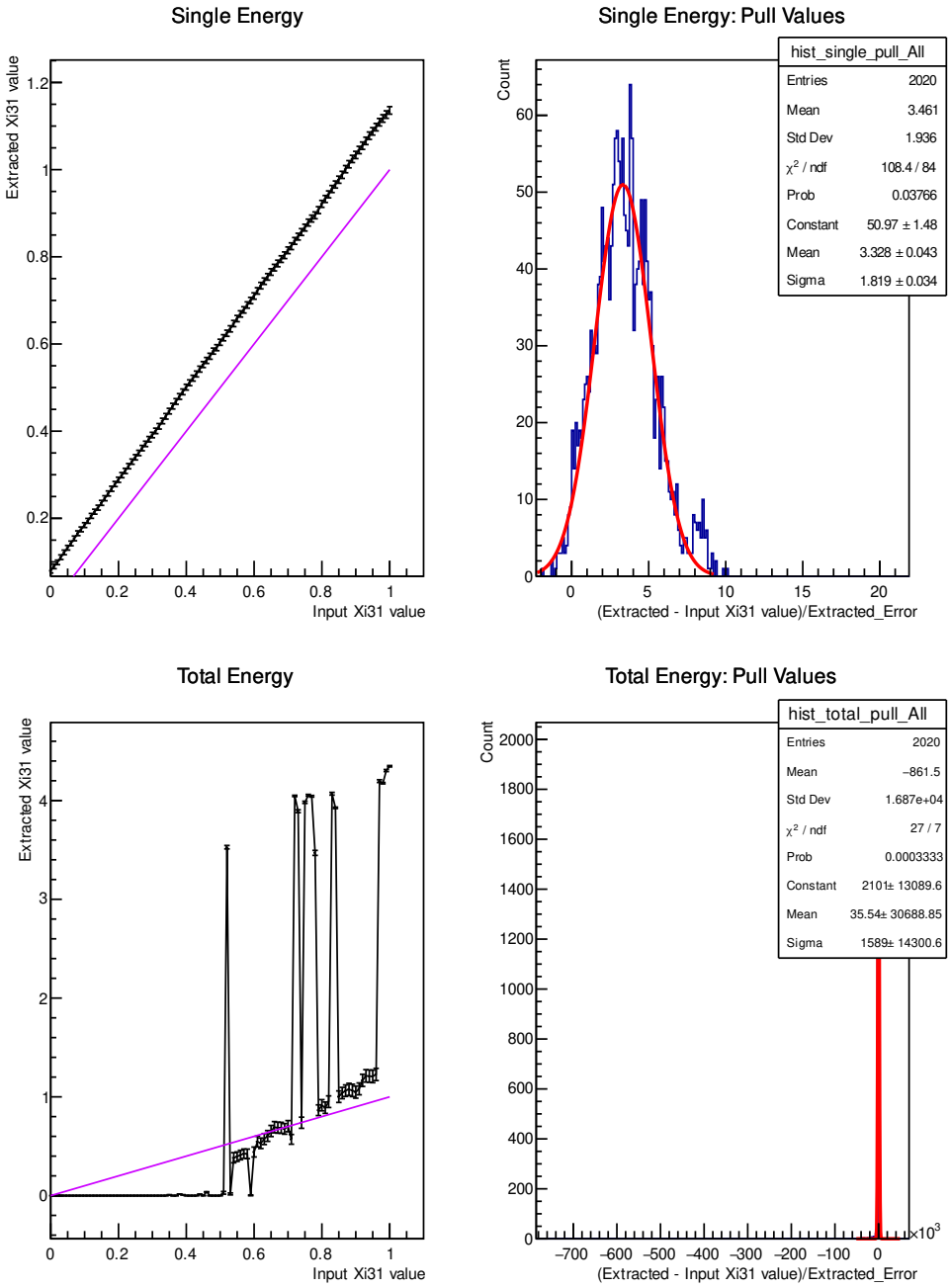

Figure 4.59 – Results of the **single observable fits** of the **energy quenched samples and fitting PDF with the mean value** with G_0, G_2 and **quenched background PDF added** to fitting PDF. To the left : Results of the average extracted ξ_{31} values (of 20 fitted samples) versus the input ξ_{31}. The error bars represent the error on the average extracted values. The violet line represents the case if the extracted values are identical to the input values. To the right : The pull distribution of the extracted results (i.e each point presents the mean of the pull of the 20 samples), fitted with a Gaussian, where the mean and sigma would represent the correctness of the fit. To the top, results of the fits of single energy; to the bottom for total distributions. Energy threshold cut at 300 keV.

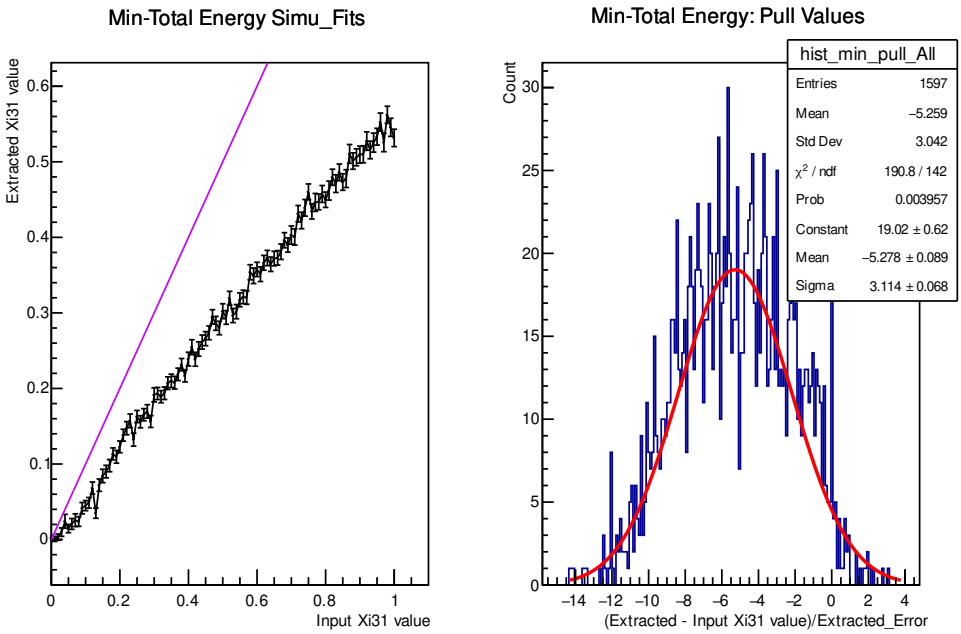

Figure 4.60 – Results of the **simultaneous fits** of the **energy quenched samples and fitting PDF with the mean value** with G_0, G_2 and **quenched background subtracted** from the sample. To the left : Results of the average extracted ξ_{31} values (of 20 fitted samples) versus the input ξ_{31}. The error bars represent the error on the average extracted values. The violet line represents the case if the extracted values are identical to the input values. To the right : The pull distribution of the extracted results (i.e each point presents the mean of the pull of the 20 samples), fitted with a Gaussian, where the mean and sigma would represent the correctness of the fit. To the top, results of the fits of maximum-minimum energy; to the bottom for minimum-total distributions. Energy threshold cut at 300 keV.

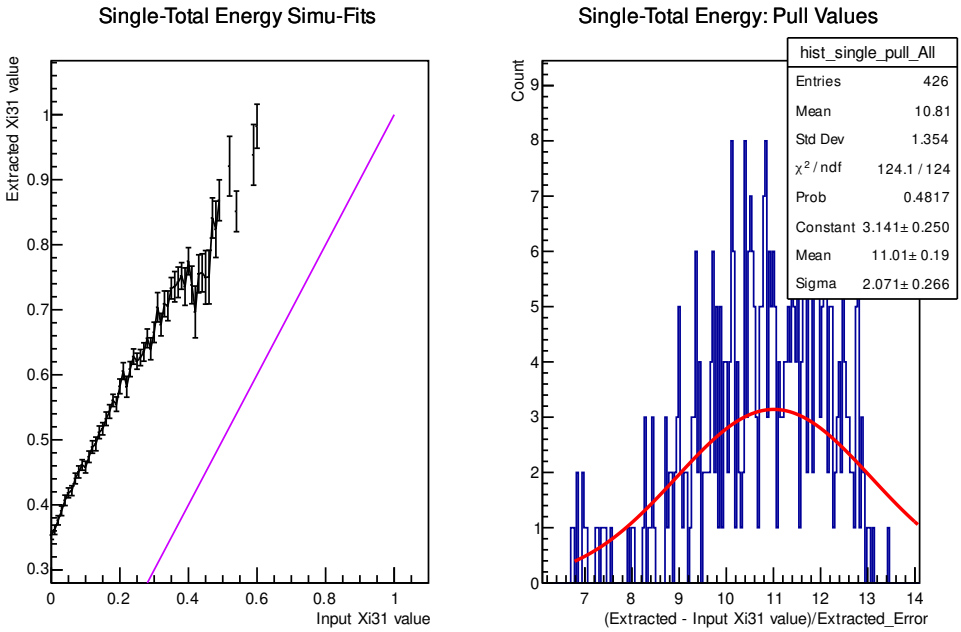

Figure 4.61 – Results of the **simultaneous fits** of the **energy quenched samples and fitting PDF with the mean value** with G_0, G_2 and **quenched background subtracted** from the sample. To the left : Results of the average extracted ξ_{31} values (of 20 fitted samples) versus the input ξ_{31}. The error bars represent the error on the average extracted values. The violet line represents the case if the extracted values are identical to the input values. To the right : The pull distribution of the extracted results (i.e each point presents the mean of the pull of the 20 samples), fitted with a Gaussian, where the mean and sigma would represent the correctness of the fit. To the top, results of the fits of total-single energy; to the bottom for all energy distributions. Energy threshold cut at 300 keV.

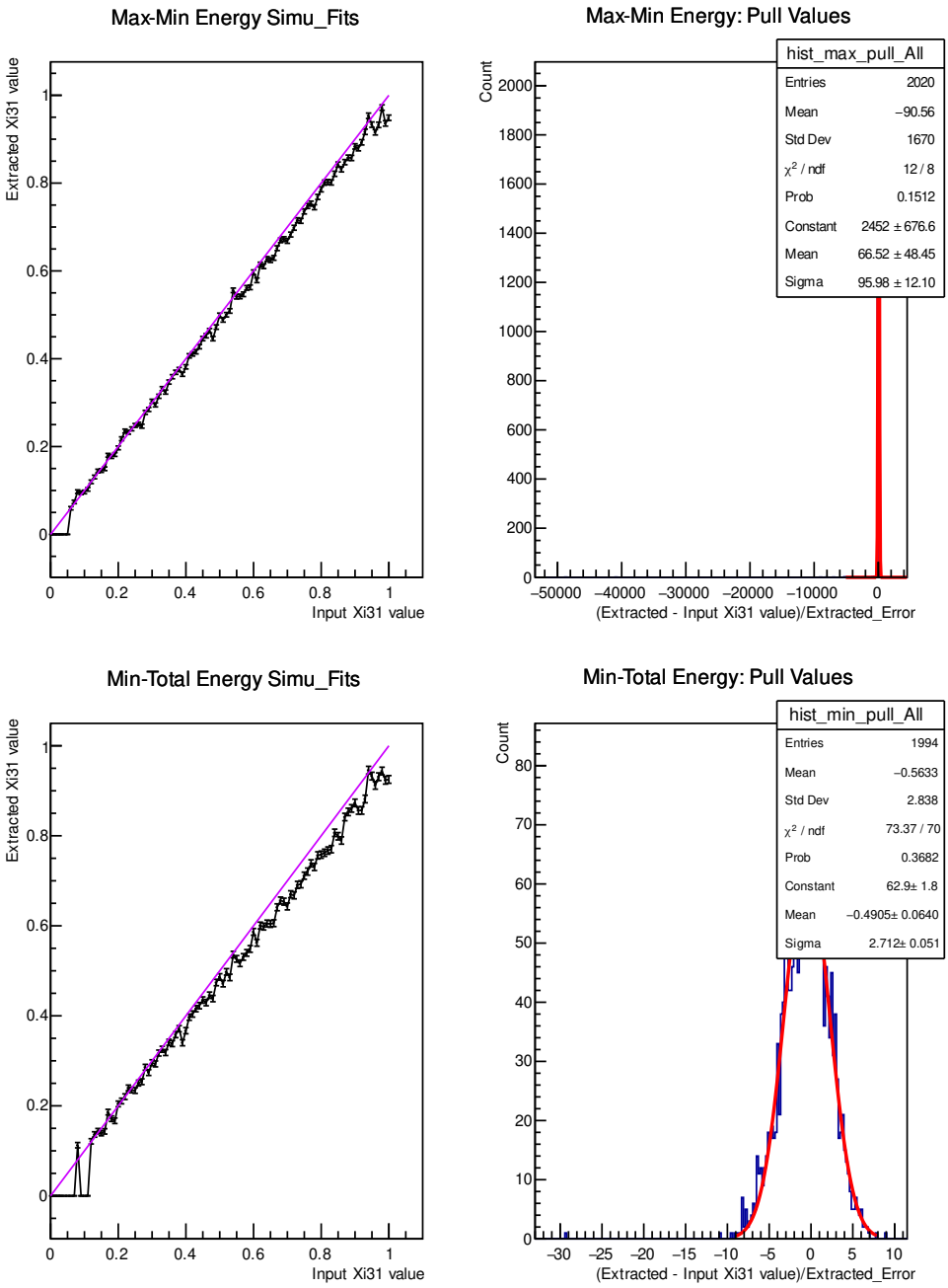

Figure 4.62 – Results of the **simultaneous fits** of the **energy quenched samples and fitting PDF with the mean value** with G_0, G_2 and **quenched background PDF added** to the fitting PDF. To the left : Results of the average extracted ξ_{31} values (of 20 fitted samples) versus the input ξ_{31}. The error bars represent the error on the average extracted values. The violet line represents the case if the extracted values are identical to the input values. To the right : The pull distribution of the extracted results (i.e each point presents the mean of the pull of the 20 samples), fitted with a Gaussian, where the mean and sigma would represent the correctness of the fit. To the top, results of the fits of maximum-minimum energy; to the bottom for minimum-total distributions. Energy threshold cut at 300 keV.

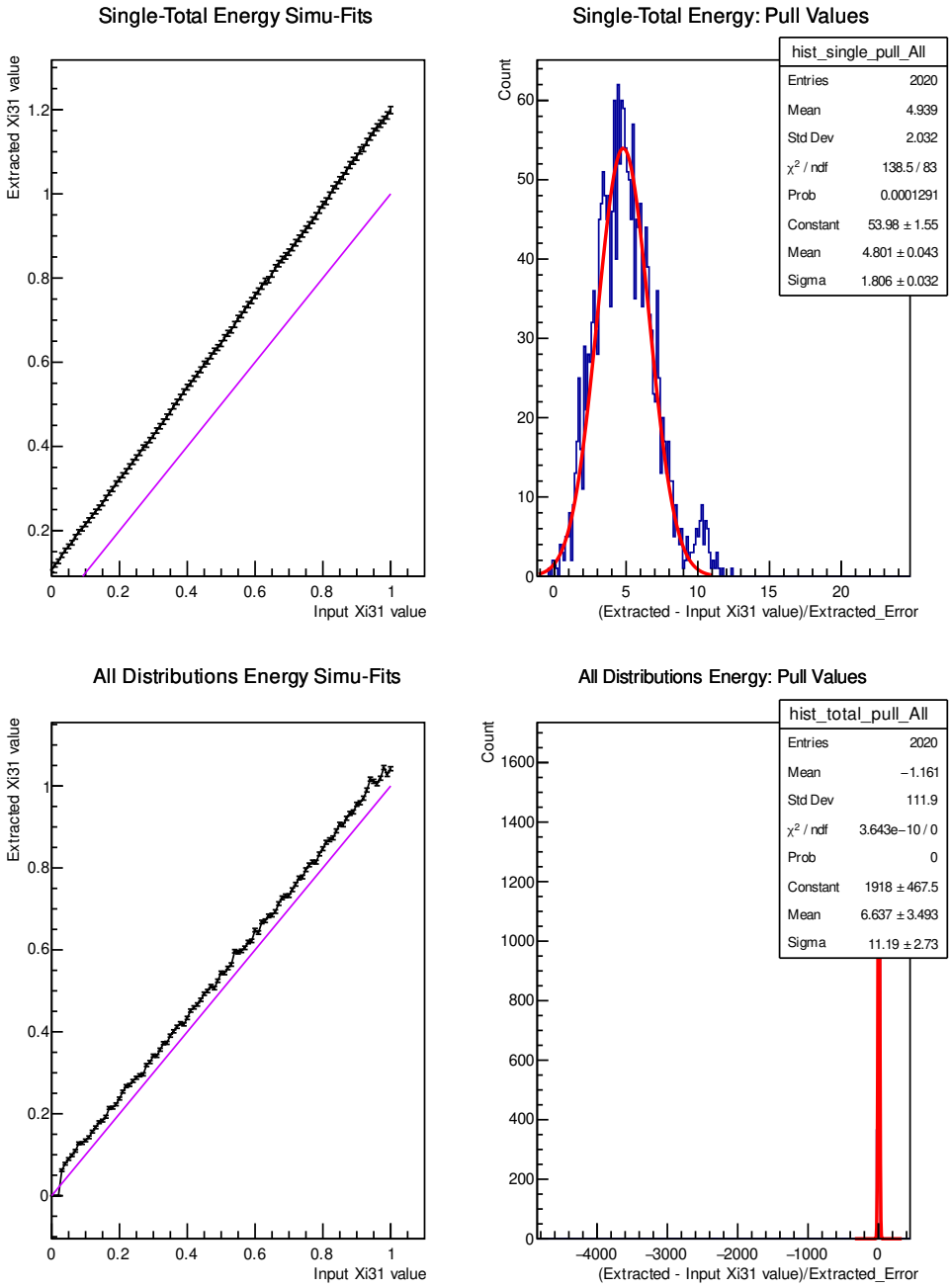

Figure 4.63 – Results of the **simultaneous fits** of the **energy quenched samples and fitting PDF with the mean value** with G_0, G_2 and **quenched background PDF added** to the fitting PDF. To the left : Results of the average extracted ξ_{31} values (of 20 fitted samples) versus the input ξ_{31}. The error bars represent the error on the average extracted values. The violet line represents the case if the extracted values are identical to the input values. To the right : The pull distribution of the extracted results (i.e each point presents the mean of the pull of the 20 samples), fitted with a Gaussian, where the mean and sigma would represent the correctness of the fit. To the top, results of the fits of total-single energy; to the bottom for all energy distributions. Energy threshold cut at 300 keV.

Calculating the Results using Upper and Lower Errors on Quenching Value to Calculate the Systematics

Using the method of single observable fit with minimum energy distribution and subtracting background from the sample, with mean quenching correction value applied on the samples and on the fitting PDF. Using the same method, we extract the results in the case of upper and lower errors on this mean quenching factor applied to the fitting PDF (the samples have the mean correction value applied on them), to have a better description of the systematic errors on the ξ_{31} values. These systematics result from the introduction of energy quenching correction. The result of this study is presented in figure 4.64 for the case of lower error bound and in figure 4.65 for upper error values. We see a different behavior resulting from applying the three corrections. In the case of low error correction, a positive bias appears for all extracted values, while for upper error correction there is a negative bias. The pull sigma and mean values of the minimum energy distribution fits are 1.07 $\pm$ 1.32 for low error quenching factor and -0.97 $\pm$ 1.38 for upper error correction, compared to 0.047 $\pm$ 1.37 for the mean value correction. These biases are taken into account in the systematics due to energy quenching.

The bias for the error on the energy quenching correction values could be understood from the curves in 4.54. Looking at the correction curves below 0.5 MeV, the lower energy correction (which is applied to the fitting PDF) increases the probability of low energy electrons compared to the mean correction value (which is applied to the samples). Since G_2 is characterized by the emission of more electrons at low energies, the fit attributes more G_2 events than what exists, and ends up over estimating its contribution, and hence creates this bias in the extracted values. The effect is opposite for the upper error on energy correction, in this case it decreases the probability at low energies than that of the mean correction value, which induces smaller G_2 contribution, and it ends up underestimating the G_2 contribution, and hence a negative bias is created.

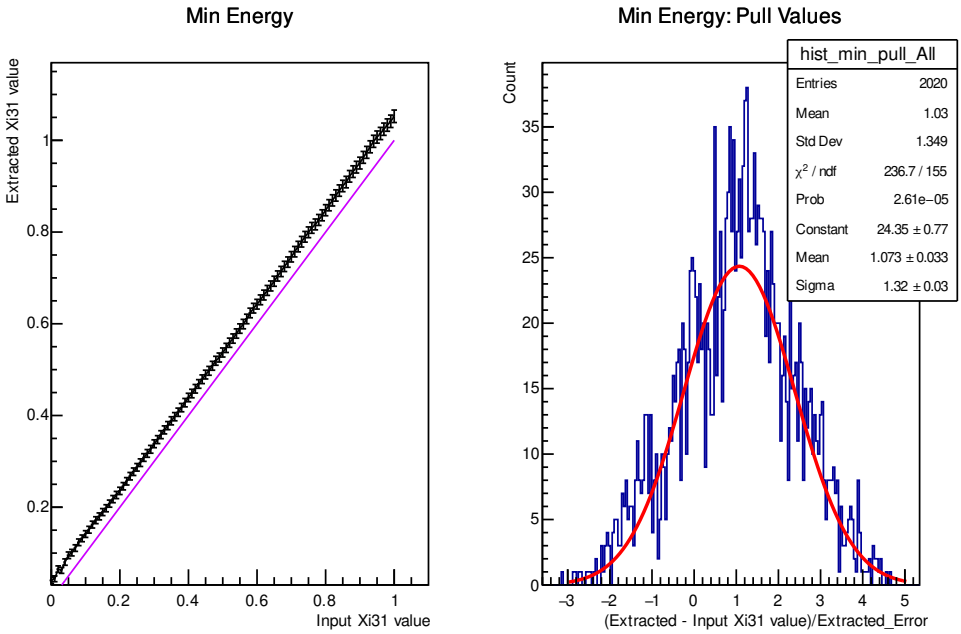

Figure 4.64 – Results of the **single parameter fits** of the **energy quenched samples and fitting PDF with the lower error value** with G_0, G_2 and **quenched background subtracted** from sample. To the left : Results of the average extracted ξ_{31} values (of 20 fitted samples) versus the input ξ_{31}. The error bars represent the error on the average extracted values. The violet line represents the case if the extracted values are identical to the input values. To the right : The pull distribution of the extracted results (i.e each point presents the mean of the pull of the 20 samples), fitted with a Gaussian, where the mean and sigma would represent the correctness of the fit. The results are for the fits of minimum energy. Energy threshold cut at 300 [keV].

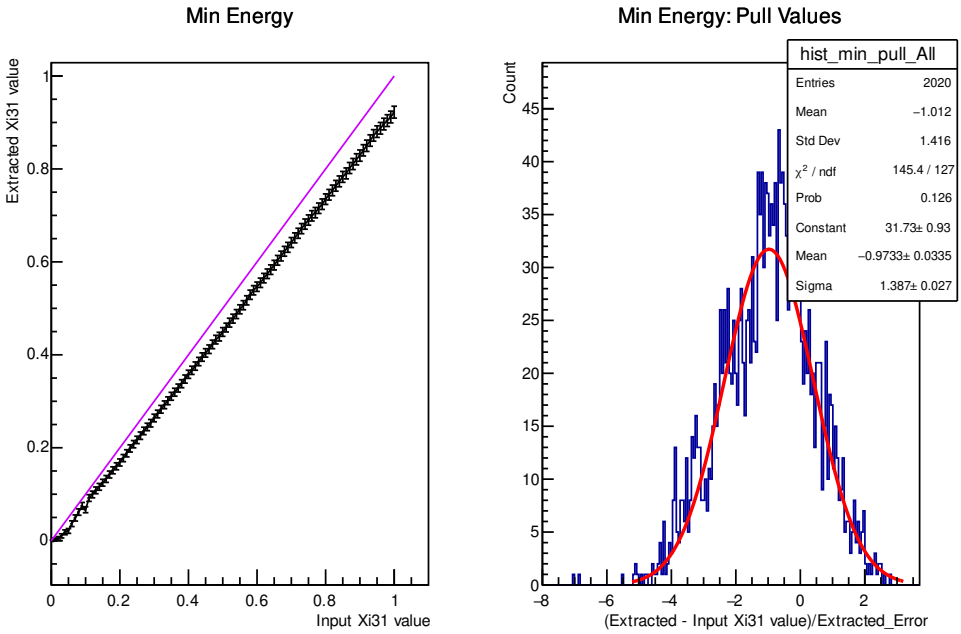

Figure 4.65 – Results of the **single parameter fits** of the **energy quenched samples and fitting PDF with the upper error value** with G_0, G_2 and **quenched background subtracted** from sample. To the left : Results of the average extracted ξ_{31} values (of 20 fitted samples) versus the input ξ_{31}. The error bars represent the error on the average extracted values. The violet line represents the case if the extracted values are identical to the input values. To the right : The pull distribution of the extracted results (i.e each point presents the mean of the pull of the 20 samples), fitted with a Gaussian, where the mean and sigma would represent the correctness of the fit. The results are for the fits of minimum energy. Energy threshold cut at 300 [keV].

Similar to the plots introduced before, I present the pull values of the extracted ξ_{31} versus the input ξ_{31} value, in figures 4.66, 4.67 and 4.68, this way we can observe the accuracy of the results. The observables that we have chosen, single observable fit for minimum energy distribution, the pull values are included in the range [-0.5, 0.5] for the 300 keV energy threshold cut in the case of correcting with the mean energy quenching value. For the case where we correct with the lower error value of quenching, the pulls fall into the range [-0.5, 1.5], reflecting the positive bias we observed before. For the case where we correct with the upper error value of quenching, the pulls fall into the range [-2, 0.5], reflecting the negative bias also observed before.

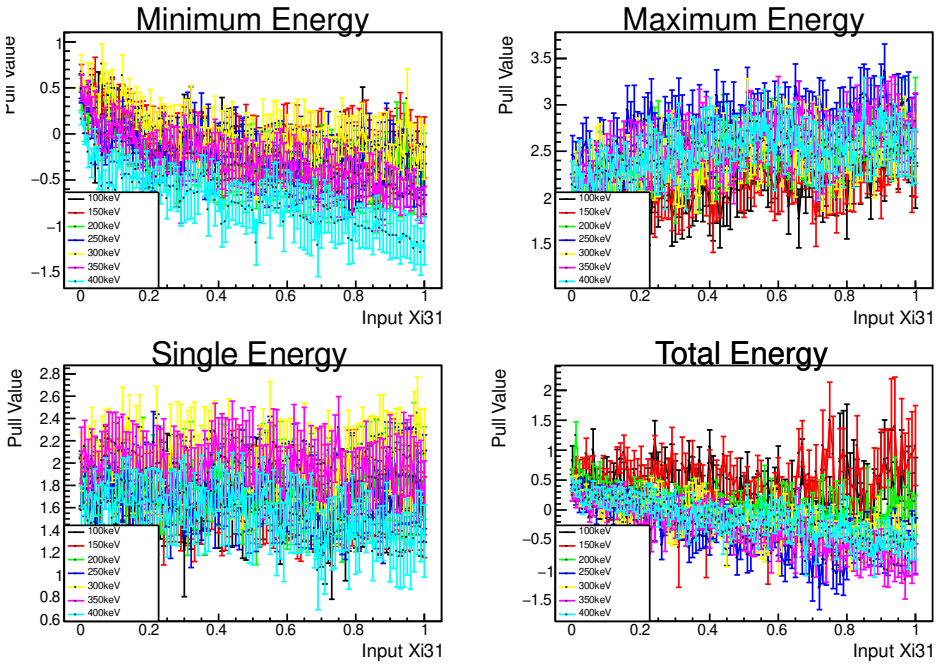

Figure 4.66 – Pull value of each average extracted ξ_{31} value versus the input ξ_{31} value. Each color presents and energy threshold cut applied on the samples. The results are for **single observable fi**t for energy quenched samples with the **mean value of quenching**, and **subtracting the background from the sample**.

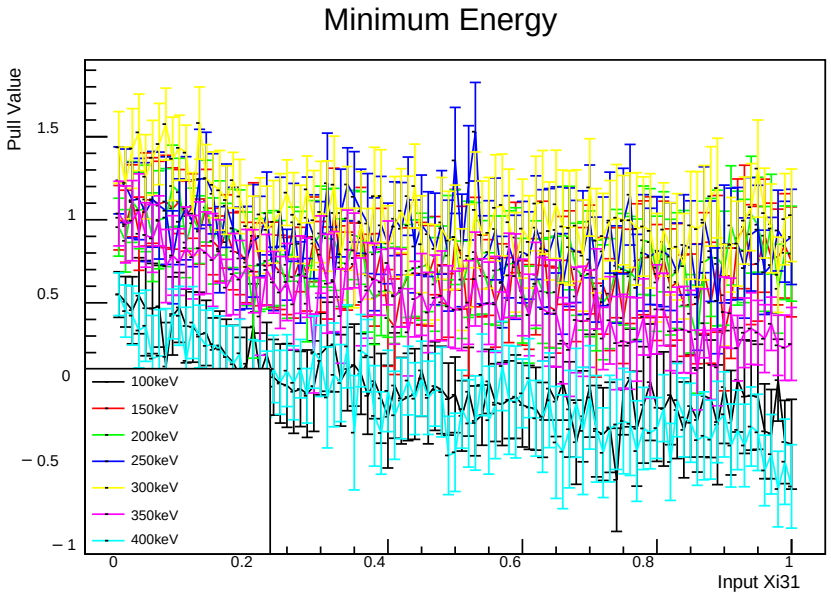

Figure 4.67 – Pull value of each average extracted ξ_{31} value versus the input ξ_{31} value. Each color presents and energy threshold cut applied on the samples. The results are for **single observable fit** for energy quenched samples with the **lower error value of quenching**, and **subtracting background from the sample**.

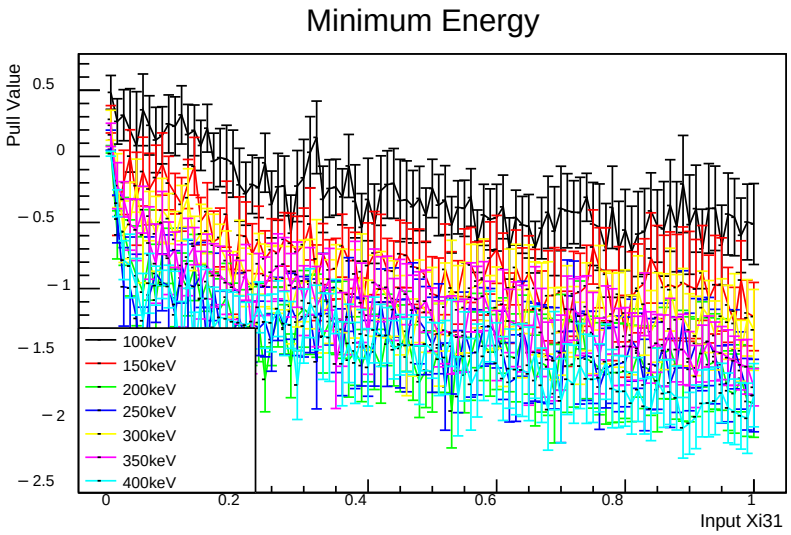

Figure 4.68 – Pull value of each average extracted ξ_{31} value versus the input ξ_{31} value. Each color presents and energy threshold cut applied on the samples. The results are for **single observable fit** for energy quenched samples with the **upper error value of quenching**, and **subtracting the background from the sample**.

Sensitivity of SuperNEMO Taking into Account Energy Quenching

As previously done, we find the sensitivity of SuperNEMO to the HSD and SSD values at $\xi_{31} = 0$ and $\xi_{31} = 0.373$, respectively. Using the single observable fit for the minimum energy distribution.

In figure 4.69, I present the extracted results form the analysis in the case of SSD (top) and HSD (bottom). From here we have :

- **SSD ($\xi_{31} = 0.373$) at 300 keV** : $\xi_{31} = 0.3669 \pm 0.0393$ (stat) + 0.0007 (sys energy cut) - 0.0392 (sys energy cut) + 0.0401 (sys quench) - 0.0384 (sys quench)

- **HSD ($\xi_{31} = 0.00$) at 300 keV** : $\xi_{31} = 0.00865 \pm 0.03261$ (stat) + 0.00221 (sys energy cut) - 0.00589 (sys energy cut) + 0.00728 (sys quench) - 0.03181 (sys quench)

The SSD results are presented in figure 4.70, where I plot the effective value of g_A versus the M_{GT-3} nuclear matrix elements calculations. The curve for the case of SSD value at 0.373 is plotted in dashed green. For the QRPA calculations, it is in solid blue for Argonne and solid yellow for CD-Bonn. Plotted also is the Shell model calculations for the different methods(GCN, JUN and JJ). The result

of this study is plotted in solid black color. The errors of this plot represent the 2σ error for 95% C.L in dashed red color. The statistical error was multiplied by 1.37, which represents the sigma of the pull distribution for the fits at 300 keV energy cut.

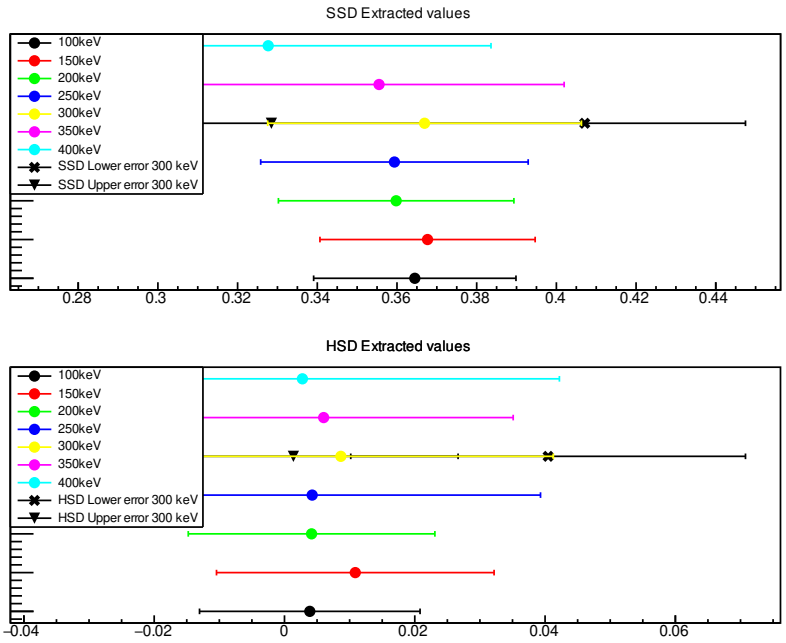

Figure 4.69 – The extracted value of ξ_{31} for an input of, to the top : 0.37 (SSD = 0.372) and to the bottom 0.0 (HSD) with the energy quenching correction added to both the samples and fitting PDF. The different point represent the different energy threshold cuts applied.

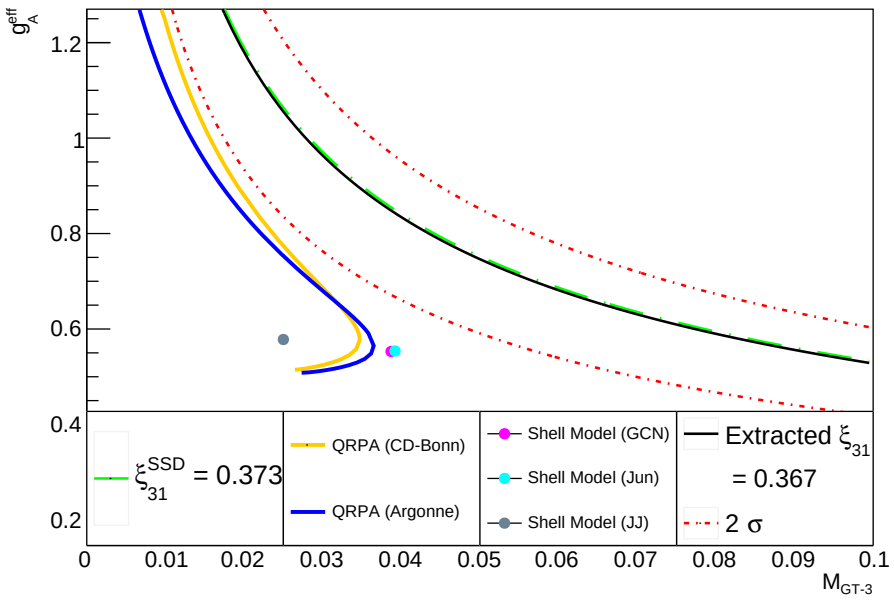

Figure 4.70 – Possible values of g_A^{eff} versus M_{GT-3}. The SSD value for ^{82}Se is plotted in the plane in dashed light green. The theoretical models of QRPA and shell model are presented. The fitted value from the SuperNEMO analysis is shown in the case where we take into account the energy quenching inside the scintillator, where the value is ξ_{31} = 0.3669 $\pm$ 0.0393 (stat) + 0.0007 (sys energy cut) - 0.0392 (sys energy cut) + 0.0401 (sys quench) - 0.0384 (sys quench), the errors are shown in red. The statistical error in the plot are multiplied by 1.37, which corresponds to the sigma of the pull distribution in figure 4.56; this value represents the underestimation in the error calculations.

A more advanced study can be performed to see how the sensitivity changes with the addition of the two phase space factors not taken into account during this analysis, G_{22} and G_4; and hence the addition of a second free parameter that is ξ_{51}, which would increase the uncertainty of the calculations.

In paragraph 4.2.3, I have mentioned that the two g_A processes, G_0 and G_2 have different angular distributions. Figure 4.71 (from [49]) shows the angular correlation coefficient between the electrons emitted in the $2\nu\beta\beta$ decay of ^{82}Se, ^{96}Zr, ^{100}Mo, ^{116}Cd and ^{150}Nd, as functions of ξ_{31}. The blue circles represent the values of the correlation in case of an SSD value of the ξ_{31}.

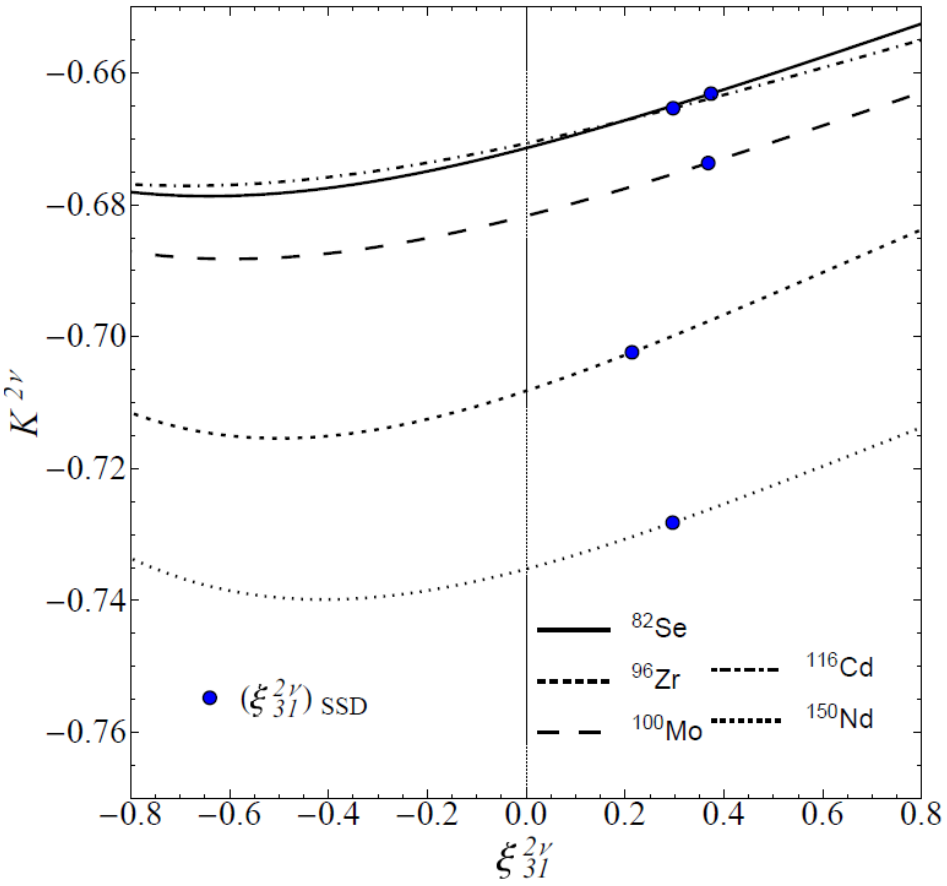

Figure 4.71 – Angular correlation coefficient between the electrons emitted in the $2\nu\beta\beta$ decay of ^{82}Se, ^{96}Zr, ^{100}Mo, 116Cd and ^{150}Nd, as functions of ξ_{31}. The blue circles represent the values of the correlation in case of an SSD value of the ξ_{31}.

But the study of the angular distribution is not easy. Equation 4.22 defines the angular correlation (from [49], equation 26), where H_i and G_i (i=0,2,22,4) are phase space factors, and ξ_{51}, similarly to ξ_{31}, is a ratio of matrix elements defined in the beginning of this chapter.

$$K^{2\nu}(\xi_{31},\xi_{51}) = -\frac{H_0 + \xi_{31}H_2 + \frac{5}{9}\xi_{31}^2 H_{22} + (\frac{2}{9}\xi_{31}^2 + \xi_{51})H_4}{G_0 + \xi_{31}G_2 + \frac{1}{3}\xi_{31}^2 G_{22} + (\frac{1}{3}\xi_{31}^2 + \xi_{51})G_4} \tag{4.22}$$

To perform a thorough analysis, we need to apply the full parameters of equation (4.22), which leads to a complicated analysis with two free parameters ξ_{31} and ξ_{51}, and the distributions of all the phase space factors. But even if we neglect higher order terms, we need to make different simulations for each input ξ_{31} value. The strategy will be quite different compared to the analysis performed

using energy distributions. Taking another look at figure 4.71, we can also see that there is a small dependency between the angular correlation coefficient and the ξ_{31} values.

To conclude, I found that the best method to retrieve the ξ_{31} factor to study the sensitivity is by fitting the minimum energy distribution, while subtracting the background from the sample. Results were extracted for the standard energy threshold cut at 300 keV. Adding, A study was performed taking into account the energy quenching that happens in the scintillators to check the stability of the results. These results show that with minimum energy distribution, and with the case of confirming the SSD case experimentally, we can exclude the theoretical models that are Shell Model and QRPA at 95$\%$ C.L. These results needs to be confirmed while using the decay rate equation with the higher order terms taken into account. This kind of precision and exclusion is not possible while using total energy distribution ; which gives an advantage for tracker-calorimeter experiments (single energy measurements) like SuperNEMO over other experiments using only calorimeter (total energy measurements) detectors.

Conclusion

The observation of the hypothetical neutrinoless double beta decay ould determine the Majorana nature. This means that we will be able to explain the matter anti-matter asymmetry in the universe.

SuperNEMO uses a unique tracker-calorimeter detection method, it is able to study double beta isotopes with highly efficient particle identification with the study of the full kinematics of the decay, all in an ultra-low background environment.

To make sure that the calorimeter is working well, I performed the calibration in time of each individual optical module. This was carried out by using a ^{60}Co source that emits simultaneously two gammas. The calibration and several background studies were performed to find the perfect cut on the taken data. The final results were presented with respect to a reference optical module of choice. The precision on these results was better than 0.2 ns, which is good enough to make time of flight calculations for background reduction. The complete and more precise time alignment of the calorimeter will be later finalized, using crossing electron events using the ^{207}Bi calibration source.

Also, using the same data, I extracted the time resolution per optical module for gammas at 1 MeV. The results corresponded to what we expect for gammas ($\sim$ 600 ps), with the systematic errors retrieved from varying the cuts made of the data.

The sensitivity of SuperNEMO to the quenching of the axial-vector coupling constant (g_A) was also studied using SM allowed double beta decay. I implemented in the SuperNEMO simulation the different phase-space factors of the double beta with two-neutrinos emission, using calculations provided by theoreticians and validated this implementation. Then I determine the optimal method of SuperNEMO demonstrator to constrain this quenching and its sensitivity. For that, I created psuedo-data samples simulated in the SuperNEMO environment (geometry and background), and received from theoreticians the different energy spectra of the phase space factors connected to g_A (G_0 and G_2) from theoretical calculations. I performed several studies and fitting procedures : with background and without it, using single observable fits or simultaneous observable fits. From the different methods tried, I eventually found out which one gives the most efficient results, i.e where SuperNEMO is the most sensitive to the quenched value of g_A. The most efficient method was the single observable fit of the minimal energy distribution of the psuedo-data samples, while subtracting the background contribution from the sample.

The method finally takes into account the quenching of light, which appears inside the scintillators. This study followed the same methods mentioned. Eventually the final results concluded that we are able to set accurate limits on the g_A quenching factor and exclude nuclear models that aim to describe the nuclear

decay. If the Single State Dominance is true, the SuperNEMO demonstrator could exclude at 2σ the theoretical calculations from Shell Model and QRPA, confirming the higher sensitivity provided by a tracko-calo like detector.

5 - Résumé Français

5.1 . Introduction

La désintégration double beta ($2\nu\beta\beta$) est une désintégration radioactive premise par le Modèle Standard. Elle a été obserée pour 12 isotopes, et se caractérise par l'émission de 2 électrons et 2 anti-neutrinos électronique.

Comme le neutrino est une particule neutre électriquement, il pourrait être identique à son antiparticule. Dans ce cas c'est une particule Majorana. Le moyen d'identifier la nature des neutrinos est la détection de la désintégration double beta sans neutrinos ($0\nu\beta\beta$), présentée dans la figure 5.1. C'est une désintégration radioactive hypothétique au-delà du Modèle Standard, caractérisée par la violation du nombre leptonique et l'émission de deux électrons et aucun antineutrino électronique.

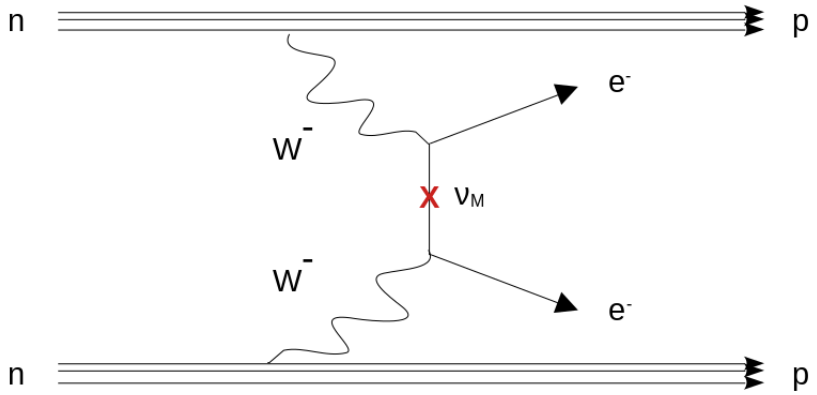

Figure 5.1 – La désintégration double beta sans l'émission de neutrinos, ici généré par le mécanisme d'échange d'un neutrino de Majorana léger. Ce processus est interdit par le Modéle Standard. Il est caractérisé par l'emission de 2 électrons dont l'énergie est égale à l'énergie libérée dans la réaction.

La signature expérimentale de cette désintégration est un pic à la fin du spectre de l'énergie des électrons émis par désintégration $2\nu\beta\beta$, voir figure 5.2. Pour bien voir ce pic, il est nécessaire que l'éxperience ait un bruit de fond extrêmement faible et une bonne résolution en énergie.

SuperNEMO est une expérience qui recherche cette désintégration. C'est une expérience unique qui a la source double beta, le tracker et le calorimetre separés. Cela permet la détection de l'énergie individuelle de chaque particule, le temps d'arrivée dans le calorimètre des électrons et ainsi une reconstruction complète de la topologie.

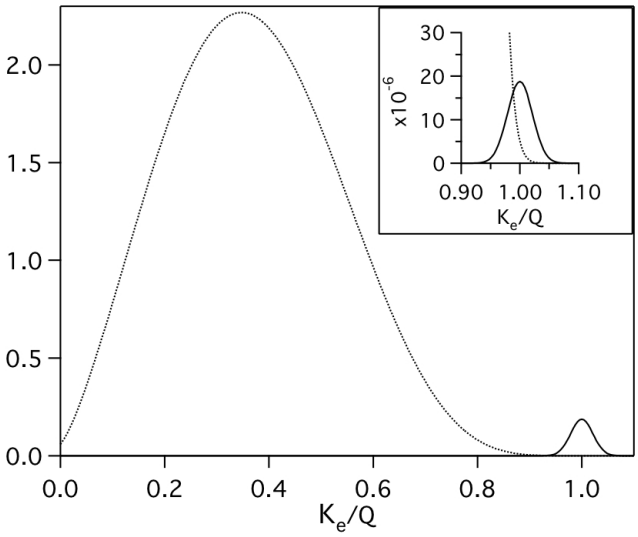

Figure 5.2 – La signature de la désintégration $0\nu\beta\beta$. C'est un pic à la fin du spectre de la somme des énergies des électrons émis par la désintégration $2\nu\beta\beta$

5.2 . SuperNEMO

SuperNEMO utilise la méthode tracko-calo pour la détection de la désintégration, voir figure 5.3. La désintégration se produit dans la source double beta, et ensuite chaque particule est détectée par le tracker où la trajectoire est reconstruite. Enfin, l'énergie et le temps de détection sont aussi enregistrés par le calorimetre.

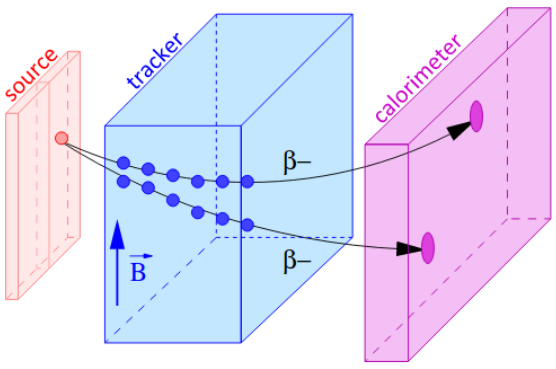

Figure 5.3 – La méthode de détection de SuperNEMO où la source, le tracker et le calorimetre sont séparés.

La source utilisée est une feuille source double bêta, principalement composée

de ^{82}Se, avec un $Q_{\beta\beta}$ = 2.998 MeV. Le tracker est une chambre à dérive à fil, avec des cellules fonctionnant en mode Geiger. La chambre est remplie avec un gaz composé à 95% d'Heluim.

Le calorimetre est consiste en 712 modules optiques en plastique intégrés dans des murs. La résolution énérgetique est 8% FWHM pour electrons à 1 MeV. La resolution temporelle pour electrons devrait etre moins de 400 ps pour des electrons à 1 MeV.

Toute la configuration sera entourée par une tente anti-Radon pour empecher la diffusion de Radon à l'intérieur du detecteur. L'ensemble sera placé à l'intérieur d'un blindage va entouré par un blindage en fer pour empecher les rayons gammas provenant de l'extereur. Enfin, un deuxième blindage contre les neutrons les thermalise pour qu'ils n'interagissent pas dans le détecteur.

5.3 . Caractérisation Temporelle du Calorimeter

Quand cette étude a été faite, le tracker ne fonctionnait pas, et le blindage n'etait pas installé.

Cette étude a été effectuée avec une source de ^{60}Co placée derrière le calorimètre. La source émet deux gammas à peu près instantanés, avec des énergies connues, et l'énergie déposée par les deux gammas sont enregistrées par le calorimetre ansi que le temps de détection (figure 5.4).

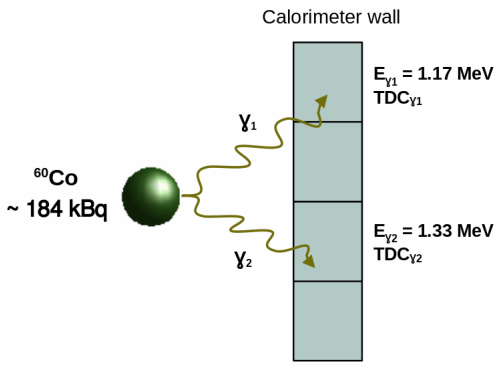

Figure 5.4 – L'emplacement de la source ^{60}Co derriere le calorimetre. La source émet deux gammas peuvent être détectés, et pour lesquels l'énergie déposée et le temps d'interaction sont enregistrés.

En étudiant la coincidence entre les modules optique (OM) differents, nous pouvons aligner en temps chaque OM vis-à-vis d'un OM de référence, et connaitre la résolution temporelle aussi. Les temps enregistrés par deux OMs sont respectivement nommés $t_{\gamma 1}$ et $t_{\gamma 2}$, et on note par Δ(t) la difference entre le deux :

$$\Delta(t) = t_{\gamma 1} - t_{\gamma 2} \tag{5.1}$$

Un ajustement de l'écart temporel entre les deux temps détectés est effectué, pour toutes les coïncidences détectées entre deux OMs, à l'aide d'une gaussienne comme en figure 5.5. La moyenne permet de calibrer en temps les OMs, tandis que le sigma sert à déterminer la résolution temporelle.

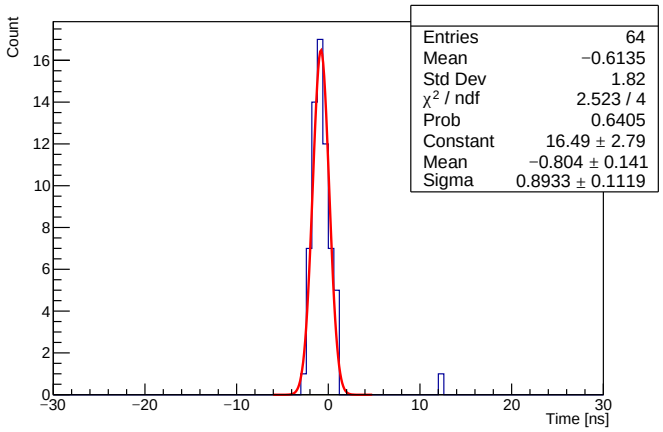

Figure 5.5 – Différence de temps entre deux OMs déclenchés par l'interaction de 2 gammas de la source de ^{60}Co entre deux OMs en coincidence. Le plot correspond à un OM choisi par hasard.

5.3.1 . Calibration du Temps

L'alignement en temps de chaque OM se fait relativement à un OM de référence : un pour chaque mur, et un pour les X-Walls et G-Vetos. Les retards entre chaque OMs correspondent à ce qui est attendu compte-tenu des retards induits par les longueurs des câbles qui relient les OMs aux cartes électronique.

La résultat final de la calibration est presentée dans les figures 5.6, 5.7, 5.8 et 5.9. La précision de ces mesures est mieux que 0.2 ns, suffisamment bonne pour faire un rejection de bruit de fond avec les calculs de temps de vol.

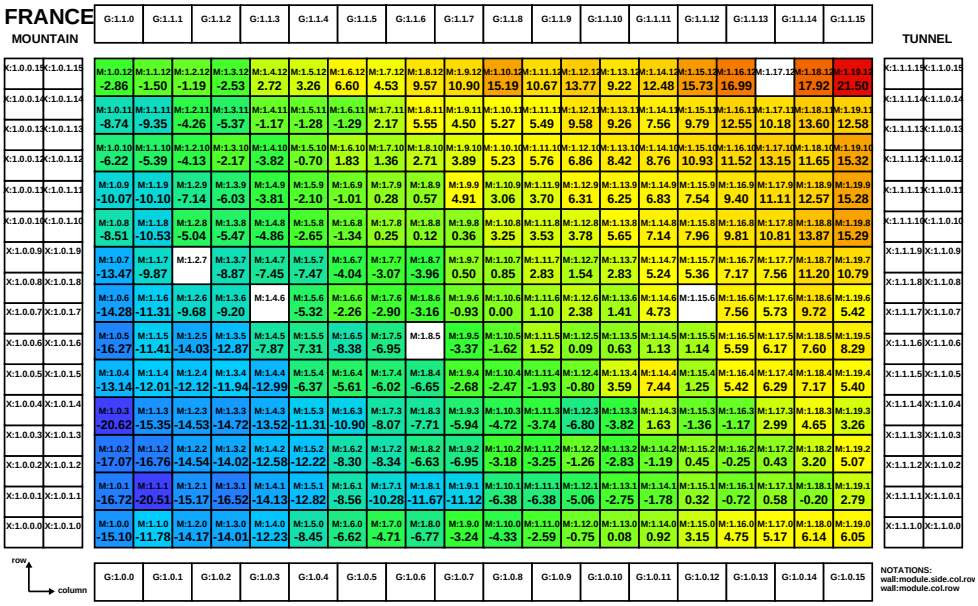

Figure 5.6 – Valeurs finales de décalage par rapport au zero pour chaque OM en ns de la French Main Wall. par rapport à un OM de référence.

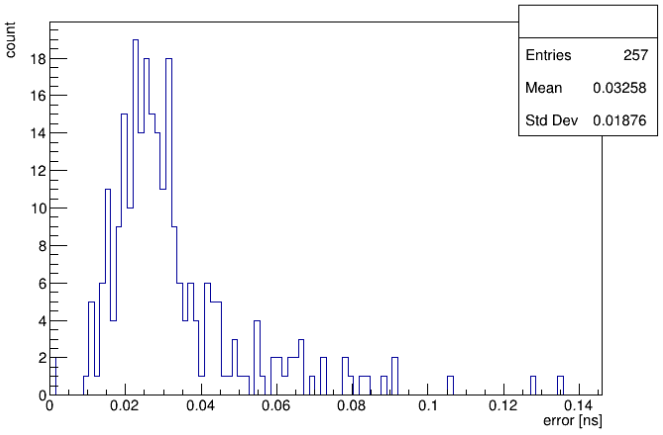

Figure 5.7 – Distribution de l'erreur sur le décalage temporel pour les OMs du mur principal, en ns.

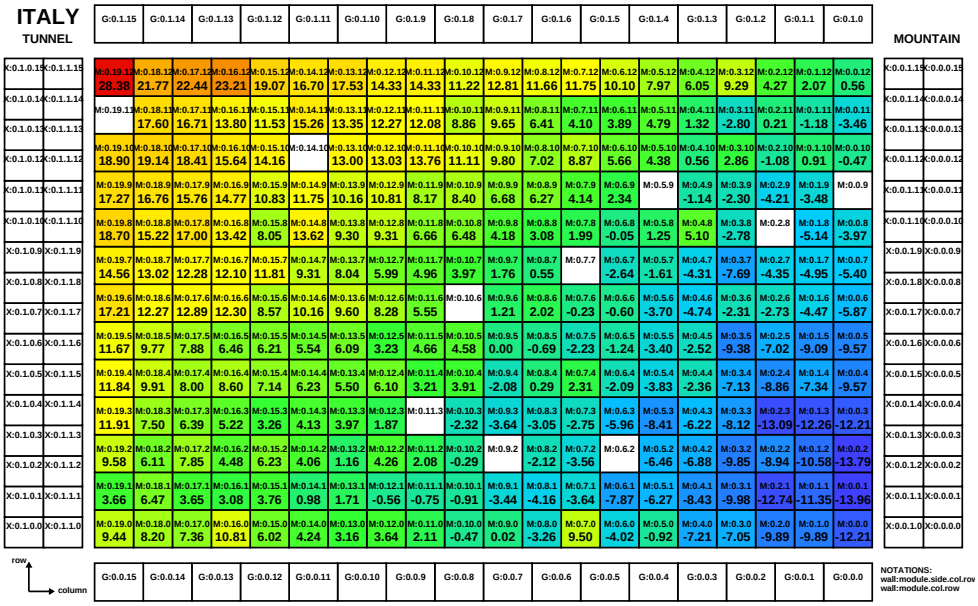

Figure 5.8 – Décalage temporel (en ns) pour les OMs du mur italien.

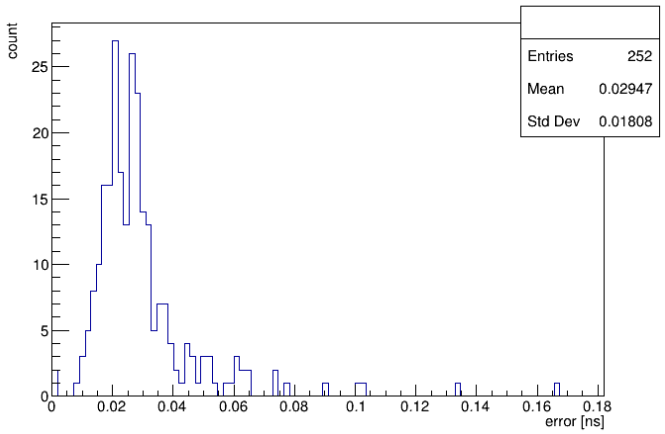

Figure 5.9 – Distribution de l'erreur en ns sur le décalage temporel pour les OMs du mur italien.

5.3.2 . Résolution Temporelle de Gammas de la Calorimeter

La résolution temporelle de gammas à 1 MeV a été déterminée pour chaque mur :

Mur français : 0.619 ± 0.002 (stat) + 0.049(sys) – 0.004(sys)

Mur italien : 0.614 ± 0.002 (stat) + 0.064 (sys) – 0.000 (sys)

Cette détermination a été obtenue pour des gammas, pour lesquels l'interaction en profondeur dans le bloc du scintillateur dégrade la précision temporelle par

rapport à des électrons qui interagissent en surface.

5.4 . Sensibilité de SuperNEMO au Quenching de la constante de couplage axial-vecteur

le problème du quenching de la constante de couplage axial-vecteur, qui pouvait fortement affecter le taux de désintégration bêta sans émission de neutrinos, a été soulevé. Des théoriciens ont calculé de manière plus précise le taux de désintégration $2\nu\beta\beta$. Presentée dans l'article [56], la formule complete du taux est présentée, mais ici je présente l'équation simplifiée considérée dans notre étude :

$$(T^{2\nu}_{1/2})^{-1} \simeq (g_A^{eff})^4 |M^{2\nu}_{GT-3}|^2 \frac{1}{|\xi_{31}|^2}(G_0 + \xi_{31} G_2) \tag{5.2}$$

où g_A^{eff} est la valeur efficace de la constante du couplage axial-vector. M_{GT-3} est l'élément de matrice nucléaire, il décrit le déroulement de la désintégration nucléaire et les différents effets nucléaires. G_0 et G_2 sont facteurs de deux l'espaces de phase. Ils ont chacun une cinématique différente (énergies électroniques individuelles et distributions angulaires). Le parametre ξ_{31} détermine la contribution des deux espaces de phase. Connaître la valeur de ce paramètre permet une contrainte sur la valeur de g_A.

La valeur de g_A peut être différente pour les neutrons qui subissent l'interaction faible dans un noyau qui se désintégre par double bêta par rapport aux neutrons libres, ce qui peut entraîner une "quenching" de la constante de couplage g_A. La demi-vie de $\beta\beta$ dépend de la valeur de g_A à la puissance 4, donc toute incertitude sur la valeur de g_A est interprétée comme une grande incertitude sur la valeur de demi-vie. Ainsi, déterminer précisément la valeur de g_A et appliquer des contraintes est important pour le développement d'expériences sensibles.

SuperNEMO a la capacité de définir des contraintes et de rejeter des modèles théoriques pour une description et une mesure plus précises du processus de désintégration.

5.4.1 . Methode de l'étude de la Sensibilité

Pour déterminer la sensibilité de SuperNEMO, nous avons crée des échantillons de pseudo-données contenant des évenements reconstruits simulés dans l'environnement du détecteur. Ces échantillons contiennent des événements des deux processus d'espaces de phases différent : G_0 et G_2 dont ka contribution relative est déterminée par la valeur de ξ_{31}, ansi que des bruits de fonds internes et externes provenant de la contamination des feuilles sources, des modules optiques et du fond Radon. Un ensemble de coupures a été appliqué sur ces échantillons de pseudo-données pour avoir la meilleure efficacité de sélection des deux événements électroniques. Un échantillon est présenté dans la figure 5.10.

Je prends la distribution d'énergie des pseudo-données échantillons, puis je leur soustrais le bruit de fond. Idéalement, on se retrouver avec seulement des

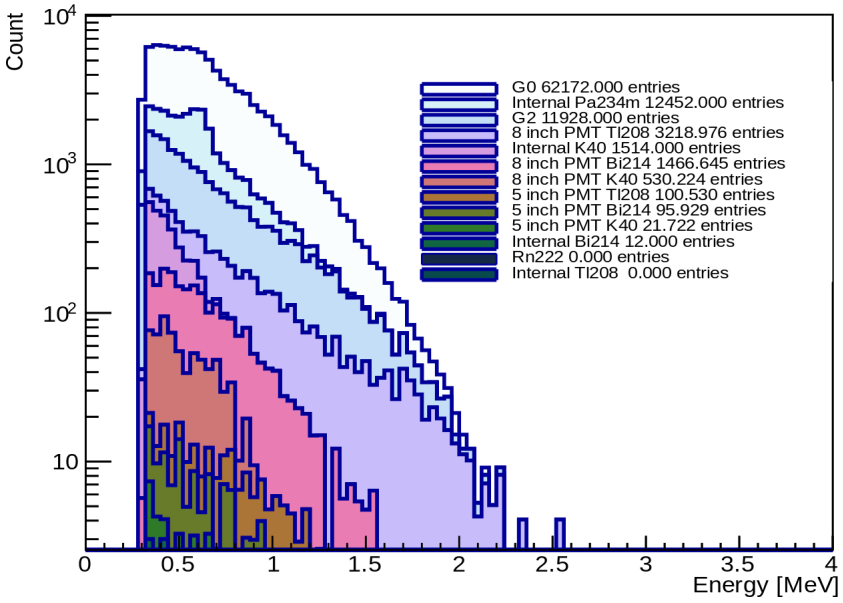

Figure 5.10 – Energies des électrons pour les processus inclus des échantillons de pseudo-données : espaces de phases G_0 et G_2 pour la $2\nu\beta\beta$, bruits de fond. La coupure sur l'énergie minimale est de 300 keV et la valeur de ξ_{31} est 0.37.

événements G_2 et G_0. Ensuite, en prenant le PDF (Probability density function) de G_0 et G_2 et en ajustant les échantillons soustraits, nous pouvons extraire à nouveau la contribution de chacun des deux processus. Puis, en recalculant le ξ_{31} à travers :

$$\xi_{31}^{extrate} = \frac{Contribution\ de\ G_2\ extraite}{Contribution\ de\ G_0\ extraite} \times \frac{Efficacit\ de\ slection\ de\ G_0}{Efficacit\ de\ slection\ de\ G_2} \quad (5.3)$$

5.4.2 . Résultats Sans l'Application du Quenching Énergétique du Scintillateur

La meilleure méthode trouvée pour déterminer la valeur de ξ_{31} consiste à ajuster la distribution d'énergie minimale des échantillons. Plusieur modeles nucléaires offerent une description de la désintégration. Parmi ces mdeles, nous choisissons : Single State Dominance (SSD) et Higher State Dominance (HSD), qui correspondent aux valeurs respectives du paramètre ξ_{31} = 0,373 ou 0.

Dans notre étude, nous avons utilisé ces valeurs dans la génération des pseudo-données et dans l'éxtraction de ξ_{31}. Les erreurs statistiques sont tirées des ajustements et de la variation systématique de la coupure du seuil d'énergie. Une visualisation des résultats est montrée dans la figure 5.11. Les résultats obtenus sont :

- **SSD (ξ_{31} = 0.373) à 300 keV :** ξ_{31} = 0.365 $\pm$ 0.039 (stat) - 0.037 (sys) + 0.001 (sys)

- **HSD (ξ_{31} = 0.00) à 300 keV** : ξ_{31} = 0.0085 $\pm$ 0.029 (stat) - 0.0047 (sys)

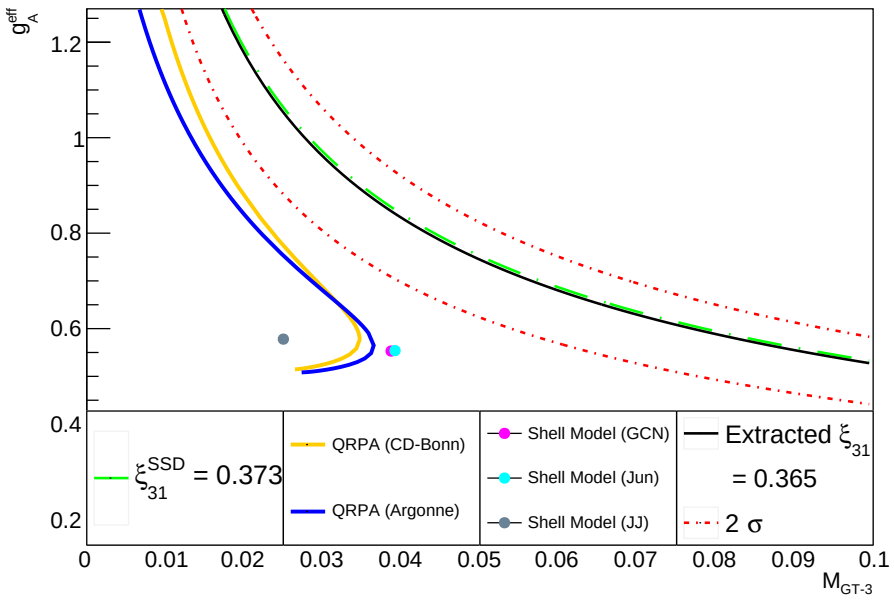

Figure 5.11 – Les valeurs possibles de g_A^{eff} en fonction de M_{GT-3}. La valeur correspondant au SSD pour ^{82}Se est tracée en vert clair. Les modèles théoriques du QRPA et du Shell Model sont aussi présentés. La courbe correspondant aux résultats extraits pour une entrée ξ_{31} = 0,37 est représentée en trait noir plein, pour laquelle l'ajustement ξ_{31} utilisant la distribution d'énergie minimale donne la valeur ξ_{31} = 0,365 $\pm$ 0,039 (statistique) - 0,037 (sys) + 0,001 (sys). Les erreurs statistiques et systématiques sont également représentées par une courbe rouge pointillée. Les erreurs statistiques sont multipliées par 1,264 (la valeur du sigma de la distribution pull) qui représente la sous-estimation des erreurs extraites.

5.4.3 . Resultats Avec l'Application du Quenching Énergétique du scintillateur

L'analyse précédente n'était pas exactement réaliste car elle ne tenait pas compte du quenching de la lumière qui se produit dans les scintillateurs. Le phénomène apparaît pour les électrons de basse énergie. Ainsi, une distorsion du spectre est attendue par cette non-linéarité lumineuse, plus la densité d'ionisation locale déposée est élevée (particules à faible énergie), plus le quenching est important. En plus du quenching de la lumière, une lumière supplémentaire induite peut être produite pour les électrons au-dessus d'une énergie donnée. Ceci conduit à un excès de lumière détectée par rapport à la lumière attendue par scintillation, et à une

surestimation de l'énergie.

Sur la figure 5.12, trois graphiques sont présentés : le bleu représente la valeur moyenne de la correction de l'énergie, les deux autres représentent la correction décalée vers son erreur supérieure (rouge) et la correction décalée vers son erreur inférieure (vert). La correction du quenching d'énergie est appliquée sur les énergies individuelles des électrons des événements des échantillons. Ensuite, l'analyse est effectuée trois fois sur les mêmes échantillons avec la correction moyenne, en appliquant une PDF d'ajustement avec soit la correction moyenne, soit la correction décalée des erreurs supérieures ou inférieures. Ceci sera effectué pour les différentes méthodes d'ajustement pour enfin pouvoir trouver la meilleure méthode pour extraire la sensibilité.

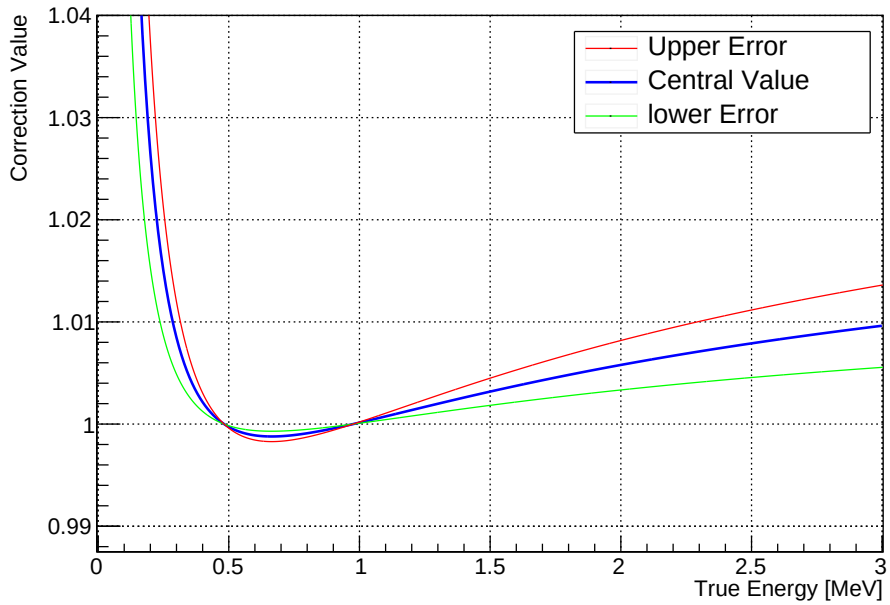

Figure 5.12 – Fonction de correction qui doit être appliquée au spectre d'énergie des électrons pour tenir compte de la quenching de la lumière de scintillation. Cette correction tient compte des deux points d'étalonnage de ^{207}Bi, assurant une bonne linéarité entre les deux points à 0,482 MeV et 0,976 MeV.

Nous trouvons la sensibilité de SuperNEMO aux valeurs HSD et SSD à $\xi_{31} = 0$ et $\xi_{31} = 0{,}373$. Utilisant l'ajustement de la distribution d'énergie minimale avec soustraction de bruit de fond.

Je présente les résultats extraits de l'analyse dans le cas de SSD et HSD :

- **SSD ($\xi_{31} = 0.373$) à 300 keV** : $\xi_{31} = 0.3669 \pm 0.0393$ (stat) + 0.0007 (sys coupure énergie) - 0.0392 (sys coupure énergie) + 0.0401 (sys quench) - 0.0384 (sys quench)

- **HSD (ξ_{31} = 0.00) à 300 keV** : ξ_{31} = 0.00865 $\pm$ 0.03261 (stat) + 0.00221 (sys coupure énergie) - 0.00589 (sys coupure énergie) + 0.00728 (sys quench) - 0.03181 (sys quench)

Les résultats SSD sont présentés dans la figure 5.13, où la valeur effective de g_A est tracée par rapport aux calculs des éléments de la matrice nucléaire M_{GT-3}. La courbe pour la valeur SSD à 0,373 est tracée en vert. Le résultat de cette étude est tracé en noir uni. Les erreurs de ce graphique représentent en rouge pointillé l'erreur 2σ pour 95% C.L. L'erreur statistique a été multipliée par 1,37, ce qui représente le sigma de la distribution de pull pour les ajustements à une coupure d'énergie de 300 keV.

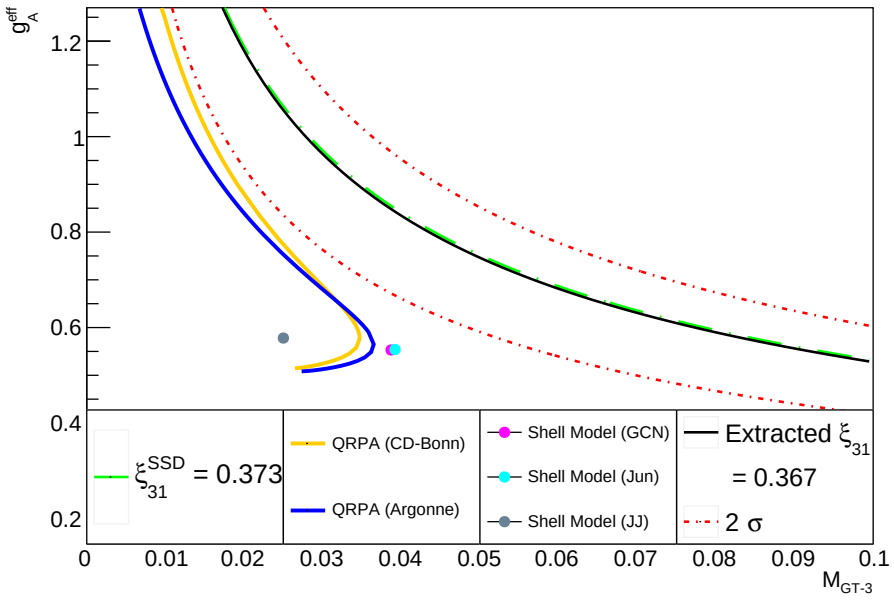

Figure 5.13 – Valeurs possibles de g_A^{eff} par rapport à M_{GT-3}. La valeur SSD pour ^{82}Se est tracée en vert clair. Les modèles théoriques du QRPA et du modèle shell sont présentés. La valeur ajustée de l'analyse SuperNEMO est indiquée dans le cas où nous prenons en compte la quenching d'énergie à l'intérieur du scintillateur, où la valeur est ξ_{31} = 0,3669 $\pm$ 0,0393 (stat) + 0,0007 (sys energy cut) - 0.0392 (sys energy cut) + 0.0401 (sys quench) - 0.0384 (sys quench). Les erreurs tracée en rouge. L'erreur statistique dans le tracé est multipliée par 1,37, ce qui correspond au sigma de la distribution pull. Cette valeur représente la sous-estimation dans les calculs d'erreur.

Une étude plus poussée peut être réalisée pour voir comment la sensibilité évolue avec l'ajout des deux facteurs d'espace des phases non pris en compte lors

de cette analyse, G_{22} et G_4 ; et donc l'ajout d'un deuxième paramètre libre qui est ξ_{51}, ce qui augmenterait l'incertitude des calculs.

5.5 . Conclusion

Pour conclure, j'ai travaillé sur la caractérisation du calorimètre en termes de la calibration temporelle. La précision de ces mesures était mieux que 0.2 ns. La résolution temporelle est trouvée en utilisant des gammas émis par une source de ^{60}Co. J'ai également étudié la sensibilité du démonstrateur SuperNEMO au quenching de la constante de couplage du axial-vecteur g_A, et j'ai trouvé que l'utilisation de la distribution d'énergie minimale donne la meilleure sensibilité à la valeur de g_A. A terme, SuperNEMO pourra imposer des contraintes sur la valeur des paramètres et rejeter des modèles nucléaires.

Bibliographie

[1] Kibble, T. Spontaneous symmetry breaking in gauge theories. *Philosophical Transactions Of The Royal Society A : Mathematical, Physical And Engineering Sciences*. **373**, 20140033 (2015)

[2] M. Tanabashi et al. (Particle Data Group), Phys. Rev. D 98, 030001 (2018) and 2019 update.

[3] The W and Z at LEP, 3 May 2004
https://cerncourier.com/a/the-w-and-z-at-lep/

[4] E. Fermi, Versuch einer Theorie der β-Strahlen. I, Zeitschrift für Physik vol. 88, no. 3, (1934) 161–177.

[5] Webb, Jonathan (6 October 2015). "Neutrino 'flip' wins physics Nobel Prize". BBC News. Retrieved 6 October 2015.

[6] 1967 Brookhaven National Lab press release.
https://www.bnl.gov/bnlweb/raydavis/research.htm

[7] Neutrinos : Majorana or Dirac ?, S. M. Bilenky, oint Institute for Nuclear Research, Dubna, R-141980, Russia, arXiv :2008.02110 [hep-ph].

[8] M. Aker et al., First direct neutrino-mass measurement with sub-eV sensitivity, arXiv :2105.08533 [hep-ex]

[9] M. Tanabashi et al.(Particle Data Group), Phys. Rev. D98, 030001 (2018).

[10] M. Goeppert-Mayer, Double Beta-Disintegration, Phys. Rev. 48, 512

[11] Planck Collaboration, N. Aghanim et al., Planck 2018 results.VI. Cosmological parameters, arXiv :1807.06209.

[12] M.Turk, in Proceedings of the 7th Python in Science Conference, Pasadena, CA, 2008, edited by G. Varoquaux, T. Vaught, and J. Millman, pp. 46-50

[13] Neutrinos in Cosmology
https://pdg.lbl.gov/2020/reviews/rpp2020-rev-neutrinos-in-cosmology.pdf

[14] Michael Moe, The First Direct Observation of Double-Beta Decay, Annual Review of Nuclear and Particle Science, Vol. 64 :247-267 (Volume publication date October 2014)
https://doi.org/10.1146/annurev-nucl-102313-025411

[15] Benjamin J. P. Jones, The Physics of Neutrinoless Double Beta Decay : A Primer, arXiv :2108.09364v1 [nucl-ex] 20 Aug 2021.

[16] Michael Duerr, Manfred Lindner, Alexander Merle, On the Quantitative Impact of the Schechter-Valle Theorem, arXiv :1105.0901 [hep-ph]

[17] Andrea Giuliani, Alfredo Poves, "Neutrinoless Double-Beta Decay", Advances in High Energy Physics, vol. 2012, Article ID 857016, 38 pages, 2012. https://doi.org/10.1155/2012/857016

[18] J. D. Vergados, H. Ejiri, F. Simkovic, Theory of neutrinoless double beta decay arXiv :1205.0649v2 [hep-ph], 5 Jun 2012.

[19] Ejiri Hiroyasu,Nuclear Matrix Elements for β and $\beta\beta$ Decays and Quenching of the Weak Coupling gA in QRPA, Frontiers in Physics vol. 7 2019, DOI=10.3389/fphy.2019.00030.

[20] Michelle J. Dolinski, Alan W.P. Poon and Werner Rodejohann, Neutrinoless Double-Beta Decay : Status and Prospects, nnu. Rev. Nucl. Part. Sci. 2019. 69 :219–51.

[21] Walter Pfeifer, An Introduction to the Interacting Boson Model of the Atomic Nucleus, https://arxiv.org/pdf/nucl-th/0209039.pdf , 1998.

[22] Y. F. Niu, G. Colo, E. Vigezzi, C. L. Bai, H. Sagawa, Quasi-particle random phase approximation with quasi-particle-vibration coupling : application to the Gamow-Teller response of the superfluid nucleus 120Sn arXiv :1609.02341 [nucl-th].

[23] Jouni T. Suhonen, Value of the Axial-Vector Coupling Strength in β and $\beta\beta$ Decays : A Review, Frontiers in Physics vol. 5 2017, DOI=10.3389/fphy.2017.00055.

[24] KamLAND-Zen Collaboration, Precision measurement of the ${}^{136}_{0}Xe$ two-neutrino $\beta\beta$ spectrum in KamLAND-Zen and its impact on the quenching of nuclear matrix elements, 12 Jan 2019, arXiv :1901.03871v1 [hep-ex].

[25] R. Arnold et al., Final results on 82 Se double beta decay to the ground state of 82 Kr from the NEMO-3 experiment, Eur. Phys. J. C (2018) 78 :821 https://doi.org/10.1140/epjc/s10052-018-6295-x

[26] F. Simkovic, R. Dvornicky, D. Stefanik, and A. Faessler, Phys. Rev. C 97, 034315 (2018).

[27] J D Vergados, H Ejiri and F Simkovic, Theory of neutrinoless double beta decay, Reports on Progress in Physics

[28] M. Agostini et al. (GERDA Collaboration), Final Results of GERDA on the Search for Neutrinoless Double-Beta Decay, Phys. Rev. Lett. 125, 252502 – Published 17 December 2020

[29] Hans Volker Klapdor-Kleingrothaus, First Evidence for Neutrinoless Double Beta Decay - and World Status of Double Beta Experiments, arXiv :hep-ph/0512263

[30] J.M.López-Castaño, Recent Results of the Majorana Demonstrator Experiment, arXiv :1909.07509 [hep-ex]

[31] Abgrall N. et al. The large enriched germanium experiment for neutrinoless double beta decay (LEGEND), https://publications.jrc.ec.europa.eu/repository/handle/JRC107882

[32] CUORE Collaboration, Improved Limit on Neutrinoless Double-Beta Decay in 130Te with CUORE, arXiv :1912.10966 [nucl-ex]

[33] D. Chiesa et al. Double beta decay results from the CUPID-0 experiment, arXiv :2012.00644 [nucl-ex]

[34] V. Alenkov et al. First Results from the AMoRE-Pilot neutrinoless double beta decay experiment, arXiv :1903.09483 [hep-ex]

[35] G. Anton et al., Search for Neutrinoless Double-Beta Decay with the Complete EXO-200 Dataset, arXiv :1906.02723 [hep-ex]

[36] nEXO Collaboration, nEXO : Neutrinoless double beta decay search beyond 1028 year half-life sensitivity, arXiv :2106.16243 [nucl-ex]

[37] J.J.Gomez-Cadenason behalf of theNEXT collaboration, The NEXT experiment, Nuclear and Particle Physics Proceedings Volumes 273–275, April–June 2016, Pages 1732-1739, https://doi.org/10.1016/j.nuclphysbps.2015.09.279

[38] KamLAND-Zen Collaboration First Search for the Majorana Nature of Neutrinos in the Inverted Mass Ordering Region with KamLAND-Zen. (arXiv,2022), https://arxiv.org/abs/2203.02139

[39] Y. Fukuda, Y.Kamei, Narengerile, A.Obata, S. Moriyama, I.Ogawa, T. Gunji, R. Hayami and S.Tsukada, ZICOS - A new project for neutrinoless double beta decay using Zirconium complex in organic liquid scintillator, Journal of Physics : Conference Series, 1342 (2020) 012093, doi :10.1088/1742-6596/1342/1/012093

[40] K. Tetsuno et al., Status of 48Ca double beta decay search and its future prospect in CANDLES, 2020 J. Phys. : Conf. Ser. 1468 012132

[41] The SuperNEMO Collaboration, The BiPo-3 detector for the measurement of ultra low natural radioactivities of thin materials, 2017, arXiv :1702.07176 [physics.ins-det]

[42] Steven Calvez, Gamma-tracking and sensitivity to gamma-emitting backgrounds in SuperNEMO, PoS(ICHEP2016)1025, DOI :10.22323/1.282.1025

[43] Thomas Poschl, Daniel Greenwald, Martin J. Losekamm, Stephan Paul, Measurement of ionization quenching in plastic scintillators, arXiv :2007.08366v2 [physics.ins-det] 12 Nov 2020

[44] HAMAMATSU PHOTONICS K.K, CHAPTER 10 MCP-PMT, 2007 https://www.hamamatsu.com/content/dam/hamamatsu-photonics/sites/documents/99_SALES_LIBRARY/etd/PMT_handbook_v3aE-Chapter10.pdf

[45] E. Chauveau, K. Lang, M. Macko, C. Macolino, C. Marquet, F. Perrot, M. Proga, R. Salazar, Proposal on the energy calibration setup of the SuperNEMO demonstrator

[46] Girard-Carillo, C. Study of ^{208}Tl background rejection influence on the $0\nu\beta\beta$ decay sensitivity, characterisation of SuperNEMO demonstrator calorimeter timing performance. (2020), http://www.theses.fr/2020UPASP097/document,2020UPASP097

[47] Frédéric Perrot and the CENBG/LSM staff, Radiopurity measurements for 8" PMTs and preliminary budget for the SN demonstrator, SuperNEMO collaboration meeting, Bardonecchia, January 12, 2017

[48] C. Patrignani et al. (Particle Data Group), Review of particle physics, Chin. Phys. C 40 (2016) 100001.

[49] Nitescu, O.; Dvornicky, R.; Stoica, S.; Simkovic, F. Angular Distributions of Emitted Electrons in the Two-Neutrino $\beta\beta$ Decay. Universe 2021, 7, 147. https://doi.org/10.3390/universe7050147

[50] KamLAND-Zen Collaboration, Precision measurement of the 136Xe two-neutrino $\beta\beta$ spectrum in KamLAND-Zen and its impact on the quenching of nuclear matrix elements, Phys. Rev. Lett. 122, 192501 (2019), https://doi.org/10.1103/PhysRevLett.122.192501

[51] M.Sambataro, N.Sandulescu, C.W.Johnson, Isoscalar and isovector pairing in a formalism of quartets, https://doi.org/10.1016/j.physletb.2014.11.036

[52] F Simkovic, P Domin and S.V Semenov, The single state dominance hypothesis and the two-neutrino double beta decay of 100Mo, J.Phys. G 2001, 27, 2233.

[53] NEMO-3 Collaboration, Final results on 82Se double beta decay to the ground state of 82Kr from the NEMO-3 experiment, https://doi.org/10.1140/epjc/s10052-018-6295-x

[54] NEMO3/SuperNEMO Collaboration, Conseil Scientifique IN2P3 Experience SuperNEMO, 25 octobre 2018

[55] RooFit https://root.cern/manual/roofit/

[56] Fedor Simkovic, Rastislav Dvornicky, Dusan Stefanik and Amand Faessler, Improved description of the $2\nu\beta\beta$-decay and a possibility to determine the effective axial-vector coupling constant. DOI : 10.1103/PhysRevC.97.034315

[57] Non-linearities : MIGRAD versus HESSE versus MINOS http://www.fresco.org.uk/minuit/cern/node32.html

[58] The Falaise Git hub directory https://github.com/SuperNEMO-DBD/Falaise

[59] O. Azzolini et al, Evidence of Single State Dominance in the Two-Neutrino Double-β Decay of ^{82}Se with CUPID-0

[60] Private conversations

[61] Internal notes of the collaboration

[62] G Adhikari et al, nEXO : Neutrinoless double beta decay search beyond 1028 year half-life sensitivity, arXiv :2106.16243v2 [nucl-ex] 22 Feb 2022
https://arxiv.org/pdf/2106.16243.pdf

[63] Shaobo Wang, PandaX-III high pressure xenon TPC for Neutrinoless Double Beta Decay search,
https://doi.org/10.1016/j.nima.2019.162439

[64] AMoRE Experiment
https://amore.ibs.re.kr/about/amore-experiment/

[65] Julieta Gruszko, Neutrinoless Double-Beta Decay Searches in Germanium, Neutrino 2022
https://media.neutrino2022.org/talk/talk_session_apply/41/20220531231928_14.pdf

[66] Julieta Gruszko, Neutrinoless Double-Beta Decay Searches in Germanium, Neutrino 2022,
https://media.neutrino2022.org/talk/talk_session_apply/41/20220531231928_14.pdf

[67] Stefan Schönert, Perspectives of future neutrinoless double beta decay experiments, Neutrino 2022,
https://media.neutrino2022.org/talk/talk_session_apply/39/20220531201612_13.pdf

[68] Irene Nutini, Updated results and progresses of the CUORE experiment, Neutrino 2022,
https://media.neutrino2022.org/talk/talk_session_apply/17/20220531161523_12.pdf

[69] Anastasiia ZOLOTAROVA, CUPID and its demonstrators : scintillating bolometers for 0n2b search, Neutrino 2022,
https://media.neutrino2022.org/talk/talk_session_apply/64/20220601170900_10.pdf

[70] LÉONARD IMBERT, Background studies for CUPID-Mo and CUPID $0\nu\beta\beta$ experiments, P2IO MEETING
https://indico.in2p3.fr/event/26463/contributions/106431/attachments/69875/98856/P2IO_meeting_2022_vfinal.pdf

[71] Yoomin Oh, AMoRE, Neutrino 2022,
https://media.neutrino2022.org/talk/talk_session_apply/21/20220602103043_13.pdf

[72] J.B. Albert et al, Search for Neutrinoless Double-Beta Decay with the Upgraded EXO-200 Detector, arXiv :1707.08707v1
https://doi.org/10.1103/PhysRevLett.120.072701

[73] nEXO Collaboration, NEXO : Neutrinoless double beta decay search beyond 1028 year half-life sensitivity
https://doi.org/10.1088/1361-6471/ac3631

[74] Michel Sorel, Gaseous detectors for neutrinoless double beta decay searches : NEXT and PandaX-III, Neutrino 2022,
https://media.neutrino2022.org/talk/talk_session_apply/26/20220531043815_5.pdf

[75] Azusa Gando, KamLAND-Zen, Neutrino 2022,
https://media.neutrino2022.org/talk/talk_session_apply/20/20220530190936_4.pdf

[76] Pia Loaiza, BiPo Status, Orsay collaboration meeting presentation, 18th April 2018
http://nile.hep.utexas.edu/DocDB/ut-nemo/docs/0046/004651/001/BiPo_status_Orsay_avril_2018.pdf

[77] Birks Law
https://en.wikipedia.org/wiki/Birks%27_law